Author:
Ball, Emily R

Title:
The dynamics of polar vortices and jets on Mars and beyond

investigating large-scale atmospheric circulation on terrestrial planets

The dynamics of polar vortices and jets on Mars and beyond

Investigating large-scale atmospheric circulation on terrestrial planets

By

EMILY R. BALL

School of Geographical Sciences
UNIVERSITY OF BRISTOL

A dissertation submitted to the University of Bristol in accordance with the requirements of the degree of DOCTOR OF PHILOSOPHY in the Faculty of Science.

APRIL 2023

Word count: 40,770

Abstract

In recent years, there has been a growing appreciation for the value of modelling planetary atmospheres at varying levels of complexity. This 'hierarchical modelling' bridges the gap between theory and fully-comprehensive simulations, and builds physical understanding in a way that is not possible with either one of these alone. Improving understanding of planetary atmospheric dynamics through hierarchical modelling places the circulation patterns seen in Earth's atmosphere in a broader context, and allows deeper insight into which planetary parameters play a key role in driving circulation. This thesis uses an idealised modelling framework to study how both physical processes and planetary parameters impact large-scale atmospheric circulation, with a focus on polar vortices.

First, the modelling framework and reanalysis datasets are employed to study Mars's present-day northern polar vortex. The annularity of this vortex is surprising: such a morphology is expected to be unstable, so its persistence indicates the presence of a restoring mechanism. Here, a process-attribution study investigates the relative roles of possible such mechanisms and compares results to reanalyses.

The modelling framework is subsequently utilised to investigate both northern and southern Martian polar vortices across a range of possible orbital configurations. Mars's orbital parameters have varied substantially across its history; these changes may be linked to the formation of the polar layered deposits. Effective diffusivity, a geometric method used to quantify mixing, is calculated for the first time in Mars's atmosphere in order to quantify the extent to which the polar vortices may act as transport barriers.

Finally, motivated by exoplanetary atmospheres, the range of planetary parameters studied is broadened further still to investigate the relationships between dynamical metrics for tropical width. Given the uncertainty concerning relationships between these metrics in models, reanalyses, and observations in Earth's atmosphere, this study helps to contextualise their coupling in a broader parameter space.

Dedication and acknowledgements

Firstly, I would like to thank my supervisors, Dann and Will, whose support throughout my PhD has been invaluable. To Will, thank you for your endless patience with me and your guidance on some of the more technical aspects of my project. To Dann, thank you for always encouraging me to step back and think about the bigger picture when I was getting lost in those technical details, and for your willingness to chat about fantasy novels with me instead of work. It has been fantastic to work with you both: you have been wonderful mentors and guides, always helping me to see the value in what I was doing when I couldn't see it for myself. Secondly, I am very grateful for the insight and guidance I received from colleagues in Exeter: thanks to my supervisor Geoff, whose engaging discussions always left me full of ideas, and to Stephen, who always had the time of day when I had (a lot of) questions about Isca.

To my amazing friends: there are so many of you that I would like to thank but I will try to keep the list (relatively) short. To the friends I have made in Browns, you have been a wonderful community. In no particular order - to Rebecca, Saskia, Leanne, Erin, Elliot and Annie, Damiano, and Viola: thank you for your friendship and support, as well as all the much-needed (and very frequent) tea and cake breaks. A very special thanks to Isolde, who has put up with living and working with me for nearly four years. Sharing the highs and lows of this experience with you has been a real pleasure, and I am so grateful for all the moral support and encouragement that you have given me. To Elinor, Luca, Claire, Amy, Zoë, and Cai: you have all provided me with so much support, fun, distraction, and inspiration. I can't thank you all enough.

Finally, to my wonderful family: your love and support throughout this journey has meant the world to me. Thank you for always being there for me, and for being my biggest supporters in anything I do.

AUTHOR'S DECLARATION

I declare that the work in this dissertation was carried out in accordance with the requirements of the University's *Regulations and Code of Practice for Research Degree Programmes* and that it has not been submitted for any other academic award. Except where indicated by specific reference in the text, the work is the candidate's own work. Work done in collaboration with, or with the assistance of, others, is indicated as such. Any views expressed in the dissertation are those of the author.

TABLE OF CONTENTS

List of Tables

List of Figures

Figure **Page**

List of Acronyms and Abbreviations

Acronyms and abbreviations in use throughout this thesis (in alphabetical order). Each term is redefined at its first use in an individual chapter if used frequently.

CDOD	Column dust optical depth
EDJ	Eddy-driven jet
EMARS	Ensemble Mars Atmosphere Reanalysis System [Greybush et al., 2012]
GCM	Global climate model (or General circulation model)
GDS	Global dust storm
GFDL	Geophysical Fluid Dynamics Laboratory
HC	Hadley Cell
HS	Held-Suarez [Held and Suarez, 1994]
HiRISE	High Resolution Imaging Science Experiment (aboard MRO)
Isca	Roman name for Exeter, primarily a GCM framework
L_s	(Areocentric) Solar longitude
MACDA	Mars Analysis Correction Data Assimilation [Montabone et al., 2014]
MCS	Mars Climate Sounder (aboard MRO)
MGCM	Mars GCM
MGS	Mars Global Surveyor
MOC	Mars Orbital Camera (aboard MGS)
MOLA	Mars Orbiter Laser Altimeter (aboard MGS)
MPVU	Martian potential vorticity units

MRO	Mars Reconnaissance Orbiter
MY	Martian year
OpenMARS	Open access to Mars Assimilated Remote Soundings [Holmes et al., 2020]
PK	Polvani-Kushner [Polvani and Kushner, 2002]
(N/S)PLD	(North/South) Polar layered deposit
PV	Potential vorticity
SSW	Sudden stratospheric warming
STJ	Subtropical jet
TES	Thermal Emission Spectrometer (aboard MGS)
TPW	Transient polar warming

CHAPTER 1

INTRODUCTION

Recent decades have seen improvements in observational, computational, and modelling capabilities that have allowed the scientific community to understand and simulate dynamical processes in Mars's atmosphere better than ever before. The atmosphere of Mars, both past and present, is a compelling field of study for a multitude of reasons, not least because it exhibits striking circulation patterns. Present-day interannual (or year-to-year) variability is primarily driven by large variations in atmospheric dust abundance, to an extent that is not seen here in Earth's atmosphere. Inherently fascinating processes currently occur in the Martian atmosphere that make it a worthy subject of study. Moreover, studies of Mars's geology, mineralogy and isotopic data reveal that its early climate system could have been warmer, wetter, and with a thicker atmosphere than currently [Haberle et al., 2017a, and references therein]. This more Earth-like climate state may have harboured liquid water at the surface, and is the most likely period in the planet's history in which life may have originated [Haberle et al., 2017b].

The endeavour to understand Mars's past and current climate thus links many areas of research, all of which aim to resolve unanswered questions about the planet and its

evolution. Appreciation of the large-scale features of its atmospheric circulation may be crucial to understanding the formation of geological features and thus past climate, as well as to assessing locations of future lander missions, or even potential habitability. On Earth, it is well understood that atmospheric circulation patterns such as zonal jets, the overturning Hadley circulation, and polar vortices all contribute to the transport and distribution of heat, chemical species, and other atmospheric constituents throughout the atmosphere. Such distributions are important for a number of reasons, including (but not limited to) habitability, the distribution of precipitation, and phenomena such as the stratospheric ozone hole. These circulation patterns on Mars and other planets will no doubt also have an important influence on such distributions, although the relative sparsity of observations means that these influences are less well-studied. How these atmospheric circulation patterns depend on planetary parameters and the physical processes within an atmosphere will be explored within this thesis.

This chapter firstly introduces the atmosphere of Mars in Section 1.1. Secondly, polar vortices and their dynamics on Earth and Mars are described in Section 1.2. The Hadley circulation is discussed in Section 1.3. The primary aims of the thesis are given in Section 1.4 and key methodological choices are explained in Section 1.5. Finally, Section 1.6 outlines the structure of this thesis.

1.1 The atmosphere of Mars

The atmosphere and planetary characteristics of Mars share many similarities with those of Earth: this fact, along with the increasing number of observations available, means that Mars is an ideal test case for theories of planetary atmospheric circulation and climate. Both planets are terrestrial planets with a relatively thin atmosphere: notable similarities include Mars's obliquity (its axial tilt from its orbital plane), its rotation rate, and its mean radius. Mars has radius approximately half the size of Earth's and surface gravity

Parameter	Earth	Mars
Radius (km)	6371.0	3389.5
Rotation Rate (rad s^{-1})	7.29×10^{-5}	7.08×10^{-5}
Obliquity (°)	23.44	25.19
Eccentricity	0.0167	0.0935
Major atmospheric component	78.1% N_2	95.1% CO_2
Average temperature (K)	288	210
Surface gravity (m s^{-2})	9.798	3.71
Surface pressure (hPa)	1014	6.1

Table 1.1: **A comparison of planetary, orbital, and atmospheric parameters on Earth and Mars.**

approximately one third of Earth's. Its atmosphere is thin (with mean surface pressure around 6.1 hPa compared to Earth's 1014 hPa) and cold, with a much smaller greenhouse effect than on Earth. A table comparing various relevant parameters is given (Table 1.1); all of these factors influence the circulation of both atmospheres.

1.1.1 Overview

The atmosphere of Mars is substantially cooler than Earth's and comprises around 95% carbon dioxide (CO_2) by volume, which leads to the interesting phenomenon that its major component is condensible (condensation does indeed frequently occur, particularly during the winter polar night). This is unlike the atmosphere of Earth (whose primary component is nitrogen, N_2, which does not reach pressures or temperatures suitable for condensation on Earth). This difference sets apart the circulation on the two planets as CO_2 condensation on Mars can lead to seasonal atmospheric mass loss of up to 30% [Tillman, 1988], which can have significant dynamical impacts. On Earth, pressure changes due to mass loss from rainfall (water vapour being the main condensible component in Earth's atmosphere) are minor [Pierrehumbert and Ding, 2016].

Mars currently has an obliquity similar to Earth's ($\varepsilon = 25.19°$) but much greater eccentricity (orbital ellipticity; $\gamma = 0.093$). As a consequence of this relatively large eccentricity, seasonality on Mars is much larger; perihelion occurs just prior to Northern Hemisphere (NH) winter solstice. This means both that southern winter lasts much longer than northern (due to orbital speed being larger at perihelion) and that the increased insolation at this time contributes to a more vigorous circulation during northern winter [e.g. Leovy, 2001][1]. In Mars's history, it has undergone significant orbital oscillations, driven in part by proximity to Jupiter and the gravitational perturbations exerted by other solar system planets, and amplified by secular spin-orbit resonances [e.g. Bretagnon, 1974; Forget et al., 2017; Ward and Rudy, 1991]. In the last 10Ma, obliquity has varied between $\varepsilon = 5 - 55°$ (with a significant jump in mean obliquity around 5Ma), and eccentricity between $\gamma = 0 - 0.12$ [Laskar et al., 2002, Fig. 2]. Over the past 4Ga, Mars is thought to have had a most probable obliquity of 42° and eccentricity of 0.068 [Laskar et al., 2004].

Eccentricity is not the only factor leading to large seasonality on Mars. Mars's atmosphere and surface have substantially lower *thermal inertia*[2] than Earth's, and this fact, along with its lack of oceans and lakes, means that its seasonality is much greater than on Earth [Read et al., 2018]. Winds are stronger, reaching over 150 ms^{-1} in the winter-time jet, which extends to high altitudes in reanalyses and models. The jet sits at around 70° latitude and extends throughout the atmosphere. It is tilted toward the pole at higher altitudes [Mitchell et al., 2014; Waugh et al., 2016]. This polar jet may also be referred to as the Martian polar vortex, and will be discussed in more detail in Section 1.2.3.2. A comparatively short *radiative timescale*[3] means that the atmospheric response to radiative

[1] Mars has a hemispheric dichotomy in its topography, with a lower northern hemisphere topography, which is the strongest effect on enhancing northern winter circulation compared to southern [Richardson and Wilson, 2002].

[2] A combination of a substance's thermal conductivity, density, and heat capacity. It represents the ability of a substance to both store and transport heat relative to its environment [Mellon, 2000].

[3] The length of time it takes for a thermal perturbation to relax to its equilibrium. A typical timescale near the surface of Mars might be ~ 1 sol (Martian day, which lasts 24 hours, 39 minutes) compared to ~ 20 days for Earth [Barnes et al., 2017, and references therein], and between 10-40km in altitude it might be $\sim 0.5 - 2$ sols [Eckermann et al., 2011; Seviour et al., 2017].

heating (and thereby enhanced dust loading, as will be discussed in the following section) is rapid. Nonetheless, Mars and Earth share many similarities, making it an interesting case study for comparison with atmospheric dynamics on our own planet. Furthermore, its proximity means that observational data of Mars and its atmosphere is second only to that of Earth, making it an important resource for understanding, testing, and verifying theories of atmospheric circulation.

1.1.2 Martian dust storms

A key source of variability in the atmosphere of Mars is the presence of large amounts of dust that can be lofted into the atmosphere during different times of the year. Planet-encircling *global dust storms* (GDSs) can cover a significant proportion of the planet in a dust haze, substantially altering the atmosphere's optical depth and circulation at that time (via enhanced radiative cooling and heating). Studies have shown that such storms result from the aggregation of multiple smaller-scale storms and can last for weeks to months [Wang and Richardson, 2015, and references therein]. In a given Martian Year (MY)[4], there is an estimated chance of approximately 1/3 of a GDS occurring ($18-55\%$ chance at the 95% confidence level) [Zurek and Martin, 1993]. The three most recent GDSs (in 2001, MY 25;[5] in 2007, MY 28; in 2018, MY 34) have been observed globally by satellite instrumentation, allowing characterisation of their evolution and impacts on a new level [Kass et al., 2020]. Figure 1.1 illustrates the visible difference in atmospheric opacities in the periods leading up to and during the MY 25 GDS that encircles much of the planet.

Enhanced dust loading in the atmosphere is known to have substantial influence on the atmospheric circulation. Dust aerosol suspended in the atmosphere absorbs and scatters incoming shortwave radiation, heating both the suspended dust itself and the atmosphere around it [Kahre et al., 2017]. This can impact the circulation even far from regions of

[4]Martian Years last 669.6 sols or approximately two Earth years (687 days). By somewhat arbitrary convention, MY 1 begins at northern spring equinox on April 11th, 1955 [Clancy et al., 2000].

[5]Shown in Figure 1.1.

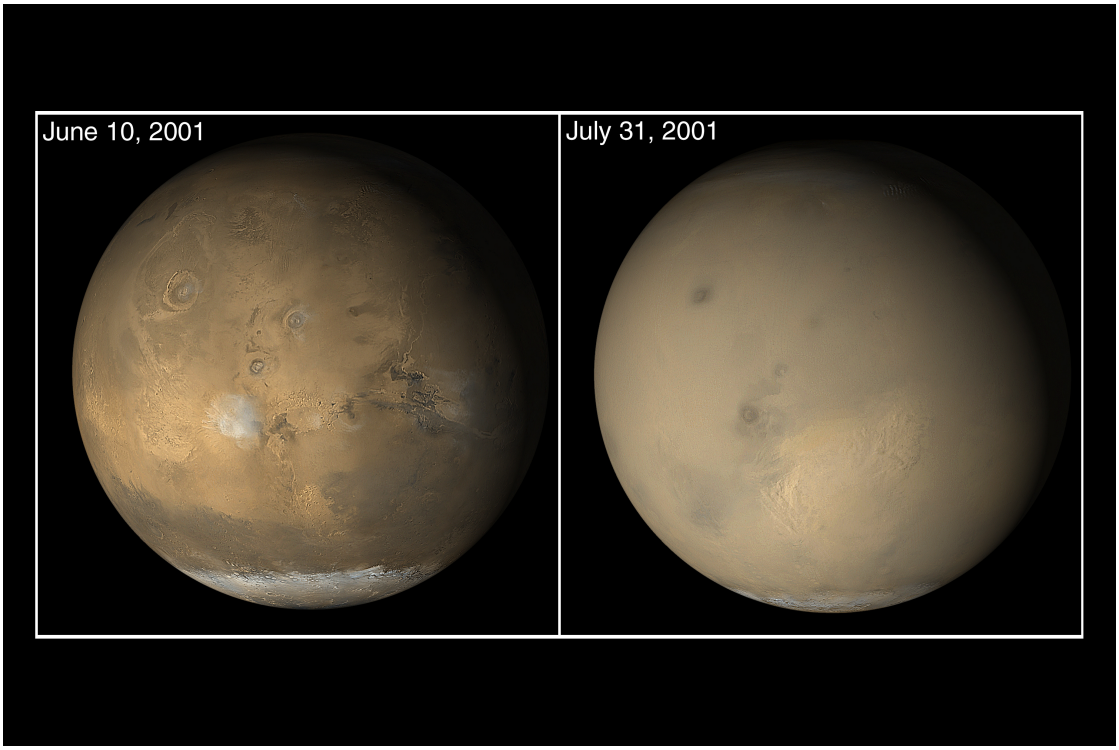

Figure 1.1: **Satellite observation of a dust storm on Mars.** A GDS encircles Mars in 2001, as captured by the MOC aboard MGS. Left panel shows a relatively non-dusty period before the storm, and right panel shows the planet at the height of the GDS. Credits: NASA/JPL-Caltech/Malin Space Sciences Systems.

elevated dust loading: for example, it has been shown that increased aerosol heating rates in the southern midlatitudes can strengthen the northern polar jet during northern winter [Guzewich et al., 2016]. Although local dust storms may occur throughout the year, the dust season occurs during southern spring and summer ($L_s = 180 - 360°$)[6] and the largest regional and global dust storms occur during this period [Smith, 2004, and references therein]. Archetypes of regional dust storms have been defined: "A" storms start early in the season (at $L_s = 205 - 240°$) and last for $15 - 40°$. "B" storms tend to occur over southern summer solstice (starting $L_s = 245 - 260°$ and lasting $5 - 20°$). Finally, "C" storms develop in late southern summer ($L_s = 305 - 320°$) and have a duration of $3 - 15°$. The different

[6] Areocentric solar longitude (L_s, degrees) is used to describe the position of Mars in its orbit around the Sun; $L_s = 0°$ defines the northern spring equinox [e.g. Spiga et al., 2018].

storm types have different characteristics: "A" and "C" storms typically cover much of the Southern Hemisphere (SH) and will often have a NH temperature response, and "B" storms will generally occur over the southern polar regions and the atmospheric response will be confined poleward of the southern midlatitudes [Kass et al., 2016]. Based on available observations, GDSs are clearly distinct from regional dust events: in dust distribution (altitude and latitude, and duration), in temperature fields, and in their initiation window [Kass et al., 2020]. All storms, regional or global, experience interannual variability in their extent, duration, and intensity.

1.2 Polar vortices

One of the influences that dust loading in the Martian atmosphere can have is its influence on the winter polar vortex. This feature of the atmospheric circulation, as well as its response to dust loading, will be discussed in Section 1.2.3.2, following an overview of polar vortices.

1.2.1 What are polar vortices?

Broadly speaking, a polar vortex may be defined to be a coherent structure of rapidly rotating flow in the polar region of a planet. This could be circumpolar (flow encircling the pole), as is the case for Earth's stratospheric[7] polar vortices, or of a smaller horizontal scale, such as synoptic-scale tropospheric[8] polar cyclones. Mitchell et al. [2021] define two types of polar vortex: the predominantly circumpolar Type I vortex, and the Type II vortex that is of smaller horizontal scale. Following Mitchell et al. [2021], one mathematical definition of a polar vortex may be that such a structure should have a value of absolute *potential*

[7]The stratosphere is the second layer of Earth's atmosphere, and extends from ~ 12km - ~ 50km in altitude. The presence of ozone causes a temperature inversion in the stratosphere, wherein temperature rises with altitude.

[8]The troposphere is the lowest layer of Earth's atmosphere, extending to ~ 12km in altitude. Temperature decreases with altitude, unlike in the stratosphere.

vorticity (PV) greater than the polar planetary vorticity [Mitchell et al., 2021]. PV is given by

$$q = \frac{\zeta_a \cdot \nabla\theta}{\rho}, \tag{1.1}$$

where ρ is atmospheric density, ζ_a is absolute vorticity, and $\nabla\theta$ is the vertical potential temperature gradient [Vallis, 2017]. PV is expected to be largest at the poles in an atmosphere at rest as this is where absolute vorticity (given by $\zeta_a = 2\mathbf{\Omega} + \nabla \times \mathbf{v}$, where $\mathbf{\Omega}$ is planetary rotation rate and $\mathbf{v}$ is the velocity field) is greatest. PV is useful in the study of polar vortices for several reasons: a) that it is conserved in frictionless, adiabatic flow and therefore can be used in some analyses as a tracer of the fluid flow; b) that it is an invertible quantity and we may use it to obtain other dynamical fields of the flow; and c) that PV gradients provide a restoring force for breaking Rossby waves[9] [e.g. Hoskins et al., 1985; McIntyre and Palmer, 1983; Vallis, 2017; Waugh, 2023]. This restoring mechanism will be discussed in Section 1.2.2.

1.2.2 Theory and dynamics

This section introduces principles of fluid dynamics that are relevant for the study of polar vortices.

1.2.2.1 Thermal wind balance

Thermal wind balance arises by assumption of *geostrophic balance* (an assumption that the dominant terms of the flow are rotation and pressure) and *hydrostatic balance* (an assumption that in the vertical momentum equation, the gravitational and pressure gradient terms balance). These two assumptions are appropriate for the large-scale circulation (where horizontal scales of motion are much greater than vertical) of the atmospheres

[9] Rossby waves are large-scale waves (of a scale at which planetary rotation is important) often generated by topography and land-sea contrasts that disturb the flow - the background vorticity gradient then propagates this as a wave.

of Earth and Mars, away from the equator [see Vallis, 2017, 2.7.4 for a discussion]. In pressure coordinates, the zonal component of the thermal wind equation is:

$$f\frac{\partial u_g}{\partial p} = \frac{R}{p}\frac{\partial T}{\partial y}, \tag{1.2}$$

where $f = 2\Omega\sin\phi$ is the Coriolis parameter at latitude ϕ, u_g is the zonal component of the geostrophic velocity[10], R is the specific gas constant, p the pressure, and T the temperature. The mechanism can be explained by temperature gradients (and therefore density gradients) inducing larger vertical pressure gradients where the fluid is colder via the assumption of hydrostasy. There is then a horizontal pressure gradient that, by geostrophic balance, is accompanied by a vertical shear in the horizontal wind [see Figure 2.6 of Vallis, 2017, Chapter 2]. It can be seen that on a surface of constant pressure, any change in the temperature gradient (a change in the right-hand-side of Equation 1.2) must induce a vertical shear in the zonal velocity (as f is constant at a given latitude ϕ), thus providing the basic mechanism for the formation of polar vortices in an atmosphere with a strong equator-to-pole temperature gradient [see Vallis, 2017, Chapter 2, for a full derivation of the thermal wind equation].

1.2.2.2 Potential vorticity gradients

Sharp PV gradients, which are relevant to the study of polar vortices, act to restore perturbations. Consider a meridional gradient of PV on an isentropic surface (a surface of constant potential temperature). Conservation of PV in the absence of frictional or diabatic effects implies that when a material contour is perturbed north-south in a wavy pattern (for example, by a Rossby wave), PV is similarly perturbed. This perturbation induces a velocity field a quarter-wavelength out of phase with the material perturbation, which propagates the disturbance westward and acts to restore this disturbance. See Hoskins et al. [1985, Figure 17] for a schematic of this restoring mechanism. The effectiveness of

[10]The zonal geostrophic velocity is defined by $fu_g \equiv -\frac{1}{\rho}\frac{\partial p}{\partial y}$, and represents a balance between rotational effects and pressure gradient effects.

the Rossby wave restoring mechanism is weaker at small scales than at large [McIntyre, 1989].

Where PV gradients are small, there may be a *mixing region*. Mixing regions may be understood in the context of *chaotic advection*, which means that there is exponential divergence of nearby fluid parcel trajectories, with rate given by the Lyapunov exponent [Pierrehumbert, 1991]. Contours of tracer lengthen exponentially over time, which increases the surface area over which irreversible microscale diffusion can occur: i.e. in such a region, mixing occurs. Barrier regions however have much slower separation of parcels, and so contours of tracer do not lengthen exponentially as stretching rates are small and thus less mixing occurs.

Finally, of relevance to the upward propagation of Rossby waves is the Charney-Drazin criterion, after Charney and Drazin [1961]. The Charney-Drazin criterion states that vertical energy propagation in standing waves in an atmosphere of uniform basic zonal velocity, $\bar{u}$, and temperature can occur when the velocity is positive but smaller than some modified Rossby critical velocity, U_0. In the beta-plane approximation at latitude ϕ_0, U_0 can be shown to be given by

$$0 < \bar{u} < U_0 \equiv \beta / \left[(k^2 + l^2) + f_0^2 / 4H^2 N^2 \right], \tag{1.3}$$

where $\beta = (2\Omega/a)\cos\phi_0$, k and l are the zonal and meridional wavenumbers of the wave, $f_0 = 2\Omega\sin\phi_0$, H the scale height (given by $H = RT/g$ for specific gas constant R and reference temperature T), and N^2 the Brunt-Vaisälä frequency. On Earth, this criterion then implies that eastward-propagating waves may extend all the way into the stratosphere if their wavenumber is sufficiently low, but higher wavenumber waves will remain trapped in the troposphere. At Earth's NH midlatitudes, this critical velocity is found to be $U_0 \sim 38\,\mathrm{ms}^{-1}$ [Charney and Drazin, 1961].

1.2.3 The morphology of polar vortices in the solar system

Polar vortices have been observed or inferred in the atmospheres of all solar system planets with a substantial atmosphere [e.g. Waugh, 2023]; there is a staggering diversity even in such a small sample. This raises the possibility of polar vortices that feature as-yet-unobserved characteristics in the atmospheres of exoplanets (an exoplanet, or extrasolar planet, is any planet beyond our solar system). To date, over 5000 exoplanet discoveries have been confirmed [NASA, 2023]; it is possible that many of these have polar vortices in their atmospheres. These polar vortices (where they exist) are likely to be influenced by a huge variety of planetary parameters, atmospheric compositions, and stellar insolation. These vortices are important for understanding the distribution of trace species in the atmosphere, as they may well form significant transport barriers that induce differences in the composition of the atmosphere within and outside the vortices [Mitchell et al., 2021]. Within this section, polar vortices that have been observed within the solar system are discussed, with emphasis on the polar vortices of Earth and Mars. Figure 1.2 illustrates a vertical cross-section of the winter polar vortices of Venus, Earth, Mars, and Titan. A strong polar jet is seen in the atmospheres of all four bodies, and on Earth, there is a distinct transition in the latitude of strongest winds from the troposphere to stratosphere.

1.2.3.1 Earth's stratospheric polar vortices

The most well-studied polar vortices in our solar system are undoubtedly those in our own atmosphere, although the term polar vortex has been used to describe several distinct features [Waugh et al., 2017]. We typically think of Earth's polar vortices as those in the stratosphere, which form in the autumn with a decrease in polar heating and strengthen into the winter. The decrease in polar heating ensures an increase in equator-to-pole temperature gradient which, by thermal wind balance, induces a stronger westerly flow.

Earth's winter-time stratospheric polar vortices extend from 10-50km in altitude and to $\sim 60^{\circ}$N/S in latitude. We may also occasionally refer to the tropospheric polar vortex; these

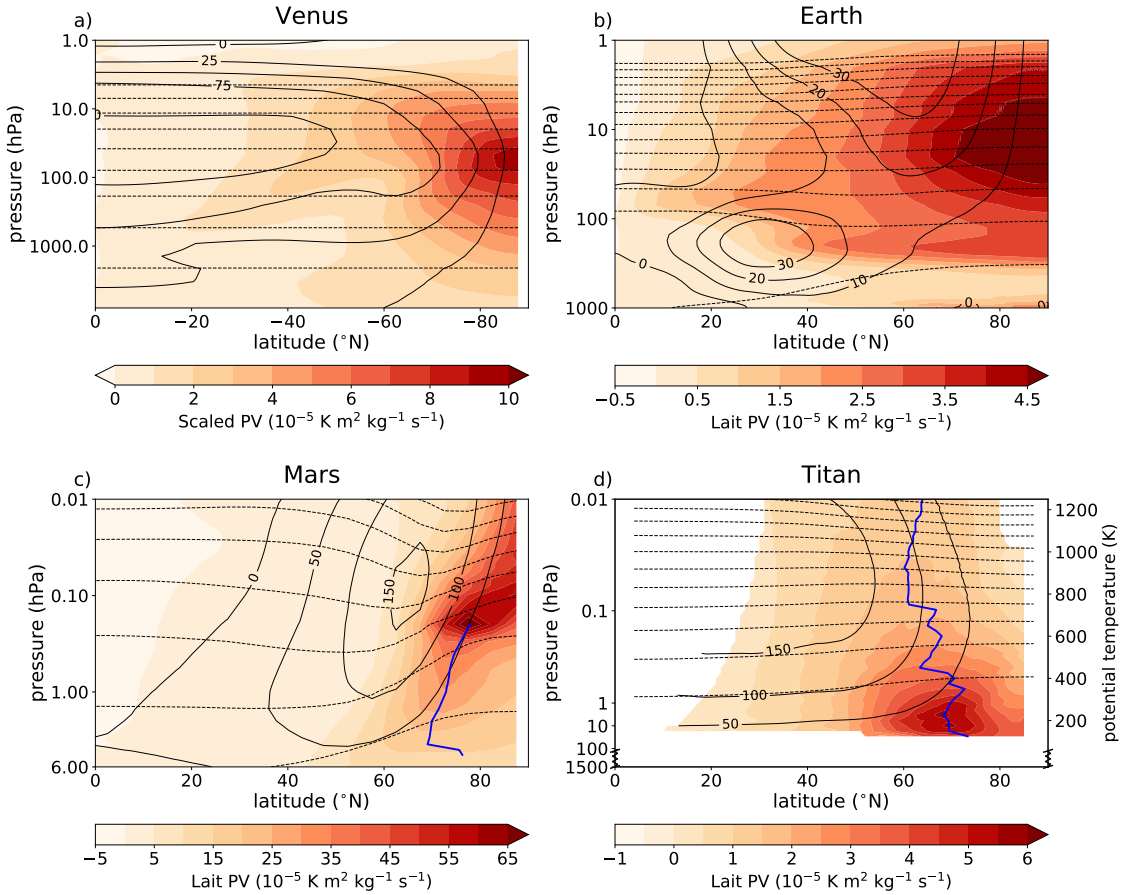

Figure 1.2: **Vertical cross-section of the winter polar vortex of four solar system terrestrial bodies.** Winter-mean zonal-mean PV (shading) and zonal wind (solid lines), along with potential temperature surfaces (dashed lines) for a) Venus, b) Earth, c) Mars, and d) Titan (stratosphere only). In panels (c) and (d), the blue line indicates the latitude of the maximum PV. Figure created by this author and published in Mitchell et al. [2021, with details on data sources, scalings, and time averages given therein]. The blue lines have been added for this thesis, to illustrate the annularity of Mars's and Titan's polar vortices.

two vortices are distinct (although both lie in the Type I category), with the tropospheric polar vortex extending much further equatorward (its edge typically lies at $40-50°$N) and persisting throughout the year [Waugh et al., 2017]. Furthermore, we can also refer to large-scale polar cyclones that develop in the troposphere that fit the description of a Type II polar vortex. References to Earth's polar vortices herein will refer to the more classical stratospheric polar vortex, although both the tropospheric and stratospheric vortices can be seen in Figure 1.2 b.

The stratospheric polar vortices exhibit significant hemispheric differences. The Antarctic polar vortex is broader and stronger (in terms of PV and winds) and experiences less interannual variability than its northern counterpart [Waugh, 2023]. These differences are primarily forced by hemispheric differences in wave-breaking. Low wavenumber Rossby waves generated in the troposphere by topography and land-sea contrasts propagate upward into the stratosphere and perturb the vortices. The Charney-Drazin criterion implies that these disruptions will primarily be wavenumber 1 or 2, as higher wavenumber waves are filtered out at lower altitudes [Charney and Drazin, 1961]. Thus the tropospheric polar vortex on Earth is influenced by waves of smaller spatial extent than the stratospheric [Waugh et al., 2017]. The polar vortex in the NH has a tendency to break down in an event called a *Sudden Stratospheric Warming* (SSW), forced by such wave-breaking. Although exact definitions of SSWs vary, broadly speaking an SSW is defined to be minor when the polar temperature gradient reverses and major when there is also a reversal in the zonal-mean zonal wind at 10 hPa and 60°N [Butler et al., 2017]. An SSW can take the form of either a vortex displacement, a split (whereby the parent vortex splits into two smaller child vortices), or some combination of the two. Downward connections between the stratosphere and troposphere mean that these SSWs can have significant impacts on surface weather [e.g. Domeisen et al., 2020; Kidston et al., 2015; Mitchell et al., 2013]. The SH polar vortex may also undergo SSWs, albeit much less frequently due to less wave-breaking - the most recent major SSW in the SH occurred in 2002 [Shen et al., 2020].

Despite these hemispheric differences in variability, the stratospheric polar vortices on Earth are both monopolar, meaning that they have a maximum in PV at the pole. Following the discussion surrounding Equation (1.1), this is generally as is expected as absolute vorticity reaches its maximum at the pole. However, observations suggest that the mesospheric polar PV does not always follow this same pattern [e.g. Manney et al., 2008] which may be caused by a polar warm anomaly at these higher altitudes [Harvey et al., 2009]. In the stratosphere, these regions of high PV are surrounded by a midlatitude *surf zone*, where PV and PV gradients are much smaller than at the equatorward vortex boundary. Indeed, studies have used the location of the steepest PV gradients to locate the edge of the vortex [Nash et al., 1996].

1.2.3.2 The Martian polar vortices

The polar vortices on Mars may be the next most well-studied after Earth, thanks to decades of successful orbital and lander missions that began with the Mariner 9 orbiter in 1971 and the Viking Landers in 1976. Mars's atmosphere, while sharing some similarities with Earth's, does not feature a stratosphere: Mars's polar vortices are an entirely tropospheric feature, but extend from low levels up to ~ 80km in altitude. At ~ 10 Pa/50km (approximately the altitude of the vortex core), the strongest winds lie at 60°N/S (see Figure 1.2 c). Early modelling studies of the Martian atmosphere predicted strong circumpolar winds and the potential for rapid polar warmings that may be analogous in some ways to SSWs on Earth [Leovy and Mintz, 1969; Schneider, 1983; Wilson, 1997]; these findings have been confirmed by observational studies [Conrath, 1981; Martin and Kieffer, 1979; McCleese et al., 2008; McDunn et al., 2013] and [James et al., 2017, and references therein].

The Martian polar vortices have been studied through numerical modelling since the late 1960s, with both modelling and observations playing an important role at this time [Conrath, 1981; French and Gierasch, 1979; Pirraglia, 1975]. The Mintz-Arakawa two-level

model adapted for Mars displayed strong winter-time zonal winds at high latitudes [Leovy and Mintz, 1969], an early indication that Mars's atmosphere may host a polar vortex. More recent models have also identified significant polar vortices in the atmosphere of Mars, and have studied their morphology and variability, for example the full global climate models (GCMs[11]) of Guzewich et al. [2016]; Toigo et al. [2017], along with the shallow water studies of Scott et al. [2020]; Seviour et al. [2017]. The polar vortices have also been studied in datasets called reanalyses: these are created by assimilating spacecraft observations into a GCM. This form of dataset is useful in the sense that it provides a physically-consistent estimate of the state of an atmosphere at a given time that is also spatially and temporally evenly-gridded. There are currently three reanalyses of Mars's atmosphere[12], between them covering the period $L_s = 103°$ in MY 24 - present, assimilating observations of temperature, dust, water vapour, and ozone into the underlying models. However, due to a gap in observational time periods between Mars Global Surveyor (MGS) and Mars Reconnaissance Orbiter (MRO), there is a temporal range ($L_s = 81°$ MY 27 - $L_s = 111°$ MY 28) in which no observations are assimilated. Studies have investigated multiple features of the atmospheric circulation on Mars using these reanalyses, notably using the MACDA dataset to compare polar vortices on Mars and Earth [Mitchell et al., 2014], and comparing the vortices across MACDA and EMARS [Waugh et al., 2016]. Recent studies have also investigated the influence of the equinoctial MY 34 GDS on both northern and southern vortex in the OpenMARS reanalysis [Streeter et al., 2021]. Both MACDA and EMARS agree quantitatively on polar vortex structure, and see patchy PV on short timescales with an elliptical PV structure on longer timescales [Waugh et al., 2016].

Unlike Earth's polar vortices, observations, reanalyses, and free-running models have

[11]May also refer to a General Circulation Model. Within this thesis, global climate model will be used, as this is the more common term for models of Mars's atmosphere. A brief introduction into their use is given later in Section 1.5.1.

[12]The Mars Analysis Correction Data Assimilation [MACDA; Montabone et al., 2014], the Ensemble Mars Atmosphere Reanalysis System [EMARS; Greybush et al., 2012], and the Open access to Mars Assimilated Remote Soundings [OpenMARS; Holmes et al., 2020].

all revealed Mars's polar vortices to be annular in terms of their PV structure, meaning that there is a ring of high PV surrounding a polar minimum in both hemispheres [Banfield et al., 2004; Barnes and Haberle, 1996; Mitchell et al., 2014; Waugh et al., 2016]. This can be seen in reanalysis data in Figure 1.2 c. This surprising result has inspired research into the question of the stability of Mars's polar vortices and their persistence, along with the potential causes of their annular structure. Typically, a ring of high PV is understood to be *barotropically unstable*: waves on either interface of the strip of high PV propagate in opposite directions (due to the opposing PV gradients on either side), interacting with each other and leading to linear instability [Dritschel and Polvani, 1992; Hoskins et al., 1985]. This wave propagation is illustrated in Figure 1.3, where an annulus of high PV (shaded) is disturbed. The persistence of this unstable state on Mars suggests that there may exist an external restoring force that maintains the annulus [Mitchell et al., 2014]. One factor that influences the polar atmosphere of Mars, and could contribute to the maintenance of the annulus, is the condensation of CO_2. Significantly, at the winter poles of Mars it reaches temperatures cold enough for this atmospheric CO_2 to condense to snow. During this phase change process, latent heat is released and warms the polar atmosphere, which could provide the restoring force for the annulus by a destruction of PV. This destruction occurs via the diabatic change in temperature with the release of latent heat, which causes a reduction in the vertical potential temperature gradient and reduces PV according to Equation 1.1. Indeed, in full GCM simulations, it has been shown that a representation of latent heat release can be sufficient to produce and maintain an annulus of PV [Toigo et al., 2017]. This forcing has also been studied in the more idealised rotating shallow-water equations, where an annular PV structure was maintained with a relevant combination of topographic and radiative forcing [Seviour et al., 2017]. CO_2 deposition has also been shown to contribute to the PV 'patchiness' of the vortex on short timescales [Rostami et al., 2018] that was previously identified in reanalyses [Waugh et al., 2016]. Other processes may influence the annular morphology: research has also linked Hadley Cell downwelling

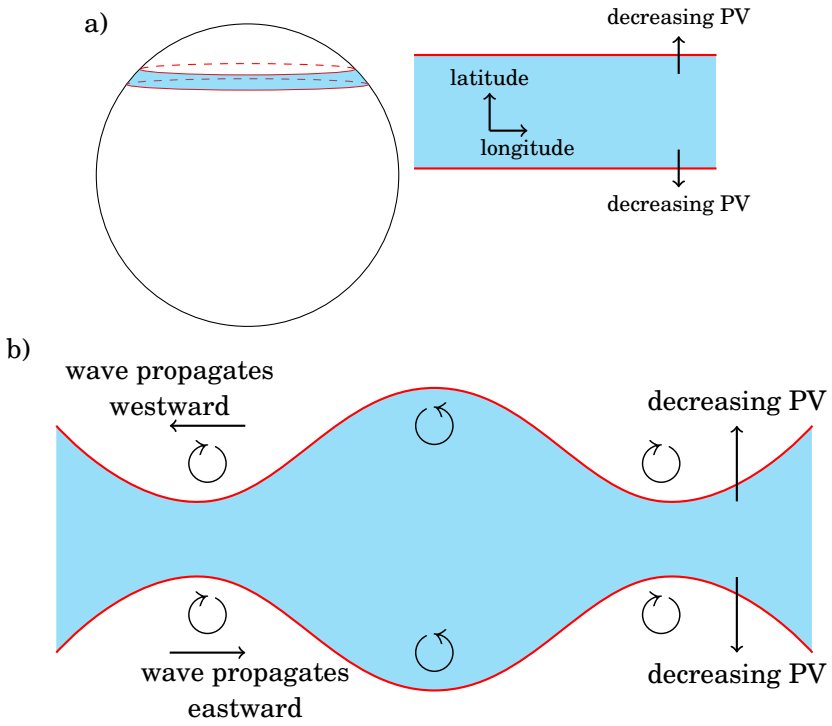

Figure 1.3: **Barotropic instability.** A schematic of the barotropic instability associated with a strip of high potential vorticity (shaded regions). Panel a) shows the undisturbed strip on the sphere and in planar geometry. Panel b) shows disturbances propagating longitudinally in opposite directions due to the opposing potential vorticity gradients on either side of the strip. Circular arrows indicate the direction of propagation of the disturbance.

with the maintenance of the annulus, which will be discussed in Section 1.3.

Somewhat analogous to Earth's SSWs, Mars's northern polar vortex can also be disrupted by an event called a *Transient Polar Warming* (TPW). During a TPW, the upper polar atmosphere of Mars can warm by several tens of degrees Kelvin on a short timescale, producing a reversed equator-to-pole temperature gradient and potentially disrupting the polar vortex for a period of a few tens of sols [Guzewich et al., 2016; McDunn et al., 2013]. These TPWs are influenced by large aerosol heating rates in the southern midlatitudes [Guzewich et al., 2016], which occur during times of particularly high atmospheric dust

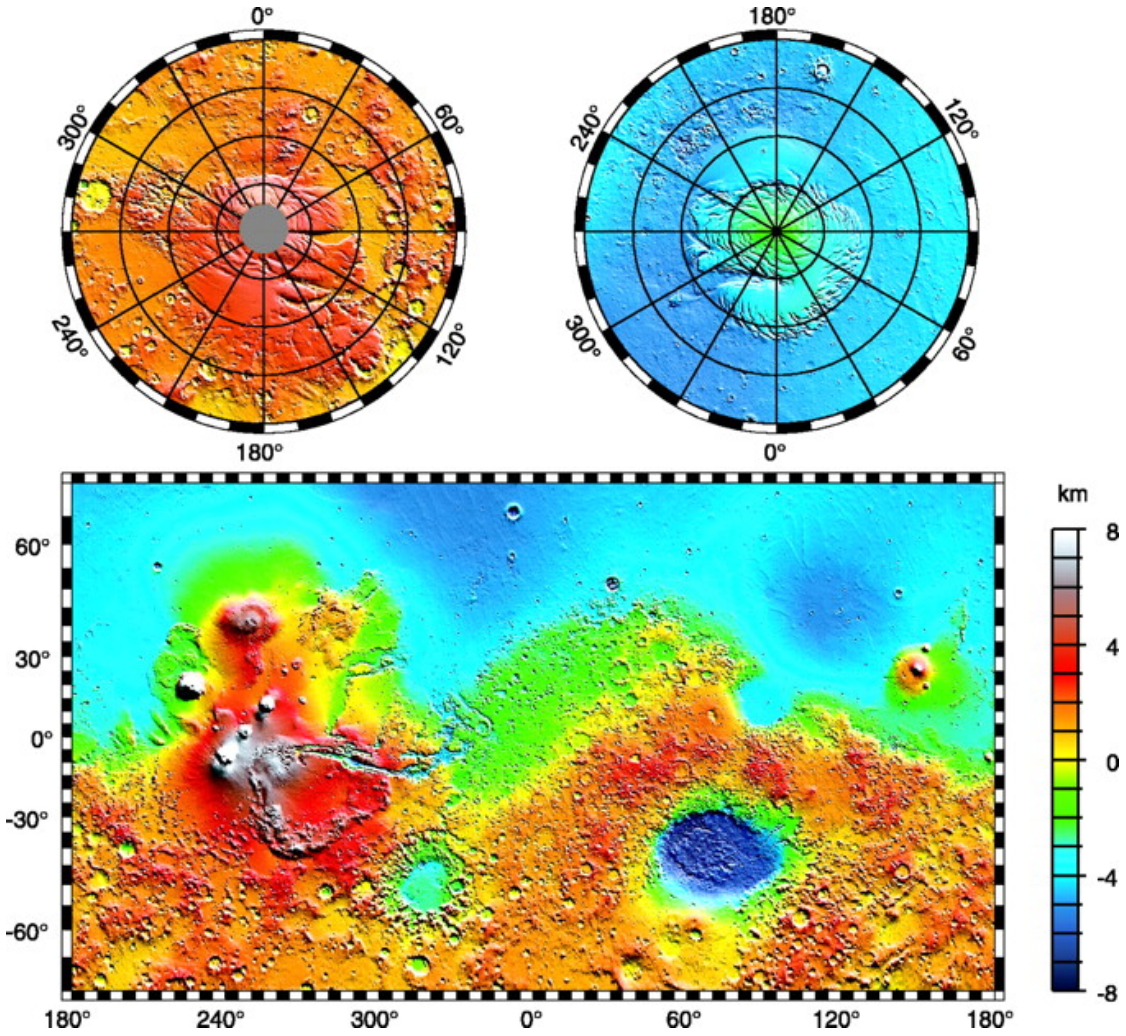

Figure 1.4: **Maps of the global topography of Mars.** The projections are Mercator to 70° latitude and stereographic at the poles with the south pole at left and north pole at right. Figure from Smith et al. [1999, Figure 2]. Note in particular the low northern topography with prominent intrusion by the Tharsis province at 220°E to 300°E.

loading. TPWs can occur throughout the winter, often in response to the occurrence of a GDS, which can strengthen the overturning circulation and push its descending branch poleward and thus cause warming in the polar upper atmosphere [Guzewich et al., 2016].

Due to the seasonality of the dust loading on Mars, typically large or global dust storms occur during northern autumn and winter, and much smaller dust loading during southern

winter precludes the occurrence of such an event at this time [Kahre et al., 2017, and references therein]. Interannual variability in the northern winter polar vortex tends to be much greater than in the southern as a result. However, increased dust loading can also lead to changes in the SH vortex: during the MY 34 GDS (a southern spring equinoctial storm) [developing prior to the window for "A" type regional dust events, Kass et al., 2020], dust was shown to induce more longitudinally-symmetric transport around both the northern and southern poles [Streeter et al., 2021]. There are further hemispheric differences that lead to differences in polar vortex morphology, notably topography and the timing of perihelion. Figure 1.4 shows topographical data obtained from the Mars Orbiter Laser Altimeter [MOLA Smith et al., 1999]: the significant protrusion of higher altitudes into the northern lowlands is the Tharsis province. The topography in the NH of Mars, which is significantly lower than in the southern, may influence the polar vortex morphology by topographically-induced wavenumber 2 planetary waves [Nayvelt et al., 1997] and is thought to induce on average an elliptical shape in PV [Mitchell et al., 2014; Streeter et al., 2021].

1.2.3.3 Further diversity of polar vortices

Beyond Earth and Mars, there have been sufficient observations of other planetary bodies in our solar system to either observe or infer the presence of polar vortices in their atmospheres. Two further examples of terrestrial planetary bodies that exhibit polar vortices are Venus, the second planet from our Sun and the first with an atmosphere, and Titan, the largest moon of Saturn. Figure 1.2 a and 1.2 d show the polar vortices of these two planetary bodies. Venus is a slowly rotating planet and its atmosphere experiences a strong greenhouse effect, with average temperatures of 700 K, as well as atmospheric superrotation. It has two features that have both been identified as a polar vortex in the literature: a hemispheric-scale midlatitude wind pattern and a tropical cyclone-like structure at each pole - given Venus's very low obliquity, both features exist in both

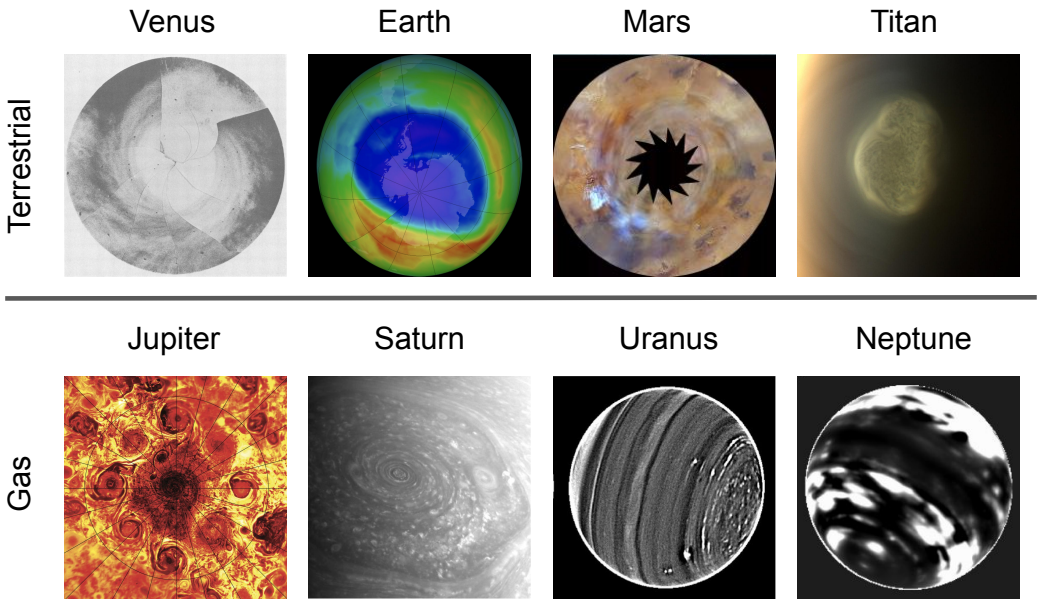

Figure 1.5: **The diversity of polar vortices across the solar system.** Observations of polar vortices or features resembling them on Venus, Earth, Mars, Titan, Jupiter, Saturn, Uranus, and Neptune. Figure is from Mitchell et al. [2021, Figure 3], and details of individual images are given therein.

hemispheres year-round [Sánchez-Lavega et al., 2017]. The polar vortices of Venus are also shown in ultraviolet in Figure 1.5 from observations.

Recent work using Cassini observations has also inferred the presence of an annular polar vortex in Titan's stratosphere [Achterberg et al., 2008; Sharkey et al., 2021]. Titan's polar vortex extends to substantially lower latitudes than the vortices on Earth or Mars (in northern winter, there is a circumpolar jet located around $30-50°$N) [Achterberg et al., 2008; Flasar et al., 2005] and acts as a significant barrier to the mixing of chemical species [Teanby et al., 2008]. The mixing barrier at 60°N leads to a significantly more enriched polar atmosphere than the atmosphere at lower latitudes, and the chemical composition of the polar atmosphere suggests that conditions are suitable for photochemical processes to occur in the isolated polar air. Titan's southern polar region is shown in Figure 1.5 in false colour.

Thinking beyond the rocky planets, the gas giants of our solar system exhibit fascinating polar vortices unlike any seen on terrestrial bodies. Indeed, Jupiter's polar vortices, unobserved until recently, form a stunning array around a central vortex at each pole. Near-infrared images from Juno reveal the northern polar vortex is surrounded by eight circumpolar cyclones (Type II vortices), and the southern by five [Adriani et al., 2018]. An example infrared image of Jupiter's northern polar vortex is shown in Figure 1.5. The polar stratosphere of Saturn has Type I polar vortices that extend to ~ 75°N/S: Cassini observations reveal that in the NH, the vortex exhibits a hexagonal boundary similar to Saturn's tropospheric wave that is believed to be a Rossby wave [Allison et al., 1990; Fletcher et al., 2018]. The Saturnian stratospheric polar vortices are believed to be stronger in the summer hemisphere, with a warm polar collar, due to solar absorption by high-altitude stratospheric aerosols [Fletcher et al., 2008]. Saturn's northern polar region is shown in the visible in Figure 1.5.

Finally, despite the relatively fewer observations of Uranus and Neptune that are available, data from the Voyager flybys as well as ground-based observations suggest that these two planets also feature a single polar cyclone [Brueshaber et al., 2019, and references therein]. Near-infrared images of Uranus and Neptune from Keck II are shown in Figure 1.5.

The diverse display of observed vortices (in terms of their morphology, scale, and persistence) naturally leads to the question of the relative importance of different processes on each planet and how polar vortex features are determined by these processes. Recent reviews of polar vortices in planetary atmospheres [Mitchell et al., 2021; Waugh, 2023] discuss the dynamics involved in the formation, maintenance, and disruptions of these coherent structures. Ranging from perhaps the simplest representation of vortices (vortex patches) to their representation in full GCMs, numerical models and laboratory experiments have been used for many years to understand more about their behaviour [see Mitchell et al., 2021, and references therein, for a comprehensive introduction into the

modelling of polar vortices].

It is useful to consider the roles of both planetary parameters and external forcings when discussing factors that influence polar vortex behaviour. Considering first the role of planetary parameters, for gas giant planets it is the planetary Burger number ($Bu = (L_d/a)^2$, where L_d is the Rossby deformation radius[13] of a planet, and a its radius) that primarily controls the dynamical regime of the polar vortex [Brueshaber et al., 2019; O'Neill et al., 2015].

By considering meridional vorticity gradients generated by both planetary rotation and the existence of a polar cyclone, Gavriel and Kaspi [2021] identified two equilibrium points in the atmosphere of Jupiter that a coherent cyclone forming at lower latitudes may reach, one of which is stable and lies at approximately 84°N/S; this latitude is in approximate agreement with the location of Jupiter's observed circumpolar array of cyclones. Zonal stability arguments were similarly able to predict the number of cyclones present at each of Jupiter's poles. Despite the similarities between Jupiter and Saturn, the analysis of Gavriel and Kaspi [2021] did not identify any equilibrium for the poles of Saturn, consistent with there being no observed array of cyclones and suggesting that the polar vortices of these two planets may be largely controlled by the barotropic dynamics.

Despite the identification of certain key parameters that may allow some form of polar vortex classification, the cause of many of the differences noted between planetary polar vortices is not known [Mitchell et al., 2021]. Highly planet-specific external forcings, including planetary characteristics such as topography, or the presence of atmospheric constituents such as specific aerosols or gases, could be the cause of some such differences. For example, a key feature that influences Earth's vortex variability is topography. Topography and land-sea contrasts on Earth may induce upward propagating planetary waves that break and influence polar vortex variability, particularly in the NH [Waugh et al., 2017].

[13] L_d is given by $L_d = \sqrt{gH}/f$, for a typical scale height H and gravity g, and is the scale at which rotation effects become important.

Topographical wave forcing is also thought to influence the northern Martian polar vortex, inducing an elliptical polar vortex on average by propagation of wavenumber-2 waves from the large topographical variations [Mitchell et al., 2014]. Atmospheric aerosols may also play important roles in polar vortex morphology, for example with dust on Mars causing large interannual variability [Guzewich et al., 2016]. On Earth, the presence of increased chlorofluorocarbons in the stratosphere is well understood to have induced stratospheric ozone depletion, leading to the phenomenon of the ozone hole in the Antarctic [e.g. Farman et al., 1985; Solomon, 1990].

1.2.4 Polar vortices as barriers to transport

It is known that the polar vortices on Earth act as an efficient barrier to quasi-horizontal (isentropic) transport, although not necessarily to the overturning Brewer-Dobson circulation (tropospheric air rising into the stratosphere in the tropics, moving poleward before descent in the mid-high latitudes) [e.g. Juckes and McIntyre, 1987; McIntyre, 1995; Pierce and Fairlie, 1993]. This has implications for the distribution of heat and chemical species throughout the atmosphere [e.g. Schoeberl and Hartmann, 1991], notably in the formation of the Antarctic ozone hole.

On Earth, the polar vortex boundary is characterised by sharp PV gradients that inhibit inward mixing of heat and constituents and thus the vortex has a tendency to act as an isolated air mass (via the processes outlined in Section 1.2.2) [Juckes and McIntyre, 1987]. However, high PV air from within the vortex may be mixed into the lower latitude surf zone in a process known as *filamentation*, which occurs at small-scales, since the PV gradient restoring mechanism is less effective at these scales. Intrusion of material *into* the vortex is much less common due to an asymmetry in the structure of the strain in the flow, wherein perturbations on the vortex edge feel a strong strain on their outer edge but little-to-no equivalent on their inward side [Juckes and McIntyre, 1987; Polvani and Plumb, 1992]. On short timescales (of up to approximately one week), PV can be used as a

tracer to demonstrate this filamentation and wave breaking at the edge of the stratospheric polar vortices on Earth [e.g. McIntyre and Palmer, 1983]. Rossby waves may also induce mixing (or chaotic advection) in the polar vortex surf zone, an important process for the distribution of chemical species in the atmosphere.

On Earth, the more stable SH polar vortex forms a stronger mixing barrier that isolates cold polar air, leading to significant destruction of ozone in the SH [Schoeberl and Hartmann, 1991]. Planetary wave activity is greater in the NH, which induces more horizontal mixing and thus ensures less isolated air than in the SH [Pierrehumbert, 1991]. A similar and related process may occur at the poles of other planets: for example, CO_2 can condense out of the cold polar air at the poles of Mars and form seasonal CO_2 ice caps. This process releases latent heat and creates a complex and distinct picture from that of Earth's isolated Antarctic air. Saturn's moon Titan is also known to have tracer-enriched air at its poles which may enhance radiative cooling there [Teanby et al., 2017].

One method used to quantify the differences in mixing between the surf zone and at the polar vortex boundary is to consider contour length via the area-based diagnostic *effective diffusivity* [Nakamura, 1996]. This is a geometric method of understanding mixing, whereby the *equivalent length* of a contour of constant tracer is calculated. Equivalent length is large where the flow's geometric structure is complex; as mixing regions have large stretching rates and produce complex flow geometry, one expects large equivalent length (and hence effective diffusivity) in such a region [Haynes and Shuckburgh, 2000a]. Studies have considered mixing in the stratosphere using effective diffusivity across the mid to high latitudes and on multiple vertical levels [e.g. Abalos et al., 2016; Haynes and Shuckburgh, 2000a,b]. Using effective diffusivity reconfirms the result that Earth's stratospheric polar vortices form a region of isolated air over the pole, with relatively frequent filamentation into the lower latitude regions with small meridional PV gradients. This method has not been used to study isentropic mixing in planetary atmospheres, and the existence of opposing PV gradients inside the annulus on Mars suggests that mixing

may look qualitatively different in the Martian polar regions compared to on Earth.

1.3 The Hadley Cell and jets

Another feature of the atmospheric circulation on Earth that is important for meridional transport is the Hadley circulation. In Earth's upper troposphere, the subtropical jet (STJ) forms at the poleward edge of the Hadley Cell (HC) via conservation of angular momentum. On Mars, the circumpolar jet (i.e. the winds of the polar vortex) may be thought of as the equivalent jet, as it is inextricably linked to the Hadley circulation and forms via the same mechanisms.

1.3.1 What is the Hadley circulation?

On Earth, the HC is a thermally direct tropospheric circulation with warm ascending motion over the equator and cool descending motion at around 30°N/S. It is responsible for the transport of heat and momentum poleward [e.g. Lu et al., 2007]. In a steady axisymmetric flow with Newtonian cooling to a radiative equilibrium temperature[14], parcels of air are lifted near the equator (where maximum heating is assumed) and transported poleward via the presence of an equator-to-pole temperature gradient in an angular momentum conserving flow. In order to conserve angular momentum, they begin to gain eastward velocity as they move to higher latitudes, and lose heat as they do so by thermal wind balance (Equation 1.2). At around 30°N/S, the air parcels sink and then return equatorward at low-levels. One can derive a prediction for this latitude of descent via conservation of angular momentum and an assumption of thermal wind balance [Held and Hou, 1980, hereafter HH80]. Even in this axisymmetric theory, at the upper poleward edge of the HC, a large temperature gradient induces a maximum in the westerly flow: the

[14]Radiative equilibrium temperature is the hypothetical, three-dimensional, temperature field that the atmosphere would obtain if there were no atmospheric or oceanic motion, given the composition and radiative properties of the atmosphere and surface [Vallis, 2017, Chapter 14].

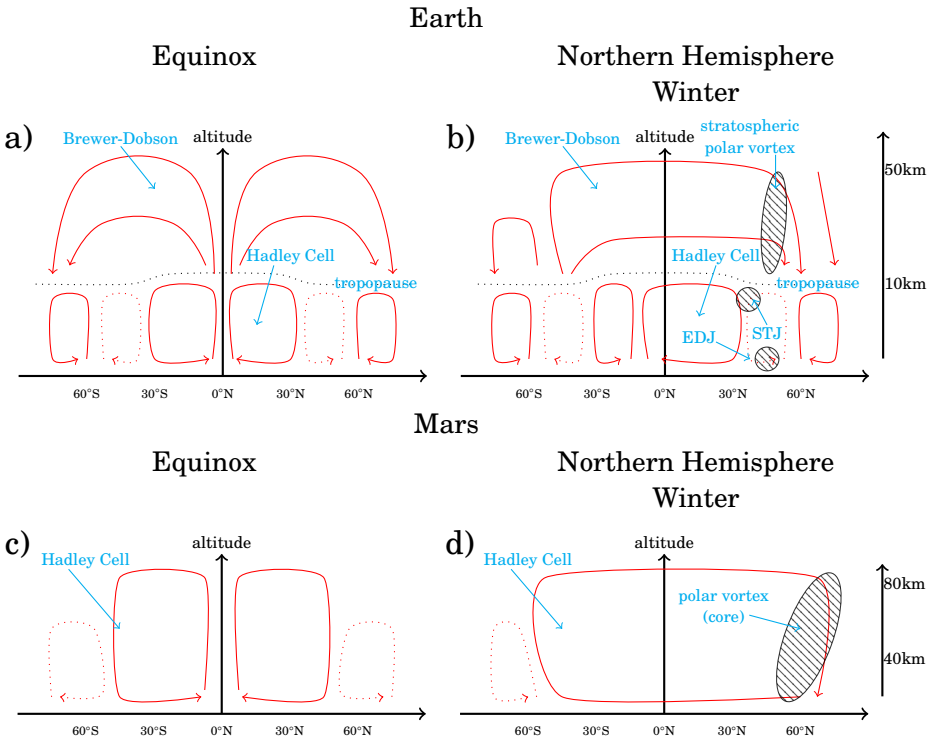

Figure 1.6: **The overturning circulation on Earth and Mars.** A schematic of the overturning circulation in Earth's troposphere and stratosphere during equinox (a) and Northern Hemisphere winter (b). The overturning circulation in Mars's troposphere during equinox (c) and Northern Hemisphere winter (d). Overturning circulation cells (red arrows) are labelled, and in b), d) winter-time jets are shown (black hatched ellipses).

STJ. Further detail about the formation of the HC and the STJ is given below in Section 1.3.2.

Figure 1.6 shows a schematic of the overturning circulation of both Earth (a, b; showing tropospheric and stratospheric circulations) and Mars (c, d). The tropospheric winter-time overturning circulation on Mars shares similarities with both the stratospheric Brewer-Dobson circulation and the tropospheric HC on Earth [Mitchell et al., 2014]. At equinox, the Hadley circulation on both planets is similar in its morphology, with rising air over the equator, but the circulation diverges away from this time period. This is due to the much smaller thermal inertia on Mars (due to its lack of oceans), which enables the rising

branch to drift further poleward than it does on Earth. On Mars, the polar vortex is inextricably linked to the Hadley circulation, which extends much further poleward than its counterpart on Earth. The extent and the strength of the Martian Hadley circulation experience significant internal and interannual variability, and changes in its extent induce significant changes in the polar middle atmosphere. One cannot consider mixing and transport into the polar regions without considering the Hadley circulation. Indeed, HC downwelling on Mars may be partially responsible for the maintenance of the annular polar vortex [Scott et al., 2020].

This leads to the question of the Hadley circulation on more Earth-like planets, and whether changes in planetary parameters affect the relationships we see with atmospheric jets, which can be induced by the Hadley circulation. In particular, it is known that on Earth the edge of the winter HC extends further poleward with decreasing rotation rate via a reduction in eddy scale that increases the equator-to-pole temperature gradient [Guendelman and Kaspi, 2019; Singh, 2019; Walker and Schneider, 2006]. Similarly, increasing obliquity also extends the HC [e.g. Guendelman and Kaspi, 2018; Lindzen and Hou, 1988; Walker and Schneider, 2006]. However, its dynamical relationship with the STJ and the lower-level eddy-driven jet (EDJ), both in terms of their relative locations and their covariability, has not been thoroughly explored across changes in these parameter values.

1.3.2 Theory

There exist many models of varying complexity that represent the Hadley circulation. Its initial proposition came in 1735 by George Hadley, who supposed that differential heating caused air to rise at the equator, move poleward and lose heat, gaining sufficient density to thereby sink once again [Hadley, 1735]. This argument has since been revised, and theory and numerical models have been developed that aid understanding of this circulation and can predict the latitude or strength of the HC for a given flow. One such theoretical model

is the axisymmetric inviscid model of HH80, which considers the primitive equations on a hemisphere confined by a surface below and a rigid lid above, and forced by a radiative heating. The flow is near angular momentum-conserving and predicts the width of the cell based on gravity, imposed height of the cell, equator-to-pole temperature gradient, and planetary rotation rate and radius.

Theoretical and modelling studies have calculated or identified theoretical and empirical scaling laws for the width of the HC dependent on various planetary parameters. For example, in the HH80 model (with equatorially-centred heating), it can be shown that the extent of the HC scales like:

$$\phi_{\mathrm{HC}} \sim \left(R \frac{\Delta_h}{\theta_0} \right)^{1/2}, \tag{1.4}$$

where $R = gH_t/(\Omega^2 a^2)$, H_t is the imposed height scale of the HC, θ_0 a global-mean potential temperature, Δ_h the equator-to-pole temperature gradient, Ω the rotation rate, and a the planetary radius [Held and Hou, 1980]. This model was subsequently extended to include off-equatorial heating by Lindzen and Hou [1988], who found a stronger and wider cell with heating centred off-equator (for example, with $\phi_{\mathrm{HC}} \sim 35^\circ$ when maximal heating occurred at 6° off-equator compared to $\phi_{\mathrm{HC}} \sim 23^\circ$ when centred at the equator).

In reality, the circulation on Earth (and other planets) is not axisymmetric. Midlatitude eddies can have an impact on the width and strength of the HC: in both dry and moist atmospheres, there is good correlation between the HC edge and the latitude at which eddies deepen and reach the upper troposphere [Davis and Birner, 2019, and references therein]. Rotation rate and radius influence the width of the HC via eddy momentum fluxes, and HC strength increases with latitude of off-equatorial heating in the eddy-permitting model also [Walker and Schneider, 2006]. Returning to the axisymmetric model, one may sketch an argument that as the wind shear increases in the poleward-moving upper branch of the cell, the flow will become baroclinically unstable[15] at some latitude, which will indeed

[15]Consider a pair of Rossby waves propagating one above the other. In the Earth's atmosphere, we could

induce eddy activity [Vallis, 2017, Chapter 14]. In the Earth's atmosphere, baroclinic eddies are most active in the midlatitudes, and convergence of their westerly momentum flux drives a westerly jet there [Lee and Kim, 2003]. This jet (the EDJ) may also be referred to as the polar front or polar jet, and is in fact the same jet that is sometimes referred to as the tropospheric polar vortex [see Maher et al., 2019a; Manney et al., 2022, for an explanation of why the tropospheric polar vortex may sometimes however be referring to the STJ]. Earth's STJ and EDJ are often distinct and are fundamentally driven by different processes, but may at times be colocated as these processes interact with and impact each other [e.g. Davis and Birner, 2019]. Both have been used as metrics for tropical width, along with the edge of the HC [e.g. Adam et al., 2018; Waugh et al., 2018], so understanding their dynamical relationships is crucial to predicting future changes.

1.3.3 Hadley Cell morphology on Earth and Mars

1.3.3.1 On Earth

The HC on Earth extends to around 30°N/S on average, and approximately 15km vertically, and is important for the poleward transport of heat and moisture. The latitudinal extent of the HC varies seasonally and hemispherically, with one study of multiple reanalyses showing that the HC extends to 28°–38°S in the SH and to 25°–44°N in the NH throughout its seasonal cycle [Nguyen et al., 2013]. The edge of the tropics, located at the descending branch of the HC, are typically a region of low precipitation due to the dry descending motion at this point. Observations and reanalyses, as well as future modelling, show that the HC is expanding (and is expected to continue to do so) under increasing greenhouse gas forcing [e.g. Archer and Caldeira, 2008; Davis and Rosenlof, 2012; Grise and Davis, 2020]

take one such wave near the surface and one close to the tropopause, for example during NH winter: in this scenario, there is a negative equator-to-pole temperature gradient in the lower troposphere and a positive equator-to-pole PV gradient at the upper level. The negative low-level temperature gradient induces a vertical wind shear by thermal wind balance, which is enhanced by the temperature anomalies of the perturbation. This vertical shear means that the induced velocity fields of the two waves may overlap, and if this is the case one finds that they act to keep each other in step (phase-locking), and make each other grow [Section 6 of Hoskins et al., 1985, describes this mechanism in more detail].

which has significant implications for populations living at these latitudes, for example by shifting precipitation patterns [Seager et al., 2007].

1.3.3.2 On Mars

On Mars, the HC extends substantially further poleward than on Earth. Typically, it features one large cross-equatorial cell, with ascending motion in the summer hemisphere midlatitudes and descending in the winter high latitudes (although around the equinoxes the circulation is briefly symmetric about the equator). The ascending and descending branches of the circulation typically lie between $30-60°$N/S [Leovy, 2001]. In SH winter, the extent and strength of the circulation is somewhat smaller, likely due to topographic differences and dust seasonality. Indeed, GCM simulations varying timing of perihelion and meridional topographic asymmetries indicate that the stronger NH winter cell is primarily topographically driven [Richardson and Wilson, 2002], suggesting an inherent handedness to the system that has been present throughout recent Martian climate history. Within the cell, angular momentum is approximately conserved, leading to much of the Martian atmosphere being angular momentum-conserving given the extent of the solsticial overturning circulation [Waugh et al., 2016]. In both an axisymmetric model and full eddy-permitting shallow-water simulations, HC downwelling has been linked to the annular morphology of the northern Martian polar vortex, although an additional latent heating was also required to maintain a polar minimum in PV [Scott et al., 2020].

A terrestrial analogue for the seasonal changes in overturning circulation on Mars is the stratospheric circulation on Earth (the Brewer-Dobson circulation) [Barnes et al., 2017], in the sense that this circulation extends further poleward than Earth's tropospheric HCs and is generally dominated by one cross-equatorial cell that has rising motion in the summer hemisphere and descending in the winter. Thus in two senses, one may think of analogies between Earth's stratosphere and Mars's troposphere: in the context of their polar vortices and their Hadley circulation.

1.4 Aims of thesis

This thesis aims to illustrate how idealised model hierarchies may be employed to better understand features of large-scale circulation in planetary atmospheres. Its primary goal is to better understand the processes and morphology of the Martian polar vortices, as well as how they could have influenced transport into the polar regions over a range of past orbital configurations, which is especially relevant for the formation of the polar layered deposits. The scope of this research is then broadened further to investigate the relationships between the HC, STJ, and EDJ, which are explored via an examination of Earth-like exoplanets across a range of planetary parameters and model complexities.

The primary questions this thesis aims to answer are the following:

1. What are the key processes influencing the morphology and variability of the northern Martian polar vortex?

2. Do the Martian polar vortices act as barriers to quasi-horizontal mixing, similar to the stratospheric polar vortices on Earth?

3. If so, how has horizontal mixing across the polar regions changed throughout the planet's history, and in particular what are the influences of obliquity and global dust abundance?

4. Are there hemispheric differences in these responses?

5. How do planetary parameters affect the relationships between zonal jets (particularly the STJ and EDJ) and the edge of the HC in the atmosphere of an Earth-like exoplanet?

6. How do these relationships depend on model complexity?

1.5 Methodological choices

In this section, I give an overview of the broad methodology employed in this thesis, placing it in the context of other recent work. More specific descriptions of, for instance, simulations and data analysed, are given in the respective results chapters.

To answer the above questions, the idealised GCM framework called Isca is employed throughout this thesis. Isca is highly flexible [Vallis et al., 2018], and allows its user to make an assortment of modelling choices, which makes the modelling of a variety of planetary atmospheres a relatively simple task. Furthermore, the ability to make these choices allows the user to construct a range of individual models with varying levels of complexity; it is thus possible to test the robustness of results to a range of modelling choices entirely within the Isca framework. A description of multiple planetary configurations of varying complexities is given in Thomson and Vallis [2019b]. To analyse the atmosphere of Mars, the previous version of Isca-Mars (described in Thomson and Vallis [2019b]) is developed in Chapter 2 to better represent the present-day atmosphere: new process additions include a dust scheme and a representation of latent heat release during CO_2 condensation. The newly-developed Isca-Mars is further compared with reanalysis datasets of recent years in the observational record to validate the model. A passive tracer is initialised in Isca-Mars in order to investigate mixing over a range of obliquities in Chapter 3. Finally, Isca is also used to investigate the jets and overturning circulation in a simple representation of Earth's atmosphere, as well as to perform a parameter sweep over obliquity and rotation rate in this framework (Chapter 4). Individual chapters give further details on the relevant configurations of Isca used therein.

1.5.1 Overview of global climate modelling

A GCM solves fluid equations of motion on a rotating sphere. Starting from the full Navier-Stokes equations, various simplifications can be made such that these are often reduced to

the primitive equations. Typically the sphere is subdivided into latitudinal, longitudinal and vertical gridboxes in which these equations are solved simultaneously. The dynamical core of the Isca framework is a spectral core from the GFDL that discretises in spectral space rather than physical [Vallis et al., 2018]. The higher the model resolution (i.e. the greater the number of gridboxes), the more computationally expensive this process will be, although changing model resolution can influence model output in certain scenarios [see Toigo et al., 2012, for a study of the impacts of altering horizontal resolution in a Mars GCM (MGCM)]. The particular equations solved and the boundary conditions imposed vary depending on the modelling and complexity desired for a given scenario. For example, relatively simple models could prescribe radiative-convective equilibrium temperature profiles and impose relaxation to these [the benchmark model of Held and Suarez, 1994, is one such example]. Depending on the model complexity, representations of oceanic processes in a full Earth GCM may include atmosphere-ocean coupling, prescribed sea-surface temperatures or a slab ocean. Other physical processes in the atmosphere, cryosphere, ocean, and land may be represented or parameterised.

Adapting GCMs that were developed primarily to understand Earth's atmosphere in order to understand the atmospheres of other planets is interesting for a variety of reasons.

1. First and foremost, the use of these models in exploring the dynamics of planetary atmospheres is interesting in and of itself: planetary atmospheres feature inherently alien circulation patterns that are not seen in the atmosphere of Earth. Understanding how these form is fascinating.

2. Secondly, simulating such diverse atmospheres allows model users to test the robustness of their models. Such tests are important as models ought to be robust to changing parameters in a number of scenarios, for example for future predictions of climate change or for paleoclimate studies.

3. Thirdly, GCM simulations complement the observations we have available. Indeed,

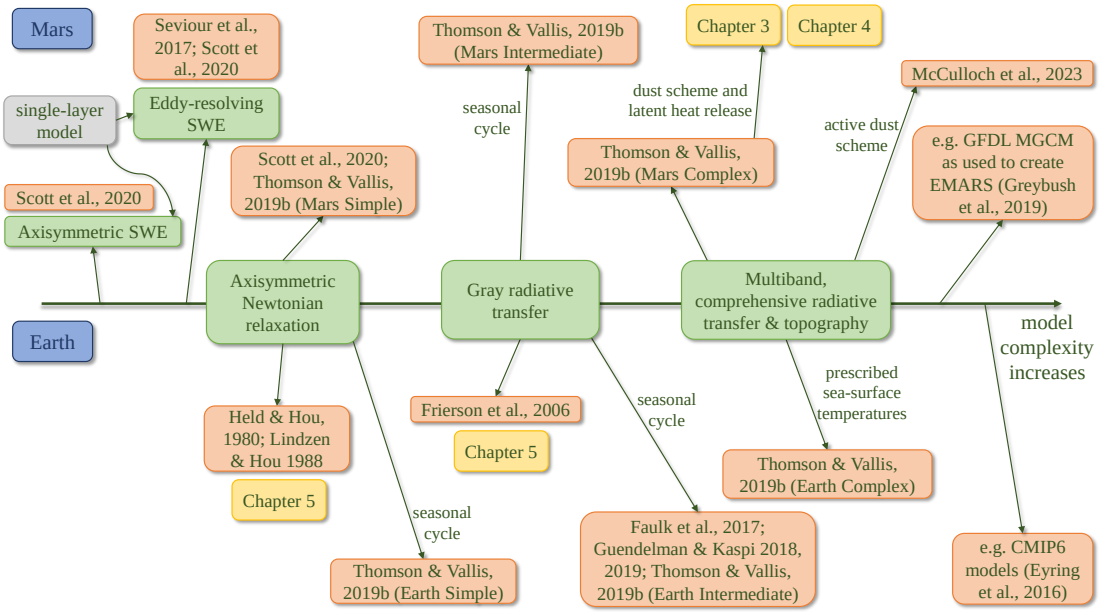

Figure 1.7: **A schematic showing how model complexity varies for a selection of relevant numerical simulations of the atmosphere of both Earth and Mars.** Relevant citations are shown in orange, the chapters of this thesis in yellow, and a brief summary of the model type in green. Model complexity increases from left to right, and Martian models are shown above the x-axis, Earth models below. Configurations of Isca are given in Thomson and Vallis [2019b]. The models shown do not form an exhaustive list.

model simulations allowed scientists to predict the behaviour of the Martian atmosphere before observations were readily available, and predictions were then confirmed by observations once possible. Additionally, there exist very few direct observations of wind fields from the atmosphere of Mars, yet the use of GCMs allows the generation of such fields in a physically consistent manner.

4. Planetary GCMs can also further understanding of Earth's atmosphere, either by comparison with similar atmospheres, or by performing parameter sweeps over planetary parameters to contextualise the atmospheric dynamics of Earth in a broader space.

Figure 1.7 shows a selection of relevant models that have been used in the study of

either Earth's or Mars's atmosphere (with a focus on models that have been used to explore the Martian polar vortices). Models mentioned range from axisymmetric shallow-water equation (SWE) treatment of the Martian northern polar vortex [Scott et al., 2020] on the left through to full Coupled Model Intercomparison Project 6 (CMIP6) models that describe Earth's atmosphere under a range of forcing scenarios [Eyring et al., 2016] on the right. This schematic illustrates how a variety of model complexities and domains may be used to simulate either a specific circulation feature or a full atmosphere, and that models initially developed to simulate the atmosphere of Earth have been readily adapted to Mars. For example, a version of the Met Office's Unified Model (UM) that has been recently adapted to model Mars's atmosphere for the first time is described in McCulloch et al. [2023]. All models mentioned can be and have been used to draw conclusions about the dynamical behaviour of an atmosphere, and there are many further configurations and complexities that are useful to modellers that are not mentioned here. Although this schematic implies a linear progression in model complexity, this is not entirely accurate. Models can have variations in complexity across different components. For example, one model may have a more complex radiation scheme but less complex representation of the ocean than an alternative model. This linear framework is thus not necessarily the most realistic way to conceptualise model hierarchies, although it remains illustrative. The model configurations employed within this thesis sit within the intermediate complexity range, such that all simulations are stratified (i.e. not single layer) but do not aim to model the atmospheres of Earth or Mars as accurately as possible by including the most complex representations of as many features as possible. They bridge the gap between theory and more complex GCMs, thus allowing the user to gain physical insights by isolating the more fundamental physics under investigation without muddying the waters with more complex processes. Such models are also often more computationally efficient than more complex GCMs, meaning that they are useful in parameter sweep studies in which many simulations must be run.

1.5.2 The use of parameter sweeps

A relatively simple way to adapt a GCM beyond Earth would be to incrementally and systematically increase/decrease planetary parameters, including rotation rate, obliquity, eccentricity, or insolation, in a process known as a parameter sweep. Changing some of these parameters, such as obliquity and eccentricity, influences the amount and distribution of incoming solar radiation that reaches a planet's atmosphere. Previous studies have explored climate and atmospheric circulation on Earth-like or gas giant exoplanets over a range of planetary parameters and atmospheric compositions. Parameter sweeps have also previously been used to investigate planetary atmospheres (including both Earth and Mars), as described below.

1.5.2.1 Contextualising Earth's circulation

Varying planetary parameters from an Earth-like base case is a useful way to contextualise the circulation seen in Earth's atmosphere. Previous modelling studies have investigated features of the Hadley circulation over a range of planetary parameters, such as width, location of ascending and descending branches, and strength [Guendelman and Kaspi, 2018, 2019, 2020; Hill et al., 2019; Kaspi and Showman, 2015; Lewis et al., 2021]. By varying orbital period (and hence rotation rate), simulations of tidally-locked exoplanetary atmospheres have investigated potential stratospheric circulation patterns and found that a standing tropical Rossby wave can induce equatorial superrotation and suppress equator-to-pole transport in the stratosphere (with this effect being strongest on planets with shortest orbital periods) [Carone et al., 2017]. Other studies focus more on a planet's habitability, for which the Hadley circulation may be important due to its role in heat distribution [e.g. Kopparapu et al., 2017, 2016; Linsenmeier et al., 2015]. Polar vortices have also recently been investigated across a range of obliquities, rotation rates, and orbital periods. Despite modelling assumptions made that do not necessarily reflect a given planet's atmosphere, similar behaviours were identified in model simulations to those

observed in solar system terrestrial bodies, suggesting that some fundamental dynamical processes are linked to these parameters. This same study also identified polar vortex regimes that have no counterpart in our solar system [Guendelman et al., 2022].

1.5.2.2 Understanding Martian climate history

Adaptation of GCMs and theory in order to study other planets has a long history: the very first attempt at modelling the atmosphere of Mars came from Leovy and Mintz [1969], with a suite of studies following [Haberle et al., 2003; Hollingsworth and Barnes, 1996; Lewis, 2003; Nayvelt et al., 1997; Pollack et al., 1979; Richardson and Wilson, 2002; Schneider, 1983; Wilson, 1997]. Mars GCM (MGCM) parameter sweeps have also been undertaken to understand changes in past climate: Mars's orbital parameters have varied significantly more than Earth's in its history, which will likely have had significant impacts on atmospheric circulation: understanding these remains an open question in Mars science [e.g. Smith et al., 2020; Toigo et al., 2020; Toon et al., 1980]. Due to the large range of eccentricities Mars has experienced, as well as the complications of the timing of perihelion, studies have preferred to focus on obliquity variations, although there have been some considerations of illustrative eccentricity values (typically current eccentricity, $\gamma = 0.093$, or no eccentricity, $\gamma = 0$). Nevertheless, obliquity turns out to have the more significant impact on atmospheric circulation as it affects solar insolation distribution to a greater degree [e.g. Haberle et al., 2003].

1.6 Thesis structure

This thesis contains three individual research chapters, each of which aims to use an idealised GCM approach to understand a particular feature of the dynamics in a planetary atmosphere. Two of these three chapters have been submitted for publication in the American Astronomical Society's *Planetary Science Journal*, one of which has been

published.

- **Chapter 2 - Ball et al. [2021]** titled *The roles of latent heating and dust in the structure and variability of the northern Martian polar vortex* is published in the *Planetary Science Journal*. This chapter investigates the northern polar vortex on Mars and three key factors that influence its morphology and variability. This is achieved by developing an idealised GCM, as well as by comparing the model outputs to reanalysis datasets.

- **Chapter 3** titled *The importance of isentropic mixing in the formation of the Martian polar layered deposits* has been submitted for publication in the *Planetary Science Journal*. This chapter considers hemispheric differences in transport and mixing in the polar regions of Mars over a range of different orbital configurations and atmospheric dust abundances.

- **Chapter 4** titled *The coupling between the Hadley cell and zonal jets across planetary parameters* has been written as an article suitable for publication in a scientific journal, but has not yet been submitted. This chapter investigates the relationships between the Hadley circulation, subtropical and eddy-driven jets in Earth-like exoplanets across a range of obliquities and rotation rates in a highly idealised model. Initially, the results are considered in a dry model, before the influence of moisture is discussed.

- **Chapter 5** summarises and discusses the results of this thesis, and proposes possible future avenues of investigation.

CHAPTER 2

THE ROLES OF LATENT HEATING AND DUST IN THE STRUCTURE AND VARIABILITY OF THE NORTHERN MARTIAN POLAR VORTEX

This chapter sets the scene for the investigation into the dynamics of large-scale features of atmospheric circulation on other planets. The northern polar vortex of Mars makes an ideal base case from which to start, given its fascinating dynamics and the comparative abundance of observations available.

Driving mechanisms of the Martian polar vortices remain poorly understood, in particular the influence of latent heat release and dust on their morphology and variability. Due to the inherently biased nature of the Martian climate system (that is to say, its fundamental handedness due to topography and timing of perihelion), the northern wintertime polar vortex is investigated herein. To study the drivers of the polar vortex, a 'process-attribution' experiment is performed, whereby three features are systematically turned on or off in order to understand their individual and combined influences.

This chapter aims to understand these driving mechanisms, and how they influence both the vortex's morphology, its internal variability, and its interannual variability. The vortex response to the MY 28 Global Dust Storm is examined. Model simulations are

compared to reanalyses, and an investigation into inter- and intra-reanalysis differences is undertaken.

The content of this chapter has been published as an article titled '*The roles of latent heating and dust in the structure and variability of the northern Martian polar vortex*' in the The Planetary Science Journal [Ball et al., 2021]. The material here is essentially identical to that in the published paper, except that the figures and tables have been renumbered and re-captioned to be consistent with the other chapters. The supplementary materials have been placed in Appendix A of this thesis.

Author contributions: the authors of this paper variously contributed to the work, with E.R.B. performing the simulations, analysing the results, and writing the draft of the manuscript. D.M.M. and W.J.M.S. assisted in the design of the investigation and provided guidance throughout. S.I.T. provided invaluable help with model development, in particular with suggestions for the latent heating scheme, and G.K.V. provided helpful discussion throughout. All authors contributed to the proofreading and editing of the manuscript.

2.1 Abstract

The winter polar vortices on Mars are annular in their potential vorticity (PV) structure, a phenomenon identified in observations, reanalysis and some numerical simulations. Some recent modelling studies have proposed that condensation of atmospheric carbon dioxide at the winter pole is a contributing factor to maintaining the annulus through the release of latent heat. Dust and topographic forcing are also known to be causes of internal and interannual variability in the polar vortices. However, coupling between these factors remains uncertain, and previous studies of their impact on vortex structure and variability have been largely limited to a single Martian global climate model (MGCM). Here, by further developing a new MGCM, we decompose the relative roles of latent heat, topography, and dust as drivers for the variability and structure of the northern

Martian polar vortex. Additionally, we analyse a reanalysis dataset, finding that there are significant differences in vortex morphology and variability according to the spacecraft instrument used for the data assimilation. In both model and reanalysis, high atmospheric dust loading (such as that seen during a global dust storm) can disrupt the vortex, cause the destruction of PV in the low-mid altitudes (> 0.1 hPa), and significantly reduce spatial and temporal vortex variability. Through our simulations, we find that the combination of dust and topography primarily drives the eddy activity throughout the Martian year, and that although latent heat release can produce an annular vortex, it has a relatively minor effect on vortex variability.

2.2 Introduction

Of all the planets in the solar system and beyond, Mars's atmosphere is the best-observed besides Earth and so is one of the best suited for study and comparison with Earth's. On both planets, there are regions of strong mid-high latitude zonal winds in the winter hemisphere, known as the polar vortices. Whilst Mars's tropospheric and Earth's stratospheric polar vortices are comparable in their latitudinal extent (the Martian polar vortices extend to around 70° N/S and Earth's to around 60° N/S), the Martian winter tropospheric polar vortices have been shown to be annular in nature. The annulus (which may be thought of as a ring of high PV enclosed between opposing PV gradients) has a local minimum in Ertel's potential vorticity (PV) near the pole [Mitchell et al., 2014]. This contrasts with the polar vortices on Earth, where PV increases monotonically towards each pole - although an annular structure has been found in the mesosphere [Harvey et al., 2009]. The annular nature of the Martian polar vortices is likely to affect meridional gas and aerosol mixing, along with vertical wave propagation [Toigo et al., 2017]. In general, air in the polar low altitudes is some of the 'oldest' (i.e. most isolated) in Mars's atmosphere, but it has been proposed recently that the annulus of PV at the solstice reduces the age of air in the polar

low altitudes through increased mixing with mid-latitude air [Waugh et al., 2019]. Mars's polar vortices have been found to extend through the troposphere, decrease in area with height, and retain the same orientation in the vertical [Mitchell et al., 2014]. Unlike on Earth, zonal winds are maximal equatorward of the maximum PV gradient [e.g. Seviour et al., 2017].

Given that a ring of high PV is barotropically unstable [Dritschel and Polvani, 1992], the persistence of the annular polar vortices on Mars in observations, reanalyses and simulations [e.g. Banfield et al., 2004; Barnes and Haberle, 1996; Waugh et al., 2016] suggests that there must exist some restoring force that maintains the annulus [Mitchell et al., 2014]. Multiple processes have been identified and shown to maintain and stabilise the annular vortex, including diabatic heating by the descending branch of the Hadley circulation [Scott et al., 2020]. Recent modelling using a single-layer shallow water model with a representation of carbon dioxide (CO_2) condensation showed that Mars's short radiative timescale may be responsible for stabilising the annulus [Seviour et al., 2017].

The main constituent of the Martian atmosphere is CO_2, which makes up approximately ~95% of the atmosphere by volume. CO_2 is present in gaseous form and as CO_2 ice clouds. In polar regions during the winter seasons, temperatures can fall below the pressure-dependent sublimation point of CO_2 (around 149 K), leading atmospheric CO_2 to condense and form a layer of CO_2 ice on top of the permanent polar ice caps. Latent heat is released into the atmosphere during the phase change from gaseous to solid CO_2 and this can increase temperatures in the polar lower altitudes by up to 10 K [Toigo et al., 2017]. This means that Mars's atmosphere has a non-dilute condensible component, unlike Earth, whose primary condensible component is water vapour, which reaches a molar concentration of up to a few percent. Toigo et al. [2017] showed that in a comprehensive Mars Global Climate Model (MGCM), an annular polar vortex is maintained if the release of latent heat from CO_2 condensation is well-represented in the model and that without this forcing, a monopolar vortex (i.e. PV increasing monotonically to the pole) forms.

Rostami et al. [2018] found that while the annulus is smooth on a time scale of multiple sols (Martian days), the patches of high PV observed when viewing the vortex at a single moment time are likely caused by the inhomogeneous deposition of CO_2.

Global dust storms (GDSs) remain a major influence on Martian atmospheric dynamics, including the polar vortices. They provide a major source of interannual variability, and one that is not yet fully understood, given the relatively few years of observations. Historically, GDSs appear to dominate the Martian atmosphere approximately once every three southern summers (northern winters) [Shirley, 2015]; there have been only 3 GDSs since Martian Year (MY) 24, occurring in MY 25, MY 28 and most recently in MY 34.[1] Understanding of the drivers of GDSs remains incomplete, although recent work suggests the influence of solar system dynamics [Shirley, 2015] and orbit-spin coupling [Shirley et al., 2020]. Regional and global dust storms may partially or fully disrupt the winter polar vortex in what is termed a 'rapid polar warming' event, when temperatures rise rapidly within the vortex, apparently a response to increased dust aerosol heating enhancing the meridional circulation [Guzewich et al., 2016; Mitchell et al., 2014]. The most recent GDS, occurring in MY 34, is thought to have expanded from an initial equatorial regional storm which created a zonal temperature gradient and hence increased winds, creating a positive feedback [Bertrand et al., 2020]. The impact of the MY 34 GDS has been shown to be different in the north and south polar vortices, an effect likely influenced by the timing of the storm, which occurred when the southern polar vortex was decaying [Streeter et al., 2021]. The southern polar vortex weakened significantly, while the northern polar vortex remained a robust transport barrier.

In MY 28, a GDS developed at around $L_s \sim 265°$, shortly before the northern winter solstice. Dust concentrations were elevated (with dust opacity larger than 1) primarily in

[1] Martian years are numbered according to Clancy et al. [2000], where MY 1 begins at the northern spring equinox ($L_s = 0°$) on April 11th, 1955. Each Martian year is roughly the length of two Earth years, and midwinter in the northern hemisphere is at $L_s = 270°$. Thanks to a recent increase in the number of satellites orbiting Mars, there has been almost continuous observation of the Martian atmosphere since 1999, corresponding to $L_s \sim 104°$, MY 24.

the midlatitudes, but reached up to 40°N [Wolkenberg et al., 2020]. The impact of these recent dust storms on the polar vortices has not yet been fully explored, although Guzewich et al. [2016] investigated the impacts of different timings and magnitudes of GDS.

Along with atmospheric dust loading, Martian topography may also play a role in the morphology of the polar vortices. The southern hemisphere is dominated strongly by wavenumber 1 waves, but in the northern hemisphere eddies show a wavenumber 2 pattern [Hollingsworth and Barnes, 1996], likely influenced by the hemispheric topographical asymmetries. It is also thought that the northern polar vortex has an elliptical shape on average in part due to topographically-forced zonal wavenumber 2 waves [Mitchell et al., 2014; Rostami et al., 2018]. Indeed, recent work has shown that the suppression of wavenumber 2 stationary waves during the MY 34 GDS corresponded to the reduction of the ellipticity of the northern polar vortex [Streeter et al., 2021]. In both winter hemispheres, there is a 'solsticial pause' in the amplitude of low-altitude transient waves. Studies have attributed this in part to topographic zonal asymmetry [Lewis et al., 2016; Mulholland et al., 2016].

It is not yet fully understood how the Martian polar vortices are influenced by the interplay of topography, latent heating and dust loading. Work by Guzewich et al. [2016] and Toigo et al. [2017] investigates how dust and latent heat release each separately influence the polar vortices in modelling studies but there has not yet been any study investigating the combined effects. In this paper, we investigate the transience and variability of the northern Martian polar vortex through the use of a reanalysis dataset and idealised simulations from a newly-developed Martian configuration of the flexible modelling framework Isca [Thomson and Vallis, 2019b; Vallis et al., 2018]. We focus here on the northern polar vortex due to previous work suggesting that the northern hemisphere exhibits a stronger solsticial pause [Lewis et al., 2016], and due to the findings of Guzewich et al. [2016], who note that the northern vortex is more heavily influenced by dust loading than the southern vortex. In their simulations, the southern vortex is found to be reasonably invariant to

southern winter dust loading.

Thanks to prolonged observations of the Martian atmosphere, there is sufficient data available to create a Martian reanalysis dataset spanning several MY, of which there are currently 3 available [Greybush et al., 2019; Holmes et al., 2020; Montabone et al., 2014]. A reanalysis dataset assimilates observations into a general circulation model to provide a three-dimensional, gridded estimate of the atmospheric state, including variables that cannot be directly measured. We use the newly-developed Open access to Mars Assimilated Remote Soundings (OpenMARS) reanalysis product [Holmes et al., 2020] to investigate features of the northern Martian polar vortex. Previous studies of Martian polar vortices in reanalyses have focused particularly on MY 24-27 [Mitchell et al., 2014; Waugh et al., 2016]. We are particularly interested here in the impacts of the MY 28 GDS, as this is the only solsticial GDS in the reanalysis period and provides an exciting opportunity to study the effect of dust on the northern polar vortex during this time. GDSs primarily occur between $L_s \sim 200 - 340°$ [Kass et al., 2016], leading to there being no equivalent southern winter solsticial GDS during the reanalysis period.

We aim to understand the mechanisms that drive the northern Martian polar vortex. We identify significant features of the vortex in OpenMARS and explore these using the flexible modelling framework Isca. Using Isca, we perform an attribution-type study on the polar vortex - with topography, latent heating and dust the parameters to be changed systematically. The rest of the paper is outlined as follows: Section 2.3 introduces the quantities that we will use to investigate the vortex, the reanalysis products currently available and describes the model used in this study. From there, we discuss the northern polar vortex as seen in the reanalysis and in our simulations in Section 2.4. We present results describing the climatological state of the polar vortex and interannual variability in Section 2.4.1, and the sub-seasonal variability in Section 2.4.2. Finally, we summarise the study in Section 2.5.

2.3 Methods

2.3.1 Potential vorticity

Potential vorticity (PV) is a dynamically important quantity, the product of absolute vorticity and the gradient of potential temperature, that is particularly useful in the study of polar vortices. In general, PV is materially conserved provided frictional and diabatic processes vanish. In this paper, we use an approximation to the true PV, valid to a good approximation in a hydrostatic atmosphere, namely

$$q(\theta,t) = -g(f+\zeta_p)\frac{\partial\theta}{\partial p}, \tag{2.1}$$

where q is PV, g is Martian gravitational acceleration (3.72 m s^{-2}), f is the Coriolis parameter, θ is potential temperature, ζ_p is the vertical component of relative vorticity evaluated on a pressure surface, and p is pressure [Hoskins et al., 1985; Read et al., 2007]. PV is calculated from winds and temperature as a function of pressure in the reanalysis and model, then linearly interpolated to isentropic surfaces for our analysis. To remove the large vertical variation of PV in the atmosphere, we then use a common scaling of PV devised by Lait [1994]. To be consistent with Waugh et al. [2016], the exact scaling chosen is

$$q_s(\theta,t) = q \times \left(\frac{\theta}{\theta_0}\right)^{-(1+c_p/R)}, \tag{2.2}$$

with $\theta_0 = 200$ K an arbitrary reference potential temperature and $c_p/R = 4.0$ the ratio of specific heat at constant pressure to the specific gas constant of Martian air.[2] A common way to express PV in Earth's atmosphere is by using potential vorticity units (PVU). Here, we present PV in 'Martian potential vorticity units' (MPVU), where 1 MPVU = 100 PVU = 10^{-4} K m^2 kg^{-1} s^{-1}, adopting the convention used in Streeter et al. [2021].

[2]The code used for calculation of PV, and all other analysis in this paper, is available in Ball [2021].

2.3.2 Reanalyses

Currently, three reanalysis datasets are available for the Martian atmosphere. These are the Mars Analysis Correction Data Assimilation (MACDA) [Montabone et al., 2014], the Ensemble Mars Atmosphere Reanalysis System (EMARS) [Greybush et al., 2019], and the OpenMARS [Holmes et al., 2020] datasets. We primarily use OpenMARS within this work. OpenMARS assimilates observations of thermal profiles, water ice and dust opacities, ozone and water vapour column abundance into the UK-LMD MGCM to produce a gridded estimate of Martian weather spanning MY 24-32. Full details of the profiles assimilated into OpenMARS and the underlying MGCM may be found in Holmes et al. [2020], although we briefly discuss relevant details here. The OpenMARS dataset can be broadly separated into two distinct periods based on the retrieval instruments used. In the era MY 24-27, temperature retrievals assimilated in to the model are from the Thermal Emission Spectrometer (TES) aboard Mars Global Surveyor (MGS). TES nadir retrievals provide coverage of temperature up to around 40 km in altitude but have largest uncertainties at the lowest altitudes due to possible errors in estimating surface pressure. Systematic errors in temperature retrievals peak over the winter polar regions due to cold surface temperatures and there is a lack of coverage of column dust optical depth (CDOD) retrievals at winter high latitudes. Due to cold surface temperatures on the night-side of the planet, only day-side dust retrievals are assimilated. In MY 28-32, retrievals are from Mars Climate Sounder (MCS) aboard Mars Reconnaissance Orbiter. MCS temperature profiles have greater vertical resolution than TES (5 km rather than 10 km) and cover up to approximately 85 km in altitude [Holmes et al., 2020]. Conversely to TES, temperature retrieval errors are lowest in the lower atmosphere for MCS. There are an increased number of MCS profiles at the end of MY 28, in an effort to observe the atmosphere during the MY 28 GDS. Finally, although estimates of CDOD from MCS observations have the possibility of errors due to the extrapolation down to the surface, retrievals are possible during both daytime and nighttime polar winter. It is worth noting that there is no overlap

in the TES and MCS temperature retrievals, so there is no reanalysis data available for the northern hemisphere winter of MY 27.

OpenMARS may be seen as the 'updated version' of the MACDA dataset (the details of which are described in Montabone et al. [2014]), which spans MY 24-27 (assimilating TES thermal profiles as in OpenMARS) and is based on an older version of the same MGCM. OpenMARS in the TES period differs from MACDA in that the underlying model has been updated - for example, MACDA uses an analytical dust distribution whereas in OpenMARS dust is freely transported, then scaled to match observed dust distributions, and OpenMARS now includes a thermal plume model. A detailed description of MACDA and a discussion of how the products differ may be found in Holmes et al. [2020]; Montabone et al. [2014], respectively.

The final reanalysis dataset available is EMARS, which spans MY 24-34. Full details of the reanalysis may be found in Greybush et al. [2019] and its precursor Greybush et al. [2012]. EMARS is a 16-member ensemble reanalysis which uses the Geophysical Fluid Dynamics Laboratory MGCM along with assimilation of retrievals from TES and MCS for the periods described above. Dust is controlled by three radiatively active tracers. Temperature retrievals that fall significantly below the pressure dependent CO_2 condensation point, T_c, are modified to match the condensation temperature, and when temperatures within the model are projected to be below T_c, gaseous CO_2 is removed from the atmosphere and placed on the surface as CO_2 snow. In contrast, for OpenMARS, when temperature retrievals fall significantly below T_c, these are simply filtered out before assimilation into the model.

We here present results using the OpenMARS dataset, although we do verify any results that we find in OpenMARS against EMARS and find broadly similar results. Where there are any notable differences, we include supplementary figures showing the results in EMARS and discuss these differences.

2.3.3 Model

In addition to the OpenMARS reanalysis dataset, we use an idealised climate model to investigate the role of different physical processes in shaping polar vortex structure and variability. We make use of Isca, an idealised modelling framework developed with flexibility in mind, first described in Vallis et al. [2018]. One significant advantage of Isca, which we exploit here, is the relative ease of including or excluding different physical processes within model configurations. Here we include a brief description of the Isca representation of the Martian atmosphere we build upon in this work: additional details can be found in Section 4 of Thomson and Vallis [2019b] (our simplest 'control' configuration is identical to the configuration described in their Section 4.3). Isca uses a spectral, primitive equation dynamical core in spherical co-ordinates along with the multi-band, comprehensive SOCRATES radiation scheme [Manners et al., 2017; Thomson and Vallis, 2019a]. The spectral files used were originally created for the ROCKE-3D model [Way et al., 2017], and have been adapted to include dust aerosol as described below. We use a T42 spectral resolution (corresponding to a 64 x 128 (~ 2.8° x 2.8°) spatial grid), and 25 vertical sigma levels reaching approximately 0.05 Pa. We use topography from the Mars Orbiter Laser Altimeter (MOLA) measurements aboard MGS [Smith et al., 1999].

To investigate the potential dynamical and thermal impacts on the northern Martian polar vortex, we have additionally developed and implemented[3] an idealised dust scheme and representation of latent heating due to the condensation of CO_2, described below. These were identified to be the primary missing processes in the representation of Mars's atmosphere within the Thomson-Vallis configuration of Isca-Mars, and, as shown below, are fundamental in attaining a reasonable representation of the polar vortices in the model. We do not include any representation of radiatively active ice clouds, which have been shown to significantly influence temperatures and atmospheric circulation in MGCMs [Madeleine et al., 2012].

[3]This configuration of Isca is currently available here: https://doi.org/10.5281/zenodo.4627264

2.3.3.1 Representation of latent heating from carbon dioxide condensation

For this work, we have developed a simple representation of the latent heat released from CO_2 condensation as this has been proposed to play a crucial role in driving the annular polar vortex in MGCMs [Toigo et al., 2017]. The latent heat release from CO_2 condensation in Isca does not involve any CO_2 phase changes, but a simple prescribed temperature tendency once the condensation point of CO_2 is reached. Following Lewis [2003] and Way et al. [2017], the condensation point of CO_2, T_c, is derived from an approximate solution to the Clausius-Clapeyron relation, namely

$$T_c = 149.2 + 6.48 \log_e \left(\frac{1}{p_0} p \right), \tag{2.3}$$

where p is model pressure in Pascals and T_c is in Kelvin. $1/p_0 = 0.00135$ is derived from reference pressure p_0. Condensation and sublimation of CO_2 within OpenMARS is also calculated according to this relation [Holmes et al., 2020]. When temperature projected by the model, T^*, falls below T_c, model temperature T is set to T_c, as in Forget et al. [1998]. The difference $T_c - T^*$ is used to calculate the amount of latent heat that would be released, by estimating the mass of CO_2 that would condense according to this temperature difference.

We have not yet implemented within Isca any representation of the mass loss itself that occurs when CO_2 condenses. Although this can be a significant amount — up to 30% of the mass of the atmosphere can be lost over the course of a Martian winter [Tillman, 1988] — it has been shown previously that the dynamical effect of the pressure changes caused by the mass loss has less impact on the structure of the northern Martian polar vortex than the latent heat release associated with the CO_2 condensation [Waugh et al., 2019]. As we represent dust using an analytical profile rather than as a tracer, there is no opportunity for dust particles to act as condensation nuclei for CO_2 ice, a process that allows more atmospheric CO_2 to condense in a dusty atmosphere [Gooding, 1986]. There is also no representation of CO_2 sublimation from surface ice into the atmosphere. In this

regard, our choice not to update the pressure where CO_2 condensation occurs makes sense in that otherwise eventually the atmospheric mass would disappear if we did consider the mass lost.

2.3.3.2 Dust scheme

Dust is known to be an important feature in many Martian atmospheric processes. We choose a simple representation of dust - prescribing an analytical latitudinal and vertical profile that has been used in several MGCMs without explicitly modelling dust lifting processes.

The effective radius and variance of dust particles are given by $r_{\text{eff}} = 1.5\mu$m and $v_{\text{eff}} = 0.3\mu$m respectively, consistent with simulation 2 of Madeleine et al. [2011]. The size distribution of the dust particles follows a modified-gamma profile and the spatial distribution of dust radiative properties is uniform. The parameters of the modified-gamma distribution are determined by the values of r_{eff} and v_{eff}, according to Hansen and Travis [1974]. The refractive indices of dust have been chosen according to Wolff et al. [2006]. Scattering properties are then calculated using a Mie scattering algorithm. Although dust particles have been noted to be cylindrical with diameter-to-length ratio 1.0 [see, for example, Wolff et al., 2009], here our choice of the SOCRATES radiation scheme means that they must be modelled as spherical. However, the approximation does not introduce systematic effects above the 5% level in radiance [Wolff et al., 2006], and is computationally much more efficient.

Zonally-averaged infrared absorption CDOD normalised to the reference pressure of 610 Pa product is input and converted to a surface mass mixing ratio by the SOCRATES interface within the model. The vertical and latitudinal distribution of dust in the model then follows the modified Conrath-v profile described in Montmessin et al. [2004]. The top of the dust layer is given by z_{max} (km), dependent on solar longitude L_s (degrees) and latitude ϕ (degrees), calculated as

$$z_{max}(\mathrm{L}_s,\phi) = 60 + 18\sin(\mathrm{L}_s - 158) \\ -(32 + 18\sin(\mathrm{L}_s - 158))\sin^4\phi - 8\sin(\mathrm{L}_s - 158)\sin^5\phi. \tag{2.4}$$

From this, the dust mass mixing ratio a is calculated using the following expression:

$$a = a_0 \exp\left\{\nu\left[1 - \max\left\{\left(\frac{p_{ref}}{p}\right)^{70\ \mathrm{km}/z_{max}}, 1\right\}\right]\right\}, \tag{2.5}$$

where a_0 is a constant mass mixing ratio at pressure p_0, determined by dust opacity at the surface [see Conrath, 1975; Pollack et al., 1979, for details], which is scaled to produce realistic model temperatures and winds. p_{ref} is the reference pressure 700 Pa. The Conrath-ν profile allows well-mixed dust in the lower atmosphere, with exponentially decreasing concentrations of dust at higher altitudes and has been used in many MGCMs, such as Guzewich et al. [2016]; Madeleine et al. [2011]; Montmessin et al. [2004]. However, recent work showing the evidence of detached dust layers suggests this profile might not be as appropriate as once thought, particularly in the tropics [Heavens et al., 2014]. We choose however to use it here both for its simplicity, ease of adaptation, and for comparability with other models. Since dust is determined by an analytical expression within the model and is not lifted from the surface into the atmosphere, there is no capacity for spontaneous generation of dust storms. However the flexibility to choose an analytical distribution within the model allows the user to investigate the impact of a high dust loading in an area of their choosing. All dust distributions underlying the simulations in this study are zonally symmetric, although Isca presents the user with the option of a full latitudinally- and longitudinally-varying dust distribution.

2.3.3.3 Dust Scenarios

We present results from simulations from Isca with various dust scenarios. The model uses the Mars Climate Database (MCD) [Forget et al., 1999; Millour et al., 2018] dust

year climatologies [Montabone et al., 2015, 2020] to form simulations that isolate the role of interannual dust variability, the years of which may be compared directly to the years available in OpenMARS. Details of the dust cycle used in the MCD are described in Madeleine et al. [2011]. These dust products inform the surface dust mass mixing ratio, a_0, and all years of simulations then follow the Conrath-ν vertical profile (Equation 2.5). These 'yearly' simulations all include representations of dust, latent heat release, and topography as we are interested in the influence of dust in each MY in our most realistic simulations.

We also use the MCD standard dust scenario, which is built by averaging the kriged yearly climatologies MY 24-31 (excluding the GDS events of MY 25 and MY 28) [Montabone et al., 2015], to investigate how latent heat release, dust, and topography influence the polar vortex in a suite of process-attribution simulations. Using this climatological dust product allows us to simulate our best guess of a Martian year with 'typical' dust loading. The evolution of surface and vertical dust mass mixing ratio is shown in Figure 2.1 for the process-attribution dust simulations. An explicit list of the simulations performed, the processes turned on, and dust products used in each can be found in Table 2.1.

Each simulation was run for 4 Martian years and results shown are the average of the three final years (ensemble members) of each simulation. The first year was discarded, as this is found sufficient to reach an equilibrated state from rest. The exception is MY 28, which was run for 10 years to fully investigate the internal variability during the GDS caused by different initial conditions. Given the short radiative timescales on Mars, and the lack of freely moving dust or CO_2 microphysics, there is little ensemble spread in general. Figure 2.1 shows the evolution of surface and equatorial vertical dust mass mixing ratio throughout the 'climatological year', illustrating the peak in dust loading around the northern winter solstice. The vertical profile is informed by the Conrath-ν profile. Absorption CDOD normalised to 610 Pa for individual years can be seen in Figure 21 of Montabone et al. [2015], illustrating dust loading across individual Martian years.

Figure 2.1 also illustrates a proxy for the amount of latent heat released over the course

Simulation Name	Short Name	Topography	Latent Heating	Dust	Dust Product, Scaling
Control	Control	None	No	No	-
Latent Heat	LH	None	Yes	No	-
Dust	D	None	No	Yes	Climatology, 1x
Latent Heat and Dust	LH+D	None	Yes	Yes	Climatology, 1x
Topography	T	MOLA	No	No	-
Latent Heat (Topography)	LH+T	MOLA	Yes	No	-
Dust (Topography)	D+T	MOLA	No	Yes	Climatology, 1x
Latent Heat and Dust (Topography)	LH+D+T	MOLA	Yes	Yes	Climatology, 1x
Yearly	Yearly	MOLA	Yes	Yes	Yearly (MY 24-32), 1x
High Dust	High Dust	MOLA	Yes	Yes	Yearly (MY 24-32), 2x

Table 2.1: **Table of simulations in Chapter 2.** The scaling of the dust product refers to the scaling of the surface mass mixing ratio, q_0, compared to its value in the 'Dust' simulation. In all simulations, the dust mass mixing ratio follows the Conrath-ν profile.

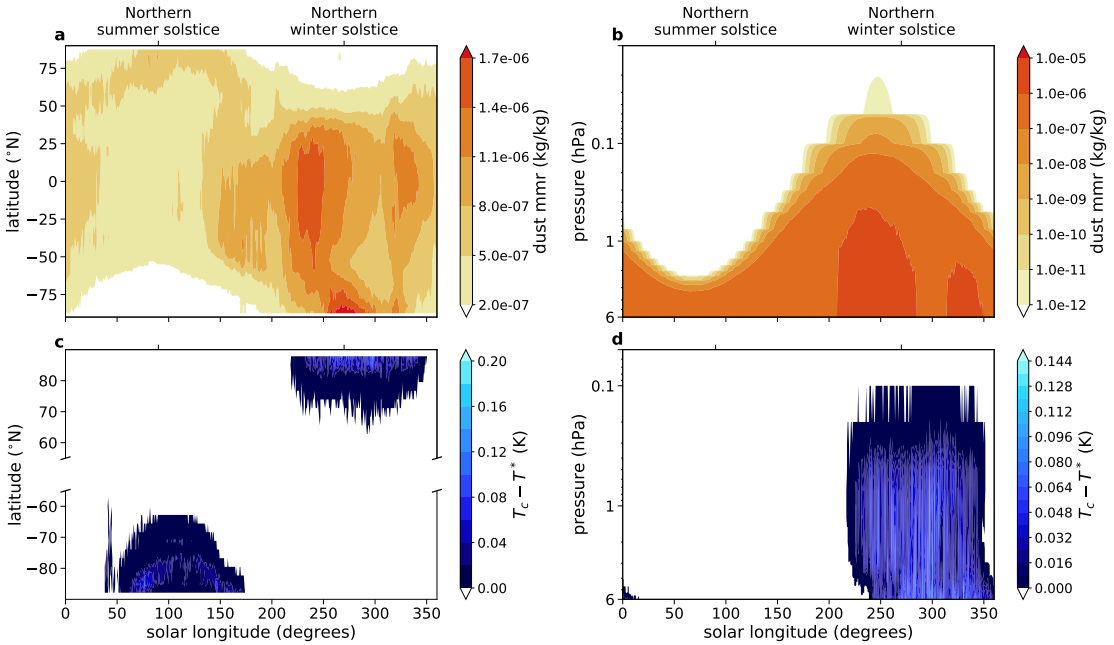

Figure 2.1: **Model dust and latent heating profiles in a climatological year.** Evolution of (a) surface and (b) vertical equatorial dust mass mixing ratios (mmr) for the 'climatological' dust product over the course of a Martian year. Temperature below condensation point (details in text) in the 'Latent Heat and Dust (Topography)' simulation (c) on the 2 hPa surface and (d) at 85° N.

of a Martian year during the 'Latent Heat and Dust (Topography)' simulation including dust, topography and latent heat release. The proxy for latent heat release shows where temperature T^* falls below the pressure-dependent condensation point of CO_2, as defined in Equation 2.3. We see that latent heat release occurs throughout northern winter, up to ~ 0.1 hPa.

2.4 Results

2.4.1 Polar vortex mean state and interannual variability

We will initially discuss the structure of the mean-state winter (averaged over $L_s = 270 - 300°$) polar vortex. Figure 2.2 shows the vertical cross-section of zonal-mean PV over each

winter of OpenMARS data. PV has been scaled according to Lait [1994] to remove vertical variation due to exponentially decreasing pressure with altitude (see Section 2.3.1 for details). It can be seen that the maximum in PV (blue contour) lies away from the pole, meaning an annular vortex, below ~ 0.1 hPa, in each Martian year, save MY 28. In MY 28, the zonal-mean zonal winds are weaker and the maximum in PV lies at the pole.

We also note that there appears to be a systematic difference in the vertical structure of the PV cross-section in the different periods of OpenMARS. The TES period (MY 24-27, Figure 2.2a-c) shows a very strong vortex core, confined roughly below 0.1 hPa, whereas the MCS period (MY 28-32, Figure 2.2d-h) displays a stronger vortex at higher altitudes. EMARS also displays this high PV at high altitudes in the MCS period (not shown). Since MCS temperature retrievals reach approximately 80 km (~ 0.05 hPa) in altitude, compared with TES retrievals at ~40km (~ 3 hPa), this would reinforce the finding of Waugh et al. [2016] that differences between MACDA (noting that MACDA is only available for the TES period, and shows a very similar structure to OpenMARS TES) and EMARS vortex structure above 0.1 hPa are largely due to differences in the underlying models, and the reanalyses below 0.1 hPa are controlled by the assimilated data. We also note that the observations assimilated in the MCS era lead to a stronger jet core which extends to higher altitudes, with zonal-mean zonal winds exceeding 150 ms^{-1} reaching well into the upper atmosphere (< 0.01 hPa).

Figure 2.3 shows winter Lait-scaled PV and zonal winds in OpenMARS on the 300 K isentropic surface. The annular, elliptical vortex is visible in all years, save in MY 28 (Figure 2.3d). In MY 28, we also observe reduced zonal wind speeds (by up to 40 ms^{-1}) and the destruction of the polar vortex in the winter period. The GDS of MY 25 (Figure 2.3b), which ended at around $L_s \sim 245°$, appears not to have had this effect. Given the relatively short radiative relaxation time scales on Mars (~0.5-2 sols) [Eckermann et al., 2011], this is perhaps not surprising. Indeed, an average over the period $L_s = 235 - 245°$ equivalent to Figure 2.3 shows that, during this period, the polar vortex in MY 25 was greatly weakened,

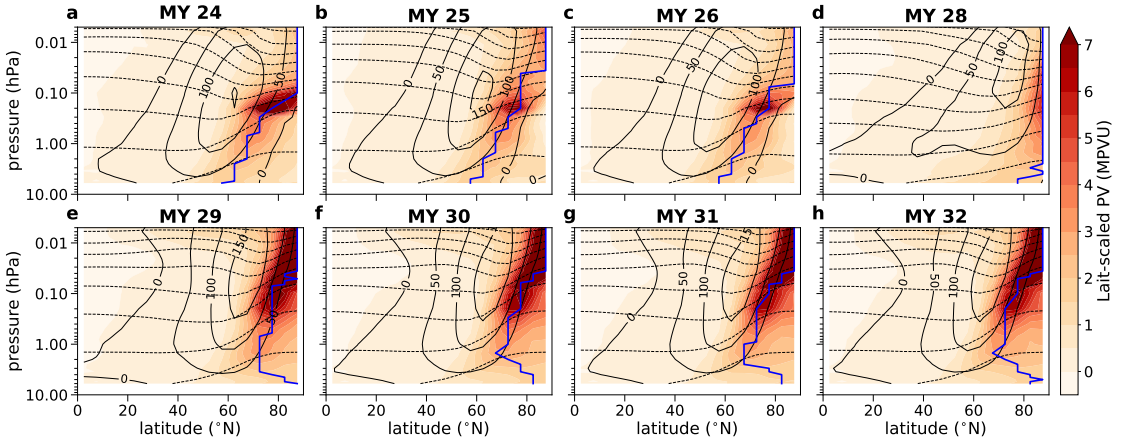

Figure 2.2: **Vertical cross-section of the northern polar vortex in OpenMARS.** Winter-mean zonal-mean Lait-scaled potential vorticity (shading) and zonal-mean zonal wind (solid black contours) for each Martian winter in the OpenMARS reanalysis dataset. Note that the winter of MY 27, when there were no TES or MCS temperature retrievals, is not shown. Dashed contours correspond to the 200, 300, ... K potential temperature surfaces and the solid blue contour marks the latitude at which PV takes it maximum value at each pressure level. The Martian winter solstice falls at $L_s = 270°$, and each panel is averaged over $L_s = 270 - 300°$.

but clearly recovers by the winter solstice (not shown).

In order to understand the structures seen above we sequentially 'turn on' certain processes within Isca, so forming a hierarchy of process-attribution simulations. Figure 2.4 shows that a representation of dust is necessary within the model to achieve the high zonal winds and temperatures seen in OpenMARS. This is due to the atmospheric heating caused by the addition of dust aerosol into the atmosphere. Dust within the model enhances both the jet strength and the polar high altitude warming, a characteristic feature of the Martian winter atmosphere caused by enhanced poleward meridional transport of warm air [Guzewich et al., 2016]. Polar temperatures at low altitudes (> 1 hPa) in simulations that include latent heat release (Figure 2.4c,e) are up to 10 K warmer than those without (Figure 2.4b,d), consistent with the amount of warming seen in Toigo et al. [2017]. This is in much better agreement with the temperatures seen in reanalysis (Figure 2.4a). However, we note that the small area over which CO_2 condenses appears insufficient to strongly

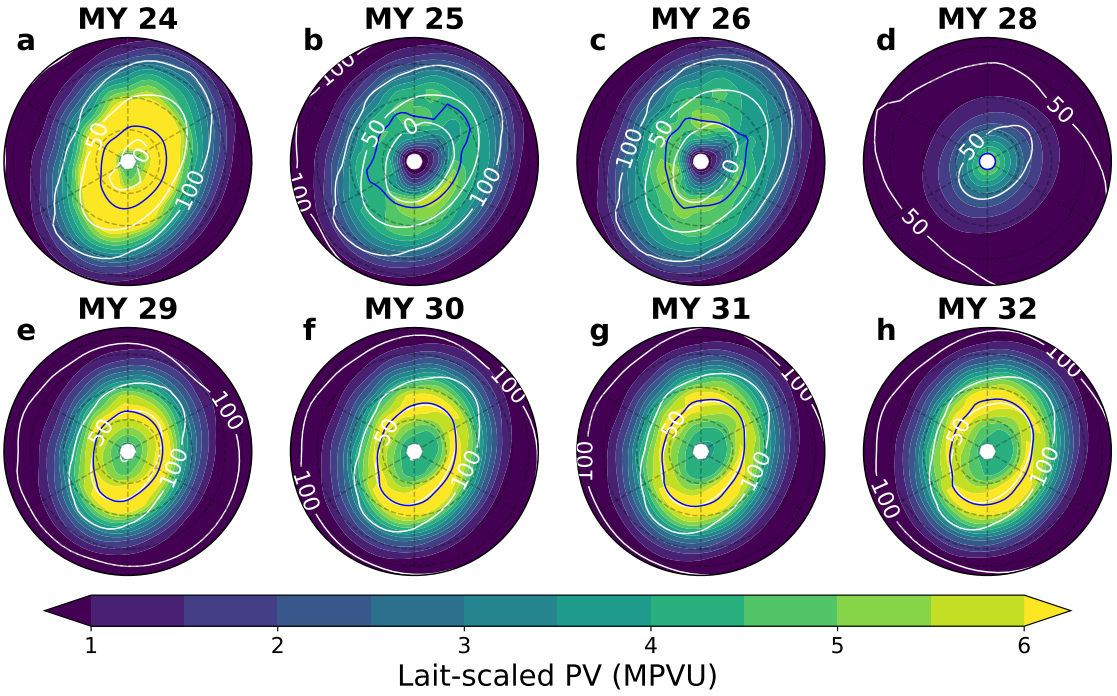

Figure 2.3: **Horizontal cross-section of the northern polar vortex in OpenMARS.** Winter-mean ($L_s = 270 - 300°$) north polar stereographic maps of Lait-scaled PV (shading) and zonal wind (contours) on the 300 K (~ 0.5 hPa) surface from each winter of OpenMARS data. The solid blue contour shows the latitude of maximum PV. Dashed latitude lines correspond to 60° N, 70° N, and 80° N, with each panel bounded at 55° N. Dashed longitude lines start from $0°E$ at the bottom of each panel. Note that the elevated topography of Tharsis province is located between $220 - 300°E$ (not shown).

affect zonal-mean zonal winds, aside from a small weakening in winds.

Figure 2.5 shows winter zonal-mean PV for various Isca configurations, all with topography. By observing the solid blue contour in Figure 2.5c,e, it is clear to see that latent heating in the model does indeed push the maximum in PV away from the pole, particularly at altitudes between 1-0.1 hPa, compared to simulations that do not include representation of latent heat release. This suggests that latent heat release at the pole is acting to reduce PV there, thereby driving the annulus. We also see that dust in the model pushes the jet core further poleward, reducing the latitudinal extent of the polar vortex, as may be expected from an enhancement of the mean meridional circulation. Dust also increases

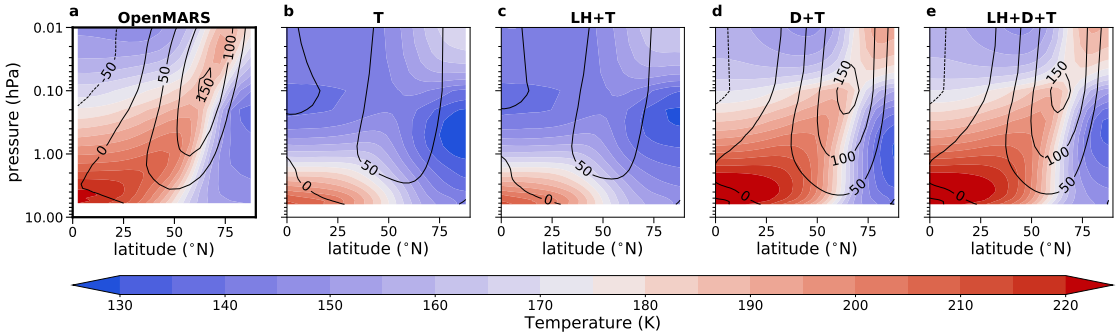

Figure 2.4: **Comparison of the vertical cross-section of the northern zonal wind and temperature in OpenMARS and Isca.** Winter cross-sectional profiles ($L_s = 270 - 300°$) of zonal-mean temperature (shading) and zonal-mean zonal wind (contours) in the northern hemisphere for (a) all years of OpenMARS and (b-e) the process-attribution simulations with topography. For each simulation, winds and temperatures have been averaged over 3 ensemble members.

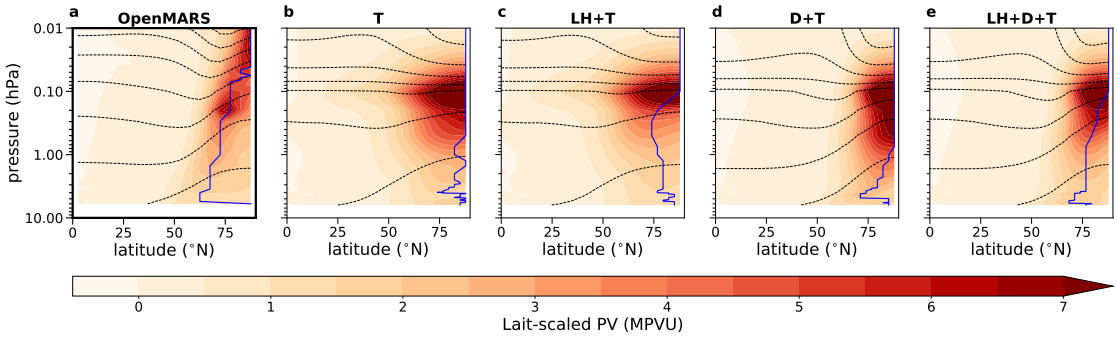

Figure 2.5: **Vertical cross-section of the northern polar vortex in OpenMARS.** Winter ($L_s = 270 - 300°$) zonal-mean Lait-scaled potential vorticity (shading) and potential temperature surfaces (dashed contours, corresponding to 200, 300, ... K) in the northern hemisphere for (a) all years of OpenMARS and (b-e) the process-attribution simulations with topography. For each simulation, winds and temperatures have been averaged over 3 ensemble members. The solid blue contour shows the latitude of maximal Lait-scaled PV at each pressure level, as in Figure 2.2.

the vertical potential temperature gradient at lower altitudes (consider the tightening of the isentropes seen in Figure 2.2b,d, for example) and it is this that contributes to the strengthening of PV at around 1 hPa.

Another way to visualise the influence of turning on processes in our process-attribution simulations is to consider polar stereographic projections of the polar vortex, as shown

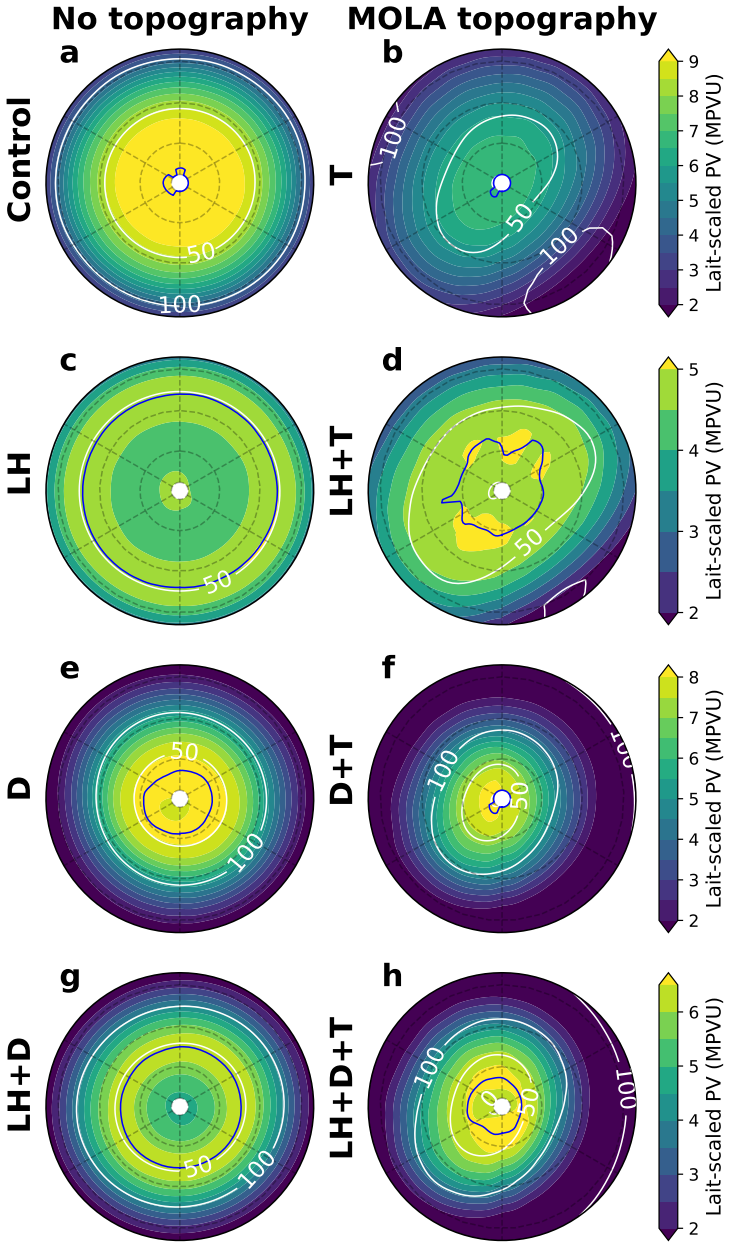

Figure 2.6: **Horizontal cross-section of the northern polar vortex in the process-attribution experiment.** Winter-mean ($L_s = 270 - 300°$) north polar stereographic maps of Lait-scaled PV (shading) and zonal wind (contours) on the 300 K surface from all process-attribution simulations. The solid blue contour shows the latitude of maximum PV. Dashed latitude lines correspond to 60° N, 70° N, and 80° N, with each panel bounded at 55° N. Note that each row has a different colour scale. Dashed longitude lines start from $0°E$ at the bottom of each panel. In simulations where topography is included, note that the elevated Tharsis province is located between $220 - 300°E$ (not shown).

in Figure 2.6. We note several effects. Turning on latent heating increases the width of the annulus (the distance from the pole to the maximum value in PV) in all experiments. Turning on dust may actually also increase the width of the annulus in those experiments where latent heating is not present (see Figure 2.6a,e), likely due to the downwelling of warm air from enhanced meridional circulation. However when latent heating is also turned on, dust reduces the width of the annulus (e.g. Figure 2.6c,g), suggesting a complex relationship between these two factors. Turning on topography always reduces the width of the annulus when one exists (Figure 2.6c-h), a result consistent with Seviour et al. [2017], who found that topographic forcing of large enough amplitude would lead to a monotonic PV distribution in a shallow-water model. Turning on topography also forces the elliptical wave-2 shape of the northern polar vortex. The ellipse is particularly noticeable in simulations without dust (Figure 2.6b,d). This is consistent with previous studies that showed increased loading during the MY 34 dust storm pushed the jet poleward away from the wavenumber 2 topographic forcing, thus reducing the ellipticity of the vortex [Streeter et al., 2021].

To investigate the influence of interannual dust variability, we also ran the 'yearly' simulations described in Table 2.1. Figure 2.7 shows PV for each year on the 300 K surface, which is just below the core of the vortex in OpenMARS. Although the dust signal is relatively weak compared to the reanalysis, MY 28 (Figure 2.7d) sees the annulus shrink toward the pole, particularly noticeable when only compared to other MCS years (MY 29-32, Figure 2.7e-h). On the 300 K level, PV actually strengthens in MY 28, although the weakening seen in OpenMARS does occur at higher levels (> 350 K) (not shown). Although the zonal winds do not appear much weaker in MY 28 simulations, as they are in the reanalysis (Figure 2.3d), when dust mass mixing ratio is increased further within the model, thereby increasing the total atmospheric dust loading, zonal winds weaken and PV is completed destroyed in MY 28 (Supplementary Figure A.1d). Hence, one might conclude that although the dust signal is somewhat weaker in our model than in the reanalysis, dust

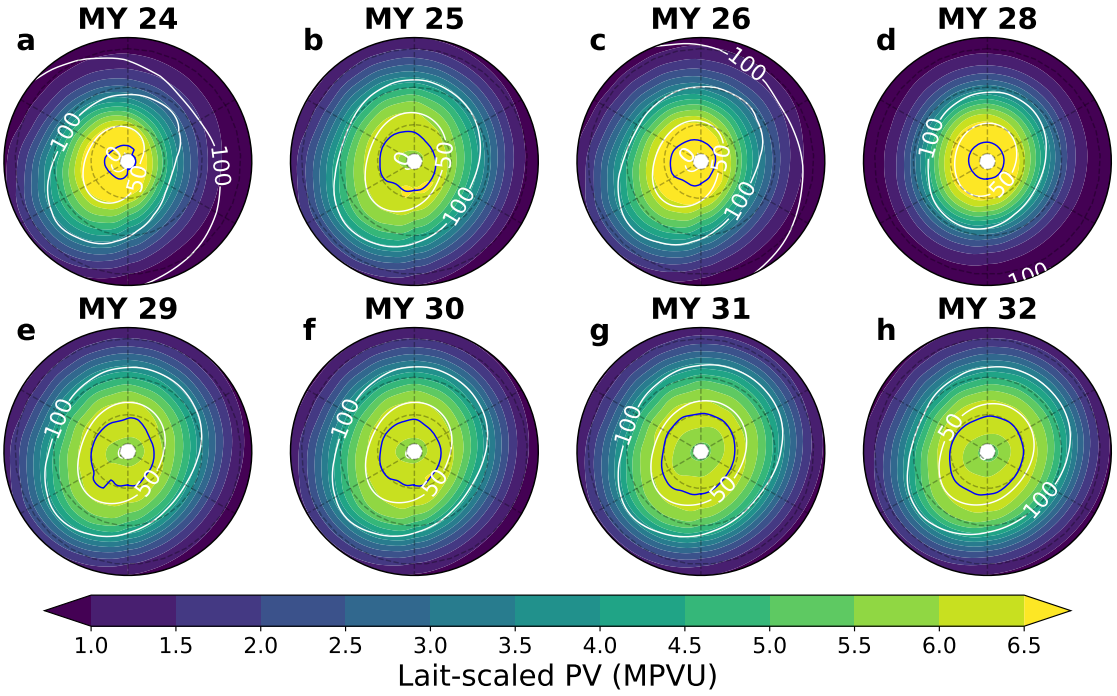

Figure 2.7: **Horizontal cross-section of the northern polar vortex in the yearly model simulations.** Winter-mean ($L_s = 270 - 300°$) north polar stereographic maps of Lait-scaled PV (shading) and zonal wind (contours) on the 300 K surface from 'yearly' model simulations. The solid blue contour shows the latitude of maximum PV. Please see Table 2.1 for a description of the processes turned on in these simulations. Each year consists of three ensemble members. Dashed latitude lines correspond to 60° N, 70° N, and 80° N, with each panel bounded at 55° N. Dashed longitude lines start from $0°E$ at the bottom of each panel. Note that the elevated topography of Tharsis province is located between $220 - 300°E$ (not shown)

.

was indeed a major contributor to the vortex weakening in MY 28. This is in agreement with the nonlinear response of the zonal wind speed to aerosol heating rate, or equivalently, dust loading [Guzewich et al., 2016].

In the 'yearly' simulations, the morphology of the northern polar vortex also changes somewhat between the TES and MCS eras of observations, as it does in OpenMARS. In the TES era (Figure 2.7a-c), the vortex is confined to higher latitudes, while in the MCS era the annulus is clearer, although it is weaker in terms of its mean PV. This suggests that

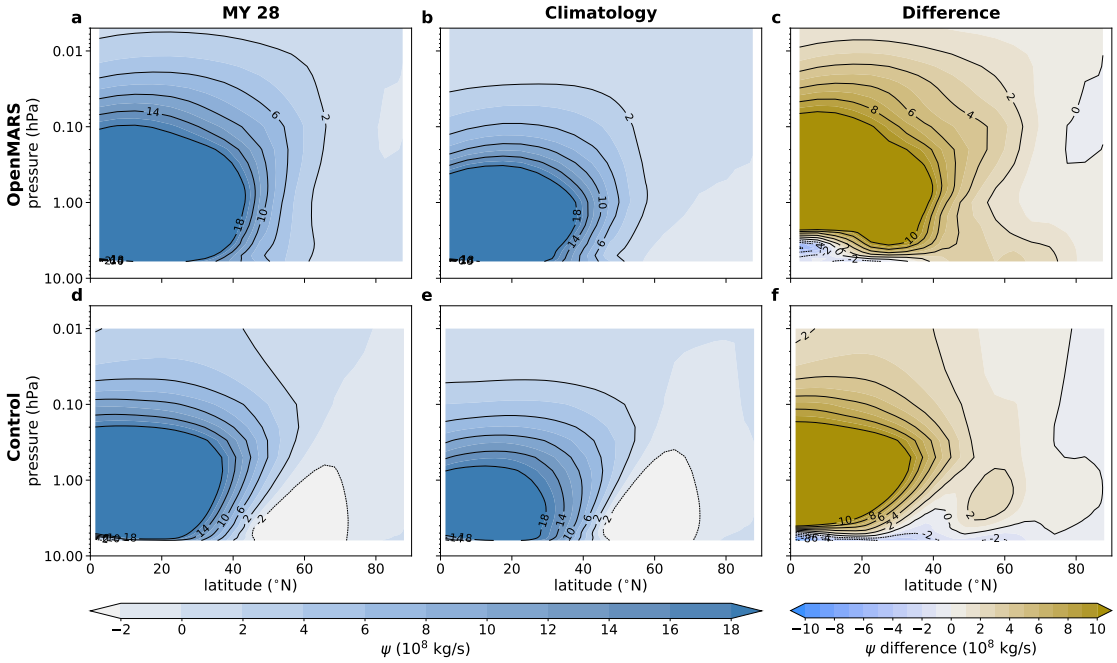

Figure 2.8: **Comparison of the overturning streamfunction in OpenMARS and model.** Winter ($L_s = 270 - 300°$) northern hemisphere Eulerian meridional mass streamfunction ψ for OpenMARS (top row) and Isca (bottom row). OpenMARS data is (a) MY 28 and (b) a climatological average over MY 24-26, 29-32. For Isca, the data shown are (d) the MY 28 'yearly' simulation and (e) the 'Latent Heat and Dust (Topography)' simulation. The difference (MY 28 - Climatology) is shown for (c) OpenMARS and (f) Isca.

dust optical depth retrievals from the two instruments may be sufficient to cause some systematic differences in OpenMARS.

Given that Hadley cell outflow has been found to be sufficient to form a PV maximum at 60° N in a full eddy-resolving model [e.g. Scott et al., 2020], changes in the morphology of the polar vortex may well be linked to changes in meridional circulation. For example, Streeter et al. [2021] found that there were longitudinally asymmetric changes in meridional transport into and out of the polar vortices during the MY 34 GDS. To illustrate the difference in circulation between MY 28 and other years in both the reanalysis and model, we now investigate the Eulerian meridional mass streamfunction, given by

$$\psi(\phi, p) = \frac{2\pi r}{g} \cos\phi \int_0^p \bar{v}(\phi, p)\, dp, \tag{2.6}$$

where r is Mars's radius (3.39×10^6m), g is gravitational acceleration, and $\bar{v}$ is zonal-mean meridional wind. In both reanalysis and model, we see the typical Martian cross-equatorial Hadley cell (Figure 2.8b,e). In MY 28, this is strengthened and the descending branch of the overturning cell is pushed further poleward (Figure 2.8c,f). Our results in reanalysis and model are consistent with previous work that has shown the presence of atmospheric dust strengthens the Hadley circulation, and that a GDS can push the descending branch poleward, particularly at high altitudes [e.g. Guzewich et al., 2016]. The model has a persistent anti-clockwise cell north of 40° N (Figure 2.8d,e). Although this does not appear in the multi-annual average for OpenMARS, it is seen in MY 29-32 (not shown), implying differences in meridional circulation during the two observational eras.

2.4.2 Sub-seasonal polar vortex variability

We now turn to investigate the factors driving shorter-term, sub-seasonal variability of the northern polar vortex, again drawing on our model simulations and reanalysis data. First, we look at the sub-seasonal changes in jet strength and overturning circulation during a GDS in Figure 2.9. During the period of the MY 28, the meridional circulation strengthens considerably, the jet weakens, and both the jet latitude and Hadley cell edge shift poleward. We see a difference in the strength of the overturning circulation, defined as the maximum value of ψ at 50 Pa in the northern hemisphere, for the two retrieval eras in Figure 2.9a. The mean meridional circulation is somewhat weaker in the TES period than in the MCS period. In the MCS era, the strength of the mean meridional circulation shows little interannual variability, save for in MY 28 during the GDS, which strengthens the circulation through aerosol heating. The edge of the Hadley cell, or the latitude at which ψ at 50 Pa first crosses zero north of the equator, is shown for each year

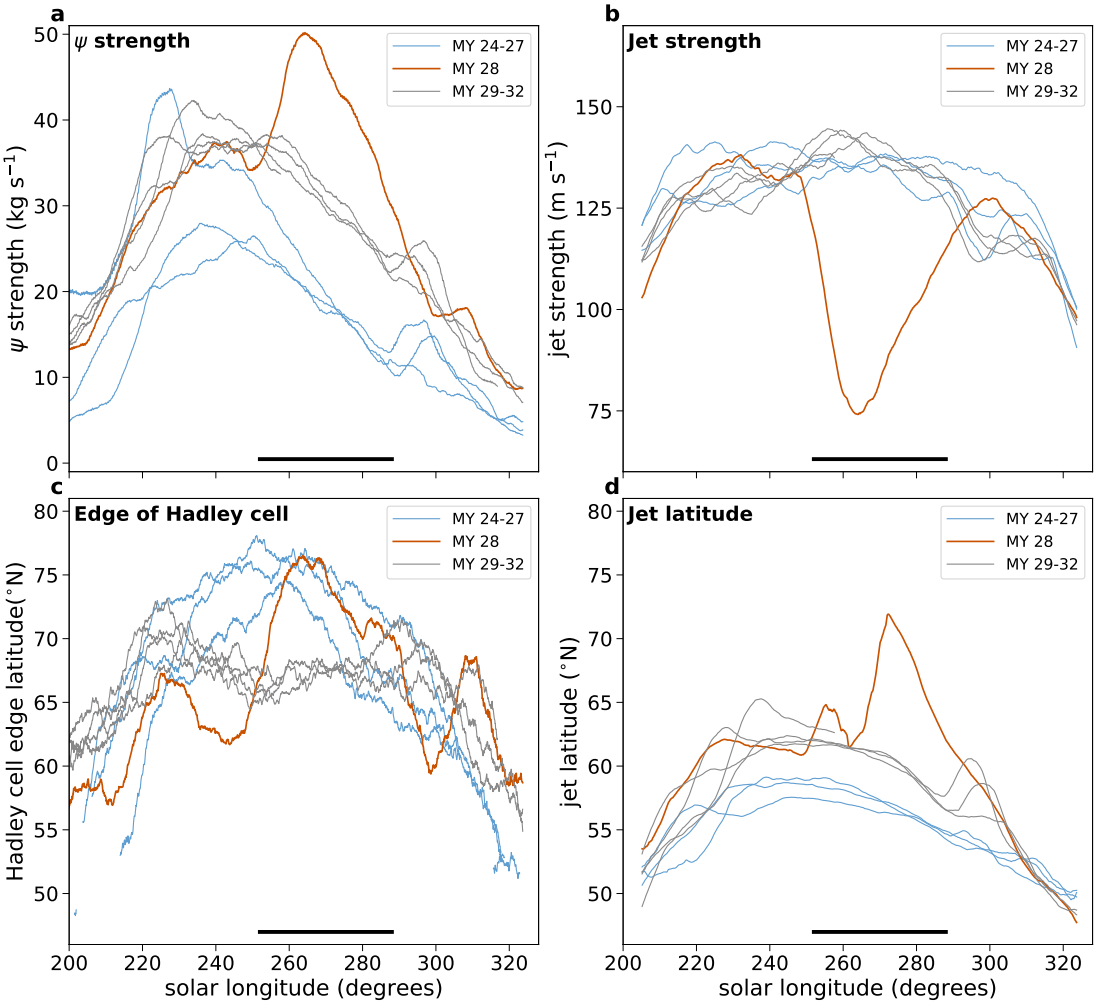

Figure 2.9: **Variability of the jet and Hadley circulation strength and their latitudes.** Smoothed evolution on the 50 Pa surface of (a) the strength of the overturning streamfunction and (b) jet strength. The corresponding latitudes of (c) the edge of the Hadley cell and (d) the jet core are shown. We define the jet latitude and strength, and the edge and strength of the Hadley cell in the main text. Data are from OpenMARS. Lines are coloured according to the era of data (TES, MY 28, and MCS). The solid black line indicates the MY 28 global dust storm period.

of the OpenMARS reanalysis in Figure 2.9c. We see that the maximum latitude reached by the Hadley cell edge differs according to the era. During the TES period, the edge of the Hadley cell reaches roughly 75° N, and this maximum occurs just following winter solstice ($L_s \sim 280°$). This is not the case for the MCS period. Instead, there is a local minimum in latitude over the late fall period, and a maximum of around 70° N is reached at $L_s \sim 240°$.

Jet strength is remarkably consistent on the pressure level shown across all years of OpenMARS (Figure 2.9b). The largest deviation during the reanalysis occurs during the MY 28 GDS, when jet strength is weakened by around 50 m s^{-1}. Figure 2.9d shows the latitude of maximum zonal-mean zonal wind at 50 Pa, the location of the jet core at that altitude. We see that during the MCS era, the jet latitude can be up to 5° poleward of the jet latitude in the TES era throughout fall and winter. Finally, by comparing panels c and d, note that the difference between jet latitude and the edge of the Hadley cell is larger in the TES era ($\sim 15-20°$) than in the MCS era ($\sim 5°$). Not shown here are the seasonality of the Hadley circulation and polar jet in our model simulations. We find that dust is the primary controlling factor for the strength of the jet and the Hadley circulation (strengthening both features). The effects of latent heat release and topography are of relatively minor importance, both acting to weaken the jet slightly.

Next, we consider the seasonal evolution of PV, looking at a polar cap average over 60° N - 90° N. Figure 2.10 shows that PV begins to accumulate near the north pole at $L_s \sim 150°$ in both reanalysis (Figure 2.10a) and model (Figure 2.10b). This occurs regardless of the presence of dust, latent heating, or topography (Figure 2.10c). PV in the reanalysis appears to evolve differently according to the data assimilated: in both eras, PV initially begins to increase at around $L_s 150°$, with our model simulations and the reanalysis in good agreement. In the TES era, there is a distinct peak in PV around the winter solstice ($L_s = 270°$) which is not present in the MCS era. In the MCS era, PV reaches it maximum at around $L_s \sim 200°$ and remains at roughly this strength until past $L_s \sim 300°$, when it begins to weaken. The exception to this winter maximum in PV is MY 28, which sees a

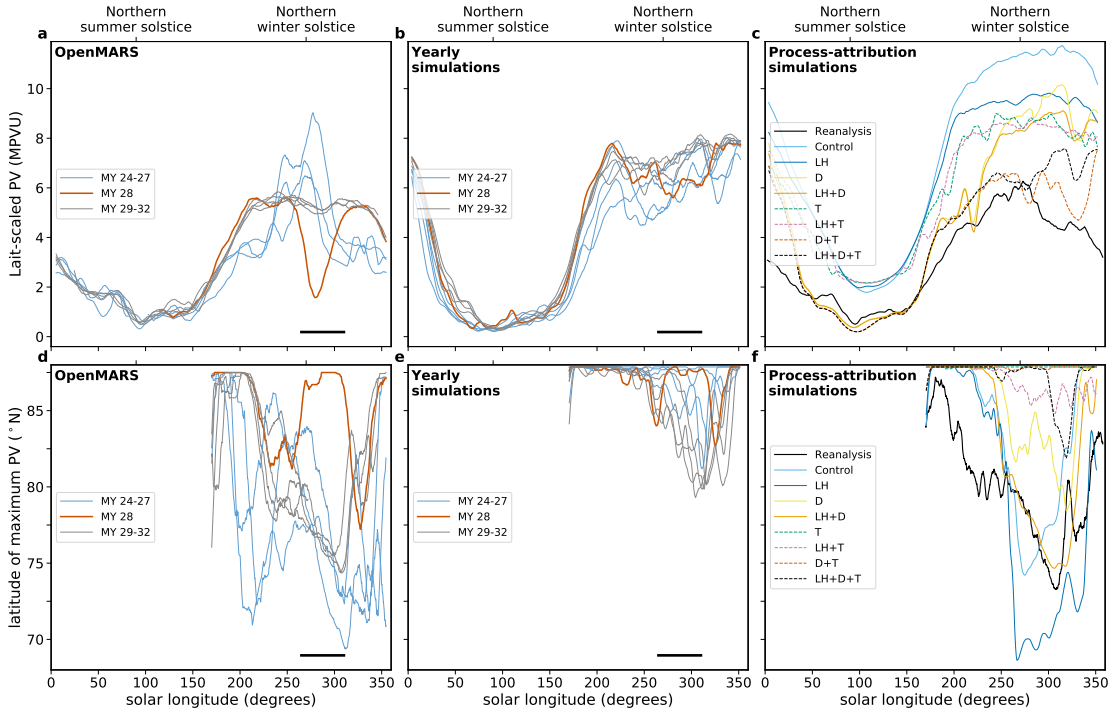

Figure 2.10: **Variability of the northern polar vortex strength and the latitude of maximum PV.** Smoothed evolution of mean PV between 60° N - 90° N on the 350 K isentropic surface for (a) OpenMARS, (b) 'yearly' simulations, and (c) process-attribution simulations. Panels (d-f) show the corresponding latitude of maximum PV on the 350 K surface. Each simulation is averaged over 3 MY. In panels (a,b,d,e), lines are coloured according to the era of observations (TES, MY 28, and MCS). The solid black line indicates the MY 28 global dust storm period. In panels (c) and (f) the black line (Reanalysis) shows the average of all OpenMARS years, excluding the GDS periods in MY 25 and MY 28.

local minimum in PV at around $L_s \sim 275°$. This corresponds to the weakened PV seen in Figure 2.2, caused by the GDS. Following the GDS, PV in the vortex recovers once dust loading has reduced. As previously identified, Isca weakly captures this impact in the 'yearly' simulations (Figure 2.10b).

The process-attribution simulations all show a minimum in PV during northern hemisphere summer (Figure 2.10c), as expected. This minimum is deepened by the presence of dust, to the point that it agrees well with the reanalysis. However, the winter peak in PV is stronger in the model than in the reanalysis and lasts until the end of the Martian year.

The winter peak in PV is reduced when dust is turned on, particularly during northern hemisphere fall ($L_s \sim 200°$) when the model agrees reasonably well with the reanalysis in all dusty process-attribution simulations. When turned on, both dust and topography always reduce the PV polar cap average throughout the dusty season. Latent heating primarily influences the seasonal evolution of PV between $L_s \sim 200 - 360°$, as expected since this is when the northern hemisphere polar cap is cold enough to allow this process to occur (Figure 2.1). The effect of latent heating, which is to weaken PV throughout winter, is predominantly seen in the 'Control' versus 'Latent Heating' simulations - when dust or topography are turned on, the influence is weaker, suggesting that these are the dominant processes in polar PV evolution.

We also consider the annular nature of the vortex by looking at how the latitude of maximum PV changes over the Martian year. As previously seen in Figure 2.3, the maximum in PV can be found well away from the pole in most years (Figure 2.10d), between $\sim 70 - 80°$ N over winter. There is more interannual variability in the annularity of the polar vortex in the TES era than in the MCS era of OpenMARS, particularly in fall. In the MCS era, typically the annulus begins to widen just following $L_s \sim 200°$, increasing in width until around $L_s \sim 300°$, where it begins to shrink back toward the pole. In MY 28, the typical widening of the annulus is disrupted, with the maximum in PV found at the pole during the GDS, although the annulus recovers toward the end of the dust storm. This destruction and recovery of the annulus is also captured in our 'yearly' simulations (Figure 2.10e), although we note that in general the northern polar vortex in our simulations is significantly less annular than the reanalysis. This is, in part, due to the exclusion of any CO_2 microphysics and dust as an active tracer in Isca, which means that dust particles cannot act as cloud condensation nuclei for CO_2. In spite of this, in our simulations we do see the larger spread in both PV and the location of it maxima that is visible in TES era OpenMARS.

Considering the influence of latent heating, dust and topography on the annularity

of the polar vortex (Figure 2.10f) suggests that topography and dust both act to push the maximum in PV further poleward. Indeed in 'Topography' and 'Dust (Topography)' simulations, the maximum is at the pole throughout the lifetime of the polar vortex, indicating an entirely monopolar vortex. The influence of turning on dust is particularly noticeable before $L_s \sim 300°$, with the greatest shift poleward occurring then. This pushes the peak in annularity past $L_s \sim 300°$ in all dusty simulations. As expected, latent heating increases the annularity of the vortex in all cases. The effects of dust and latent heating are of similar magnitude, but the effects of topography are dominant (noting for example that in the 'Latent Heating' and 'Latent Heating (Topography)' simulations, the PV maximum moves from 70° N to 85° N).

We now look at the internal variability of the northern polar vortex. Scott et al. [2020] investigated the transient nature of the Martian polar vortex by using an eddy-resolving shallow water model. They considered a quantity called integrated eddy enstrophy, given by

$$Z = \frac{1}{4\pi r^2} \int q'^2 dA, \tag{2.7}$$

where $q' = q_s - \bar{q_s}$ is the departure from the zonal-mean (scaled) potential vorticity and dA is an area integral. Integrated eddy enstrophy is a scalar measure of the flow's rotational energy, as it is a sum of zonal asymmetries in potential vorticity, and is useful in understanding the transience of the flow. An increase in eddy enstrophy indicates elevated eddy activity, and an increase in its variability reveals greater vortex variability. They found that a representation of stronger latent heating led to increased mean and variance of the eddy enstrophy, indicating that both mean eddy activity and the transience of the vortex increase as the vortex becomes more annular, and so more unstable. Here we also investigate eddy enstrophy in the northern polar vortex, in order to understand how vortex variability develops over the course of a Martian winter, and how it is influenced by topography, dust, and latent heat release.

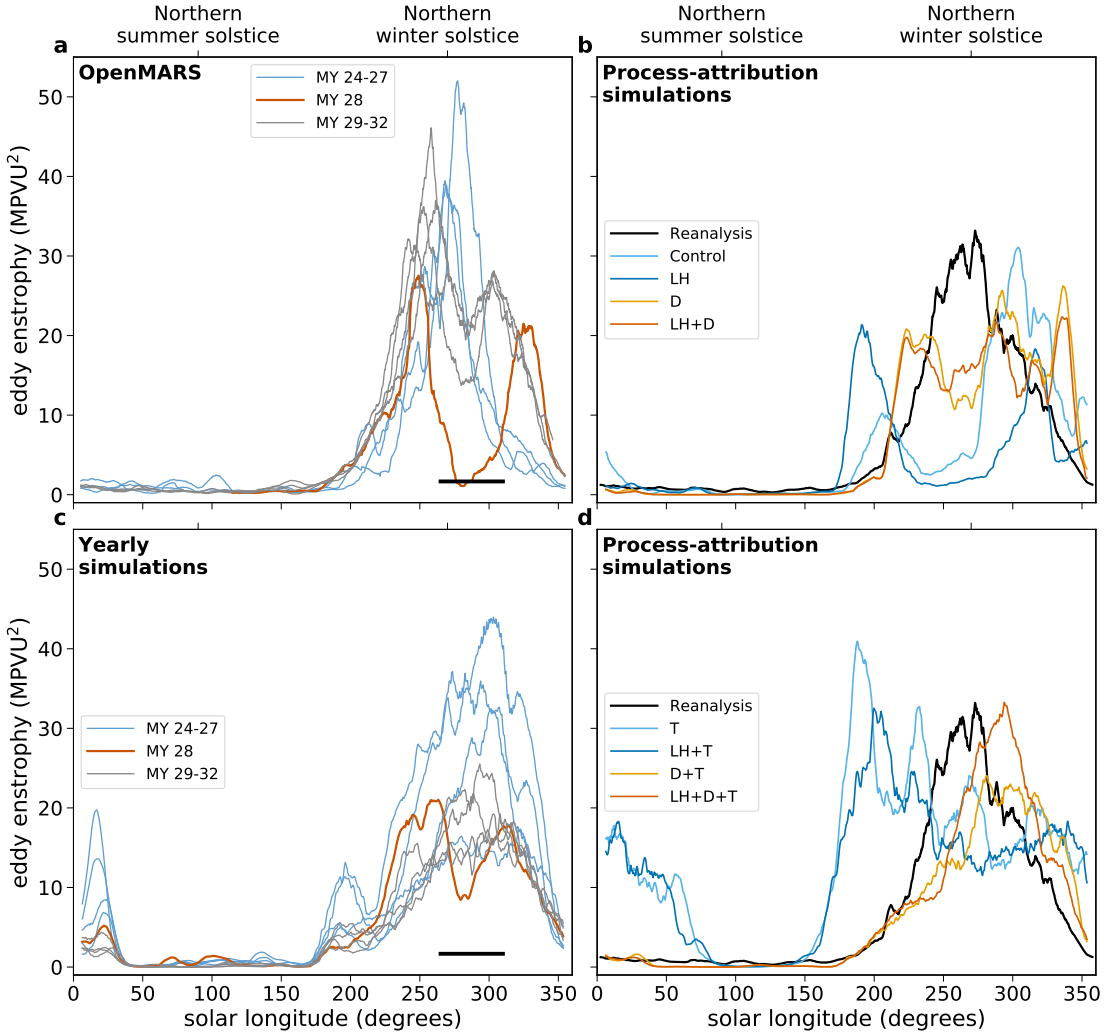

Figure 2.11: **Evolution of eddy enstrophy for OpenMARS and all simulations.** Smoothed evolution of eddy enstrophy on the 350 K isentropic surface for (a) OpenMARS, (c) 'yearly' simulations, and for process-attribution simulations (b) without topography and (d) with topography. Each simulation is averaged over 3 MY. In panels (a,c), lines are coloured according to the era of observations (TES, MY 28, and MCS). The solid black line indicates the MY 28 global dust storm period. In panels (b,d), the black line (Reanalysis) shows the average of all OpenMARS years, excluding the GDS periods in MY 25 and MY 28.

We see in Figure 2.11 that eddy enstrophy is heavily influenced by dust loading in the Martian atmosphere. In Figure 2.11a,c, note that MY 28 experiences a significant drop in eddy enstrophy around winter solstice, at the onset of the GDS. Indeed, in the reanalysis (Figure 2.11a), eddy enstrophy is almost zero, suggesting that eddy activity within the core of the vortex was minimal. The finding that the polar vortex in MY 28 was almost entirely destroyed from a PV point of view (Figure 2.10a) is corroborated by this drop in eddy enstrophy, which is necessarily reduced when PV is almost zero.

We also identify here for the first time the interesting double-peaked structure of eddy enstrophy in the later reanalysis years (Figure 2.11a, grey lines), which is not displayed in the earlier ones (blue lines). This pause in eddy enstrophy is reminiscent of the 'solsticial pause' in temperature eddies at low altitudes [Lewis et al., 2016; Mulholland et al., 2016]. Intriguingly, this feature is only observed in the OpenMARS reanalysis - there is only a drop in EMARS eddy enstrophy during MY 28 (see Supplementary Figure A.2b). This suggests that the pause in eddy enstrophy is likely a combination of the underlying UK-LMD MGCM used in OpenMARS and a systematic feature of the MCS retrievals, and that the high dust loading in MY 28 does indeed cause a significant drop in eddy enstrophy.

Figures 2.11b,d show the effect of topography, latent heating, and dust on eddy enstrophy in the northern polar vortex. The addition of topography to the model increases eddy enstrophy significantly in the fall ($L_s \sim 200-270°$). This coincides with the large-amplitude zonal wavenumber 1 waves identified in this season by Wilson et al. [2002], which were noted to have the characteristics of a Rossby wave. The increased variance in the eddy enstrophy on small time scales also indicates that the vortex is more transient when topography is included. In simulations with topography, the inclusion of dust appears to suppress eddy activity around $L_s \sim 0-75°$ and $L_s \sim 150-225°$ (Figure 2.11d). Without topography, this effect is less substantial and occurs over a shorter period of time, but is still present. Further analysis is necessary here to investigate the causes of these changes in eddy enstrophy between model configurations, along with the processes that are affected,

but this is beyond the scope of this paper.

Overall, we see that it is the combination of dust and topography that allows the model to best capture the shape of eddy enstrophy evolution seen in the reanalysis, although the peak in eddy enstrophy falls slightly later in the year in the model compared with the reanalysis. Hence these processes can be seen to be important in capturing realistic vortex variability. Perhaps surprisingly, adding latent heat release to the model does not seem to have a particularly large or consistent effect on the eddy enstrophy. Where latent heat release does cause a drop or increase in eddy enstrophy (e.g. Figure 2.11b, $L_s \sim 200°$), we find that this is where there is largest ensemble spread in our model simulations (not shown).

In general, our simulations show little ensemble spread. In response to the MY 28 dust storm, polar cap temperature rises, and there is a small increase in zonal wind and decrease in PV on the 350 K surface, in all 10 ensemble members. The ensemble spread is greatest in our process-attribution simulations without dust, particularly at times of high eddy activity, such as early fall (not shown). Given the larger ensemble spread at these times, it is difficult then to draw conclusions about the influence of latent heat release on mean eddy activity, which is perhaps surprising given the results of Scott et al. [2020]. However we do note consistency with Scott et al. [2020] at the winter peak in eddy enstrophy ($L_s \sim 300°$), which increases in magnitude with the inclusion of latent heating. When dust is included in the model, it appears to significantly impact the eddy enstrophy evolution, along with topography, far more so than latent heating, noting that 'Latent Heating' and 'Latent heating and Dust' simulations have broadly the same shape in both panels (b) and (d). This suggests that dust and topography are primarily the driving mechanisms behind eddy enstrophy evolution, and hence polar vortex zonal asymmetry and sub-seasonal variability.

Finally, to investigate further the drop in eddy enstrophy noted in MY 28, we also show a temperature proxy for the latent heat released, as in Figure 2.1. Figure 2.12a

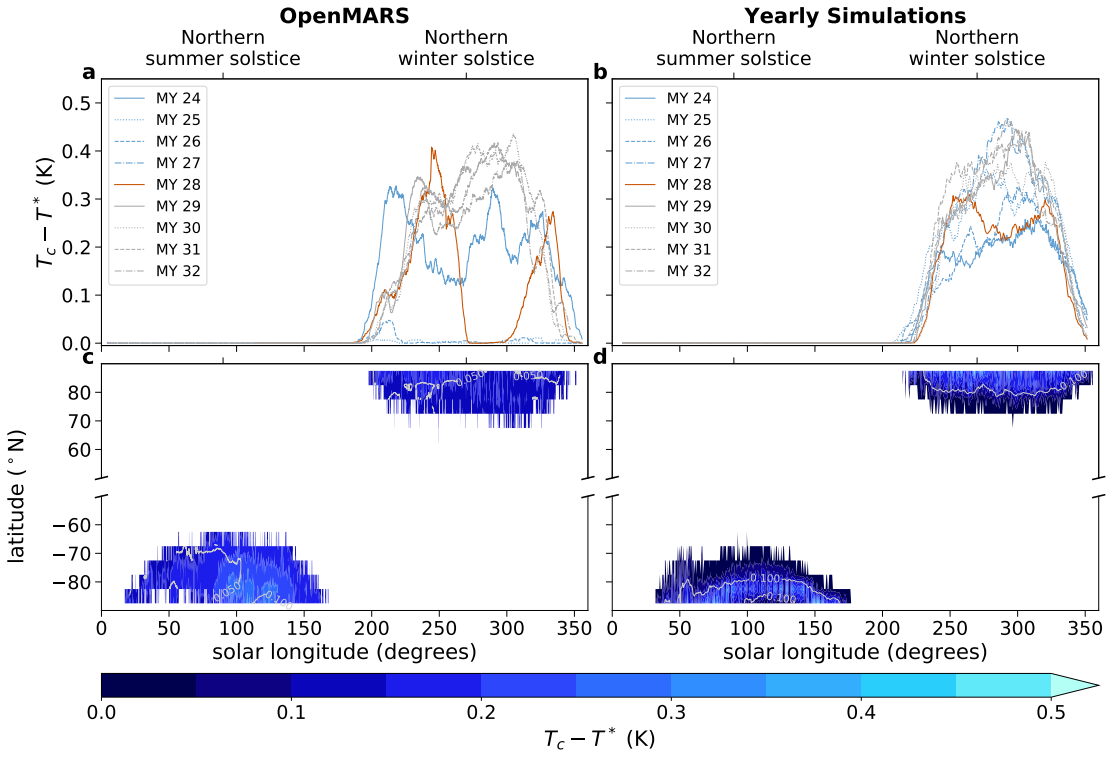

Figure 2.12: **Variability in latent heat release for OpenMARS and yearly model simulations.** Difference $T_c - T^*$ (K) for (a) each OpenMARS year and (b) individual 'yearly' simulations on the 2 hPa pressure level. T_c is given in Equation 2.3. For (a), T^* is taken to be the temperature in OpenMARS and for (b) T^* is the temperature predicted by the model before the temperature floor at T_c is applied. In (a) and (b) we calculate an area-weighted average over 60°-90°N to show a proxy for the amount of latent heat released. Panels (c) and (d) show the zonally-averaged climatology of the evolution of $T_c - T^*$ (K) on the 2 hPa pressure level (shading). The climatology is obtained by averaging over MY 24-32 for both (c) OpenMARS and (d) the 'yearly' simulations, and standard deviation (K) is also shown (contours).

shows that in MY 28, following the onset of the GDS, the amount of latent heat released is considerably lower than in all later years during the same time period. This suppression of latent heat release is due to vigorous downwelling at the pole causing higher temperatures within the polar vortex (see Figure 2.8). This is similarly reflected in the yearly model simulations, where MY 28 once again shows less latent heat release than later years.

We remark also on the apparent difference between the TES and MCS eras in Figure 2.12a. It is unclear to us what is causing the particularly small drop below T_c in MY 25-26, and why MY 24 looks different. As there is no evidence of a similar pattern in our simulations (in fact, we see that MY 24 has the least amount of latent heat released in the model TES period), we suggest that this could be caused by temperature retrievals strongly dominating the free-running MGCM in the reanalysis. Differences in the quality control procedures for the TES- and MCS-period dust opacity retrievals mean that only dust opacity retrievals where surface temperature was greater than 220 K were assimilated into OpenMARS during MY 24-27. On the other hand, both daytime and nighttime dust opacity retrievals from MCS were assimilated [Holmes et al., 2020], allowing the reanalysis to reach these colder temperatures in later years, although this does not explain the difference between MY 24 and MY 25-26. One potential reason for this difference could be the dust optical depths in the reanalysis. Dust loading during the polar winter in the TES era varies from year to year, due to the lack of retrievals in this region and the assimilation process [Figure 8 of Holmes et al., 2020]. In particular, MY 26 has particularly high dust loading at northern high latitudes, which warms the atmosphere there above the condensation point of CO_2.

2.5 Summary

Building on previous work by Guzewich et al. [2016] and Toigo et al. [2017], in this study we have explored the structure, interannual variability and sub-seasonal transience of the

northern Martian polar vortex, and how these are influenced by an interplay of topography, latent heat release and dust loading. In agreement with Toigo et al. [2017], we have shown that latent heat release plays a vital role in the annular potential vorticity structure of the polar vortex. We showed that the northern polar vortex is heavily affected by the atmospheric dust loading in the reanalysis. In particular, during the global dust storm of Martian year 28, there was a total destruction of polar potential vorticity and zonal winds were dramatically reduced. During this time, eddy activity within the vortex was also significantly reduced, the Hadley circulation was strengthened and its edge moved further poleward. We have confirmed the idea that the vertical potential vorticity structure of the northern polar vortex in the current reanalyses is well constrained by the observations assimilated into the model, as proposed by Waugh et al. [2016]. In the upper levels of the Martian atmosphere (above ~ 40km), differences correspond to whether there are observations available (during the MCS era) or not (during the TES era). During the TES era, it is likely that the polar vortex morphology is almost entirely driven by the free-running model at these higher altitudes due to the lack of observations there. Alongside differences in the mean-state of the northern polar vortex, our analysis has also shown significant differences in the sub-seasonal transience of the northern polar vortex according to which era of the reanalysis is investigated.

We found that seasonal evolution of potential vorticity occurs differently in the two periods - there is a winter solstice peak in potential vorticity during the TES era that is not seen in the MCS era. Similarly, eddy activity weakens around winter solstice in MCS-era OpenMARS, but not in TES-era. Finally, we find that the edge of the Hadley cell lies further north in the TES period than the MCS but that the jet core lies further north in the MCS period. The meridional overturning circulation is also stronger in the MCS period compared to the TES period.

From our process-attribution simulations, we found that the combination of dust and topography is responsible for the evolution of the zonal asymmetry of the vortex (as

measured by eddy enstrophy) throughout the Martian year, which peaks in the northern high latitudes in winter. Indeed, it is only with the inclusion of dust that we can properly capture the mean-state (in particular the temperatures and winds) and variability of the northern polar vortex in the model. The release of latent heat from carbon dioxide condensation plays a relatively minor role in capturing the magnitude of of eddy activity during northern winter. When there is no dust represented in our model, eddy activity varies significantly from the reanalysis, particularly during northern autumn. Further investigation is needed to understand the processes leading to these differences.

It is our hope that the Martian configuration of Isca developed for this work, which significantly extends that of Thomson and Vallis [2019b] by including representations of dust and latent heating, will be useful in future research regarding Martian atmospheric dynamics. While more idealised than some other Martian global climate models, it has the advantage of being highly flexible and allows users to easily isolate the effects of different parameters and physical processes on the atmospheric circulation. The model allows easy-to-configure representations of latent heat release, dust and topography, all of which may be adapted to best suit the user's research interests.

Future research may further investigate how different degrees of latent heating affect the annulus within our flexible global climate model by changing the threshold temperature at which carbon dioxide condenses, in a manner similar to Scott et al. [2020]. Within this study, we have used a zonally symmetric dust distribution in our simulations. Given that many regional dust storms on Mars can have significant dust loading but do not encircle all longitudes, further research might also address the effects of longitudinally asymmetric dust storms on the Martian polar vortices. We have also focused here on the northern hemisphere polar vortex, but there is plenty of scope to investigate processes affecting the southern hemisphere vortex. Guzewich et al. [2016] showed that the southern vortex was less strongly affected by winter-time dust loading than the northern, but given the topographical and dust loading hemispheric asymmetries on Mars, such processes may

play different roles in the southern polar vortex.

CHAPTER 3

THE IMPORTANCE OF ISENTROPIC MIXING IN THE FORMATION OF THE MARTIAN POLAR LAYERED DEPOSITS

Having understood key driving mechanisms of the northern polar vortex in Mars's present day atmosphere, the existence of layered deposits at the poles of Mars leads to the question: do the planet's polar vortices influence this layering via changes in their morphology and how have they evolved throughout the Mars's history? How might the inherent hemispheric asymmetries in the atmospheric circulation affect the mixing seen in each hemisphere?

This chapter aims to extend the previous by considering the dynamics of the Martian polar vortices across a range of past orbital configurations and atmospheric dust abundances. The model developed in Chapter 2 is employed to perform a parameter sweep over an illustrative range of obliquities and dust abundances. Eccentricity also takes either its current value or is set to zero to remove the influence of the timing of perihelion. A passive tracer is initialised in all model simulations, and the diagnostic 'effective diffusivity' is calculated to explore mixing changes.

The content of this chapter has been submitted as an article titled '*The importance of isentropic mixing in the formation of the Martian polar layered deposits*' in the The Plane-

tary Science Journal. The material here is essentially identical to that in the submitted manuscript, except that the figures and tables have been renumbered and re-captioned to be consistent with other thesis chapters. The supplementary materials have been placed in Appendix B of this thesis.

Author contributions: the authors of this manuscript variously contributed to the work, with E.R.B. designing the experiment, performing the simulations, analysing the results, and writing the draft of the manuscript. W.J.M.S. and D.M.M. contributed to the design of the investigation and provided guidance throughout. All authors contributed to the proofreading and editing of the manuscript.

3.1 abstract

Layers of ice and dust at the poles of Mars reflect variations in orbital parameters and atmospheric processes throughout the planet's history, and may provide a key to understanding Mars's climate record. Previous research has investigated transport changes into the polar regions and found a nonlinear response to obliquity that suggests Mars may currently be experiencing a maximum in transport across the winter poles. The thickness and composition of layers within the polar layered deposits is likely influenced by changes in horizontal atmospheric mixing at the poles, which is an important component of the transport of aerosols and chemical tracers. No study has yet investigated horizontal mixing alone, which may be influenced by polar vortex morphology. We show that mixing in an idealised Martian Global Climate Model varies significantly with obliquity and dust abundance by using a diagnostic called effective diffusivity which has been used to study the stratospheric polar vortices on Earth and understand their role as a mixing barrier, but has not been applied to Mars's polar vortices. We find that mixing in the winter southern hemisphere doubles with either an octupling of dust loading, or with an increase in obliquity from 10° to 50°. We find a weaker response to changing dust loading or obliquity in the

northern hemisphere. We demonstrate that horizontal mixing is an important component of transport into Mars's polar regions, may contribute to the formation of the PLD, and presents effective diffusivity as a useful method to understand mixing in the Martian atmosphere.

3.2 Introduction

3.2.1 Polar layered deposits

The polar layered deposits (PLD) are layered ice deposits at the poles of Mars that may provide a key to understanding the Martian climate record. Understanding their formation remains an open and important question in the study of Mars's atmosphere and its evolution [Smith et al., 2020] and is currently listed as one of NASA's higher priority goals for the scientific exploration of Mars [MEPAG, 2020]. The PLD were first observed by Mariner 9 during southern early spring [Murray et al., 1972] and may represent variations in orbital parameters [Laskar et al., 2002], as well as indicate changes in transport into the polar regions throughout Mars's history.

Mars has undergone much larger changes in its orbital parameters (including obliquity and eccentricity) than Earth has, with initial predicted variations in obliquity of $15-35^\circ$ [Ward, 1973], although more recent statistical calculations suggest variations in obliquity of $5-60^\circ$ and in eccentricity of 0-0.12 over the last 10Ma [Laskar et al., 2004; Laskar et al., 2002]. Previous studies have linked changing orbital parameters with the layering observed in Mars's polar regions [e.g. Hvidberg et al., 2012; Perron and Huybers, 2009], but attributing these changes to different processes on Mars still needs to be examined. In particular, no studies have considered the isentropic transport of dust and other atmospheric tracers in Mars's atmosphere, which is typically associated with eddy activity. This dynamical 'mixing' from chaotic advection stretches and deforms material contours of tracers, along which sub-grid scale molecular diffusion occurs. In this study,

we aim to explore what role atmospheric mixing may have played throughout Mars's history, its dependence on orbital forcing and global dust abundance, and how it may have contributed to the layering we observe at the poles of Mars.

The bulk composition of the northern polar layered deposit (NPLD) is $\sim 95\%$ water ice [Grima et al., 2009], but individual layers are thought to contain varying amounts of dust and CO_2 ice (see Figure 3.1). The southern polar layered deposit (SPLD) is also thought to be primarily composed of water ice [with $0-10\%$ dust, Plaut et al., 2007], although these layers sit upon a partially buried $\approx$ 1km bed of CO_2 ice [Smith et al., 2020, and references therein]. There are significant complexities in understanding the composition of individual layers of the PLD, as the reflected intensity of individual layers depends on local slope, surface roughness, and layer dust and water/ice proportions, as well as illumination due to the season of observation [Laskar et al., 2002; Perron and Huybers, 2009]. It is also unclear the extent to which layering in the PLD is due to enhanced sublimation of water ice during some periods (leaving behind layers of higher dust concentration) or due to increased water ice deposition relative to dust deposition, although recent studies hypothesise that it is likely a combination of the two effects [Courville et al., 2021].

3.2.2 Atmospheric circulation

The winter atmosphere of Mars is characterised by a strong polar jet and annular potential vorticity (PV) structure, i.e., with a minimum in PV over the pole and a region of higher PV surrounding it. The annular PV structure contrasts with the morphology of Earth's stratospheric polar vortices, which are monopolar. PV is often used in the study of polar vortices, and has been investigated on Earth, Mars, and other planetary bodies [e.g. Mitchell et al., 2014; Sharkey et al., 2021; Waugh et al., 2016]. Mars's annular PV structure is thought to be influenced by the release of latent heat during CO_2 condensation [e.g. Ball et al., 2021; Seviour et al., 2017; Toigo et al., 2017], along with Hadley cell downwelling [Scott et al., 2020]. The atmosphere of Mars experiences particularly large interannual

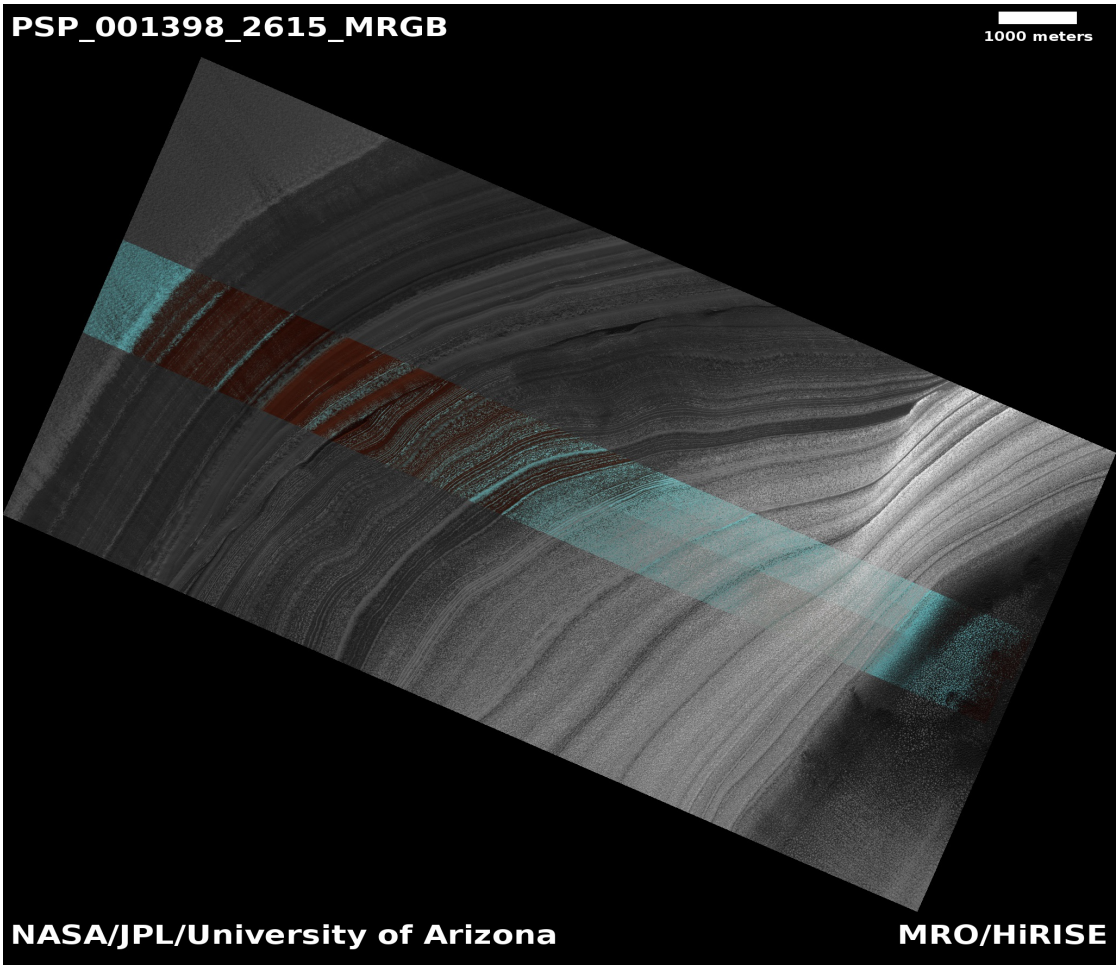

Figure 3.1: **Satellite observation of the north polar layered deposits.** HiRISE image PSP_001398_2615 of layers in the north polar layered deposits. This image is centred at 81.515°N, 47.300°E. Credit: NASA/JPL-Caltech/Univ. of Arizona

variability, due primarily to the variability in the occurrence and size of dust storms; during particularly dusty years, the Hadley circulation may expand poleward and the PV structure may collapse to a monopole [e.g. Ball et al., 2021; Streeter et al., 2021]. Previous studies have suggested that the annular polar vortex may act as a partial barrier to transport across the polar regions [Toigo et al., 2020; Waugh et al., 2019]. Furthermore, modelling studies suggest that the amount of CO_2 condensing may have varied significantly with obliquity or peak dust loading, possibly with significant implications for dust and ice sedimentation over the poles [Toigo and Waugh, 2022].

Previous studies have simulated the atmosphere of Mars at various obliquities and/or eccentricities [e.g. Haberle et al., 2003; Newman et al., 2005; Toigo et al., 2020]. Haberle et al. [2003] showed that obliquity has the stronger influence of the two parameters on the climate system due to its larger effect on the latitudinal variation of solar insolation. Similarly, Mischna [2003] showed that the location and stability of surface ice is most closely linked to obliquity in Mars Global Climate Model (MGCM) simulations varying obliquity, eccentricity, and longitude of perihelion. Newman et al. [2005] showed that at low obliquity, there are permanent CO_2 ice caps at both poles, lowering global mean surface pressure. At high obliquities, they found that there was a stronger and broader meridional circulation and a larger seasonal CO_2 ice cap, and that this stronger circulation increased dust lifting by wind stress, providing a positive dynamical feedback. However, no studies have yet considered the impact of a finite surface dust supply in varying-obliquity simulations, which may limit the positive feedback effect as was shown to be the case in simulations of the present-day Martian atmosphere [Newman and Richardson, 2015].

Several modelling studies have investigated timescales for transport in the Martian atmosphere, including Barnes et al. [1996], who looked at 'ventilation timescales' and found that there was faster ventilation of the atmosphere above 1hPa (i.e. more vigorous transport) during the dusty solstice season compared to equinox. An idealised 'age-of-air' tracer initialised in an MGCM was found to be oldest in the polar lower atmosphere, and

a transport barrier intrinsically linked to polar vortex morphology was identified, with the presence of smaller-scale vortices (or 'patches' of PV) being linked to a decrease in 'age-of-air' within the annulus of PV [Waugh et al., 2019]. Toigo et al. [2020] used this same tracer in a parameter sweep over obliquity to identify a turning point in transport into the polar regions, with the most efficient transport occurring at approximately Mars's current obliquity across the simulations performed.

Other work has studied the impact of dust loading on the Martian atmospheric circulation. Elevated dust loading can influence features of the northern polar vortex by, for example, initiating a 'transient polar warming' (in which polar temperatures may rise $2-10$K during a typical year or more during a GDS year) at high altitudes over the pole, and by strengthening the polar jet and steepening the poleward tilt of the jet core at low altitudes [Guzewich et al., 2016]. This warming occurs via a strengthening of the overturning circulation with higher dust loading during the dusty northern winter, which warms the polar upper atmosphere through stronger adiabatic heating from the descending branch of the Hadley circulation. Toigo et al. [2020] also suggested that larger polar warmings (in which temperatures can rise up to 70K between $1-0.1$Pa) occur each simulated winter for obliquities above 35° under typical dust conditions, while they are reliant on the presence of higher dust loading at present-day obliquity. An 'opposite season' dust event (with peak dust loading prescribed during the southern winter, rather than during northern winter when it is always observed) was shown to lead to a more vigorous overturning circulation compared to standard dust loading at that time [Guzewich et al., 2016]. Hemispheric differences in the response to obliquity have also been noted; Toigo et al. [2020] found that 'age-of-air' is consistently older at the north pole in all simulations regardless of the timing of peak dust loading, and proposed that dust deposition would vary on half the period of a full obliquity cycle between $5-55^\circ$ (due to an increase in transport up to obliquity $\varepsilon = 25^\circ$, and a decrease above this).

In this paper we examine the influence of polar vortex morphology on transport into the

Martian polar regions under different orbital forcings or global dust abundances. We vary obliquity, eccentricity, and dust scaling, and use a diagnostic called 'effective diffusivity' to understand horizontal mixing in the polar regions in an idealised MGCM. Effective diffusivity is a geometric description of the stirring in a flow, and has been well-used to study mixing in Earth's stratospheric polar vortices [e.g. Abalos et al., 2016; Haynes and Shuckburgh, 2000a,b] as well as across hurricane eyewalls, which have an annular vorticity structure similar to Mars's current polar vortices [Hendricks and Schubert, 2009; Mitchell et al., 2021]. Hendricks and Schubert [2009] find two regions of high effective diffusivity (indicating strong mixing) in simulations of unstable rings of vorticity - an inner mixing region within the annulus, and an outer mixing region outside of the annulus. The annulus of vorticity itself has low effective diffusivity, separates the inner and outer regions and acts as a partial barrier region. Alongside this modelling of rings of high vorticity, Hendricks and Schubert [2009] also studied effective diffusivity in a storm with monotonically increasing vorticity. For these monopolar vortices, similarly to Earth's stratospheric polar vortices, Hendricks and Schubert [2009] found that the centre of the storm acted as a partial barrier and air was not easily mixed.

The use of effective diffusivity allows us to isolate the changes in isentropic mixing (or mixing that occurs on isentropes, surfaces of constant potential temperature) from changes in large-scale transport via the Hadley circulation. This distinction is an important one as isentropic mixing primarily refers to mixing due to eddies, and acts to flatten tracer distributions on these surfaces, yet the diabatic mixing that occurs across isentropes tends to have the opposite effect [Andrews et al., 1987; Haynes and Shuckburgh, 2000a]. Furthermore, given the generally decreasing concentrations of dust with altitude, the deposition of dust via mixing has the potential to be larger than that via Hadley circulation, which may in general transport material into the polar regions at higher altitudes. As yet, no studies have used the effective diffusivity diagnostic to understand mixing in the Martian atmosphere. Here, we attempt to understand whether the annular polar vortex

on Mars behaves in a similar way, acting as a mixing barrier between the polar regions and midlatitudes. We also consider how effective diffusivity (and hence mixing) changes under different orbital parameters or dust abundances, and thus how it may contribute to the layering observed in the polar regions.

3.3 Methods

3.3.1 Isca

We use the flexible modelling framework Isca [Vallis et al., 2018] to model the atmosphere of Mars. Specifically, the MGCM component of Isca (henceforth Isca-Mars) has been developed to simulate the circulation of the Martian atmosphere at varying levels of complexity [Thomson and Vallis, 2019b]; further processes have since been added to more accurately represent the modern Martian atmosphere [Ball et al., 2021]. The processes and data that are currently available in Isca-Mars are the SOCRATES radiation scheme [Manners et al., 2017], a prescribed dust profile, and latent heat release representation associated with CO_2 condensation, as well as topography from the Mars Orbiter Laser Altimeter [Smith et al., 1999]. While a full model description is given in Ball et al. [2021], we include here a brief description of the dust profile in use. Initially, zonally-averaged infrared absorption CDOD from the Mars Climate Database (MCD) 'standard dust scenario' [Montabone et al., 2015] normalised to the reference pressure of 610 Pa product is inputted and converted to a surface mass mixing ratio by the SOCRATES interface within the model. This then informs the surface mass mixing ratio parameter a_0 within modified Conrath-ν profile as described in Ball et al. [2021]; Montmessin et al. [2004], from which we obtain a vertical and latitudinal profile. The MCD scenario is built by averaging climatologies of MY 24-31 CDOD (excluding the GDS events of MY 25 and MY 28), thus giving a dust profile with 'typical' dust loading [Ball et al., 2021; Montabone et al., 2015]. Figure 1 of Ball et al. [2021] shows the temporal evolution of the latitudinal and vertical profiles

of dust used within Isca-Mars. The latent heat release representation within Isca-Mars is a simple temperature floor scheme, wherein model temperatures are prohibited from falling below the pressure-dependent frost point of CO_2, and is detailed in Ball et al. [2021]. The atmospheric mass lost during this phase change is not considered within the model, although it has been previously shown that the dynamical effect of the associated pressure changes has less impact on the structure of the northern Martian polar vortex than the latent heat release associated with the CO_2 condensation [Waugh et al., 2019].

The advantage of using Isca herein is its flexibility: although it is an idealised model and several processes are not represented (for example radiatively active ice clouds, an active dust scheme, or CO_2 ice microphysics), we are able to modify basic planetary parameters with ease and so isolate some of the most important processes of interest. Despite the idealised nature of Isca-Mars, the inclusion of dust within the SOCRATES radiation scheme gives reasonable agreement with reanalyses [for example the OpenMARS dataset described in Holmes et al., 2020] of the Martian atmosphere [see Figure 4 in Ball et al., 2021, which compares temperatures and winds of different Isca configurations with the OpenMARS reanalysis dataset].

3.3.2 Simulations

To investigate the transport and mixing in the polar regions, we run a suite of simulations in Isca, varying orbital parameters and dust scaling. The basic simulation is the full version of Isca-Mars [Ball et al., 2021, with all features 'switched on'] and from there obliquity, eccentricity and dust scaling are varied. Key fixed and varying model parameters for each experiment are described in Table 3.1. Obliquity (ε) is varied between $\varepsilon = 10 - 50^\circ$ at intervals of 5°, representative of obliquity variations over the last 5Ma and beyond [Laskar et al., 2004], and eccentricity (γ) takes the value of either $\gamma = 0.093$ (current) or $\gamma = 0$ (to isolate the effect of varying only obliquity and to remove any influence from the timing of perihelion in our results).

The current obliquity of Mars is $\varepsilon = 25.19°$ and its eccentricity is $\gamma = 0.093$, a significantly more eccentric orbit than that of Earth. Perihelion on modern Mars occurs at the areocentric solar longitude (L_s) of $\sim 251°$ [Haberle et al., 2003], not long before northern hemisphere winter solstice ($L_s = 270°$)[1]. Newman et al. [2005] found that atmospheric circulation is strongest when the longitude of perihelion aligns with the northern hemisphere winter solstice (due to hemispheric topographic differences), suggesting that modern Mars may be experiencing particularly strong atmospheric circulation. We find that our simulations at $\varepsilon = 25°$ and $\gamma = 0.093$ give quantitatively similar results as those at $\varepsilon = 25.19°$ and $\gamma = 0.093$ (not shown), and so we take this to be our present-day reference simulation.

We perform $\gamma = 0$ simulations to isolate the effect of changing obliquity, and when $\gamma = 0.093$, perihelion occurs at its modern-day timing of $L_s \approx 251°$. We do not perform a parameter sweep over further values of eccentricity as it would necessitate consideration of precession of perihelion. Furthermore, it has been shown that obliquity has the larger influence on atmospheric circulation so our focus will be on this [Haberle et al., 2003; Mischna, 2003]. Finally, we also vary the dust mass mixing ratio by scaling the constant reference mass mixing ratio a_0 at pressure p_0 by $\lambda = 1/2, 1, 2, 4, 8$ [Equation 5 in Ball et al., 2021]. This range of dust scalings includes a peak dust loading during the dusty season (in the $\lambda = 8$ simulation) that is approximately equivalent to $2\times$ the loading of the MY28 GDS, which was found to be sufficient to cause a breakdown of the vortex in Isca-Mars in Ball et al. [2021]. We note that by using a present-day dust seasonality (via our choice of both MCD scenario and Conrath-ν profile), we impose a dusty season during northern winter for all simulations, with much lower dust loading over the southern winter period. All simulations are performed at T42 spectral resolution, corresponding to a 64 $\times$ 128 ($\sim 2.8° \times 2.8°$) spatial grid, with 25 unevenly-spaced vertical sigma levels reaching approximately 0.05 Pa ($\sim$ 90km), with enhanced resolution near the surface and the model top.

[1] Southern hemisphere winter solstice occurs at $L_s = 90°$.

Simulation Name	Dust Scaling	Obliquity	Eccentricity	Winter peak CDOD (NH/SH)
Zero eccentricity	$\lambda = 1$	$\varepsilon = 10, 15, \ldots, 50$	$\gamma = 0$	0.36/0.15
Current eccentricity	$\lambda = 1$	$\varepsilon = 10, 15, \ldots, 50$	$\gamma = 0.093$	0.36/0.15
Dust scale	$\lambda = 1/2$	$\varepsilon = 25$	$\gamma = 0.093$	0.18/0.074
	$\lambda = 1$	$\varepsilon = 25$	$\gamma = 0.093$	0.36/0.15
	$\lambda = 2$	$\varepsilon = 25$	$\gamma = 0.093$	0.72/0.29
	$\lambda = 4$	$\varepsilon = 25$	$\gamma = 0.093$	1.44/0.59
	$\lambda = 8$	$\varepsilon = 25$	$\gamma = 0.093$	2.88/1.18

Table 3.1: **Table of simulations in Chapter 3.** Dust scalings are relative to the standard scaling used in Ball et al. [2021], and $\lambda = 1$ represents a modern-day climatological year. For reference, the peak CDOD during the MY28 GDS was 1.3.

3.3.3 Effective diffusivity

Alongside analysis of model output fields such as zonal winds and temperatures, we calculate Ertel's potential vorticity (PV) to understand the morphology of the polar vortices[2]. Despite PV being considered a tracer over short timescales on Earth [e.g. Waugh, 2023], one cannot say the same in the atmosphere of Mars due to the destruction of PV over the poles by the release of latent heat by CO_2 condensation. This process warms the polar air and reduces vertical potential temperature gradients, thereby reducing polar PV: PV is no longer conserved due to this diabatic heating, and so should not be considered as a tracer over the winter poles of Mars. To avoid this complication, we initialise a passive mass-less tracer c that is advected by the flow. The tracer is initialised with a sinusoidal profile and is allowed to freely evolve for 30 sols before being re-initialised with the same profile. Initial tracer distribution is given by

$$c(\phi) = 1 + \sin(\phi), \tag{3.1}$$

so that $c(-90) = 0$ and $c(90) = 2$.

Using the passive tracer, we turn to a quantity called effective diffusivity (κ_{eff}) to investigate isentropic mixing. This is a geometric method of measuring the mixing occurring in a flow which looks at the lengths of contours of a conserved tracer.

Following Nakamura [1996, 2008], for a monotonic tracer field c^*, one can transform the tracer field into a contour-based coordinate. Suppose that we have a contour of constant tracer $c^* = c$. The area $A(c,t)$ occupied by the tracer $c^* \geq c$ is such that

$$A(c,t) = \int_{c^* \geq c} \mathrm{dS}, \tag{3.2}$$

and evolves according to

$$\frac{\partial}{\partial t} A(c,t) = -\frac{\partial}{\partial c} \int_{c^* \geq c} \kappa \nabla^2 c^* \, \mathrm{dS}, \tag{3.3}$$

[2]See Ball et al. [2021] for the exact form of PV chosen here. We adopt the convention of Martian Potential Vorticity Units (MPVU), analogous to Potential Vorticity Units (PVU) used to study PV in Earth's atmosphere, where 1 MPVU = 100 PVU = 10^{-4} K m^2 kg^{-1} s^{-1}.

where κ is the molecular diffusion coefficient. Given the monotonicity of the tracer, it is possible to invert the function $A(c,t)$ to $c(A,t)$. With some intermediate steps (following Nakamura [2008]), we arrive at a relationship for the evolution of the contour c

$$\frac{\partial}{\partial t}c(A,t) = \frac{\partial}{\partial A}\left(\langle D|\nabla c^*|^2\rangle_c \frac{\partial A}{\partial c}\right) = \frac{\partial}{\partial A}\left(DL_{\mathrm{e}}^2\frac{\partial c}{\partial A}\right). \tag{3.4}$$

Here, the subscripted angular bracket $\langle\cdot\rangle_c$ is the average of a field variable (denoted here by $\cdot$) on the tracer contour $c^* = c$, such that

$$\langle\cdot\rangle_c = \frac{\partial}{\partial A}\int_{c^*\geq c}(\cdot)\,\mathrm{dS}. \tag{3.5}$$

It then remains to define L_{e}, the equivalent length of the contour, according to the right-hand-side (RHS) of Equation 3.4,

$$L_{\mathrm{e}}^2(A,t) = \langle\left|\nabla c^*\right|^2\rangle_c \Big/ (\partial c/\partial A)^2. \tag{3.6}$$

On a sphere, one can then consider the area A as a function of equivalent latitude ϕ_e, which is defined by $A = 2\pi r^2(1-\sin\phi_e)$. Examples of such contours of constant c^* are shown in Figure 3.2. In the case that $|\nabla c^*|^2$ is constant on the contour, note that L_{e} reduces to the actual perimeter length of the contour. Effective diffusivity, κ^*_{eff}, is defined by

$$\kappa^*_{\mathrm{eff}}(\phi_e,t) = \kappa\frac{L_{\mathrm{e}}^2}{L_{\mathrm{min}}^2} = \kappa\frac{L_{\mathrm{e}}(\phi_e,t)^2}{(2\pi r\cos\phi_e)^2}, \tag{3.7}$$

where L_{min} the minimum possible length of a contour enclosing A, is given in Haynes and Shuckburgh [2000a]; Nakamura [1996, 2008]. On a sphere of radius r, $L_{\mathrm{min}} = 2\pi r\cos\phi_e$. The key idea of this calculation is to transform the advection-diffusion equation for the evolution of a tracer into a diffusion-only equation.

Mixing is due to combined effect of differential advection and turbulent diffusion - advection stretches and deforms material lines while diffusion accomplishes true irreversible mixing. Effective diffusivity combines irreversible diffusion effects with reversible advection effects, via the equivalent length (which quantifies both the deformation of material lines by advection, and the interface over which diffusion can act) [Hendricks and

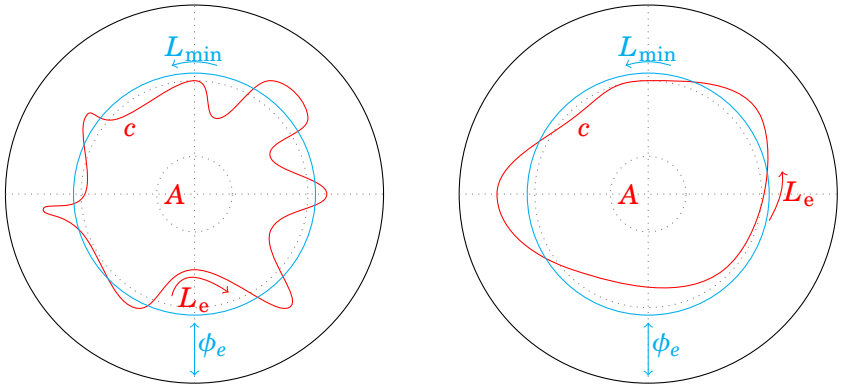

Figure 3.2: **An illustration of the effective diffusivity calculation.** Constant contours of tracer $c^* = c$ on a sphere of radius r. Left: an example of tracer geometry with large effective diffusivity. Right: an example with small effective diffusivity. In each, the red contour represents a contour of tracer $c^* = c$ enclosing the same area A. The blue contour is the shortest possible contour enclosing A, sits at latitude ϕ_e, and has length $L_{\min} = 2\pi r \cos\phi_e$. In the left panel, $L_e \gg L_{\min}$, whereas in the right, $L_e \approx L_{\min}$.

Schubert, 2009]. Equivalent length absorbs the effects of advection since the tracer contour is used as the coordinate (the RHS of Equation 3.4 demonstrates that c only evolves with contour length via L_e). If tracer contours are well-stirred (i.e. contours are well-stretched and deformed by advection), one sees $L_e \gg L_{\min}$, and hence effective diffusivity will be large [Qian et al., 2019], as there is more interface for diffusion to act over. Within this paper, we henceforth consider the normalised effective diffusivity, $\kappa_{\text{eff}} = \log_e(\kappa^*_{\text{eff}}/\kappa)$, with the logarithm taken to more clearly illustrate large variations in effective diffusivity.

An example tracer contour is given in Figure 3.2 to illustrate the geometry of a flow with high effective diffusivity (left; noting the large contour length over which diffusion may occur) and low effective diffusivity (right). In all figures in which κ_{eff} is shown, we ensure that the tracer has been allowed to evolve for at least 20 sols after initialisation to minimise any influence of initial tracer distribution.

Alongside effective diffusivity, the following metrics are used to diagnose the circulation: the strength of the polar jet at 50Pa ($u_{\max}$) and its latitude ($\phi_{u_{\max}}$), the strength of the overturning circulation ψ (ψ_{max}) and the latitude of its descending branch (ϕ_{HC}), the

Metrics	Description
$u_{\max}$ (m s^{-1})	Hemispheric maximum zonal-mean zonal wind speed at 50 Pa
ψ_{max} (kg s^{-1})	Hemispheric maximum absolute value of the vertically-integrated overturning streamfunction
PV_{max} (MPVU)	Hemispheric maximum zonal-mean PV at 300 K
$\phi_{u_{\max}}$ (°N/S)	Latitude of the jet at 50 Pa; latitude of $u_{\max}$
ϕ_{HC} (°N/S)	Latitude of the descending branch of the Hadley circulation; latitude of the 10% crossing poleward of ψ_{max}
ϕ_{PV} (°N/S)	Latitude of the annulus of PV; latitude of PV_{max}
$\kappa_{\mathrm{eff}_{300}}$	Area-weighted latitudinal average κ_{eff} poleward of 40°N/S at 300 K
c_{pole_t}	Area-weighted polar cap average (75° − 90°N/S) of tracer concentration at 300 K, t sols after initialisation

Table 3.2: **Table of metrics calculated in Chapter 3.**

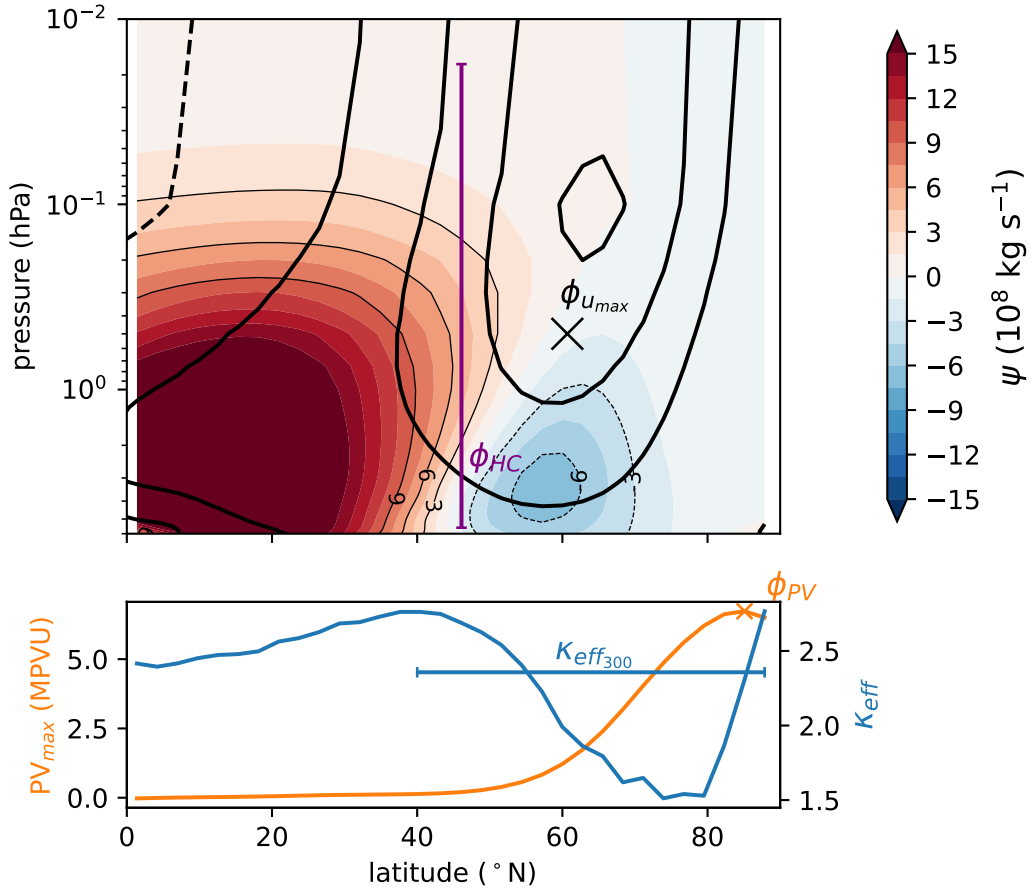

Figure 3.3: **A schematic of diagnostics in Chapter 3.** (top) Northern winter mean meridional streamfunction (shading; 10^8 kg s^{-1}), zonal-mean zonal wind (thick contours; m s^{-1}), and (bottom) zonal-mean potential vorticity (orange; MPVU) and effective diffusivity (blue) on the 300K level. The latitudes of our metrics (ϕ_{HC}, $\phi_{u_{max}}$, ϕ_{PV}, $\kappa_{\text{eff}_{300}}$) are indicated by either crosses, or, if the calculation is based on an integral or mean, by bars across the region in question. The data used is the present-day simulation ($\gamma = 0.093$, $\varepsilon = 25°$).

strength of the polar vortex at 300K (PV_{max}) and the latitude of the maximum in PV (ϕ_{PV}; this determines the width of the annulus). We show the area-weighted latitudinal average of κ_{eff} poleward of 40°N/S ($\kappa_{\text{eff}_{300}}$) to illustrate changes in the strength of mixing in the midlatitudes and polar regions. This more equatorward latitude limit ensures that we capture the existence of the mixing barrier (should one exist), which may extend significantly equatorward. We also briefly discuss overall transport across the polar regions by considering how much tracer is transported into/away from the poles in a 30-sol time period. This is simply a ratio of tracer concentration poleward of 75°N/S after 30 sols of evolution ($c_{pole_{30}}$) compared to tracer concentration at initialisation (c_{pole_0}). All metrics and diagnostics used in the analysis of our simulations are included in Table 3.2. A schematic of the overturning circulation shows the latitudes and altitudes of ϕ_{HC}, $\phi_{u_{\max}}$, and ϕ_{PV} (Figure 3.3).

3.4 Results

3.4.1 Circulation response to systematically varying parameters

The following section illustrates the circulation response to systematically varying dust, obliquity, and eccentricity. Further illustrative figures that help to visualise the atmospheric circulation across the range of parameters are also provided in the Supplementary Information for this article (Appendix B of this thesis).

The latitude of the descending branch of the Hadley Cell (ϕ_{HC}) has a clear dependence on obliquity, provided obliquity is greater than $\sim 30°$. Above this, in both hemispheres and regardless of eccentricity value, ϕ_{HC} sees a shift towards the pole over the winter solstice, excursing further at higher obliquity during the peak dust season (Figure 3.4a,c). The relationship between ϕ_{HC} and dust scaling is somewhat weaker, although increasing dust scaling also acts to push ϕ_{HC} further poleward, particularly in the northern hemisphere (Figure 3.4e). There is a strong response at $\lambda = 8$ over the southern winter solstice (Figure

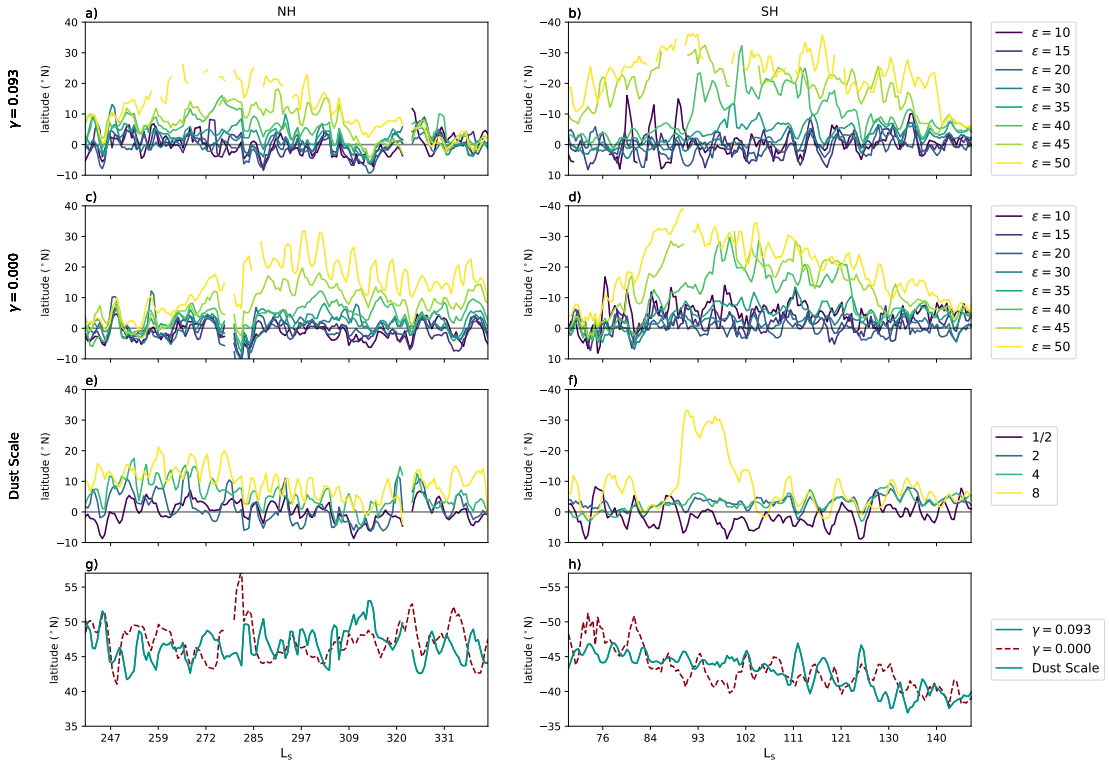

Figure 3.4: **Winter anomaly of the latitude of the descending branch of the Hadley circulation** (ϕ_{HC}) for: a,b) $\gamma = 0.093$; c,d) $\gamma = 0$; and e,f) dust scale simulations. Panels g,h) show ϕ_{HC} for $\varepsilon = 25°$ and $\lambda = 1$, and panels a-f) show the anomaly from this value in the corresponding suite of simulations. The left-hand column shows the northern hemisphere and the right-hand the southern.

3.4f).

The strength of the overturning circulation clearly increases with obliquity and also with dust scaling, in either hemisphere and for either value of eccentricity (Figure 3.5). This is due to the increased aerosol heating with higher dust loading, which has been shown to strengthen the Hadley circulation [e.g. Guzewich et al., 2016]. The strength and width of the overturning circulation are predicted to increase with obliquity in axisymmetric theory and simulations [Guendelman and Kaspi, 2019; Lindzen and Hou, 1988].

The jet on the 50Pa surface (the lower portion of the jet) also moves poleward with increasing obliquity, and this relationship is clear from the lowest obliquity ($\varepsilon = 10°$) to the

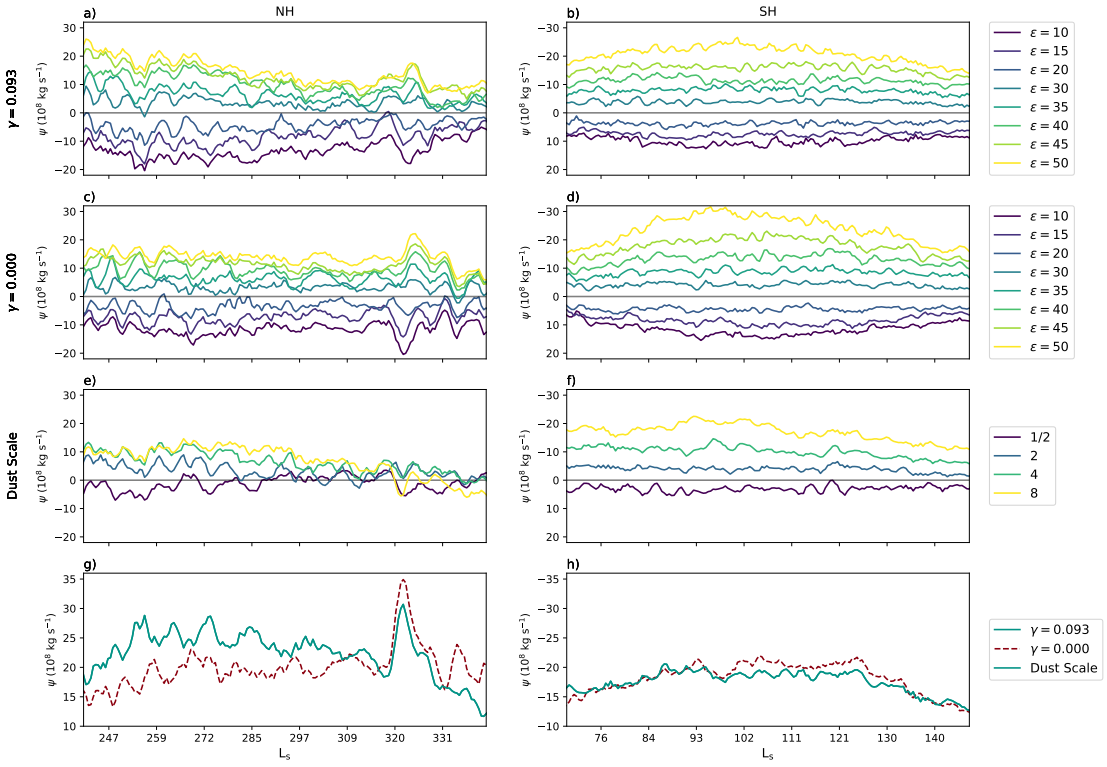

Figure 3.5: **Winter anomaly of the strength of the Hadley circulation** (ψ_{max}) for: a,b) $\gamma = 0.093$; c,d) $\gamma = 0$; and e,f) dust scale simulations. Panels g,h) show ϕ_{HC} for $\varepsilon = 25°$ and $\lambda = 1$, and panels a-f) show the anomaly from this value in the corresponding suite of simulations. The left-hand column shows the northern hemisphere and the right-hand the southern.

highest ($\varepsilon = 50°$). There is also a shift poleward with increasing dust scaling in the southern hemisphere, but there is no clear response to dust scaling in the northern, although the jet is pushed somewhat equatorward when $\lambda = 8$, reminiscent of the circulation response to a GDS [for example Ball et al., 2021; Guzewich et al., 2016].

The strength of the 50Pa jet increases with increasing dust loading in both hemispheres, although it is a proportionally much greater increase in the southern hemisphere (Figure 3.7). In the northern hemisphere, the response of the jet also saturates between $\lambda = 4$ and $\lambda = 8$, where the jet response is somewhat weaker. The dependence on obliquity is more complex. In the northern hemisphere, there appears to be little obliquity dependence up to

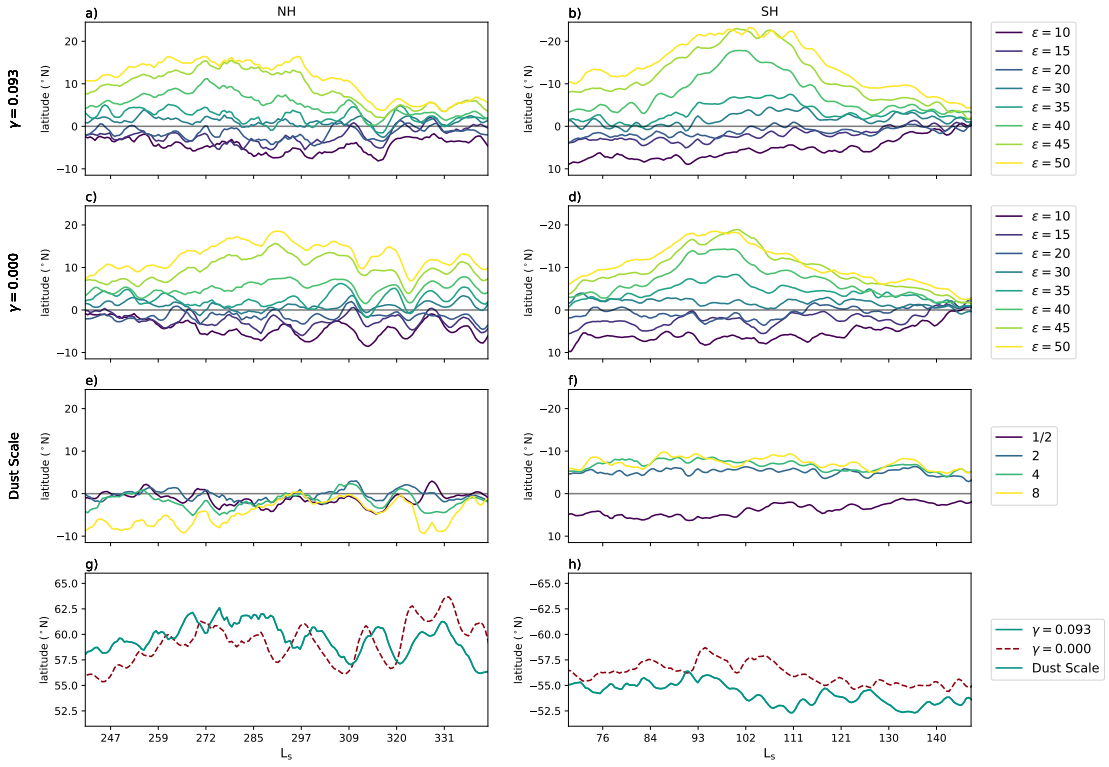

Figure 3.6: **Winter anomaly of the latitude of the jet on the 50Pa surface** ($\phi_{u_{\max}}$) for: a,b) $\gamma = 0.093$; c,d) $\gamma = 0$; and e,f) dust scale simulations. Panels g,h) show ϕ_{HC} for $\varepsilon = 25°$ and $\lambda = 1$, and panels a-f) show the anomaly from this value in the corresponding suite of simulations. The left-hand column shows the northern hemisphere and the right-hand the southern.

obliquities of $\sim 35°$. For obliquities of $\geq 40°$, there is a significant drop in the strength of the jet across most of the winter period, although this appears to recover by around $\mathrm{L_s} = 320°$ in $\gamma = 0.093$ simulations. This drop is stronger (i.e. the jet weakens more) at higher obliquities. In the southern hemisphere, there appears to be a maximum in the strength of the jet at present-day obliquity, with decreasing jet strength as ε either increases or decreases. With the combined effect of high obliquity and eccentricity (Figure 3.7b), there is a drop in jet strength over winter solstice (for $\varepsilon = 50°$, the jet can weaken by $\sim 50\%$) - this effect appears to be mitigated in the 0-eccentricity case, wherein the weakening is much lower proportionally.

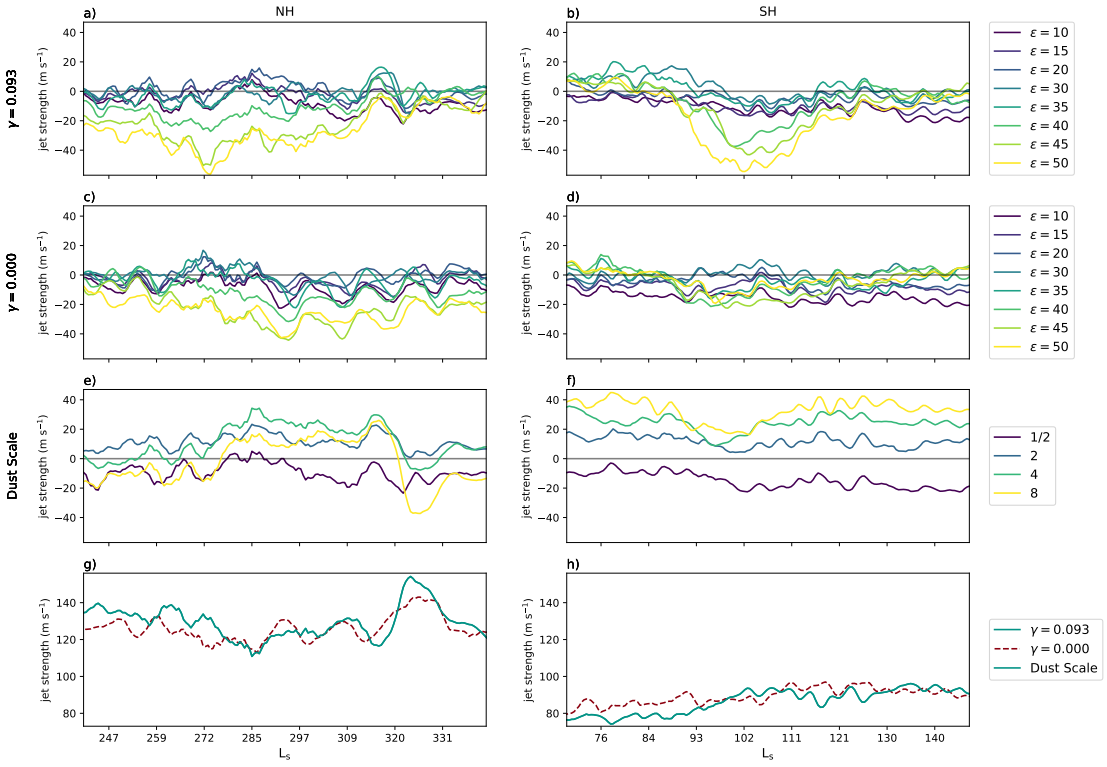

Figure 3.7: **Winter anomaly of the strength of the jet on the 50Pa surface** ($u_{\max}$) for: a,b) $\gamma = 0.093$; c,d) $\gamma = 0$; and e,f) dust scale simulations. Panels g,h) show ϕ_{HC} for $\varepsilon = 25°$ and $\lambda = 1$, and panels a-f) show the anomaly from this value in the corresponding suite of simulations. The left-hand column shows the northern hemisphere and the right-hand the southern.

Coincident with this solsticial weakening of the jet at high obliquity in the southern hemisphere is a destruction of the annulus over the winter solstice (Figure 3.8b,h). We see an overall increase in annularity with increasing obliquity in the southern hemisphere, aside from this solsticial monopole. In the northern hemisphere, the polar vortex is less annular in our model (Figure 3.8g,h), reaching a maximum in annularity at Mars's current obliquity of $\varepsilon = 25°$. In both hemispheres, there is a turning point around $\varepsilon = 25 - 30$ of maximum annularity. For the highest and lowest obliquities ($\varepsilon = 10°$ and $\varepsilon = 50°$), the vortex is monopolar for the majority of winter. The dependence on dust scaling is similar in both hemispheres, with a clear reduction in annularity with increased dust scaling (Figure

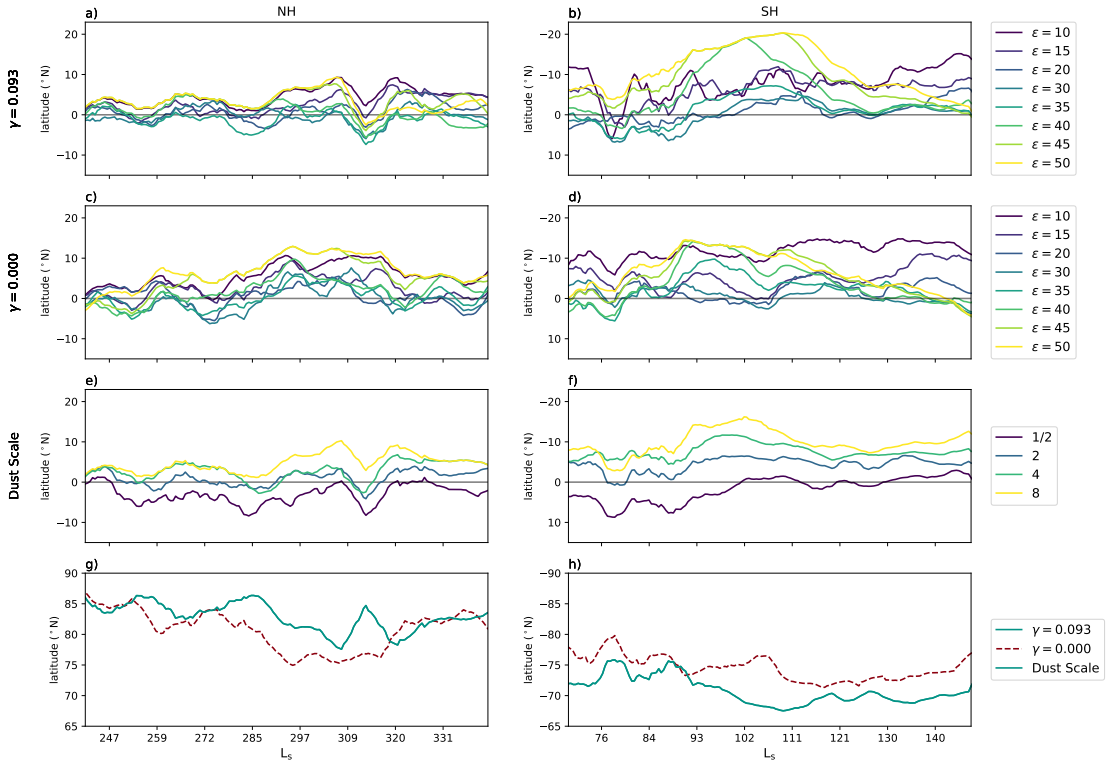

Figure 3.8: **Winter anomaly of the latitude of the maximum PV value on the 300K level (ϕ_{PV})** for: a,b) $\gamma = 0.093$; c,d) $\gamma = 0$; and e,f) dust scale simulations. Panels g,h) show ϕ_{HC} for $\varepsilon = 25°$ and $\lambda = 1$, and panels a-f) show the anomaly from this value in the corresponding suite of simulations. The left-hand column shows the northern hemisphere and the right-hand the southern.

3.8).

The strength of the vortex (PV_{max}) depends more strongly on dust scaling in the southern hemisphere than in the northern, and has the opposite response. In the southern hemisphere, as dust scaling increases so does the maximum PV, although this response saturates around $\lambda = 8$ (Figure 3.9f). In the northern hemisphere, maximum PV appears to be independent of dust loading for $\lambda = 1/2 - 2$, the larger scalings ($\lambda = 4, 8$) weaken the vortex, particularly in early-mid winter. This is consistent with our understanding of the vortex response to GDSs, although the cause of the hemispheric difference in response is not well-explored. In the obliquity simulations, there is overall a strengthening of the

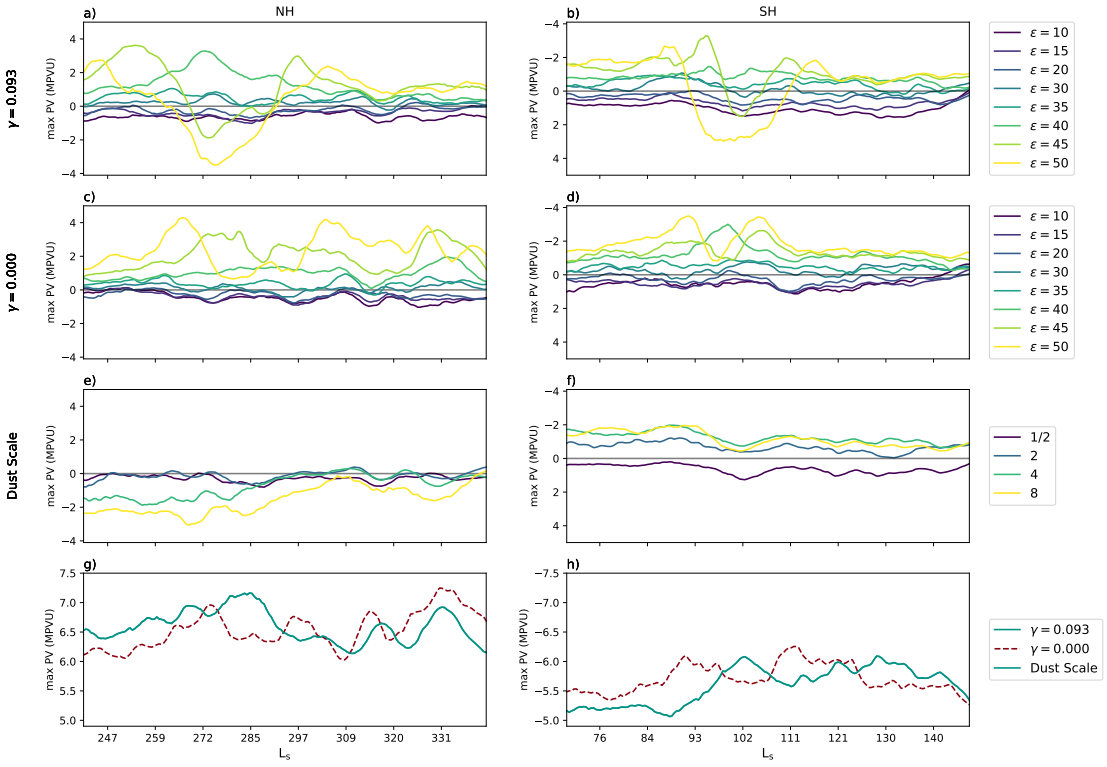

Figure 3.9: **Winter anomaly of the strength of the PV maximum ($\mathbf{PV}_{max}$)** for: a,b) $\gamma = 0.093$; c,d) $\gamma = 0$; and e,f) dust scale simulations. Panels g,h) show ϕ_{HC} for $\varepsilon = 25°$ and $\lambda = 1$, and panels a-f) show the anomaly from this value in the corresponding suite of simulations. The left-hand column shows the northern hemisphere and the right-hand the southern.

vortex with increasing obliquity, in both hemispheres and for both values of eccentricity simulated. When $\gamma = 0.093$, there is a destruction of PV for the highest obliquities over the winter solstice ($\varepsilon = 45, 50°$). When $\gamma = 0$, this effect is reduced and the weakening is not as significant, meaning that the highest obliquities still have overall the highest PV throughout the winter.

3.4.2 Mixing and transport response to systematically varying parameters

In this section, we consider how mixing responds to varying planetary parameters and the associated circulation responses of Section 3.4.1. We first consider overall transport across the polar regions throughout the winter period. Figure 3.10 shows the relative change in passive tracer concentration after 30 sols ($c_{pole_{30}}/c_{pole_0}$), averaged over the polar region ($75° - 90°$N/S). Results are shown for different initialisation periods covering each hemisphere's winter, and illustrate an example of how dust could be transported into the polar region as a function of different parameters. While our tracer is passive and does not actively influence the circulation as does dust, one may expect that more dust will be transported into/away from the poles as the tracer is.

In the southern hemisphere, transport is strongly dependent on both obliquity and dust scaling, with ~ 5% lost at $\varepsilon = 10°$ compared to ~ 50% at $\varepsilon = 50°$ at present-day eccentricity (Figure 3.10b). An increase of dust scaling by 16 times leads to tracer transport increasing from 10% to 35% (Figure 3.10d). There is a similar dependence on obliquity in the northern hemisphere (up to two times more transport into the northern polar region at $\varepsilon = 50°$ than $\varepsilon = 10°$), although there is additionally a local minimum in transport at the winter solstice when $\varepsilon = 35°$ (Figure 3.10a). In contrast, there is no clear relationship with dust scaling in the northern hemisphere, with $25 - 45$% of the tracer being transported away from the polar region in all simulations. This may be linked to the winter jet latitude at 50Pa, which is less dependent on dust scaling in the northern hemisphere in our simulations than in the southern (Figure 3.6e,f). The northern hemisphere jet also undergoes a proportionally smaller strengthening (weakening) when dust scaling increases (decreases) than the southern, which may be limiting the transport response. Indeed, this limited response may be linked to the generally weaker circulation response to increasing dust scaling in NH winter compared to SH. The higher dust loading imposed by the timing of perihelion in

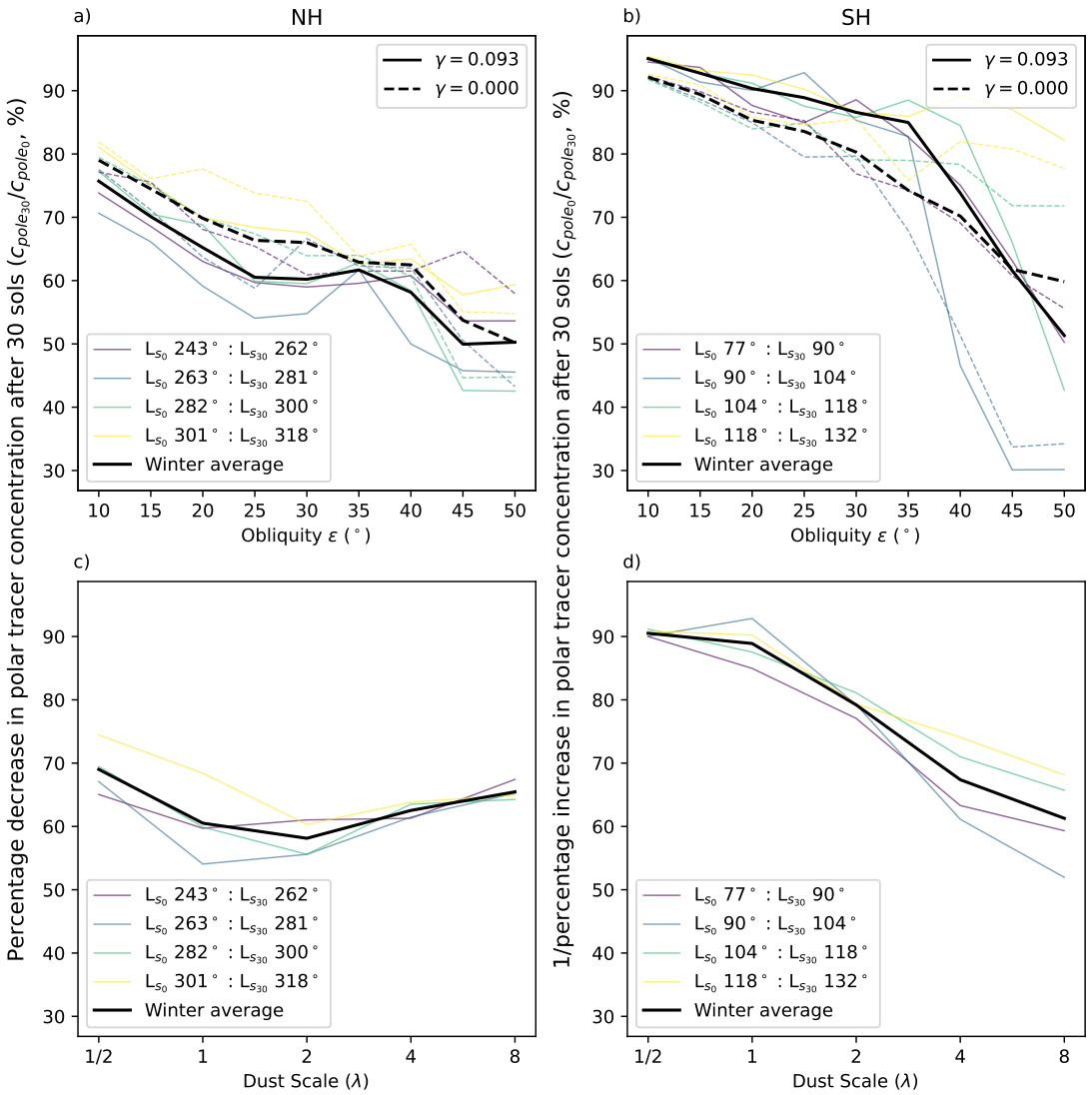

Figure 3.10: **Overall tracer transport from the poles in all simulations.** The percentage of tracer remaining above 75°N/S at 30 sols after initialisation. The concentration, given as a percentage, is given to be $c_{pole_{30}}/c_{pole_0}$ in the northern hemisphere, where c_{pole_t} is an area-weighted polar average of tracer concentration at 300K t sols after initialisation. Corresponding L_s values for initialisation (L_{s0}) and 30 sols after initialisation (L_{s30}) are given in the legend. As the tracer is initialised with a sinusoidal profile (Equation 3.1), typically it is transported *into* the southern polar region, hence we take the inverse $c_{pole_0}/c_{pole_{30}}$ in the southern hemisphere, for comparability. Lower percentages indicate greater transport, as more tracer has been transported into/away from the polar region over 30 sols. Solid lines show $\gamma = 0.093$ and dashed show $\gamma = 0$.

NH winter may be saturating the circulation, which does not undergo large changes until complete vortex breakdown is reached, while the SH winter circulation is more sensitive as initial loading is lower.

When considering the differences between the current and zero eccentricity cases, we note that more tracer is transported out of the northern polar region in current eccentricity simulations compared to zero eccentricity simulations whereas the reverse is true in the southern hemisphere. This result may be due to the timing of perihelion in current eccentricity simulations, which leads to enhanced circulation during northern hemisphere winter compared to simulations in which $\gamma = 0$. In the southern winter, however, we expect that circulation will be enhanced in simulations with $\gamma = 0$ compared to $\gamma = 0.093$, as southern winter occurs during aphelion (so that when $\gamma = 0$, insolation will be greater over southern winter than when $\gamma = 0.093$). Finally, we also note that in both hemispheres transport is greatest over winter solstice, and tends to be slightly weaker over autumn and later winter.

To understand where these concentration changes come from, we now consider solely isentropic mixing through the calculation of effective diffusivity, κ_{eff}. Figure 3.11 shows a strong mixing barrier in the northern winter polar regions at lower obliquities where κ_{eff} is small, with much higher κ_{eff} in midlatitudes. This general structure is similar to that found for Earth's stratospheric polar vortices [e.g. Haynes and Shuckburgh, 2000a], where steep PV gradients at the edge of the vortices act as barriers to mixing. By the highest obliquity ($\varepsilon = 50°$, Figure 3.11e,j), this barrier has all but disappeared, and there is mixing throughout the northern hemisphere. There is clear mixing at the pole at low obliquities, where air is confined by the barrier. Figure 3.12 shows a similar picture, with a stronger and wider mixing barrier at lower obliquity than at higher. In the southern hemisphere, mixing in the midlatitudes (equatorward of the mixing barrier) tends to increase with increasing obliquity, although we do not see this response in the northern hemisphere. Eccentricity has a much smaller influence on the mixing barrier. In the southern hemisphere, we note

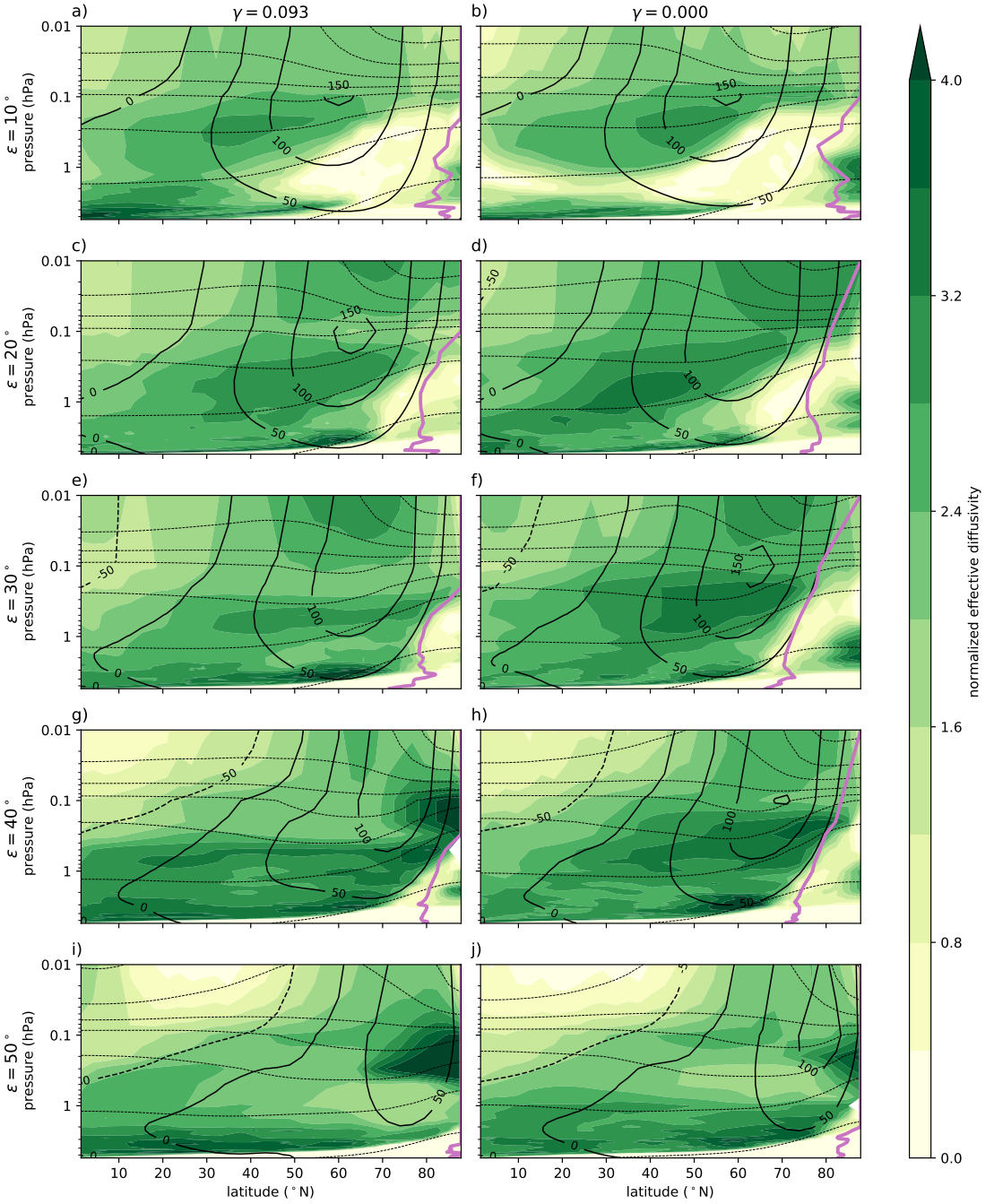

Figure 3.11: **Winter horizontal mixing in the northern hemisphere varying-obliquity simulations.** Northern hemisphere winter effective diffusivity for varying-obliquity simulations. 10 sol winter average (centred around $L_s = 270°$) cross-sections of effective diffusivity (shading), zonal-mean zonal winds (solid contours), isentropic surfaces (dashed contours; corresponding to 200, 300, ... K), and the latitude of the hemispheric maximum in zonal-mean PV (purple line). a-e) Current eccentricity ($\gamma = 0.093$) and f-j) Zero eccentricity ($\gamma = 0$).

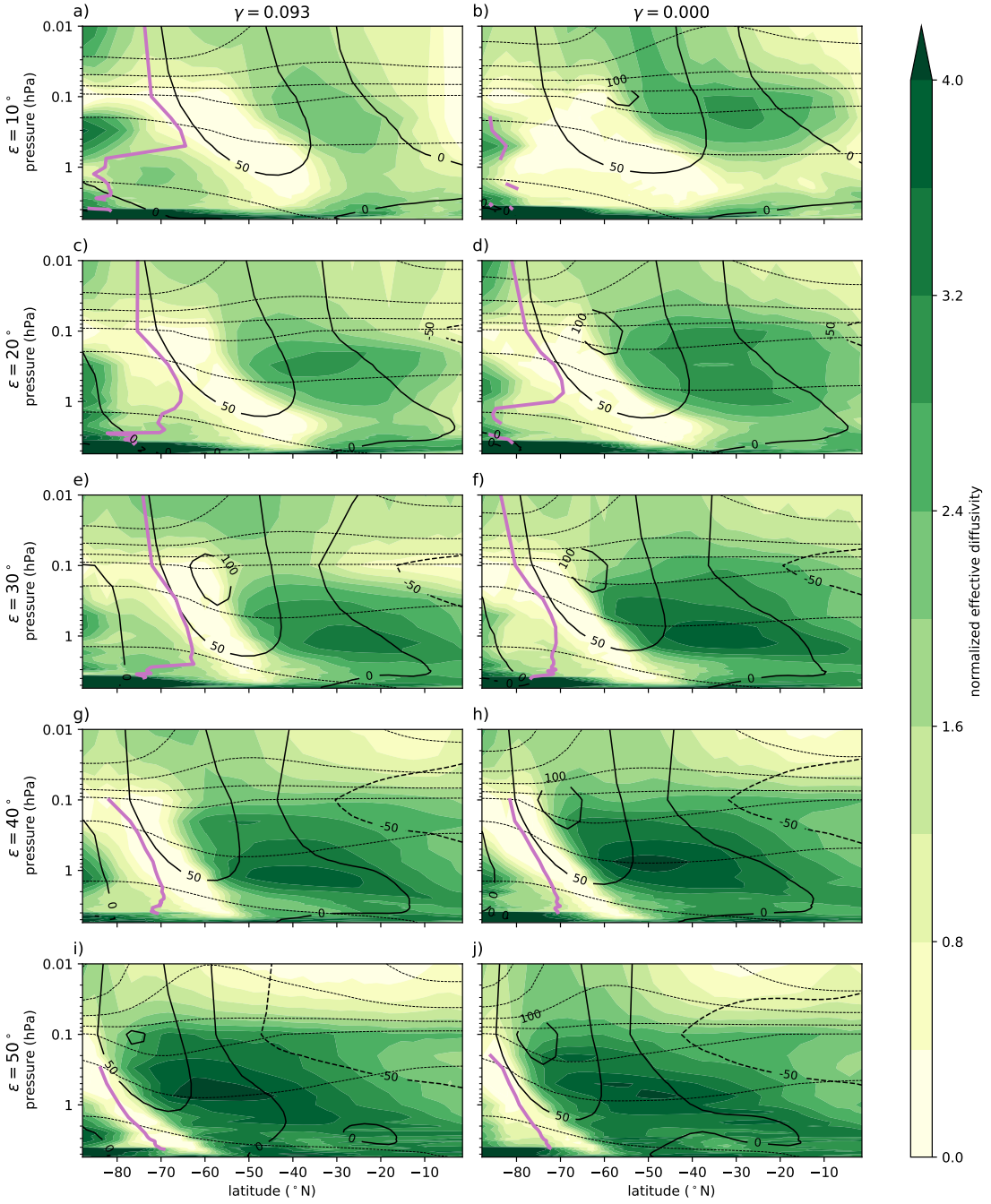

Figure 3.12: **Winter horizontal mixing in the southern hemisphere varying-obliquity simulations.** Southern hemisphere winter effective diffusivity for varying-obliquity simulations. Shading and contours as in Figure 3.11 but for the southern hemisphere (centred around $L_s = 90°$).

that the mixing barrier is generally narrower and the vortex less annular (as shown by the purple line approaching 90°S) in simulations with $\gamma = 0$ than their equivalent with $\gamma = 0.093$. This appears to be the opposite response to that of the northern hemisphere polar vortex, where $\gamma = 0$ would suggest a slightly wider annulus and stronger barrier.

Similarly, we further see a transport barrier for different values of λ, the scaling parameter for dust loading. Mixing within the polar region is strongest when dust scaling is lowest in either hemisphere, likely due to the relatively wide annulus in these simulations. As dust scaling is increased in the northern hemisphere (Figure 3.13, right), there is no clear response in either the width of the mixing barrier or the annulus. The only clear response of the annular vortex is at a dust scaling of $\lambda = 4$, wherein the vortex becomes monopolar at all altitudes, or at $\lambda = 8$, where the annulus is confined to lower altitudes than $\lambda = 1/2 - 2$. This is in contrast to the southern polar vortex, where the annulus tends to shrink with increasing dust scaling (Figure 3.13, left) but remains annular for all dust scaling scenarios. We do however see an increase in midlatitude mixing and that the mixing barrier contracts toward the pole in the southern hemisphere with increased dust scaling.

Having considered a vertical cross-section of the atmospheric circulation, we now show the evolution of effective diffusivity on the 300K surface throughout the seasonal cycle in Figure 3.14. Effective diffusivity and hence mixing is largest in the winter low-mid latitudes for all simulations, particularly in the northern hemisphere. We note that at higher obliquity ($\varepsilon = 40 - 50°$), there is a significant increasing in polar mixing in the southern hemisphere over the winter solstice (Figure 3.14d,e,i,j). This is accompanied by a destruction of the annulus and hence a monopolar vortex at this time, as well as a more poleward jet.

Figure 3.15 shows the seasonal evolution of effective diffusivity as in Figure 3.14 but for the dust scaling experiments. We see that there remains an effective mixing barrier in the southern hemisphere throughout winter at all dust loadings simulated, as well as

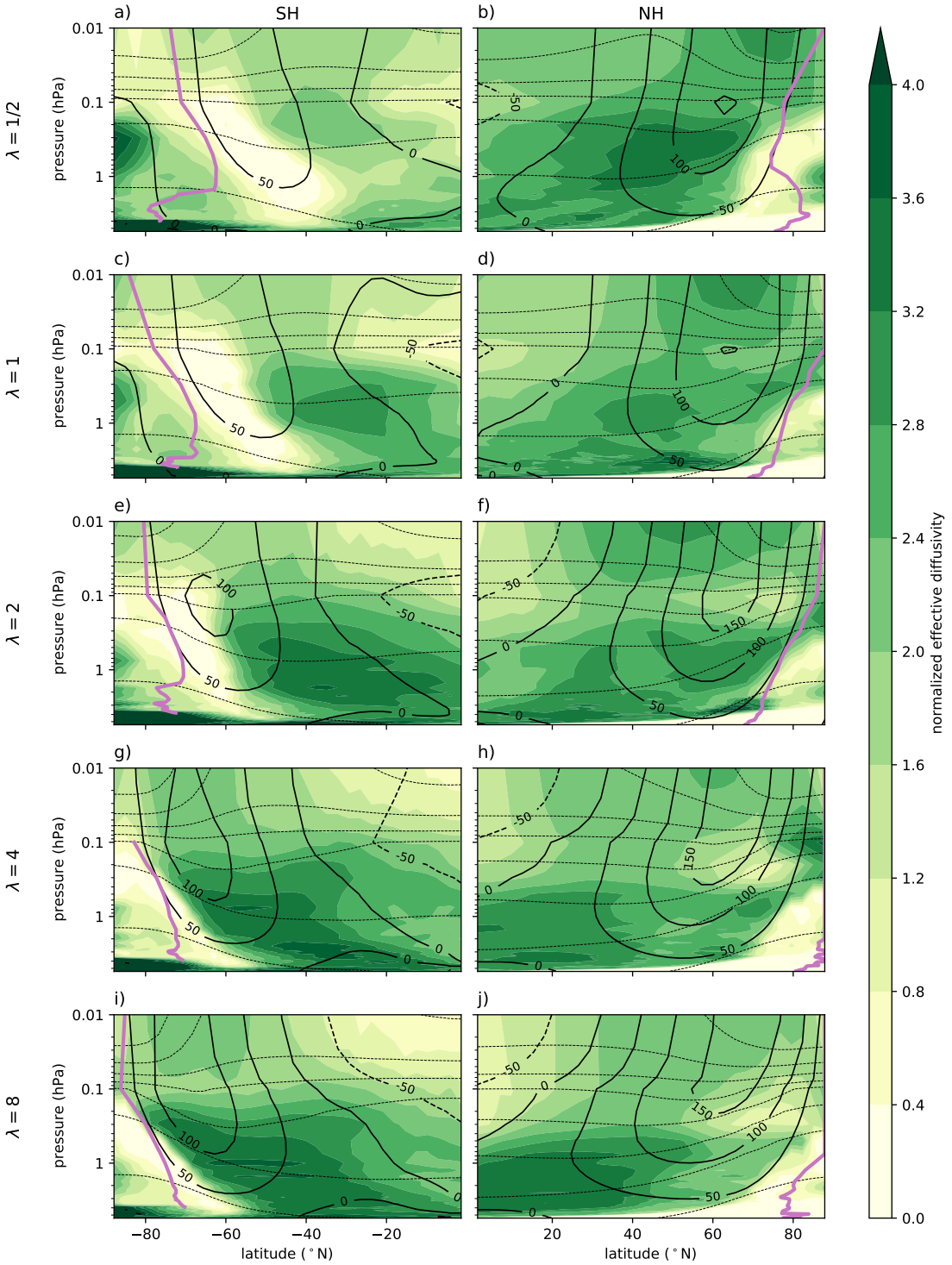

Figure 3.13: **Winter horizontal mixing in the dust scale simulations.** Winter effective diffusivity for dust scale simulations (left column SH, right column NH). Shading, contours, and time averages as in Figures 3.11 and 3.12 but for the dust-scale simulations.

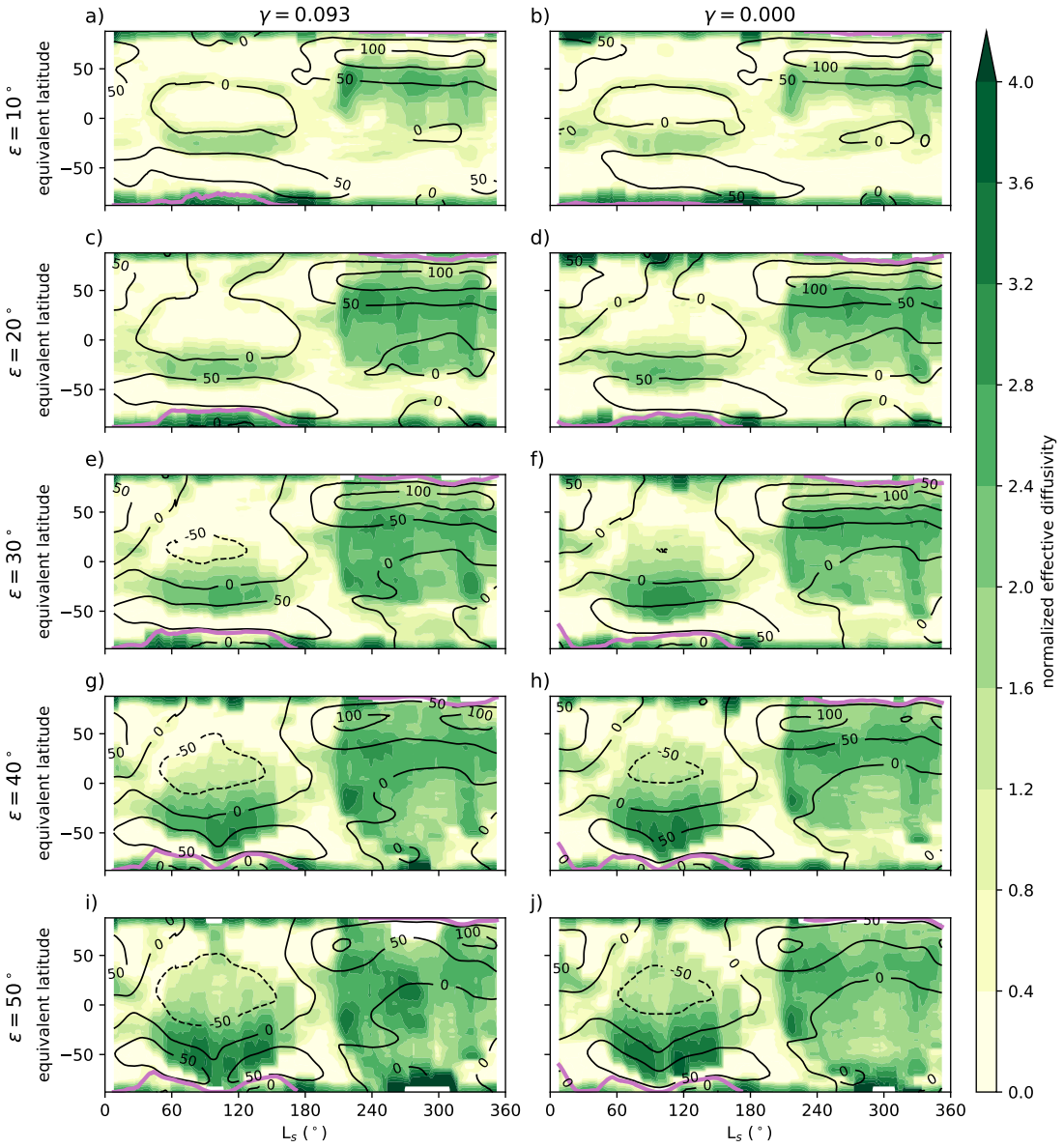

Figure 3.14: **Seasonal changes in mixing in varying-obliquity simulations.** Evolution of effective diffusivity on the 300K level (shading), zonal winds (black contours), and ϕ_{PV} (purple line). A 30-sol smoothing is applied to the model output for clarity.

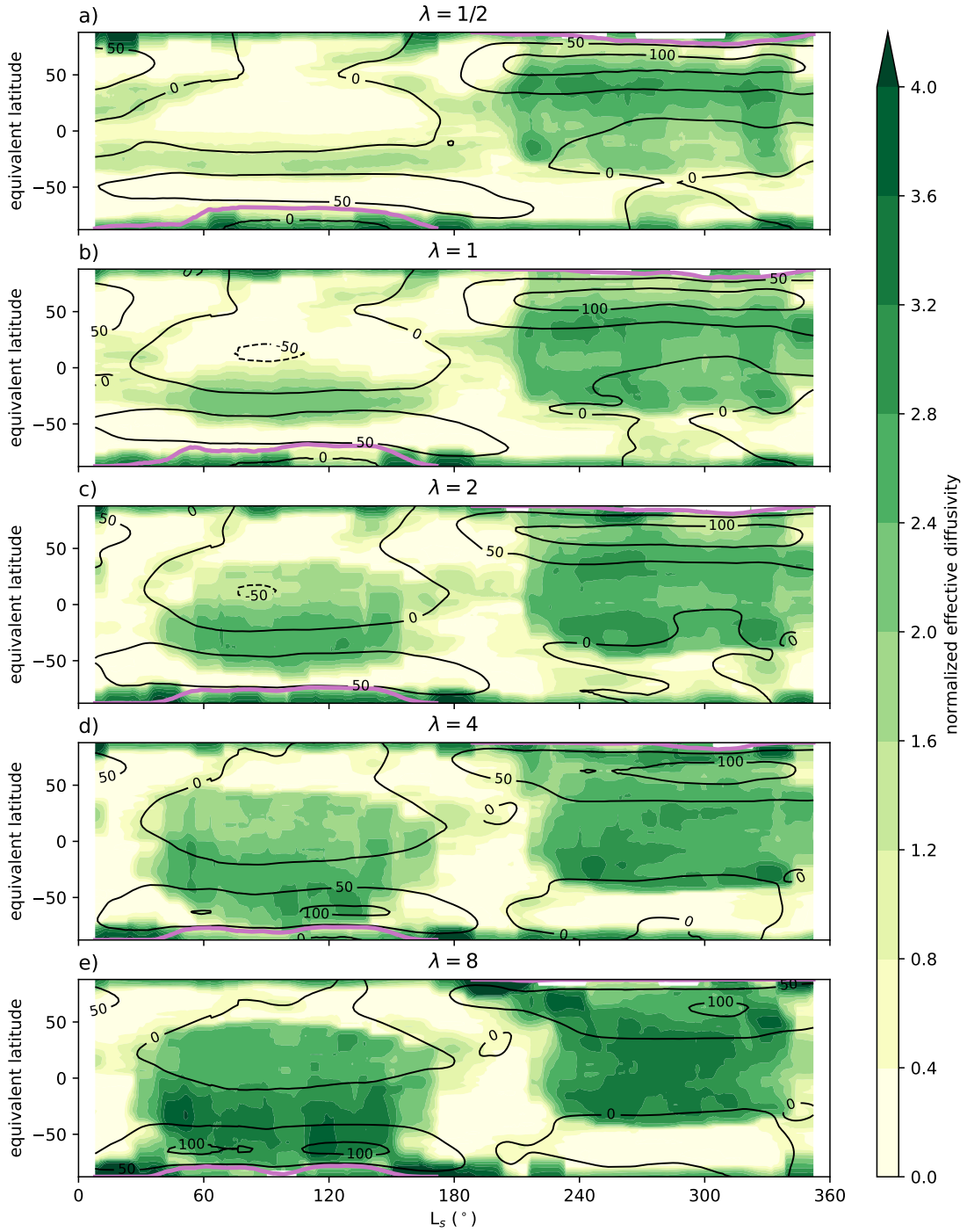

Figure 3.15: **Seasonal changes in mixing in dust scale simulations.** Evolution of effective diffusivity on the 300K level (shading), zonal winds (black contours), and ϕ_{PV} (purple line). A 30-sol smoothing is applied to the model output for clarity.

an annular vortex and mixing within the annulus. The polar vortex in both hemispheres becomes less annular with increased dust loading throughout the winter period, although the southern polar vortex remains persistently annular at all dust scalings. We note that mixing in the southern hemisphere winter becomes stronger at higher dust loadings (until it is approximately equivalent to that in the northern hemisphere at $\lambda = 4$ and $\lambda = 8$; Figure 3.15d,e). Despite there being an approximately equivalent increase in mixing at the equatorward flank of the southern hemisphere winter transport barrier, we do not see the same solsticial destruction of the annulus and mixing barrier as we see in the high obliquity simulations.

Finally, we also show changes in the large-scale atmospheric circulation with our changing parameter values. We show the winter mean (60 sols averaged about the winter solstice) values of ϕ_{PV}, ϕ_{HC}, $\phi_{u_{\max}}$, and $\kappa_{\mathrm{eff}_{300}}$ for all simulations, as well as their rates of change with obliquity and dust scaling (Figure 3.16). We see that ϕ_{HC} increases with both obliquity and dust scaling in both hemispheres, although the response tends to be slightly stronger in the southern hemisphere. There is an additional eccentricity signal at high obliquity, with current eccentricity simulations having a slightly more poleward descending branch of the HC than zero eccentricity simulations in the southern hemisphere. $\phi_{u_{\max}}$ lies approximately 10° poleward of ϕ_{HC} in almost all simulations, similarly increasing with both obliquity and dust scaling in both hemispheres, although with very little eccentricity signal in either hemisphere. In the $\lambda = 8$ simulation, $\phi_{u_{\max}}$ sits equatorward of ϕ_{HC}, consistent with the equatorward shift of the jet during GDS periods. However, the response of the annular vortex is somewhat less clear. There is a small increase in ϕ_{PV} in the northern hemisphere with dust scaling, and a larger increase in the southern, consistent with the stronger response in ϕ_{HC} and $\phi_{u_{\max}}$ in the southern hemisphere. The response to changing obliquity is less clear - in the northern hemisphere, there appears to be a turning point at around $\varepsilon = 30 - 35°$, and similarly in the southern. In the southern hemisphere, this is due to the solsticial monopolar PV structure that occurs at higher obliquities (Figure

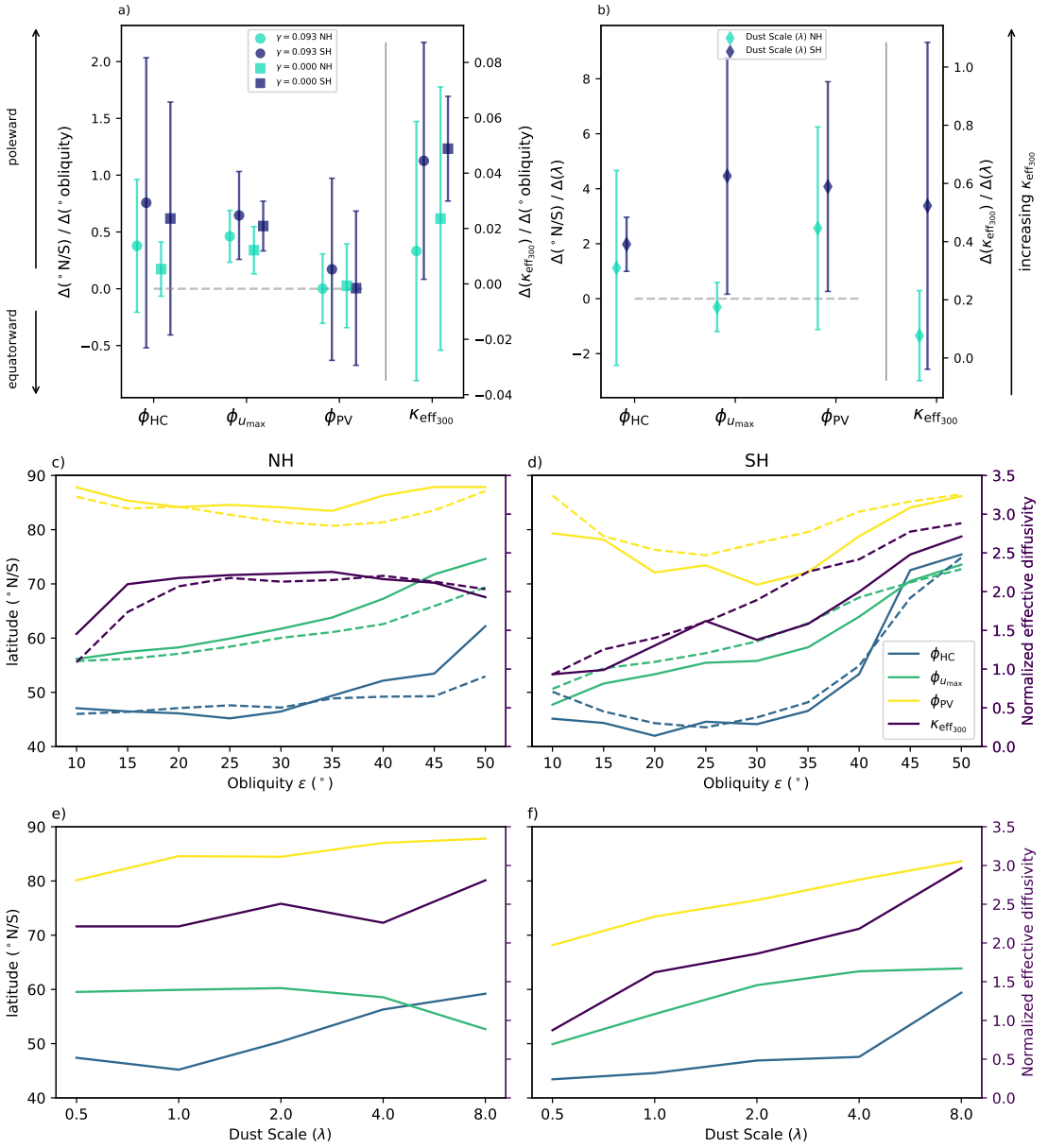

Figure 3.16: **The change in various diagnostics of the circulation with obliquity or dust scale.** a,b) Rates of change of the winter mean (60 sols averaged about $L_s = 270$ ($L_s = 90$) in the northern (southern) hemisphere) values of ϕ_{HC}, $\phi_{u_{max}}$, ϕ_{PV}, and $\kappa_{eff_{300}}$ with obliquity (a) and dust scale (b) for both the northern (light blue) and southern (dark blue) hemispheres. Descriptions of the quantities shown are given in Table 3.2 and error bars show the standard deviation of these rates of change. c-f) Winter average values of ϕ_{HC} (blue), $\phi_{u_{max}}$ (green), ϕ_{PV} (yellow), and $\kappa_{eff_{300}}$ (purple). Panels a-b) show the gradient of the lines in panels c-f). In panels c-d), solid lines show current eccentricity ($\gamma = 0.093$) and dashed show zero eccentricity ($\gamma = 0$) simulations. Note that $\kappa_{eff_{300}}$ is plotted on the right-hand axis of all panels.

3.14 - while the vortex is annular, the annulus tends to be wider in the high obliquity simulations, however this solsticial destruction reduces the mean annularity over the winter period). Overall, we find significant differences in the width of the annulus (and its response to dust scaling) in the southern hemisphere compared to its northern counterpart. Such differences are also identified in studies of the polar vortices in reanalyses and other free-running MGCMs [e.g. Mitchell et al., 2014; Streeter et al., 2021; Waugh et al., 2016], indicating that vortex morphology bears further investigation.

We now consider the mean value of κ_{eff} poleward of 40°N/S on the 300K level ($\kappa_{\text{eff}_{300}}$) in all simulations (Figure 3.16, purple lines). These values show that overall mixing in the southern hemisphere is heavily dependent on dust scaling and obliquity. Indeed, with an increase in dust scaling from $\lambda = 1/2$ to $\lambda = 8$, $\kappa_{\text{eff}_{300}}$ is almost tripled (moreover, this is an increase in the effective diffusivity on a log scale, indicating that the proportional increase is actually larger at a 7.4-fold increase). With an increase in obliquity from $\varepsilon = 10°$ to $\varepsilon = 50°$, there is an increase of an almost equivalent magnitude. However, in the northern hemisphere, the response to changing either parameter is less clear. Increasing dust loading weakly increases overall mixing (Figure 3.16e), which remains large for all simulations. Increasing obliquity increases mixing for lower values of obliquity ($\varepsilon = 10-25°$), but has less impact for values higher than this. We note that mixing is generally lower in the southern hemisphere than the northern, although at high obliquity or dust loading the greater sensitivity in the southern hemisphere means that they have reached an approximately equal strength of mixing.

These changes may be summarised by considering the rate of change of each quantity with either obliquity or dust loading (Figure 3.16a,b). We see clearly that there is a poleward trend in both ϕ_{HC} and $\phi_{u_{\max}}$ with increasing obliquity and dust scale (except in the NH dust simulations), and that the rate of change with dust loading is much greater in the southern hemisphere (Figure 3.16b, dark blue). We also see an increase in mixing poleward of 40°N/S in both experiments, the response being stronger in the southern hemisphere,

although this hemispheric difference is more significant in the dust scale experiments. However, we note that while ϕ_{PV} tends to move poleward in the dust scale simulations, its rate of change with obliquity is not significant.

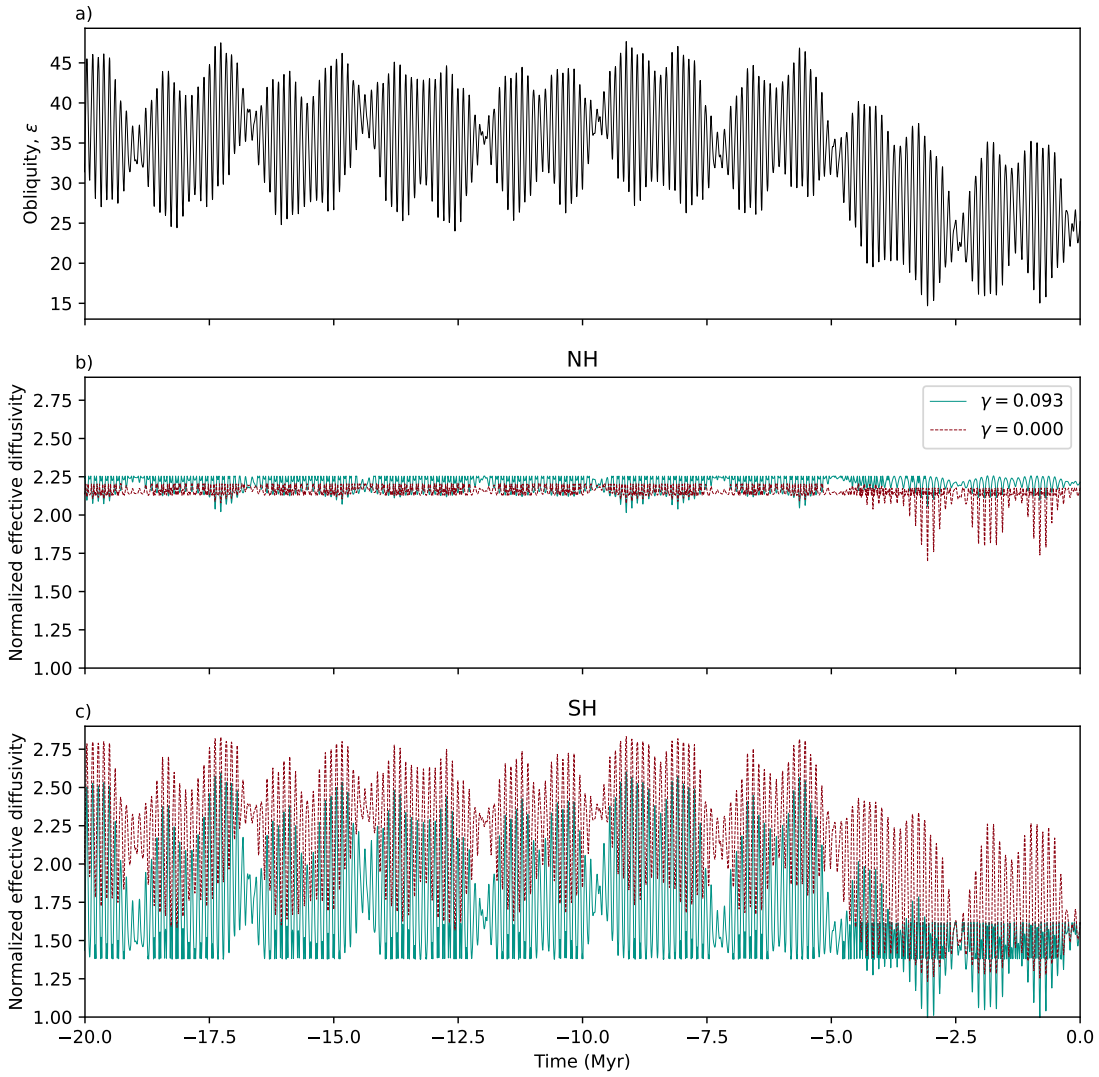

Figure 3.17: **A time series of winter-time mixing ($\kappa_{\text{eff}_{300}}$) according to historical integrations of obliquity.** Winter mean is 60 sols averaged about $L_s = 270°$ ($L_s = 90°$) in the northern (southern) hemisphere. (a) Obliquity from Laskar et al. [2004, data obtained here], and mixing changes with obliquity in (b) the northern hemisphere and (c) the southern hemisphere. We have chosen to include only variations based on obliquity due to the complication of the timing of perihelion with varying eccentricity also, although we show the time series for both $\gamma = 0.093$ (solid blue) and $\gamma = 0.000$ (dashed red).

Finally, Figure 3.17 illustrates how mixing may have varied over the last 20Myr according to obliquity variations alone. In the northern hemisphere, our simulations predict that mixing has been reasonably consistent across this time period, with lower mixing during the last 5Myr when obliquity has been at its lowest. However, in the southern hemisphere, our simulations suggest that isentropic mixing has varied significantly with obliquity, and in particular with a strong decrease again during the last 5Myr. Note that between 5Ma to 20Ma, there is a cut-off in mixing for $\gamma = 0.093$ simulations. This is due to the small non-linearity seen in mixing between $\varepsilon = 25-30°$ (Figure 3.16d). Figure 3.17c suggests that the evolution of obliquity may have a more important influence in the southern hemisphere than the northern. This figure should be treated as a demonstration that mixing may have experienced oscillatory behaviour driven by Mars's orbital parameters. It does not show mixing evolution with dust loading, or with eccentricity (as these are harder to constrain based on our simulations and knowledge of historic dust loading) and so should be treated with caution, but illustrates that mixing could contribute to the layering observed in the polar regions, particularly the south.

3.5 Discussion

Our simulations have shown that mixing into the polar regions of Mars has a strong dependence on obliquity and average dust loading, along with a much weaker dependence on eccentricity. This stronger response to obliquity compared to eccentricity echoes the results of previous studies using an MGCM to investigate orbital forcing of the water and CO_2 cycles, as well as global atmospheric circulation patterns [e.g. Haberle et al., 2003; Mischna, 2003]. The relationships we have found herein differ from those in previous transport studies [e.g. Toigo et al., 2020], likely due to model differences and the processes represented. Despite these differences, this work uses a novel technique in the study of the Martian atmosphere and successfully isolates changes in isentropic mixing from changes

in transport which have not been identified by previous studies.

In their work, Toigo et al. [2020] found a maximum in atmospheric transport into the polar regions at around $\varepsilon = 25°$, whereas in this paper we find that transport increases monotonically with obliquity (Figure 3.10a). This difference may be linked to our representation of polar tracer concentration as a proxy for overall transport compared to their more complex 'age-of-air' tracer. Model differences may also contribute here: for example, the vertical resolution of our simulations is lower than in Toigo et al. [2020], and Isca-Mars represents latent heat release via CO_2 condensation in a more simple scheme which does not update atmospheric pressure according to the mass lost. When we separate isentropic mixing from transport, however, we identify a weak maximum in mixing in the northern hemisphere over $\varepsilon = 25 - 35°$ (Figure 3.16c). Despite these differences in the precise dependence, both studies suggest that mixing and transport changes must be considered when discussing the formation of the PLD. We see that over the obliquity values Mars has experienced in the last 10Ma, transport into the polar regions may almost double in the northern hemisphere or increase almost ten fold in the southern based on changes in obliquity alone. Similarly, an octupling of atmospheric dust loading from a current climatological loading may induce approximately a tripling of transport into the southern polar region, as well as an overall increase in mixing poleward of 40°S by approximately two-fold.

It is thought that the layers within the PLD are formed of differing concentrations of dust and water ice. We have shown herein that there is a stronger mixing and transport dependence on dust loading in the southern polar region than the northern, and that mixing into the southern polar region is very high when dust scaling is also high. Given the positive feedback effects noted in Newman et al. [2005] whereby dust lifting increases with obliquity, one may expect even greater mixing increases with obliquity when an active dust scheme is used, and therefore our results may be considered to be conservative.

We note that mixing dependence on eccentricity is linked to the morphology of the

polar vortex. In all simulations, if there is a change in eccentricity that is concurrent with a small shift in the annularity of the polar vortex, there is an equivalent change in the strength of the barrier to mixing. For example, in the southern hemisphere winter, changing eccentricity from its current value to zero reduces the annularity of the vortex and we see a concurrent increase in mixing into the polar region (e.g. Figure 3.16d, solid to dashed lines). An equivalent reduction in annularity of the northern polar vortex similarly sees an increase in mixing, although this is a response to increasing the eccentricity rather than reducing it (e.g. Figure 3.16c, dashed to solid lines). Due to the timing of perihelion just prior to northern winter solstice, both such changes are linked to an increase in insolation and a strengthening of the overturning circulation.

The mixing dependence on obliquity appears less related to the annularity of the vortex, which has a nonlinear response to increasing obliquity in both hemispheres, while mixing does not (Figure 3.16c,d). In both hemispheres there is an overall increase in transport into the polar regions (Figure 3.10a,b) with increasing obliquity. The mixing barrier shrinks and shifts poleward (e.g. Figures 3.11 and 3.12), meaning that there are simulations with an almost monopolar vortex where there may exist a strong mixing barrier or no mixing barrier (3.11a,i).

We have additionally identified a broad range of obliquities ($\varepsilon = 25 - 35^\circ$) that act as a turning point for some of the metrics studied. For obliquities greater than this, we see poleward excursions of the edge of the Hadley cell and the jet (Figures 3.4, 3.6), as well as significant weakening of the jet around winter solstice (Figure 3.7). We also see that the vortex is most annular around $\varepsilon = 25 - 35^\circ$, and above this there is a pronounced solsticial monopole, particularly in the southern hemisphere. There is also a concurrent reduction in the strength of the vortex for these high obliquities (Figure 3.9). Despite the existence of this turning point, some quantities respond linearly to increasing obliquity, including the latitude of the jet at 50Pa, and the descending branch of the Hadley circulation.

In contrast to the work of Guzewich et al. [2016], we have seen that the southern

winter circulation is more sensitive to atmospheric dust loading in our model. Guzewich et al. [2016] showed that temperatures in the southern winter polar vortex were relatively invariant to a change in dust loading (from a dust-free scenario to a scenario with several times the climatological average). Here we have seen a stronger response to dust scaling in the southern hemisphere than the northern in the following quantities: annulus width, latitude of the edge of the Hadley Cell, latitude of the jet at 50Pa, and, most significantly, the mean effective diffusivity on the 300K surface (Figure 3.16). We also see substantial changes in southern polar temperatures with dust loading (Supplementary Information, Figure 13; Figure B.13). However, these differences could be due to the magnitude of the southern hemisphere dust loading explored in our simulations, which when scaled by $\lambda = 4,8$, is substantially larger than that of the 'opposite season' loading used in Guzewich et al. [2016].

There is no guarantee that dust optical properties have remained constant throughout Mars's history [Clow, 1987]. Studies have shown that altering dust optical properties in an MGCM can lead to almost equivalent circulation changes as a doubling of dust loading, although this is ascribed to an equivalent change in aerosol heating rates [Guzewich et al., 2016]. Within this study, we have scaled dust loading throughout the Martian year, taking a climatological scenario of the current dust evolution and multiplying it by a constant throughout the year, to mimic a change in global dust abundance. Other studies have investigated the influence of dust loading by changing the scaling during the peak season, or by changing the timing of the peak season [e.g. Toigo and Waugh, 2022]. We have found differing transport and mixing responses to dust loading than in this previous study, and the prescribed modern scenario of dust loading may not be representative of historical dust distributions. Indeed, Newman et al. [2005] showed that obliquity changes lead to changes in dust lifting which then influence the atmospheric circulation. A similar study with an active dust lifting scheme would be beneficial to understand how dust loading changes with obliquity would influence mixing. Inclusion of a dust lifting and settling scheme would

also further our understanding of how polar temperature changes are connected to dust settling rates, which may influence the results. For example, the greater polar insolation at high obliquity elevates polar temperatures (Supplementary Information, Figures 13 and 14; Figures B.13 and B.14), which may slow the dust settling rates at these times. Based on our modelling, we may expect this effect to be greater in the northern hemisphere than in the southern (Supplementary Information, Figure 13a,b; Figure B.13a,b), although an active dust tracer would be useful in quantifying any changes in settling rates.

Comparing the dependence of mixing on either dust scaling or obliquity, and the hemispheric differences noted therein, we note that for all obliquities there is more mixing in the northern hemisphere winter than in the southern (Figure 3.14). However for the dust scaling simulations, mixing is stronger in the northern hemisphere but remains relatively invariant to dust loading, whereas in the southern hemisphere, mixing increases with dust loading until it is approximately equivalent to that in the northern hemisphere when $\lambda = 4$ (Figure 3.15,3.16).

Our results show that effective diffusivity is a useful diagnostic of mixing in the Martian atmosphere, noting that similarities with structures on Earth provide a useful example for comparison. While there are limitations to our study, particularly in the use of an idealised model with prescribed dust, we believe that this methodology could be a valuable tool to answer questions concerning the formation of the PLD, just as it has been in understanding the chemistry of Earth's polar stratosphere. We intend this study to be seen primarily as a proof-of-concept for the use of effective diffusivity as a mixing diagnostic for the Martian atmosphere. While our results may not be entirely conclusive in regards to the contribution of horizontal mixing to the formation of the PLD due to modelling choices made herein, our findings provide a foundation for more complex GCMs to further explore these results.

3.6 Summary

We have investigated the role that isentropic mixing may play in the formation of the polar layered deposits (PLD) using an idealised Martian Global Climate Model (MGCM). To do this, we have applied a novel technique for the Martian atmosphere, namely the calculation of effective diffusivity, a Lagrangian measure of isentropic mixing. We find significant changes and hemispheric differences with obliquity, average dust loading, and, to a lesser extent, eccentricity. Our key findings are summarised below:

- We find generally high effective diffusivity in the midlatitudes, with a partial mixing barrier approximately coincident with the equatorward edge of the polar vortex. This structure is similar to that found by previous studies of Earth's stratospheric polar vortices.
- We see that midlatitude mixing in the southern hemisphere is more sensitive to obliquity or dust loading changes than that in the northern.
- Despite overall mixing in the southern hemisphere being more sensitive to changes in dust loading, we see that there is a persistent mixing barrier across all simulations performed, whereas this is not the case in the northern hemisphere.
- The mixing barrier in the southern hemisphere is colocated with a local potential vorticity maximum away from the pole (suggesting an annular vortex), both vanishing only at high obliquities over the winter solstice when polar insolation is greatest.
- In both hemispheres there is an increase in mixing and transport between the polar atmosphere and midlatitudes as obliquity increases, or as dust increases (only in the southern hemisphere).

Our results demonstrate the importance of horizontal mixing in the Martian polar atmosphere and link polar vortex morphology to the efficiency of the transport and mixing

barrier. Changes in mixing of a passive tracer with obliquity and dust loading may have important implications for the transport and mixing of dust in the polar regions. In future research, considering the influence of precession of perihelion as well as circulation response over a range of eccentricities will be important in understanding how these factors have contributed to the formation of the PLD, to complement the initial investigation here into the two illustrative eccentricity values we have chosen. Previous research has linked changes in dust loading to changing orbital parameters [e.g. Newman et al., 2005]; further investigation into mixing changes with an active dust scheme would be illuminating. Furthermore, we have once again noted significant differences in the morphology of the northern and southern polar vortices, so an in-depth study into the causes of these differences would be beneficial. These hemispheric differences suggest that the processes involved in the formation of the PLD may play unequal roles in the northern and southern hemispheres. We hope that the methods presented herein and the hemispheric differences identified provide a strong case to suggest that isentropic mixing is an important process that may have contributed to the formation of the PLD.

CHAPTER 4

THE COUPLING BETWEEN THE HADLEY CELL AND ZONAL JETS ACROSS PLANETARY PARAMETERS

Following the detailed analysis of the Martian polar vortices in Chapters 2 and 3, this chapter contains a more exploratory investigation into Earth's tropospheric overturning circulation. The tropospheric Hadley Cell on Earth is important for the transport of heat and moisture and is expected to expand under increasing CO_2 forcing. However, there are discrepancies in both the observed and predicted rates of expansion, seemingly dependent on the dataset studied as well as on the metric used to define the edge of the tropics.

Inspired by the use of a parameter sweep to study Mars's historical polar vortices and how horizontal mixing has changed over time, this chapter investigates the relationship between dynamical metrics for tropical width on Earth-like exoplanets. The edge of the Hadley circulation, the subtropical jet, and the eddy-driven jet are studied in a parameter sweep over obliquity and rotation rate.

This research aims to understand the dynamical relationships between these three metrics and to contextualise their coupling in various idealised model configurations of Earth's atmosphere across a broader parameter space. These metrics are well-coupled

in some highly idealised models of the Earth's circulation but this breaks down in more complex models, as well as in observations. The dependence of their coupling on model configuration (in particular with the inclusion of a stratosphere, moisture, or grey radiation) is also investigated.

The research here has been written in the format of a journal article, but has not yet been submitted for publication. Supplementary figures for this research have been included in Appendix C of this thesis.

4.1 Abstract

In the Earth's atmosphere, there are multiple ways to define the width of the tropics. Many of these have been used to investigate the rate of tropical expansion under climate change forcing; however, recent work has shown that different metrics can be well- or poorly-coupled with each other in terms of their internal variability, and can exhibit different rates of tropical expansion, raising questions about their underlying dynamics. In an idealised dry model, the latitude of the descending branch of the Hadley circulation (ϕ_{HC}) and the latitude of the subtropical jet (ϕ_{STJ}) have been shown to be positively correlated, but this is not necessarily the case in more complex models, reanalyses, or observations. Here we aim to further probe the dynamics of the coupling between tropical edge metrics in order to understand this apparent sensitivity. We investigate the dependence of the ϕ_{HC}-ϕ_{STJ} relationship, and their relationships with the latitude of the eddy-driven jet (ϕ_{EDJ}), on the planetary parameters used in an idealised modelling framework. We perform a systematic sweep across rotation rate and obliquity, with an Earth-like base case, in multiple model configurations. We find that relationships between metrics may vary dependent on their separation or on their mean strength (ϕ_{HC} and ϕ_{EDJ}), or on their mean latitude (ϕ_{STJ} and ϕ_{EDJ}). A distinct region of the parameter space exists wherein ϕ_{HC} and ϕ_{STJ} may be decoupled, which is replicated in a dry grey-radiation model, but not in its

moist equivalent.

4.2 Introduction

When considering atmospheric circulation on Earth, the edge of the tropics is typically thought of as the region of dry descending air associated with the descending branch of the Hadley circulation at around 30° N/S. However, there are multiple atmospheric turning points or thresholds that may be used to define the precise location at a given time. These can be related to the dynamics, such as the latitude of the descending branch of the Hadley Cell (ϕ_{HC}), the latitude of the subtropical jet (ϕ_{STJ}), or the latitude of the eddy-driven jet (ϕ_{EDJ}). There are also hydrological measures, such as the latitude at which precipitation equals evaporation ($\phi_{\mathrm{P-E}}$), as well as measures based on the radiative budget, such as ϕ_{OLR} (the latitude at which outgoing longwave radiation is $250\,\mathrm{Wm}^{-2}$), or on the latitude of the tropopause break, ϕ_{TPB}. Figure 4.1 shows the latitudes and altitudes of various metrics, along with the quantities that define them. For a more complete description of different metrics, see for example Solomon et al. [2016]; Waugh et al. [2018]. The edge of the tropics are typically characterised as a dry region due to the downwelling dry air in the descending branch of the Hadley Cell (HC). Persistent changes in the latitude of ϕ_{HC} or other metrics including $\phi_{\mathrm{P-E}}$, such as those we may see with tropical expansion, will have profound impacts on populations living in these areas. Given that downwelling at the descending branch of the HC will influence changes in surface weather and water scarcity [e.g. Birner et al., 2014; Seager et al., 2007], understanding these discrepancies in rates of tropical expansion and in the mean latitude of each metric remains an area of interest in studies of the atmospheric response to climate change forcing.

There is good evidence to suggest that the width of the tropics has been increasing over the recent observational period [e.g. Birner et al., 2014; Nguyen et al., 2013]. However, recent work has shown that using different metrics may lead to different rates of tropical

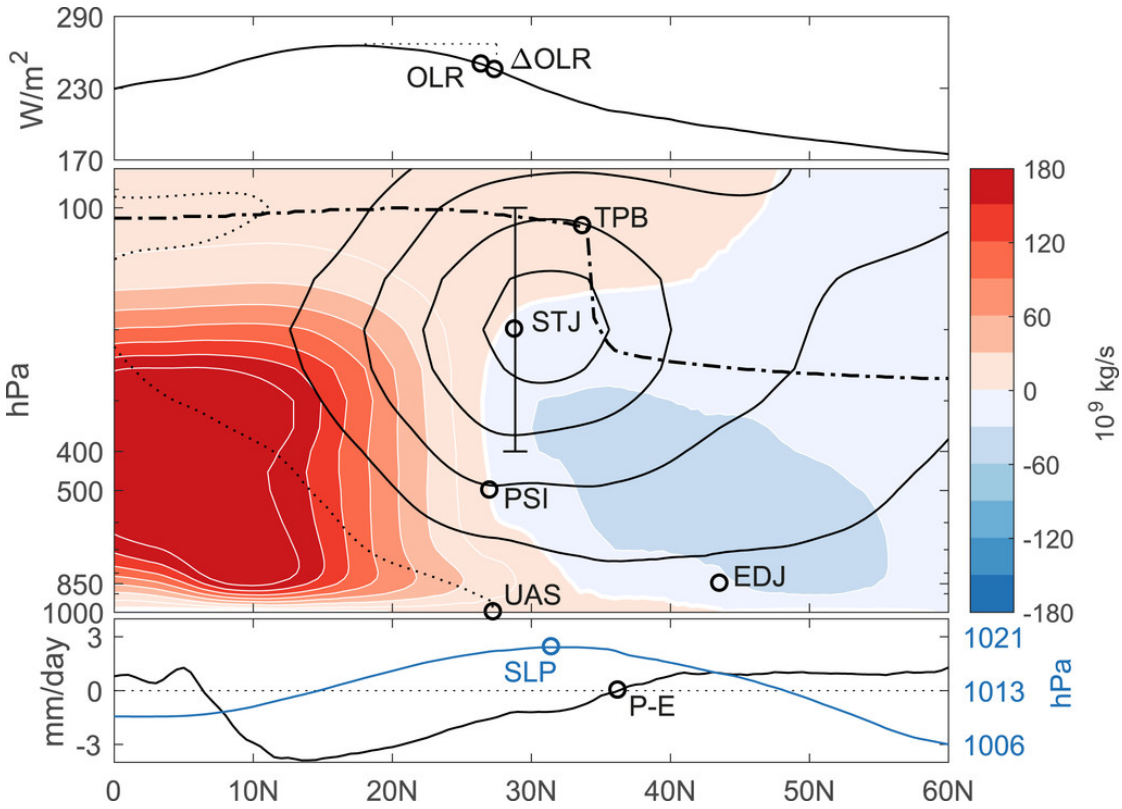

Figure 4.1: **A schematic of various metrics for tropical width.** A schematic illustrating the zonal mean circulation in the NH. The location (altitude and approximate latitude) of each metric is shown: (top) metrics based on outgoing longwave radiation; (middle) zonal wind (solid black contours), meridional streamfunction (shading), tropopause (dash-dotted line); (bottom) sea level pressure and precipitation-evaporation. Figure from Waugh et al. [2018, precise definitions given therein]. Of particular relevance to this thesis are PSI, EDJ, and STJ, which are equivalent to ϕ_{HC}, ϕ_{EDJ}, and ϕ_{STJ}.

expansion, and that metrics can be poorly correlated with each other [Waugh et al., 2018]. For example, it has been shown that in the southern hemisphere of Earth, ϕ_{STJ} is a poor metric for HC width: Solomon et al. [2016] found that ϕ_{STJ} and ϕ_{HC} are essentially uncorrelated in both their variability and response to CO_2 forcing in one model ensemble. Menzel et al. [2019] showed also that in CMIP5 (Coupled Model Intercomparison Project) models correlations between ϕ_{HC} and ϕ_{STJ} are often not significant, and can change signs between seasons. These results may be seen as surprising given that the existence of the

subtropical jet (STJ) is typically linked to poleward angular momentum transport by the HC [Held and Hou, 1980].

An additional source of uncertainty in calculations of the historical and current location and variability of the edge of the tropics is that different studies use different data sources. This includes a range of observations, reanalyses, and climate models. The same metric across different datasets may exhibit a different rate of tropical expansion [e.g. Davis and Rosenlof, 2012]. Furthermore, it is known that there are hemispheric differences in the covariability and location of tropical width metrics [Davis and Birner, 2017], although the causes of these differences are largely unknown [Waugh et al., 2018]. In the Held-Suarez (hereafter HS) benchmark model [Held and Suarez, 1994], ϕ_{HC} and ϕ_{STJ} are well-coupled (since, in this model, the STJ forms as a consequence of angular momentum conservation at the descending branch), but this is not the case in more complex models, in observations, or in reanalyses [e.g. Davis and Birner, 2017; Solomon et al., 2016; Waugh et al., 2018]. ϕ_{HC} and ϕ_{EDJ} appear to be more consistently positively coupled across a wider range of data sources. For example, Kang and Polvani [2011] showed that in CMIP3 models there is a strong correlation between ϕ_{HC} and ϕ_{EDJ} in austral summer on interannual timescales, and also in response to CO_2 forcing. More recent analysis of the CMIP5 simulations with no transient forcings (called control simulations) showed a positive correlation between ϕ_{HC} and ϕ_{EDJ} annually and across all seasons.

The driving mechanisms for different metrics may be entirely different, albeit interlinked. The STJ is driven by angular momentum transport from the deep tropics via the HC, whilst the EDJ is driven by the convergence of westerly momentum fluxes from baroclinic eddies [Lee and Kim, 2003]. However, these two processes may be linked, for example with equatorward-propagating eddies damping the STJ. Lee and Kim [2003] showed that, in an eddy-free, axially-symmetric circulation, the existence of a distinct EDJ is dictated by the strength and latitude of the STJ - if the STJ is sufficiently strong, the primary region of baroclinic wave growth coincides with the region of the STJ, and the

EDJ does not form at latitudes much higher than this. Furthermore, dynamical feedbacks associated with changes in radiative heating and eddy fluxes lead to more complexity when considering the response of a changing Hadley circulation and its influence on the STJ and EDJ [Kim and Lee, 2001a,b].

These discrepancies in the metrics used to calculate the width of the tropics have been well studied over recent years, but the extent to which their location and covariability are reliant upon Earth's planetary parameters remains relatively unknown. Such parameters might include obliquity, eccentricity, radius, surface gravity, and more, and tend to affect atmospheric circulation at large scales. The influence of these parameters on atmospheric circulation is important to understand as it enables us to place the dynamics of Earth's atmosphere within a broader context. Beyond Earth's atmosphere, several recent studies have used idealised global climate models (GCMs) to explore the behaviour of large-scale circulation on terrestrial exoplanets [e.g. Chemke and Kaspi, 2015; Faulk et al., 2017; Guendelman and Kaspi, 2018, 2019; Hill et al., 2022; Kaspi and Showman, 2015; Singh, 2019]. Such studies often focus on the habitability of these exoplanets [e.g. Linsenmeier et al., 2015], for which the overturning circulation is a key factor due to its role in the meridional transport of heat. Held and Hou [1980] derive a relationship between rotation rate and the width of the HC in axisymmetric theory, and several papers since have expanded on this to include dependence on other planetary parameters. In particular, Lindzen and Hou [1988] extend this work to consider off-equatorial heating, and scaling laws have been found that relate the location of the descending branch of the HC with planetary rotation rate and obliquity in seasonally-varying simulations [e.g. Guendelman and Kaspi, 2019]. Further studies have investigated the location of eddy-driven jets (jets primarily driven by the presence of baroclinic eddies, which form due to sharp meridional temperature gradients and deposit westerly momentum, as shown in Figure 4.2) on Earth-like exoplanets at a range of rotation rates, finding a decrease in poleward migration of these jets when rotation rate is high [Chemke and Kaspi, 2015]; or the circulation

dependence on atmospheric mass, which weakens and contracts when mass is increased [Chemke and Kaspi, 2017]. Kaspi and Showman [2015] perform an in-depth investigation into the effects of changing multiple planetary parameters on atmospheric circulation, in particular illustrating relationships between the width and strength of the HC, along with the strength and location of the STJ, with rotation rate.

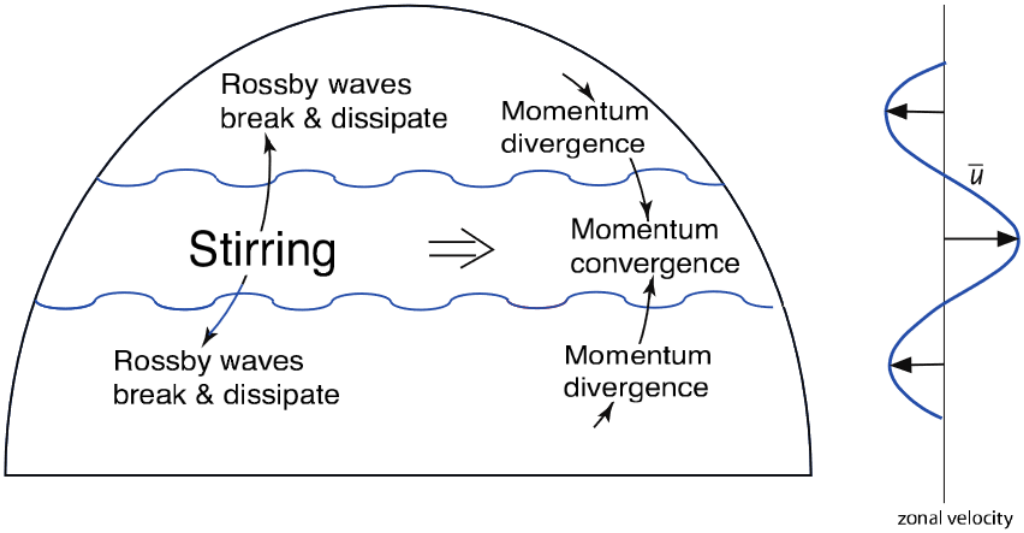

Figure 4.2: **A schematic showing the formation of an eddy-driven jet.** Stirring in the baroclinic zone generates Rossby waves that propagate away. Momentum flux associated with these waves is towards the source region, and thus momentum converges there, generating a net eastward flow. From Vallis [2017, Figure 15.3]

.

No study has yet focused on the internal variability of such features in planetary atmospheres, or how their coupling depends on the planetary parameters chosen. In this paper, we explore the relationship between ϕ_{HC}, ϕ_{STJ}, and ϕ_{EDJ} in idealised models of Earth's atmosphere, and extend the study to investigate the dependence these relationships have on both rotation rate and degree of off-equatorial heating. We consider the influence of these parameters on both metric mean location and their variability and relationships with each other. Finally, we also investigate these same relationships in a moist grey model,

as well as its dry limit, to understand the effect of a more complex radiation scheme and moisture. Previous work has found that the presence of a strong STJ drives baroclinic wave growth at this point, leading to a colocated EDJ, while a weaker STJ leads to the existence of a well-separated EDJ [Lee and Kim, 2003].

We test the following hypotheses from the theory:

1. increasing obliquity or decreasing rotation rate will broaden and strengthen the Hadley circulation.

2. the edge of the Hadley Cell and the eddy-driven jet will be more positively correlated the closer together they lie. This is due to the sensitivity of the Hadley Cell edge to shifts in the eddy-driven jet and its associated eddy momentum fluxes [Davis and Birner, 2017].

3. does a strong STJ imply that the EDJ and STJ are colocated and are strongly correlated?

In Section 4.3 we outline the methods used herein; we present dry results in Section 4.4 and results from the moist model Section 4.5. We discuss and contextualise our key results in Section 4.6 and conclude in Section 4.7.

4.3 Methods

4.3.1 Modelling framework

We make use of the flexible modelling framework Isca [see Vallis et al., 2018, for an introduction]. Isca has previously been used to simulate Earth's atmosphere, and has been adapted to model the atmospheres of other solar system planets, including Mars and Jupiter [Ball et al., 2021; Thomson and Vallis, 2019b], as well as tidally and non-tidally locked exoplanets [Penn and Vallis, 2017, 2018]. One significant advantage of its use is the ready ability to change planetary parameters, which here allows us to perform a

parameter sweep over Earth-like exoplanets; we can also easily change radiation schemes or temperature profiles.

4.3.1.1 Benchmark (dry) model

We present results primarily using the HS benchmark model [Held and Suarez, 1994] as set up in Isca. The HS model is a dry dynamical core with Newtonian relaxation to a zonally symmetric equilibrium temperature profile, T_{eq}. Typically, T_{eq} features a maximum heating at the equator and is hemispherically symmetric. To represent the effects of changing obliquity, we additionally employ a sinusoidal-with-latitude profile that shifts the latitude of maximum heating away from the equator. All simulations are at 'eternal solstice' whereby they do not feature a seasonal cycle. Similarly no simulations include moisture.

In HS simulations, model temperature is relaxed to T_{eq} according to

$$\frac{\partial T}{\partial t} = \ldots - k_T(\phi,\sigma)[T - T_{\text{eq}}(\lambda,\phi,p)], \tag{4.1}$$

where … represents the terms of the potential temperature equation[1], and the term shown here is the forcing. σ is normalised pressure, and acts as the vertical coordinate, and ϕ is latitude. T is model temperature and k_T is the thermal damping coefficient, defined as

$$k_T = k_a + (k_s - k_a)\max\left\{0, \frac{\sigma - \sigma_b}{1 - \sigma_b}\right\}\cos^4\phi, \tag{4.2}$$

following Held and Suarez [1994]. k_a is the damping coefficient in the free atmosphere and k_s the damping coefficient at the surface (here, $k_a = 1/40\,\text{days}^{-1}$ and $k_s = 1/4\,\text{days}^{-1}$). σ_b is the boundary layer depth; no relaxation is applied for $\sigma < \sigma_b$, and $\sigma_b = 0.7$ in our simulations. Equations 4.1 and 4.2 combine simply to mean that temperature follows the laws of thermodynamics with an additional damping term (right-hand-side Equation 4.1). This damping occurs over a timescale of 40 days in the free atmosphere, but in the

[1] See Equation C.1.

planetary boundary layer the relaxation timescale is shorter (the final term of Equation 4.2 is greater than 0, and decreases as $\sigma \to \sigma_b$).

T_{eq} takes the following form:

$$T_{\text{eq}} = \max\left\{T_{\text{str}}, \left[T^* - (\Delta\theta)_z \log_e\left(\frac{p}{p_0}\right)\cos^2\phi\right]\left(\frac{p}{p_0}\right)^\kappa\right\}, \tag{4.3}$$

where

$$T_{\text{str}} = T_{\text{strat}} - \varepsilon\sin\phi \tag{4.4}$$

and

$$T^* = T_0 - (\Delta T)_y \sin^2\phi - \varepsilon\sin\phi. \tag{4.5}$$

T_{strat} is the isothermal stratosphere temperature, which we modify to include a latitude (ϕ) dependence via non-zero ε. T^* is the surface temperature, set by the surface temperature at the equator T_0 and an equator-to-pole surface temperature difference $(\Delta T)_y$ (subject to further modification due to non-zero ε). In Equation 4.3.1.1, $(\Delta\theta)_z$ determines the vertical gradient of potential temperature (i.e. specifies the stratification of the relaxation profile), p_0 is a reference pressure, and $\kappa = R/c_p$.

We take T_{strat} = 200 K, T_0 = 315 K, $(\Delta T)_y$ = 60 K, $(\Delta\theta)_z$ = 10 K, p_0 = 1000 hPa, and κ = 2/7. When ε = 0, the equilibrium temperature profile reduces to that of Held and Suarez [1994]. Choosing non-zero ε forces the maximum surface temperature off-equator, and represents a change in obliquity without introducing a seasonal cycle.[2]

4.3.1.2 Representation of the stratosphere

The HS model uses an isothermal stratosphere, but research has shown that including a more realistic stratosphere can influence the position of jets in the troposphere; in particular, the addition of a cooler polar stratosphere can strengthen and shift ϕ_{EDJ}

[2] A full description of the model and its many possible configurations may be found on the Isca website.

poleward [Polvani and Kushner, 2002]. Therefore, we perform additional experiments including the Polvani-Kushner (PK) stratosphere to investigate its influence on both the location of tropical width metrics and their couplings across a broader parameter space.

All parameter values are taken to be the same in HS and PK simulations, but the choice of T_{eq} is different between the two. In PK simulations, T_{eq} takes the form

$$T_{\text{eq}}(p,\phi) = \begin{cases} T_{\text{eq}}^{trop}(p,\phi), & \text{for } p \geq p_T \\ T_{\text{eq}}^{strat}(p,\phi), & \text{for } p < p_T. \end{cases} \tag{4.6}$$

where $p_T = 100$ hPa is a nominal tropopause height. Details of the stratospheric temperature profile used may be found in the appendix of Polvani and Kushner [2002].

4.3.1.3 Moist model with grey radiation

Additionally, we consider the influence of moisture and the introduction of grey radiation on the metrics of tropical width that we are investigating. To do this, we run a coarser parameter sweep of moist simulations using the model set-up of Frierson et al. [2006], varying planetary rotation rate and diurnally- and seasonally-averaged latitudinal insolation profile (hereafter F06 simulations). The insolation profile for our parameter sweep is shown (Fig C.1 b).

Frierson et al. [2006] describe their model as a moist extension of the Held and Suarez [1994] dry model, in that it is a moist GCM that includes latent heat release, designed for use in idealised studies of planetary atmospheres. The F06 model features an explicit boundary layer model and the Newtonian relaxation is replaced by a simple grey radiation scheme. Further details about this scheme and model equations are given in Appendix C.2. The most relevant details for this study are given below. The incoming solar radiation is given by a second Legendre polynomial profile, which approximates the Earth's seasonally

averaged insolation distribution. This is given by

$$S = \frac{S_0}{4}\left(1 + \Delta_S P_2(\theta) + \Delta_{\rm sw}\sin\phi\right); \tag{4.7}$$

$$P_2(\phi) = (1 - 3\sin^2\phi)/4, \tag{4.8}$$

where S_0 is the solar constant, Δ_S sets the amplitude of the insolation profile between the equator and pole, and $\Delta_{\rm sw}$ modifies the insolation profile with a $\sin\phi$ profile. Varying $\Delta_{\rm sw}$ thus acts in the same way as varying ε, and we choose values of $\Delta_{\rm sw}$ such that the latitude of maximum surface temperature is approximately the same as those in our dry parameter sweep.

We may also adjust the humidity content in the model by considering the saturation vapour pressure e^*, which is constrained by the Clausius-Clapeyron equation. Assuming fixed latent heat of vapourisation L_v, this is

$$e^*(T) = e_0^* e^{-\frac{L_v}{R_v}\left[\frac{1}{T} - \frac{1}{T_0}\right]}, \tag{4.9}$$

where the constant e_0^* is the saturation vapour pressure at $T_0 = 273.16$K and R_v is the gas constant for water vapour. To adjust the humidity content, one can vary e_0^*. Our moist F06 simulations have $e_0^* = 610.78$Pa, and we take the dry limit $e_0^* = 0.0$ for comparison with the HS simulations (hereafter DF simulations).

4.3.1.4 Parameter sweep

We run simulations that vary both planetary rotation rate and obliquity. We vary planetary rotation rate between $1/2 - 2\Omega^*$, where $\Omega^* = \Omega/\Omega_E$ represents a scaling of Earth's rotation rate. To vary obliquity, we change the latitude of maximum surface temperature (ε) in the equilibrium temperature profile in HS and PK simulations, and the latitude of maximum insolation ($\Delta_{\rm sw}$) in F06 simulations. This latitude varies between $0-30°$N at $5°$ intervals for the full HS parameter sweep. A full summary of all simulations run is shown in Table 4.1. A comparison of the zonal-mean zonal wind and overturning circulation for two illustrative

simulations of each model configuration is shown (Fig 4.3), along with the locations of each metric. The prescribed forcings for each experiment in the parameter sweep can be seen in the supplementary materials (Fig C.1).

4.3.2 Calculating metrics for tropical width

The following subsection describes how each metric is calculated and located within this paper, following details given in Adam et al. [2018]. Illustrative examples of the location of each metric are shown in Fig 4.3. For each metric, a smooth quadratic polynomial is fitted to the quantity in the region of the maximum, in order to calculate its latitude at a finer scale than the model resolution, as in Adam et al. [2018]. When calculating the locations of each metric, we found that care must be taken in correctly identifying the STJ and EDJ across the parameter space. The STJ forms in the upper troposphere as a result of angular momentum transport from the tropics via the overturning circulation, whilst the EDJ is driven by the presence of baroclinic eddies. The processes involved in the formation of both jets are not independent: for example, when the STJ is strong, the primary region of baroclinic wave growth coincides with the region of the STJ, leading to approximately colocated jets [Lee and Kim, 2003]. This makes identifying the jets and their driving mechanisms a somewhat complex task.

4.3.2.1 The edge of the Hadley cell

To find the edge of the HC, we must first calculate the mean meridional overturning streamfunction, which is given by:

$$\psi\left(\phi,p\right)=\frac{2\pi r}{g}\cos\phi\int_0^p\bar{v}\left(\phi,p\right)dp, \tag{4.10}$$

where r is planetary radius ($r=6,371$km throughout), g is planetary gravitational acceleration ($g=9.81\text{ms}^{-2}$ throughout) and $\overline{v}$ is zonal-mean meridional wind, in ms^{-1}. We define the edge of the HC to be the latitude at which ψ first decreases below 10% of its maximum

Full	Short	Reference	Rotation rate (Ω^*)	Obliquity (°)
Held-Suarez	HS	Held and Suarez [1994]	$\frac{1}{2}, \frac{5}{8}, \frac{3}{4}, \frac{7}{8}, 1, \frac{5}{4}, \frac{3}{2}, \frac{7}{4}, 2$	0,5,...,30
Polvani-Kushner	PK	Polvani and Kushner [2002]	$\frac{1}{2}, \frac{3}{4}, 1, \frac{3}{2}, 2$	0,5,...,20
Frierson	F06	Frierson et al. [2006]	$\frac{1}{2}, \frac{3}{4}, 1, \frac{3}{2}, 2$	0,5,10,15
Dry-Frierson	DF	Frierson et al. [2006]	$\frac{1}{2}, \frac{3}{4}, 1, \frac{3}{2}, 2$	0,5,10,15

Table 4.1: **Table of simulations in Chapter 4.** Obliquity here means the latitude of the maximum heating (°N) in HS/PK simulations, and the latitude of the maximum insolation (°N) in F06/DF simulations.

tropical value poleward of the equator. On Earth, this crossing typically occurs at around 30°N/S. We calculate this value for both the value of ψ on the 500 hPa level (ψ_{500}) and for the total column integral of ψ (to avoid spurious poleward/equatorward shifts in ϕ_{HC} which are in fact due to vertical variation in the Hadley circulation). We find no qualitative differences in our results, and so we present only the former.

4.3.2.2 The latitude of the eddy-driven jet

The EDJ is a region of strong near-surface westerly winds, and is calculated as the maximum in the zonal-mean zonal wind on the 850 hPa surface (u_{850}). Due to the nature of our parameter sweep, in some simulations multiple maxima in u_{850} of similar magnitude are present in the same hemisphere. In these cases, we discard any jet with mean strength less than 25% of the hemispheric maximum. In any calculations of coupling between metrics, we choose the most poleward jet present, as we find this in all cases to be the strongest jet and to be distinct from the STJ.

4.3.2.3 The latitude of the subtropical jet

There are multiple methods used to locate the subtropical jet, which is characterised by strong upper tropospheric winds generated by angular momentum conservation at the edge of the HC. Here, we find the adjusted upper-tropospheric zonal-mean zonal wind, u_{adj}, where $u_{\mathrm{adj}} = u_{100-400} - u_{850}$ and $u_{100-400}$ is the vertically integrated zonal-mean zonal wind between 400 hPa and 100 hPa. This means that u_{adj} is a measure of vertical shear, which allows us to more clearly separate ϕ_{STJ} from the ϕ_{EDJ} signal, as the location of maximum vertical shear is a natural choice for the location of the subtropical jet [Davis and Birner, 2016]. In a similar vein to ϕ_{EDJ}, we find multiple maxima in u_{adj} for some simulations and in these cases, we take the most equatorward jet (which we find to be distinct from ϕ_{EDJ}, and in all cases the more appropriate jet than any further poleward).

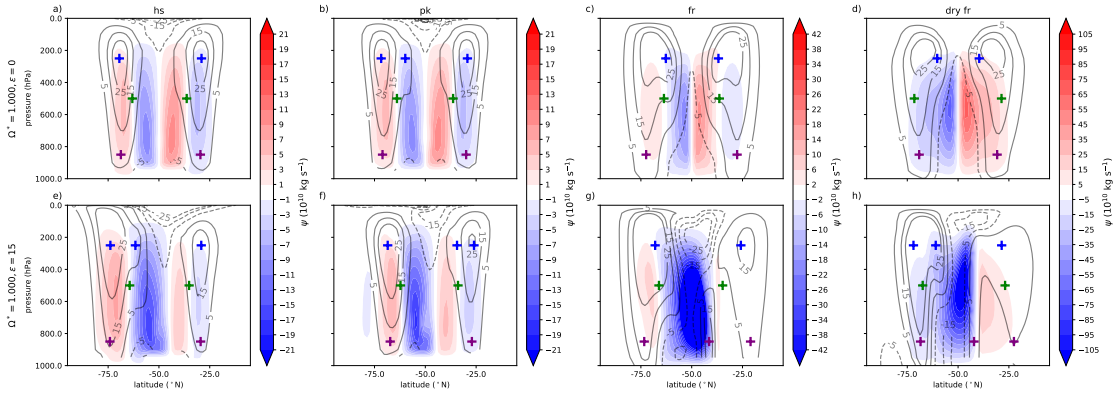

Figure 4.3: **Vertical cross-section of the circulation in some example simulations.** Vertical profile of mean meridional circulation (shading), and zonal mean zonal winds (contours, m s^{-1}). Eight example simulations are shown, with simulation type given in the panel titles, and parameter values given on the left. In each panel, blue markers illustrate maxima in u_{adj}, green show the 10% crossing of the vertically integrated ψ, and purple show maxima in u_{850}. Such maxima/crossings relate to possible locations of the STJ, EDJ, and edge of the HC. In cases where there is more than one maximum in a hemisphere, the most equatorward (poleward) maximum is used for the STJ (EDJ). See text for details. All markers are placed at either the exact altitude at which they are calculated, or at the centre point of the vertical average used.

4.3.2.4 The strength of various quantities

We will also refer to the strength of the quantities defining each metric across our parameter space. These strengths in both hemispheres are defined as follows:

- $\max_{HC}$ (kg s^{-1}): the maximum value of ψ_{500} equatorward of ϕ_{HC}. We take the maximum of the absolute value in each hemisphere to account for the negative sign in the southern hemisphere.

- $\max_{STJ}$ (m s^{-1}): the value of u_{adj} at ϕ_{STJ}, which in most cases is the hemispheric maximum in u_{adj} although these may be distinct where a weaker maximum is separated from the EDJ.

- $\max_{EDJ}$ (m s^{-1}): the value of u_{850} at ϕ_{EDJ}, which in most cases is the hemispheric maximum in u_{850}.

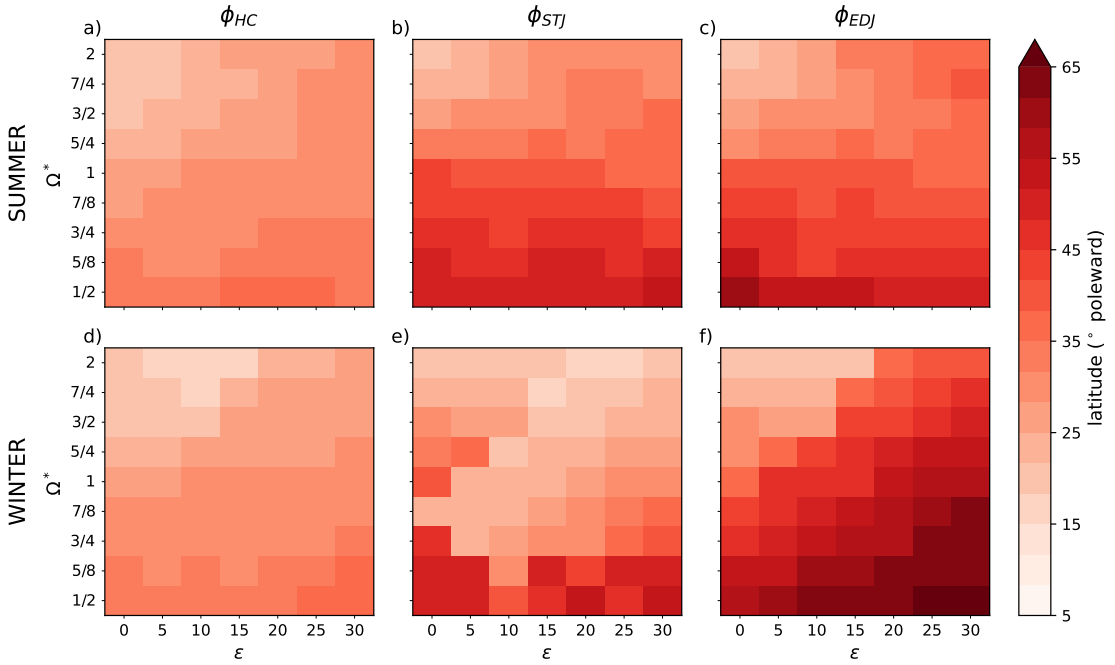

Figure 4.4: **The influence of obliquity and rotation rate on the mean location of each metric.** The mean location of each metric (left: ϕ_{HC}; centre: ϕ_{STJ}; right: ϕ_{EDJ}), in the summer and winter hemisphere (top and bottom row, respectively). In each panel, one square represents one HS simulation, with obliquity and rotation rate on the x- and y-axis, respectively.

4.4 Results in dry simulations

To investigate the relationships between metrics, we first consider only the dry HS simulations, although comparisons to the PK simulations will be made, and figures shown in Appendix C. This is to isolate the impacts of changing only rotation rate, obliquity, and stratospheric profile. Results from the grey model will be presented in Section 4.5.

4.4.1 Results in the time-mean

We consider first the change in mean latitude of each metric with changing rotation rate and obliquity in HS simulations (Fig 4.4). In the winter hemisphere, ϕ_{HC} and ϕ_{EDJ} both lie further poleward with decreasing rotation rate and increasing obliquity (Fig 4.4 d,f). ϕ_{EDJ}

is the most sensitive (in the winter hemisphere) in the time-mean to changes in rotation rate and obliquity, moving from ~ 10°S to ~ 60°S over the parameter space. There is a particularly abrupt jump from fast-rotating and low-obliquity simulations to the rest of the parameter space (Fig 4.4 f). ϕ_{STJ} is less dependent on obliquity, but does generally move further poleward with decreasing rotation rate. At the lowest rotation rates, there is no clear dependency of ϕ_{STJ} on obliquity. There is a distinct region of the parameter space (at low obliquity and faster rotation rates) that sees particularly equatorward ϕ_{HC} and ϕ_{EDJ}, and somewhat more poleward ϕ_{STJ}. We note that the benchmark HS simulation ($\Omega^* = 1, \varepsilon = 0$) lies on the boundary of this region.

In the summer hemisphere, ϕ_{STJ} shifts poleward with both increasing obliquity or decreasing rotation rate. ϕ_{HC} responds similarly, although with less overall shift (~ 10° less shift than ϕ_{STJ} over the whole parameter space). The mean latitude of the summer hemisphere EDJ depends more strongly on rotation rate than on obliquity, with some small obliquity dependence at rotation rates $\Omega^* > 1$.

The addition of the PK stratosphere has limited effect on the mean location of ϕ_{HC}, ϕ_{STJ}, and ϕ_{EDJ} (Fig C.2). In particular, ϕ_{HC} is least influenced by this addition, although ϕ_{STJ} and ϕ_{EDJ} might be moved by over 18° equatorward or poleward dependent on the emergence of a second maximum in either u_{adj} or u_{850} (Fig C.3). There is again a region of the parameter space ($\Omega^* = 3/4 - 1$) where there are sharp transitions in the location of the STJ with increasing obliquity, due to the emergence of a second jet in some of these scenarios. The STJ lies noticeably poleward when $\Omega^* = 1/2$, with obliquity having little influence at this slower rotation rate. Nevertheless, overall we see a similar response to increasing obliquity or rotation rate.

We now plot the strength of the quantities defining each metric in the time-mean. As predicted by axisymmetric theory and in agreement with the simulations of Walker and Schneider [2006], we see that the strength of the HC in the winter hemisphere HS simulations increases with increasing obliquity or decreasing rotation rate (Fig 4.5 d). We

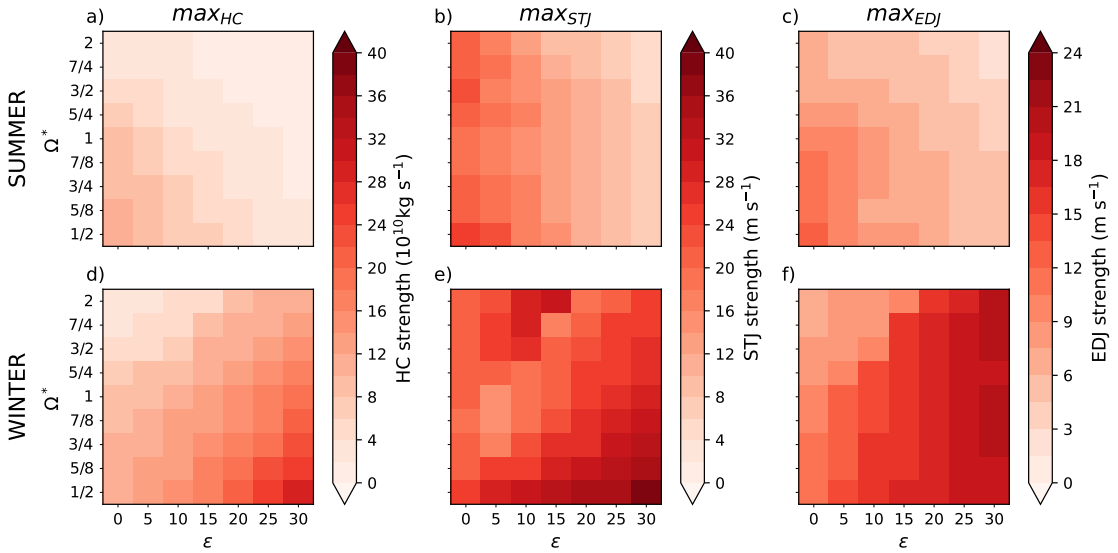

Figure 4.5: **The influence of obliquity and rotation rate on the mean strength of the quantity defining each metric.** As in Figure 4.4, except we show the mean strength of the quantities used to define each metric. The definitions of these strengths are given in the text.

also see that the strength of the subtropical jet increases with increasing obliquity when $\Omega^* \leq 1$, but varies non-linearly with obliquity when $\Omega^* > 1$ (Fig 4.5 e). For $\Omega^* > 1$, $\max_{STJ}$ reaches a maximum between $\varepsilon = 5 - 15°$, at which point it drops rapidly before beginning to increase once more. There is a particularly distinct transition at high rotation rates ($\Omega^* > 1.5$). We observe that $\max_{EDJ}$ also undergoes a distinct transition across this same region of parameter space, increasing in strength as either obliquity increases or rotation rate decreases (Fig 4.5 f). The strength of all metrics decreases in the summer hemisphere when rotation rate or obliquity increases (Fig 4.5 a-c), and in all cases is weaker than its winter hemisphere counterpart.

The PK stratosphere does not significantly influence the strength of these quantities: the overall response to changing obliquity or rotation rate is the same in PK and HS simulations (Fig C.4). However, the strength of the STJ is somewhat weakened for intermediate values of Ω^* in PK simulations, where there are two maxima in u_{adj}.

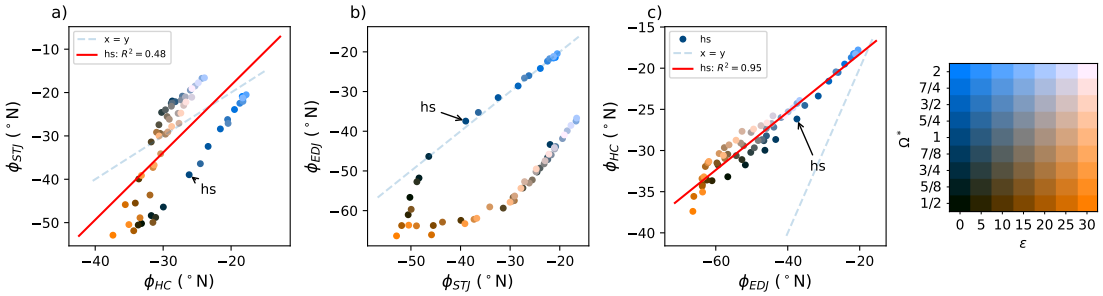

Figure 4.6: **The relative latitudes of each metric.** The mean latitude of each metric in the SH plotted against the mean latitude of other metrics. Results shown for HS simulations and the benchmark $\Omega^* = 1, \varepsilon = 0$ simulation is indicated. Markers are coloured according to the simulation's location in parameter space and, where appropriate, a linear regression is calculated (red) and its score is shown. A 1:1 line is also plotted in each panel (dashed grey).

We now consider how the mean latitudes of each metric (in the southern/winter hemisphere) compare with each other when parameter values are changed (Fig 4.6).

We see a clear linear relationship between ϕ_{HC} and ϕ_{EDJ}, with slow-rotating high-obliquity planets having both metrics the furthest poleward, shifting equatorward with increasing rotation rate or decreasing obliquity (Fig 4.6 c). The EDJ moves equatorward more rapidly than ϕ_{HC} with these changes in planetary parameters, starting at $\sim 70°$ at high obliquity/slow rotation rate but reaching $\sim 20°$ at its most equatorward. The relationship between ϕ_{STJ} and both ϕ_{HC} and ϕ_{EDJ} is more complex, appearing to take one of two different pathways depending on parameter values, despite an overall tendency to lie further equatorward with increasing rotation rate. ϕ_{STJ} and ϕ_{EDJ} are almost colocated in the slow-rotating and low-obliquity region of parameter space, with their mean latitudes changing at the same rate with changing parameter values (Fig 4.6 b, upper branch). On the alternate branch, the STJ shifts equatorward more rapidly with increasing rotation rate (Fig 4.6 b, lower branch). Similarly, ϕ_{STJ} shifts equatorward more rapidly than ϕ_{HC} in the high obliquity planets (Fig 4.6 a, upper branch), but again the parameter space may be split into two different regimes.

Interestingly, the inclusion of the PK stratosphere may force a simulation to switch from one branch to the other (e.g. in the $\Omega^* = 1, \varepsilon = 0$ case, where ϕ_{STJ} shifts from $\sim 40°$S to $\sim 20°$S with the inclusion of the PK stratosphere), but appears to still follow the same branched pattern (Fig C.5).

4.4.2 Metric variability and their relationships

Having considered the mean locations of each metric, we now turn our attention to how well the three metrics are coupled throughout the season, and what influences these relationships. We focus particularly on the winter hemisphere in this section, although summer hemisphere connections are discussed briefly.

There are positive correlations across broad regions of the parameter space in both the winter and summer hemispheres for the HS simulations, but that these may become negative at certain values (Fig 4.7). In the summer hemisphere (Fig 4.7 a-c), correlations are positive and significant across the majority of the parameter space for all metrics. In the winter hemisphere (Fig 4.7 d-f), however, the sign of the correlation between metrics depends more strongly on the region of parameter space in which the simulation lies. At fast rotation rates, metrics are broadly well-correlated, particularly at low values of ε. However, at slower rotation rates or high obliquities, ϕ_{HC} can become anti-correlated with ϕ_{STJ} and ϕ_{EDJ}. At the very least, the strength of the coupling between metrics tends to decrease away from the region of fast-rotating low-obliquity planets. This suggests that the positive correlation between ϕ_{HC} and ϕ_{STJ} seen in HS simulations of the Earth's atmosphere is somewhat sensitive to the specific planetary parameters chosen.

Obliquity appears to have a less substantial impact when a PK stratosphere is included (Fig C.6). In the winter hemisphere, we note that ϕ_{HC} and ϕ_{STJ} remain positively coupled across the parameter space, and ϕ_{EDJ} can become decoupled from ϕ_{HC} and ϕ_{STJ} at the slowest rotation rate simulated. However, the strongest positive correlations in the winter hemisphere remain between ϕ_{STJ} and ϕ_{EDJ} at fast rotation rates and low obliquity.

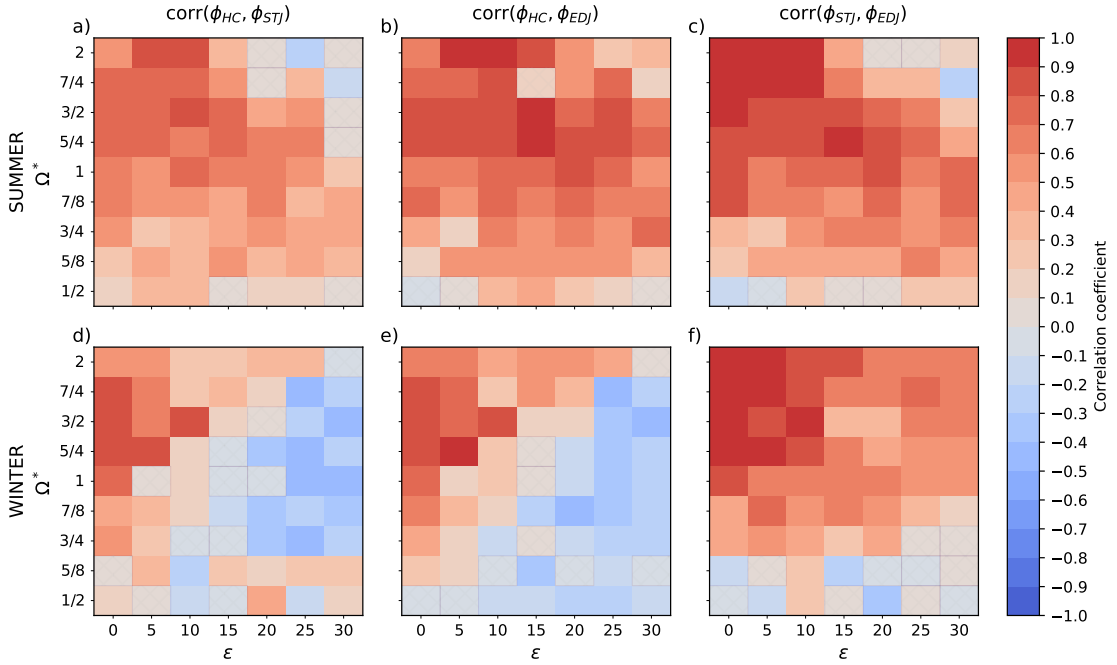

Figure 4.7: **The influence of obliquity and rotation rate on the coupling between each metric.** The Pearson correlation coefficient (colour) between metrics (left: ϕ_{HC} and ϕ_{STJ}; centre: ϕ_{HC} and ϕ_{EDJ}; right: ϕ_{STJ} and ϕ_{EDJ}), in the summer and winter hemisphere (top and bottom row, respectively). In each panel, one square represents one HS simulation, with obliquity and rotation rate on the x- and y-axis, respectively. Squares are hatched where the relationship between the two metrics is not significant (p-value greater than 0.01).

By visualising the coupling between metrics as a function of the mean latitude of each metric (Fig 4.8, considering now the winter hemisphere only), we see that correlations generally become stronger and more positive as all metrics shift equatorward in our HS simulations, although this relationship is most clear with ϕ_{EDJ}. The most equatorward (and thus most strongly-coupled) metrics tend to be those that are in the fast-rotating and low-obliquity region of the parameter space. However, it appears difficult to categorise the coupling between ϕ_{STJ} and ϕ_{HC} according to the mean latitude of either one of these metrics. For example, they show a particularly broad range in correlation coefficients ($\sim -0.5 - 0.8$) when ϕ_{STJ} lies in the midlatitudes (Fig 4.8 b). The same results appear to hold for PK simulations also (Fig C.7).

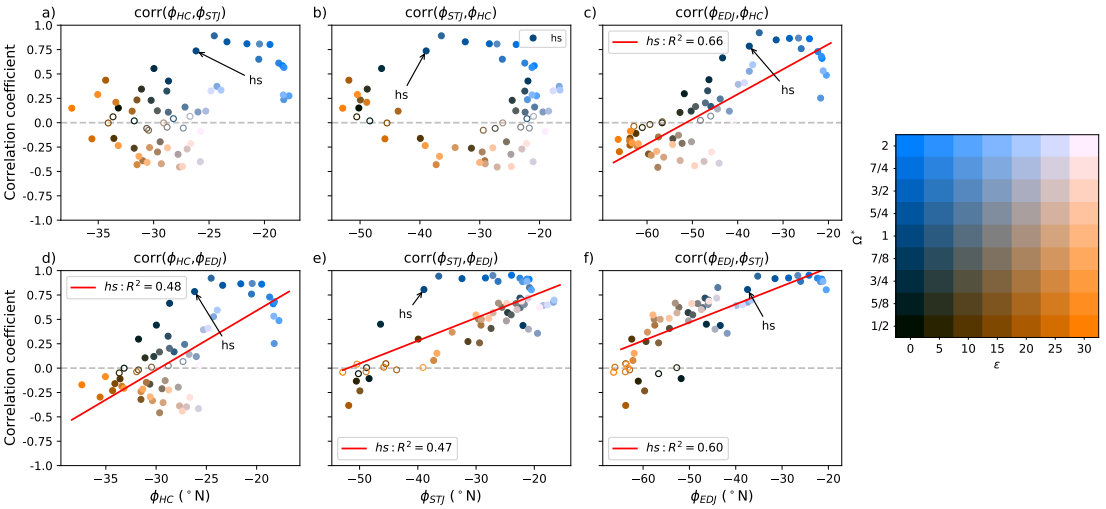

Figure 4.8: **The influence of a metric's mean location on its coupling with other metrics.** The Pearson correlation coefficient between metrics as a function of each metric's mean latitude in the winter (southern) hemisphere (left: as a function of ϕ_{HC}; centre: as a function of ϕ_{STJ}; right: as a function of ϕ_{EDJ}). Results shown for HS simulations and the benchmark $\Omega^* = 1, \varepsilon = 0$ simulation is indicated. Markers are coloured according to the simulation's location in parameter space, and are solid where the relationship between the two metrics has p-value less than 0.01. Where appropriate, linear regressions have been fitted simulations and their scores shown.

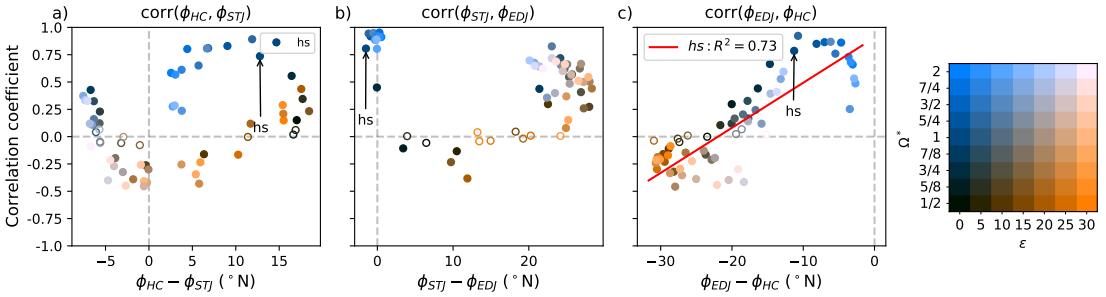

Figure 4.9: **The influence of the separation in mean location of two metrics on their coupling.** The Pearson correlation coefficient between two metrics as a function of the separation between them in the winter (southern) hemisphere (left: as a function of ϕ_{HC}-ϕ_{STJ}; centre: as a function of ϕ_{STJ}-ϕ_{EDJ}; right: as a function of ϕ_{EDJ}-ϕ_{HC}). Results shown for HS simulations and the benchmark $\Omega^* = 1, \varepsilon = 0$ simulation is indicated. Markers are coloured according to the simulation's location in parameter space, and are solid where the relationship between the two metrics has p-value less than 0.01. Where appropriate, linear regressions have been fitted and their scores shown.

We can also consider how the relationship between two of the three metrics varies according to the separation between them (Fig 4.9). There is a clear positive relationship between ϕ_{EDJ} and ϕ_{HC} in that the closer they lie to each other, the more well coupled they are (Fig 4.9 c). ϕ_{HC} and ϕ_{EDJ} are most separated at slow rotation rate and high obliquity, and it is here where they are weak-to-negatively coupled. The other relationships are not so straightforward. ϕ_{STJ} and ϕ_{EDJ} are positively correlated when they lie within 5° of each other, with the strongest coupling being those simulations at high rotation rates and low obliquity (Fig 4.9 b). This suggests that there is no distinct STJ in this region of parameter space, and that zonal mean wind maximum extends throughout the troposphere. When obliquity is increased, the separation between ϕ_{STJ} and ϕ_{EDJ} jumps to around 20° (as a second maximum in u_{adj} develops), but the metrics remain well correlated despite their separation. As rotation rate is decreased however, the coupling between the two jets tends to weaken, regardless of their separation.

Finally, the coupling between ϕ_{HC} and ϕ_{STJ} shows a distinct nonlinear relationship with the separation between these two metrics (Fig 4.9 a). A simulation with ϕ_{HC}-ϕ_{STJ}=5° could have a correlation coefficient of ~ -0.25 or of $\sim +0.75$. However, it is possible to predict the correlation and/or separation between the two metrics based on location in the parameter space, suggesting that this is a more important factor in understanding the coupling between ϕ_{HC} and ϕ_{STJ}. For example, high obliquity and high rotation rate simulations tend to have ϕ_{STJ} lying slightly equatorward of ϕ_{HC}, with the two being negatively correlated. As rotation rate is decreased from here, the coupling remains weak and negative but the STJ begins to move further poleward of the HC. From here, as obliquity is then decreased, the coupling strengthens and becomes positive but separation remains at roughly $10-15°$. Finally, as rotation rate is again increased, separation between the metrics decreases to around 5°, but their coupling remains strong and positive.

The addition of the PK stratosphere does not substantially influence the results based on metric separation (Fig C.8). ϕ_{EDJ} and ϕ_{HC} become more well-coupled the closer they lie,

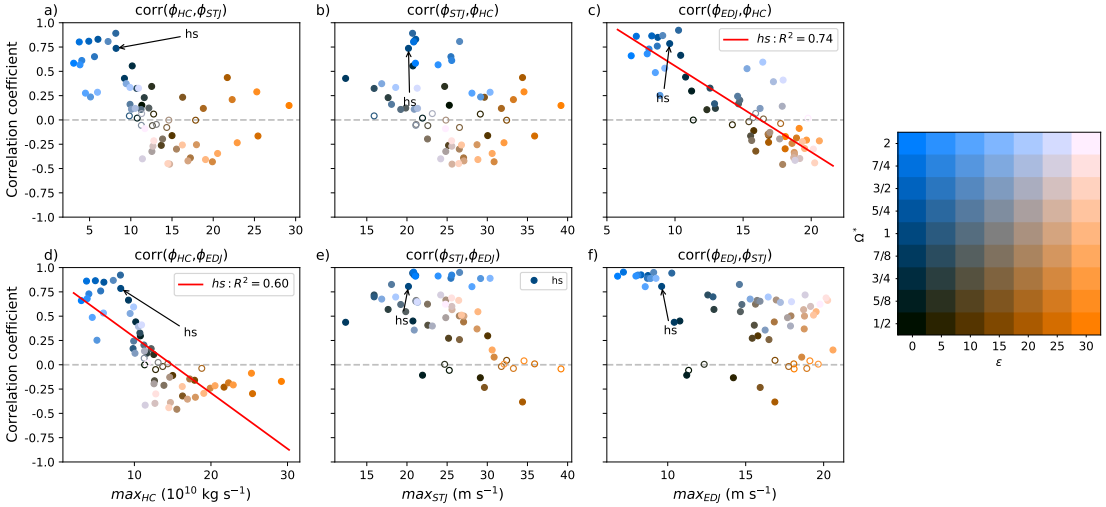

Figure 4.10: **The influence of the mean strength of the quantity defining each metric on its coupling with other metrics.** As in Figure 4.8, except showing correlation coefficient between metrics as a function of the strength of the quantity defining each metric.

ϕ_{STJ} and ϕ_{EDJ} are well-coupled when they are colocated and when they lie $\sim 20^{\circ}$ separate. ϕ_{HC} and ϕ_{STJ} follow the same pattern as in HS simulations, although are always positively correlated.

Given that the mean latitude and separation of the metrics does not fully allow us to quantify the correlation between metrics, we also investigate their dependence on the mean strength of ψ, u_{adj}, and u_{850}. All metrics become less strongly coupled as each metric strengthens in the HS simulations (Fig 4.10). Simulations with strong jets or a particularly strong overturning circulation are generally slow-rotating and high obliquity, and have weak-negative correlations between metrics (except for ϕ_{EDJ} and ϕ_{STJ}, which are weakly positively correlated with a strong EDJ or STJ). The relationship between ϕ_{HC} and ϕ_{EDJ} or ϕ_{STJ} decreases with increasing strength of the HC, although for ϕ_{EDJ} this appears to saturate once the strength of the HC reaches around 15×10^{10}kg s^{-1}. Adding the PK stratosphere does little to influence these results (Fig C.9).

Overall, we do note that the inclusion of a PK stratosphere does not tend to influence

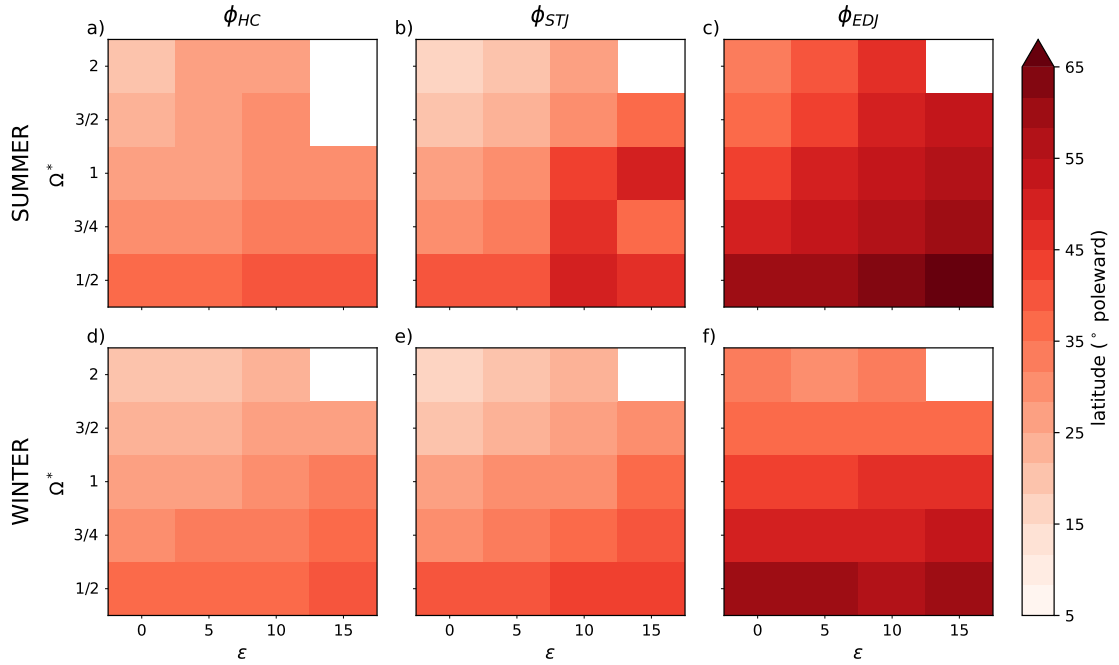

Figure 4.11: **The influence of obliquity and rotation rate on the mean location of each metric in the moist model.** The mean location of each metric (left: ϕ_{HC}; centre: ϕ_{STJ}; right: ϕ_{EDJ}), in the summer and winter hemisphere (top and bottom row, respectively). In each panel, one square represents one F06 simulation, with obliquity and rotation rate on the x- and y-axis, respectively.

the metrics and their couplings. While we may see significant differences in the mean latitude of, for example, ϕ_{HC} in the HS and PK benchmark simulations, PK simulations do not deviate from the relationships that we have found (Figs C.7, C.8). The exception to this is coupling dependency on mean metric strength, wherein we find that ϕ_{EDJ} is perhaps more strongly coupled with ϕ_{HC} given a strength of HC compared to HS simulations (Fig C.9).

4.5 Results in the grey model

4.5.1 Results in the time-mean

The response of the mean latitude and strength of each metric in response to changing obliquity or rotation rate is broadly the same in the moist grey model (F06; Figure 4.11) and dry grey model (DF; C.10) as in the benchmark HS model. DF model results are included in the appendix, and we discuss F06 results here. Overall there is a poleward shift in each metric with decreasing rotation rate or increasing obliquity in the F06 simulations. This occurs in either hemisphere, with the strongest response again being from ϕ_{EDJ} (Figure 4.11 c, f), and again we see a weak response to obliquity at low rotation rates from ϕ_{STJ}, particularly in the summer hemisphere (Figure 4.11 b). We note that the HC extends further poleward in DF simulations than F06 (particularly at low obliquity in the winter hemisphere; Figs C.10, C.11), although the response to changing parameters remains similar overall. The STJ and EDJ generally lie equatorward in DF compared to F06 simulations (with this effect seen more strongly at higher obliquity).

F06 simulations show a general decrease in the strength of the quantities defining each metric in the summer hemisphere with increasing rotation rate or obliquity (Figure 4.12 a-c). In the winter hemisphere, the HC and STJ tend to strengthen with decreasing rotation rate, whereas the EDJ weakens. All quantities strengthen with obliquity. We note also that the overturning circulation and EDJ tend to be stronger in the dry grey DF simulations (Fig C.12), although STJ strength is less influenced.

The relationships between the mean latitudes of all metrics in F06 simulations look qualitatively different to the HS simulations (Fig 4.13, triangular markers compared to circular), save for the relationship between ϕ_{HC} and ϕ_{EDJ}, which in both cases shows a clear 1-1 link between the two, and indeed both ϕ_{EDJ} and ϕ_{HC} lie at approximately the same latitudes in HS and F06 simulations. However, there is also a clear 1-1 relationship between ϕ_{STJ} and $\phi_{\mathrm{HC}}/\phi_{\mathrm{EDJ}}$ in our F06 simulations which was not present in the HS simulations

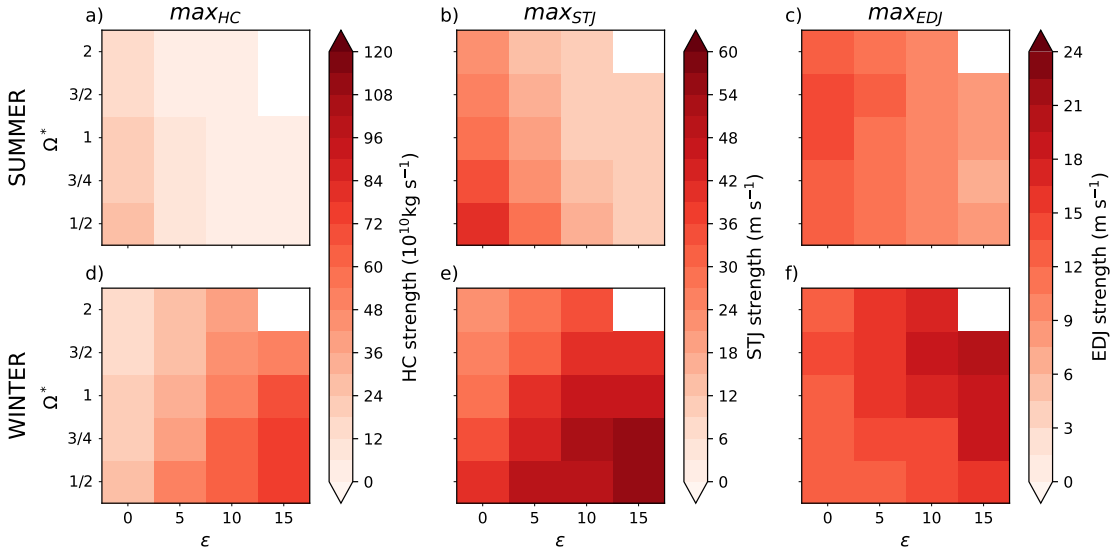

Figure 4.12: **The influence of obliquity and rotation rate on the mean strength of the quantity defining each metric in the moist model.** As in Figure 4.11, except we show the mean strength of the quantities used to define each metric. The definitions of these strengths are given in the text.

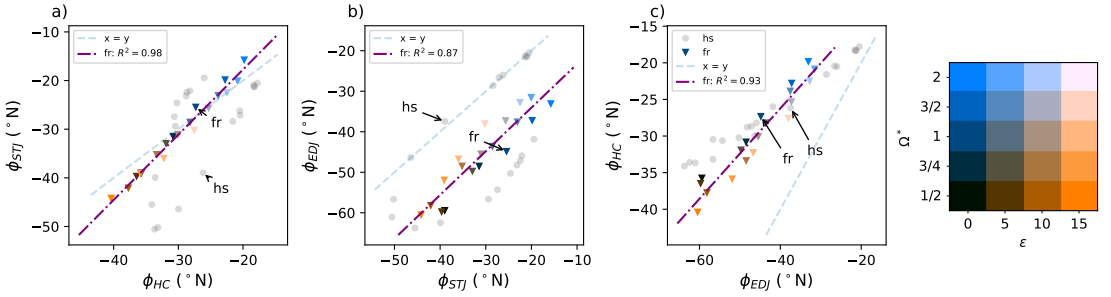

Figure 4.13: **The relative latitudes of each metric in the moist model.** The mean latitude of each metric plotted against the mean latitude of other metrics. Triangular markers show moist F06 simulations. F06 markers are coloured according to the simulation's location in parameter space and, where appropriate, a linear regression is calculated (purple dash-dotted) and its score is shown. A 1:1 line is also plotted in each panel (dashed grey), and HS simulations are shown in grey (circular) for comparison. Simulations with $\varepsilon = 0$ are indicated.

(Fig 4.13 a, b, purple dash-dotted line), and no branching is displayed. Again, we see that ϕ_{EDJ} and ϕ_{STJ} move equatorward at approximately the same rate with increasing rotation rate (or decreasing obliquity), although in the F06 simulations, ϕ_{EDJ} always lies poleward of ϕ_{STJ}, whereas in the HS simulations they may be colocated for some of the parameter space. ϕ_{HC} and ϕ_{STJ} are actually colocated in the F06 simulations instead, and respond to changes in parameter values in a similar manner.

As noted, DF simulations tend to have a more poleward-lying HC. However, the removing moist effects from the grey model fundamentally alters the relationship between ϕ_{HC} and the jets: in DF simulations, ϕ_{HC} and ϕ_{EDJ} are approximately colocated but this is not the case in the moist simulations (Fig C.13).

4.5.2 Metric variability and their relationships

Considering the coupling between metrics across the parameter space, the picture is somewhat different in our moist simulations to the HS. We note that there are more positive (albeit generally weaker) couplings in the winter hemisphere than in the HS results, particularly ϕ_{HC} with ϕ_{STJ} and ϕ_{EDJ}. We see the known result that ϕ_{HC} and ϕ_{STJ} are less strongly coupled in the benchmark F06 simulation. However, ϕ_{HC} and ϕ_{STJ} remain positively coupled across much of the parameter space in the winter hemisphere, in contrast to HS simulations.

However, we do note that in the dry grey model, ϕ_{HC} and ϕ_{STJ} in the winter hemisphere are in fact decoupled for much of the parameter space (Fig C.14 d). They are positively coupled in the region of parameter space with fast-rotating low-obliquity planets, but generally negatively coupled otherwise. We note that ϕ_{STJ} and ϕ_{EDJ} are always positively correlated in DF simulations (Fig C.14 f). These differences suggest that perhaps it is the grey radiation scheme that leads to the general pattern of positive correlation between ϕ_{HC} and ϕ_{STJ}, and that the decoupling at lower rotation rates or higher obliquities also seen in HS simulations may be a robust response in these two dry models, with moist effects

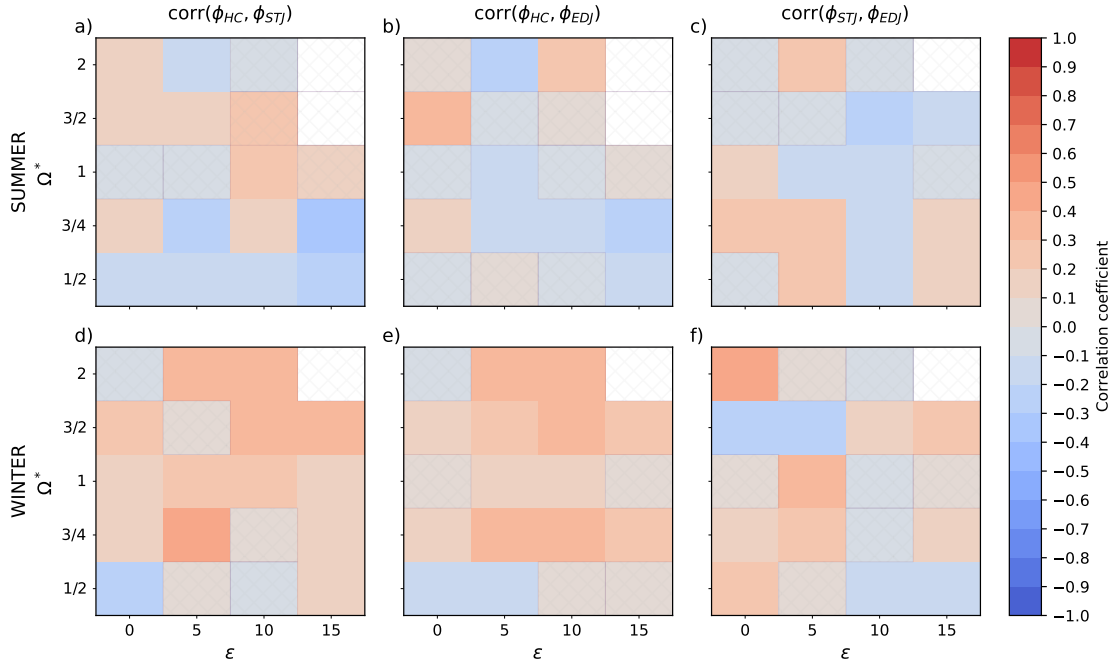

Figure 4.14: **The influence of obliquity and rotation rate on the coupling between each metric in the moist model.** The Pearson correlation coefficient (colour) between metrics (left: ϕ_{HC} and ϕ_{STJ}; centre: ϕ_{HC} and ϕ_{EDJ}; right: ϕ_{STJ} and ϕ_{EDJ}), in the summer and winter hemisphere (top and bottom row, respectively). In each panel, one square represents one F06 simulation, with obliquity and rotation rate on the x- and y-axis, respectively. Squares are hatched where the relationship between the two metrics is not significant (p-value greater than 0.01).

mitigating.

The only noticeable relationship with mean latitude is between ϕ_{EDJ} and ϕ_{HC}, which also sees stronger coupling for a more equatorward EDJ (Fig 4.15). However, the relationships between all other metrics do not have any strong dependence on the mean latitude of each metric, and most correlations are not statistically significant and weaker in general than those seen in HS simulations. This is not the case in DF simulations: correlations between ϕ_{EDJ} and ϕ_{STJ} are stronger when moist effects are removed (Fig C.15), although there is no clear increase in this coupling as the mean latitude of either metric changes.

There appears to be no significant relationship between the separation between metrics and their covariability in the moist F06 simulations (Fig 4.16, triangular markers). ϕ_{HC}

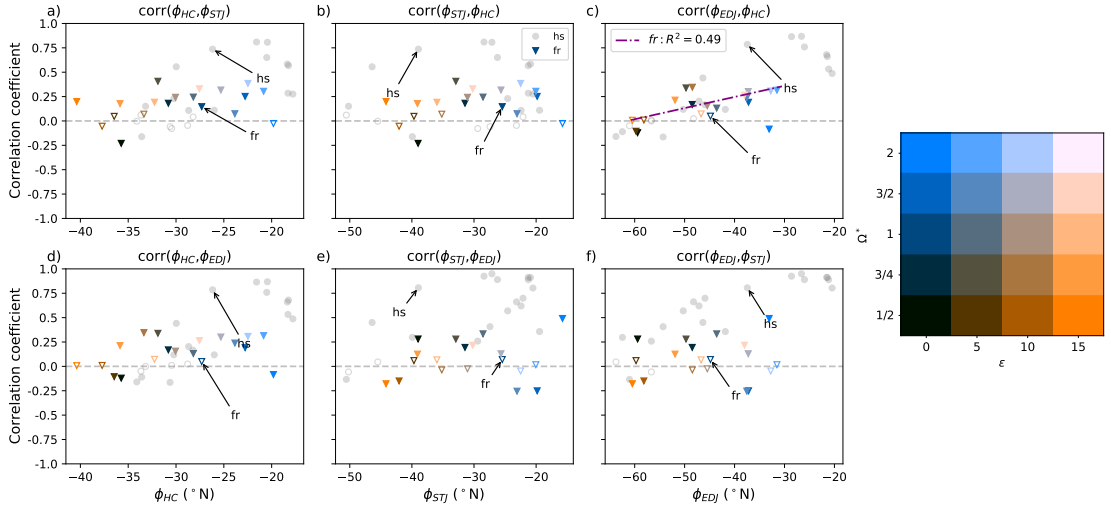

Figure 4.15: **The influence of a metric's mean location on its coupling with other metrics in the moist model.** The Pearson correlation coefficient between metrics as a function of each metric's mean latitude in the winter (southern) hemisphere (left: as a function of ϕ_{HC}; centre: as a function of ϕ_{STJ}; right: as a function of ϕ_{EDJ}). Triangular markers show F06 simulations and circular markers represent HS simulations. Simulations with $\varepsilon = 0$ are indicated. F06 markers are coloured according to the simulation's location in parameter space, and are solid where the relationship between the two metrics has p-value less than 0.01. Where appropriate, linear regressions have been fitted and their scores shown.

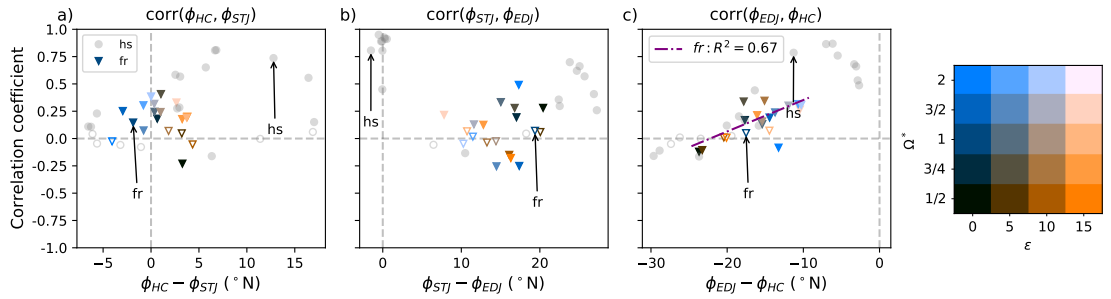

Figure 4.16: **The influence of the separation in mean location of two metrics on their coupling in the moist model.** The Pearson correlation coefficient between two metrics as a function of the separation between them in the winter (southern) hemisphere (left: as a function of ϕ_{HC}-ϕ_{STJ}; centre: as a function of ϕ_{STJ}-ϕ_{EDJ}; right: as a function of ϕ_{EDJ}-ϕ_{HC}). Triangular markers show F06 simulations and circular markers represent HS simulations. Simulations with $\varepsilon = 0$ are indicated. F06 markers are coloured according to the simulation's location in parameter space, and are solid where the relationship between the two metrics has p-value less than 0.01. Where appropriate, linear regressions have been fitted and their scores shown.

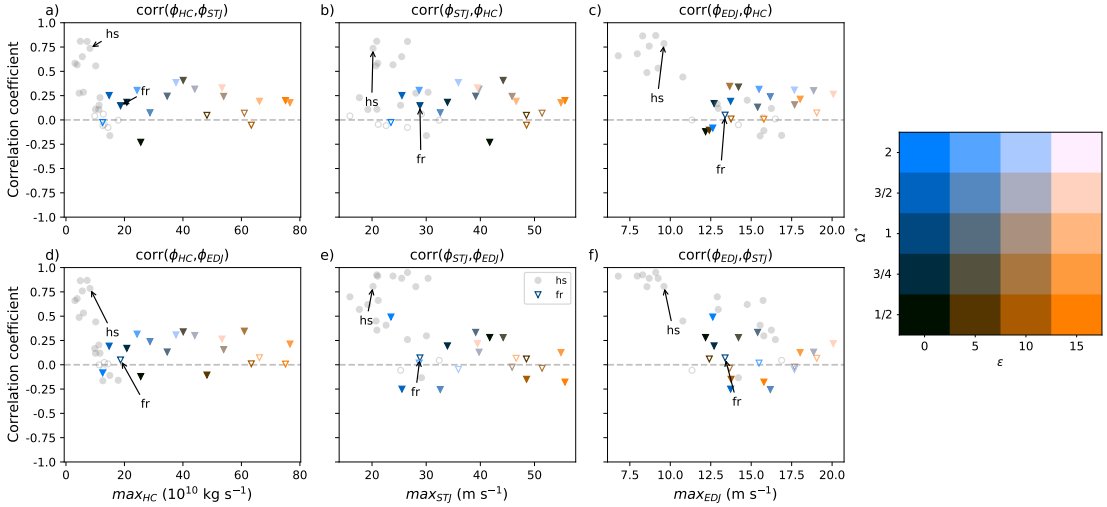

Figure 4.17: **The influence of the mean strength of the quantity defining each metric on its coupling with other metrics.** As in Figure 4.15, except showing correlation coefficient between metrics as a function of the strength of the quantity defining each metric.

and ϕ_{STJ} are approximately colocated for all parameter values (with maximum separation $\sim \pm 5^{\circ}$) and relatively weak correlation throughout (maximum correlation coefficients of $\sim \pm 0.4$). The STJ lies $\sim 10-20^{\circ}$ equatorward of the EDJ in all F06 simulations, but there is no strong coupling or anti-coupling between the two in any situation. ϕ_{HC} is always equatorward of ϕ_{EDJ}, and there is a weak increase in covariability with decrease in separation between the two. Of note is the fact the coupling between metrics in our moist simulations according to metric separation is not significantly altered from the pattern seen in the HS simulations, regardless of location in parameter space. That is to say, an F06 simulation with separation ϕ_{HC}-ϕ_{STJ}=0°, for example, has approximately the same correlation between these two metrics as a HS simulation with the same separation, regardless of the parameter values needed to obtain such a separation. The picture is different in DF simulations: ϕ_{STJ} once again lies equatorward of ϕ_{EDJ} in all simulations but with substantially stronger coupling. ϕ_{HC} is generally decoupled with the two jets in all simulations (Fig C.16).

Correlations in the moist F06 simulations overall have much less dependence on the strength of the quantities defining our metrics than in HS simulations. Generally speaking, the overturning circulation and the subtropical jet are stronger in F06 simulations than in HS, while correlations remain weak across the parameter space (Fig 4.17). In DF simulations, the overturning circulation is stronger again (Fig C.17a,d) with no clear influence on coupling. However, we note that the coupling between ϕ_{EDJ} and ϕ_{STJ} increases with both the strength of the STJ and the strength of the EDJ (Fig C.17e,f).

4.6 Discussion

Multiple studies have found scaling laws relating the location of the ascending or descending branch of the Hadley circulation with rotation rate. Under the small-angle approximation, Held and Hou [1980] showed that ϕ_{HC} scales like $\phi_{\mathrm{HC}} \sim \Omega^{-1}$ in the axisymmetric case, where Ω is planetary rotation rate. Recent work has shown that in an idealised aquaplanet GCM with varying planetary rotation rate and seasonality, the winter descending branch of the solsticial, cross-equatorial HC scales as approximately $\Omega^{-1/2}$ [Hill et al., 2022]. Walker and Schneider [2006] performed simulations using a an eddy-permitting model and its off-equatorial heating extension to find relationships between the extent and strength of the Hadley circulation as a function of rotation rate and latitude of maximum heating. They found an approximate power law relationship between the strength of the HC ($\max_{HC} \sim \varepsilon^{1/3}$ for $\varepsilon < 16°$, or $\max_{HC} \sim \varepsilon^{4/3}$ for $16° < \varepsilon < 50°$), where ε is the latitude of maximum heating. Additionally, they showed that ϕ_{HC} scales like $\Omega^{-1/5}$ ($\Omega^{-1/3}$) for smaller (larger) rotation rates when $\varepsilon = 0$. Similarly, the strength of the overturning circulation scales as $\Omega^{-1/3}$ ($\Omega^{-2/3}$) for smaller (larger) rotation rates.

Broadly speaking, in our dry HS simulations all metrics in the winter hemisphere follow a similar pattern under a simultaneous increase in obliquity and decrease in rotation rate. In the time-mean, they shift further poleward, and the quantities used to

define them strengthen, consistent with the theory presented in Held and Hou [1980]. Furthermore, ϕ_{HC} follows the same approximate power laws when $\varepsilon = 0$ obtained by Walker and Schneider [2006] (not shown). In doing so, the coupling between them tends to weaken, potentially becoming negative in some simulations. This reflects the results of Menzel et al. [2021], who found that disconnect between ϕ_{HC} and ϕ_{STJ} was possible in a dry model with Newtonian relaxation to a zonally-symmetric temperature profile, dependent on the temperature profile chosen. Here, we find that disconnect at slow rotation rates and high obliquity.

A further point to note is that the addition of a PK stratosphere does not significantly influence the correlation coefficient between two metrics (in the winter hemisphere) when considered as a function of either their latitude or their separation (Figs C.7, C.8). However, in the PK $\Omega^* = 1$, $\varepsilon = 20$ simulation, ϕ_{HC} is much more strongly correlated with ϕ_{STJ} and ϕ_{EDJ} than one might expect in the equivalent HS case for the calculated strength of the overturning circulation (Figure C.9). Overall, adding the PK stratosphere can indeed shift the mean location of a metric, but the coupling that that metric experiences in its new location is not substantially changed from a HS simulation that has metrics located approximately

The most complex response to increasing obliquity and decreasing rotation rate is in the winter hemisphere STJ, which experiences an abrupt shift equatorward with increasing obliquity for high enough rotation rates ($\Omega^* > 3/4$), before drifting poleward again. This is due to the emergence of a second maximum in u_{adj} at lower latitudes which is distinct from the EDJ, and might be thought of as the more classical STJ. This is consistent with previous work that has found that the subtropical and eddy-driven jets may appear merged in simulations with an Earth-like rotation rate, but are clearly separable at faster rotation rates [Kaspi and Showman, 2015]. In precisely those simulations that have the second subtropical jet, the eddy-driven jet merges from two weaker jets into one stronger jet. We therefore can separate the parameter space into approximately three regimes:

those simulations with one EDJ and one STJ (generally high obliquity, low rotation rate; hereafter 1E1S), those with two EDJ and one STJ (generally those with mid-fast rotation rates and high obliquity; hereafter 2E1S), and those with one EDJ and two STJ (generally those with fast rotation rate and low obliquity; hereafter 1E2S). Those simulations with negative correlations between the edge of the Hadley cell and either the subtropical or eddy-driven jet primarily lie in the 1E1S regime. The strongest positive relationships tend to occur in the 2E1S regime. The sudden jump in the strength of both u_{850} and u_{adj} (Fig 4.5 e, f) corresponds to a regime shift from 2E1S to 1E2S (Fig 4.18). Simulations in 2E1S always lie on the upper branch of ϕ_{HC}-ϕ_{STJ} space (Fig 4.4 a) and the lower branch of ϕ_{EDJ}-ϕ_{STJ} space (Fig 4.4 b). This characterisation captures the circulation expected when $\Omega^* = 1, \varepsilon = 0$ (i.e. the Earth-like base case), with this simulation belonging in 1E1S in all model configurations save PK (which sees the emergence of a weak second maximum in u_{adj}). On Earth, we do see in general one maximum in u_{adj} and one in u_{850}, although this can depend on whether the STJ and EDJ are clearly distinct (which may lead to two maxima in u_{adj}).

Quantifying the parameter space in this way allows us to reconsider the changes in strength of the quantities defining the metrics, changes in metric latitude, and separation. We note that there is a large (smaller) poleward shift in winter hemisphere EDJ (HC edge) latitude in the transition from the 2E1S to the 1E2S region, and that the STJ is particularly equatorward in the 1E2S region (Fig 4.4). The most poleward STJs lie in the 1E1S region of the parameter space, noticeably lying significantly poleward of the more oblique simulations when $\varepsilon = 0$ for $\Omega^* \leq 1$. The classical HS simulation with $\varepsilon = 0$ sits at the boundary of these two regions (Fig 4.18 e). We also see large changes in the strength of ψ, u_{adj}, and u_{850} across these boundaries (Fig 4.5 d-f). The particularly sharp transition between the 2E1S and 1E2S regimes in terms of metric latitude and strength suggests there may be some intermediate simulations in which rapid transitions from a double- to single-jet structure may occur.

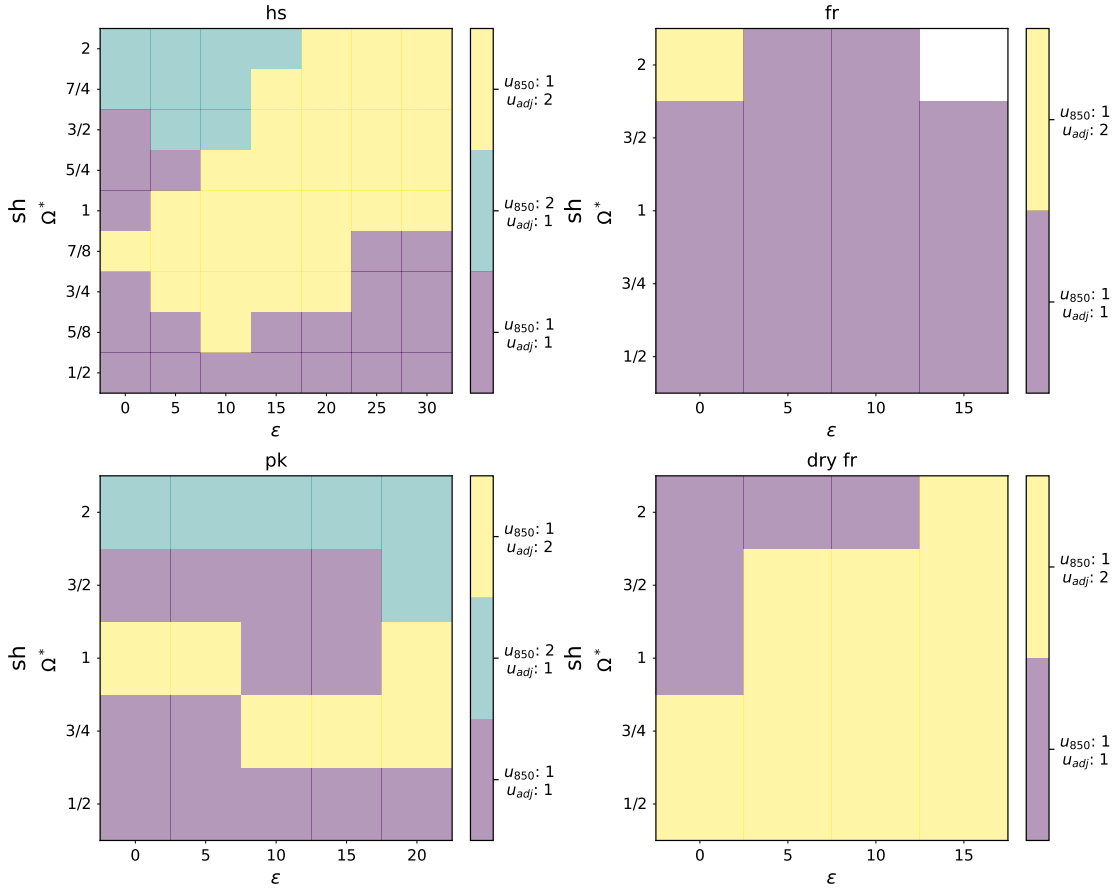

Figure 4.18: **The number of possible eddy-driven and subtropical jets.** The number of maxima in u_{adj} and u_{850} in the winter hemisphere. All simulations are shown: HS (upper left), F06 (upper right), PK (lower left), or DF (lower right).

Of our initial hypotheses, we find that the first is true in all simulations, with the Hadley cell broadening and strengthening with increasing obliquity or decreasing rotation rate. We also find that the edge of the Hadley cell and the latitude of the EDJ are more strongly correlated when they lie closer together, which is true for all model configurations. However, we do not see a relationship between the strength of the STJ and the coupling between the locations of the STJ and EDJ, as we might have expected given the previous work of Lee and Kim [2003]. Instead, we see that simulations with the strongest STJ are in fact those with a moderately well-separated STJ and EDJ, which have the weakest

correlations. We do however see that simulations with a colocated STJ and EDJ do have the strongest correlations between these two metrics, as we predicted.

4.7 Summary and Conclusion

In this study, we have used an idealised climate modelling framework to explore the relationships between three dynamical metrics for tropical width: the edge of the Hadley Cell, the latitude of the subtropical jet, and the latitude of the eddy-driven jet. We aim to bring together two fields of study: studies such as Solomon et al. [2016] and Davis and Birner [2017] that focus on the connections between these metrics on Earth, and studies such as Kaspi and Showman [2015] that focus on Hadley circulation width and jet latitude in a broader space of planetary parameters. We have looked at both metric mean latitude as a function of planetary parameters, as well as the coupling between the jets and the edge of the Hadley Cell, in an attempt to understand how the connections seen in models and observations of Earth's atmosphere fit into a wider parameter space. We have also investigated how our results are different in a model with a grey radiation scheme, with and without moist effects.

We find that, although well-coupled in our most Earth-like simulations, for some obliquities and rotation rates our chosen metrics may become weakly or negatively correlated with each other. This suggests that the strong coupling we expect between the edge of the Hadley Cell and the subtropical jet is sensitive to these changes, and in turn, sensitive to changes in the separation between metrics.

Analysis of the parameter sweep of dry simulations reveals the following key results:

1. **We identify three 'jet regimes' within the rotation rate-obliquity parameter space in the winter hemisphere.** The existence of two eddy-driven jets suggests strong positive correlations between all metrics in the southern hemisphere, but across the transition to two subtropical jets, there is a rapid change in the separation

between the subtropical and eddy-driven jets and somewhat weaker coupling in this region. In the region of parameter space where there exists only one eddy-driven and one subtropical jet, correlations vary widely; in particular, we see weakly negative correlations between the Hadley Cell edge and the subtropical jet in this region.

2. **We identify a branch in the mean location of the eddy-driven jet and Hadley Cell edge in relation to the latitude of the subtropical jet.** The most poleward simulations in each branch correspond to regions with either two subtropical jet maxima or two eddy-driven jet maxima. The branches meet in the region of parameter space where there are one of each jet (Fig C.18).

3. **The addition of the Polvani-Kushner stratosphere influences the mean latitudes of our metrics but does not significantly alter the correlations between metrics that we expect from HS based on their latitude or separation.** That is to say, different rotation rate or obliquity may be required for a PK simulation to have the same separation between metrics as a HS simulation, but their correlation will likely still be similar.

4. **Correlations in the moist model are overall weaker than in the dry model.** Few significant relationships can be identified between metric coupling and their separation, mean location, or the strength of the quantities used to define them. Indeed, there is only a weak positive relationship in the correlation between the eddy-driven jet and edge of the Hadley Cell with a more poleward eddy-driven jet, and similarly with decreasing separation between the two. However, all metrics in the moist model vary linearly with each other in terms of their mean locations, and the Hadley Cell edge and subtropical jet are approximately colocated across the whole of the parameter space.

5. **The dry limit of the moist grey model shows some agreement with HS simulations.** In the winter hemisphere, ϕ_{HC} and ϕ_{STJ} become decoupled at slow

rotation rates and/or higher obliquity, much like in HS simulations. This is not the case in moist simulations, suggesting the effects of moisture act to prevent decoupling across the parameter space.

Overall, we have found that all metrics are more strongly positively correlated the further equatorward that either of them lies, or the weaker the quantities used to define them are. We find that there is only one clear linear relationship between the strength of the coupling between metrics and their separation in the HS model. This is an increase in the strength of the coupling between the Hadley Cell edge and the eddy-driven jet latitude as they become less separated, as seen in previous studies such as Kidston et al. [2013]. The subtropical and eddy-driven jets are well correlated both when they are colocated, and when they are well-separated, with a region of weak-to-negative correlations in between. The subtropical jet and the Hadley Cell edge have the most complex relationship, and it is clear that their coupling has greater dependence on factors other than their separation.

Notably, our results are significant in that we identify regions of parameter space that display distinct behaviours, and that there can be a sharp transition from one such regime to another. For example, in the HS simulations, faster-rotating and low obliquity planets generally display strong correlations between all three metrics, but an increase in obliquity or decrease in rotation rate may cause the edge of the Hadley cell to become decoupled from the jets, and weaken the coupling between the EDJ and STJ locations. This decoupling between ϕ_{HC} and ϕ_{STJ} is surprising given our understanding that the STJ can form purely as a result of angular momentum conservation at the edge of the HC. In general, ϕ_{EDJ} and ϕ_{STJ} are positively correlated across much of the parameter space. This is true not only for HS simulations, but also for PK and DF simulations, although not for F06 simulations, suggesting that moist effects may lead to some decoupling between the STJ and EDJ, which can reflect real world conditions. However, the key result from the investigation using the grey model suggests that decoupling is also possible in some regions of the parameter space, particularly in the dry version of the model (with moist

effects dampening this tendency for ϕ_{HC} to be decoupled from ϕ_{STJ} and ϕ_{EDJ}).

Additional work in this area would aim to further probe the mechanisms for the relationships that we have found. For example, Davis and Birner [2017] have shown that the mean meridional circulation (and hence the location of the edge of the Hadley cell) is linked to the distribution of eddy momentum fluxes via subtropical baroclinicity. Menzel et al. [2021] also find that in a dry idealised GCM, ϕ_{HC} and ϕ_{STJ} can exhibit a strong coupling when eddy momentum convergence is the dominant contribution to meridional flow balance. When angular momentum advection relevantly impacts meridional flow in the subtropical upper troposphere, ϕ_{STJ} is disconnected from ϕ_{HC}. An investigation into the circulation using these perspectives would be worthwhile, but is beyond the scope of this paper. Given the sharp transition in the number of jets present in our dry simulations, a finer parameter sweep may also reveal intermediate simulations in which the number of jets changes throughout time, which leads to interesting questions about the relationships between the three metrics in this scenario.

CHAPTER 5

CONCLUSIONS

Understanding the dynamics in planetary atmospheres is an exciting topic of research: it complements observational missions and may provide a key to predicting a planet's potential habitability, it allows us to contextualise the circulation in the Earth's atmosphere, and it can help us to identify key mechanisms that drive various features of atmospheric circulation.

The research contained within this thesis is an exploration into features of large-scale atmospheric dynamics on other planets, with a primary focus on polar regions. The study was undertaken with the aim of enabling a deeper understanding of dynamics on rapidly rotating bodies such as Earth and Mars. The Mars configuration of Isca (Isca-Mars), an idealised modelling framework, is extended and employed to study the dynamics and structure of the Martian polar vortices and their role as a mixing barrier throughout the planet's history. To understand the changes in circulation in Mars's paleoclimate, a parameter sweep over obliquity and dust abundance is performed. This work is then expanded to consider atmospheric circulation under more widely varied orbital forcings, with exoplanetary circulation in mind. The key results of each research chapter are

summarised in Section 5.1, and methods developed in Section 5.2. Challenges and questions raised by the research, as well as future directions that may resolve these, are proposed in Section 5.3.

5.1 Synthesis

5.1.1 Understanding the drivers of Mars's present-day northern polar vortex

Recent studies investigating the annular polar vortices in Mars's atmosphere have shown that latent heat release from CO_2 condensation could provide a restoring force for this dynamically unstable morphology [e.g. Seviour et al., 2017; Toigo et al., 2017]. However, it remained unclear how this forcing, along with interannual dust variability and mechanical forcing from topography, interplay to contribute to both the morphology and variability of the northern polar vortex. In Chapter 2 of this thesis, a process-attribution study develops and employs the idealised Martian Global Climate Model (MGCM) Isca-Mars. The morphology and variability of Mars's northern polar vortex are revealed to be influenced by a combination of topography, dust, and latent heat release. The vortex's annular morphology depends largely on latent heat release, in agreement with previous studies, while its elliptical shape appears topographically driven, and the presence of atmospheric dust strengthens potential vorticity (PV). Internal variability is guided by the combination of latent heat release and dust, and interannual dust variability leads to large interannual variability in polar vortex morphology.

In addition, the morphology and variability simulated in Isca-Mars is compared to that found in reanalysis datasets. The vortex is somewhat less annular in simulations compared to OpenMARS, with a stronger PV maximum, but the subseasonal polar vortex variability is well-captured when all processes are accounted for. The mean state of the Martian atmosphere in Isca-Mars is in better agreement with reanalyses (in terms of zonal-

mean temperatures and zonal wind) once dust is turned on in the model. Additionally, this comparison with reanalyses illuminates significant differences within OpenMARS depending on the retrieval instrument used for each period of the dataset. During the earlier TES period (MY 24-27), the jet lies at lower latitudes than during the later MCS period (MY 28-32) while the Hadley Cell (HC) descending branch lies at higher. Somewhat less latent heat release occurs during the earlier reanalysis years, but a greater peak in vortex variability is seen over midwinter. The vortex itself appears stronger (in PV terms) across the later period, with the annulus being consistently present. The differences noted within this thesis, and within other studies [e.g. Mooring et al., 2022; Waugh et al., 2016], suggest that care must be taken in conclusions drawn both from different reanalyses and from different instrumental eras within one reanalysis.

5.1.2 The importance of mixing in the formation of the PLD

The annular morphology of the polar vortices on Mars may impact horizontal mixing in the polar regions, which is known to be important for the distribution of trace species and for atmospheric chemistry in Earth's stratospheric polar vortices. However, this had not yet been investigated in the Martian atmosphere. By applying techniques that have been used to understand transport across Earth's polar vortices, but that are novel for use in the Martian atmosphere, Chapter 3 of this research explores mixing and transport across the polar regions in different orbital configurations that Mars may have experienced. A parameter sweep across a wide range of obliquities, as well as over several possible global dust abundances, identifies significant hemispheric differences in isentropic mixing. Similarly, vortex morphology is revealed to be different in the northern and southern hemispheres in Isca-Mars, with such differences similarly noted in other MGCMs [e.g. Waugh et al., 2016]. A particularly strong response to dust loading and obliquity is identified in the southern hemisphere compared to the northern. Analysis of effective diffusivity reveals that the polar vortices act as significant barriers to isentropic mixing, in much the

same way as Earth's stratospheric polar vortices. Overall mixing increases with obliquity or dust, likely due to strengthening circulation in these simulations. The northern hemisphere has a weaker response to obliquity (and no clear response to dust). These differences could be due to hemispheric asymmetry in topographical forcing, and are likely also influenced by the seasonality of the dust loading.

Furthermore, the southern hemisphere vortex shrinks with increasing dust loading and obliquity, but the annulus is maintained in all simulations. This is not the case in the northern hemisphere, where the annulus is destroyed at the highest simulated dust loading (4× current loading) or at high obliquity ($\varepsilon = 45 - 50°$). In fact, in the northern hemisphere, the polar vortex appears to be most annular around current obliquities (within a range of around $\varepsilon = 20 - 30°$). The collapse of the annulus to a monopolar vortex at the highest dust loading could be linked to the HC, which extends to higher latitudes in the dustiest simulation in the northern hemisphere, but is relatively invariant in the southern hemisphere or at lower dust loadings. This expansion of the HC is reminiscent of the response of the circulation to the MY 28 GDS seen in Chapter 2, wherein the HC expands poleward, the annulus collapses to a monopole, and PV weakens overall.

5.1.3 Exploring the range of atmospheric circulation and its covariability in Earth-like exoplanets

The parameter sweep of Chapter 3 naturally inspires an extension of this dynamical investigation to a broader range of parameters. Previous studies have performed sweeps across a range of parameters and have contextualised Earth's circulation across these broader parameter spaces. Such studies have also found key parameters that may result in circulation features that would be identifiable in retrievals from instruments such as the James Webb Space Telescope (JWST). Chapter 4 of this thesis thus extends the study beyond Mars's atmosphere, with exoplanetary atmospheres in mind. The Held-Suarez [Held and Suarez, 1994] benchmark model version of Isca (a highly idealised model of Earth's

atmosphere) is used to explore the coupling between metrics for tropical width across a range of obliquities and rotation rates. Multiple jets emerge over the parameter sweep performed, and there are distinct regions of the parameter space where the subtropical jet (STJ) and edge of the HC are no longer connected. This is surprising due to the general understanding that the STJ can form purely as a result of angular momentum conservation at the edge of the HC, although reflects the fact that these two features are not always well-correlated in observations or more complex GCM simulations.

The primary result of this work is the identification of branching behaviour in the STJ across the parameter space; on these two branches in the STJ location, the metrics follow different coupling patterns. On one branch, the latitudes of the STJ, the eddy-driven jet (EDJ), and edge of the HC (ϕ_{STJ}, ϕ_{EDJ}, and ϕ_{HC}, respectively) lie particularly close together (indeed, ϕ_{STJ} and ϕ_{EDJ} are approximately colocated) and all metrics are positively correlated. This corresponds to the region of fast-rotating low-obliquity planets. On the other branch, ϕ_{HC} may become decoupled from the two jets. Isolating simulations by the number of maxima in the low-level or upper-tropospheric winds enables the placement of a simulation within different regimes. One such regime (with two low-level jet maxima and one upper-level) contains fast-rotating and low-obliquity planets, and it is this regime in which all metrics lie within 10° of each other and are positively correlated.

Further work investigates the same connections in a grey radiation model, also considering the influence of moisture in this framework. In both moist and dry versions of the grey model no branching behaviour is identified, although the same general trend in the location of the metrics (that as one metric lies further poleward so do the others) is noted. Weaker dependence on the strength of the quantities used to define each metric is found when compared with the idealised dry model, and there is no clear coupling dependence on the separation between metrics. The key result from the investigation using the grey model suggests that decoupling is also possible in some regions of the parameter space, particularly in the dry version of the model (with moist effects dampening this tendency

for ϕ_{HC} to be decoupled from ϕ_{STJ} and ϕ_{EDJ}).

5.2 Key methods developed

5.2.1 Extension of Isca-Mars

The work within this thesis represents a significant extension of Isca-Mars from its previous version, which was detailed in Thomson and Vallis [2019b]. The processes added herein represent the most advanced version of Isca-Mars available. Two further schemes are added: a representation of latent heat release from CO_2 condensation, and a prescribed dust scheme, both detailed fully in Chapter 2 and Ball et al. [2021]. The aim of including these new schemes is to more accurately simulate the Martian atmosphere as seen in observations, as well as in the more complex models that are available. Moreover, these features were identified to be key missing processes in Isca that have been previously shown to be important for the Martian polar vortices [e.g. Guzewich et al., 2016; Toigo et al., 2017]. Adding these two new processes further allows them to be switched on and off, in order to perform the process-attribution experiment of Chapter 2.

The dust scheme is based upon the Conrath-ν profile [Conrath, 1975] and features a prescribed vertical and latitudinal profile. This profile has also been used in other MGCMs [such as Guzewich et al., 2016; Toigo and Waugh, 2022; Toigo et al., 2017; Toigo et al., 2020; Waugh et al., 2019] allowing relevant comparisons to be drawn between Isca-Mars simulations and previous studies. Interannual differences within the dust scheme may be represented by inputting a yearly column dust optical depth file from the MCD [Montabone et al., 2015] which then scales the profile at each latitude by the zonal-mean gridded observational product. This may easily be extended to scale the profile at each latitude-longitude point. A climatological scenario is used for the 'standard dust case' which is averaged across all years of the MCD (excluding the GDS events of MY 25 and 28).

The representation of latent heat release is a simple temperature floor scheme. When

model temperatures are predicted to fall below the condensation point of CO_2, a temperature tendency is applied to prevent this. The amount of latent heat released is approximated by calculating the difference in expected temperature in the model and the temperature floor. This is a simple representation and does not include any CO_2 ice microphysics or the rather significant mass loss expected from such phase changes, but it allows the user to identify locations where CO_2 condensation would occur in the model. Moreover, the temperature floor representation acts as a sufficient restoring force to maintain a more annular vortex in all simulations where latent heating is turned 'on', as Chapter 2 of this thesis shows.

5.2.2 Flexible diagnostics for use in planetary atmospheres

Within this thesis, various diagnostics initially applied to Earth's atmosphere have been adapted for use across a range of planets, with flexibility in mind. That is to say, the code developed herein for the analysis of model simulations and reanalysis datasets is flexible to relevant planetary and atmospheric parameters (including radius, rotation rate, surface gravity, surface pressure, and specific heat constants for different atmospheres). This includes code to calculate potential temperature, PV, eddy enstrophy, effective diffusivity, and the meridional overturning streamfunction. Moreover, the calculation of metrics for tropical width may be applied to atmospheres in which there are multiple locations that satisfy the standard definitions for metrics of tropical width (for example, those in which multiple local maxima in the upper-tropospheric winds are present). The code developed herein identifies all such maxima and allows the user the choice of which maximum is most appropriate for their analysis.

The primary adaptation in this thesis of an Earth-based method for use in a planetary atmosphere is the first use of the effective diffusivity diagnostic in the Martian atmosphere. This enables the study of isentropic mixing in the midlatitudes and polar regions of Mars, and gives a first glimpse of what form this may take across different orbital configurations

and atmospheric dust loadings. The application of this diagnostic to the Martian atmosphere is novel and reveals that the polar vortices of Mars act in a similar way to Earth's stratospheric polar vortices, with a barrier to mixing at their equatorward edge.

Finally, one further emphasis of this research is for it to be open source and available for reproduction: all code used to perform model simulations, calculate diagnostics, and analyse model outputs has been maintained and documented on GitHub[1].

5.3 Challenges and future directions for the community

This thesis has raised questions concerning the dynamics of a variety of planetary atmospheres, including dependence on model choice and configuration. These questions and challenges, and how they might be addressed in future research, will be discussed below.

5.3.1 What processes form the polar layered deposits?

Isolating mixing changes in the Martian atmosphere from those in total transport (which includes vertical, cross-isentrope transport) is an important question that remains unanswered. The results of this thesis represent a key initial step towards such an analysis; Chapter 3 separates quasi-horizontal mixing from the overall transport, therefore providing new insights into the processes that act in the Martian atmosphere. However, it still remains unclear the extent to which the PLD result from changes in global dust abundance or changes in dynamics and mixing. These two features are connected, with dust abundance influencing the circulation, and circulation changes potentially resulting in altered dust distributions that could influence layering in the polar regions. It is therefore a complex question to approach, but is an important link from the PLD to underlying climate.

[1] All code is available on my personal GitHub or the Bristol Climate Dynamics group GitHub.

Coupling MGCM studies with analysis of future observations from orbital and ground-based missions will allow the Martian scientific community to better understand physical and chemical processes in the atmosphere. Understanding how the results of this thesis, which uses an idealised modelling approach, fit into the broader context of current observations and more complex MGCMs available is vital. Speaking broadly, future work investigating the formation of the PLD may more widely focus on understanding the timespan, completeness, and temporal resolution of the climate history recorded in the PLD [Smith et al., 2020]. The advent of greater technological advancements means that we may well see geological samples returned from Mars in just over a decade, and that a landed polar mission may well be feasible within the coming years [Smith et al., 2020]. The theory of atmospheric circulation that we study, whether it be idealised laboratory experiments, simple models or full GCMs, must both guide and be guided by such sample returns and landed missions. In this way, the Martian scientific community can work together to understand the historical evolution of Mars's atmosphere, which remains an important factor in assessing potential past habitability as well as providing a useful comparison to Earth's own climate record.

5.3.2 How are simulations of the Martian polar vortices influenced by modelling choices?

Chapter 2 illustrates the substantial influence of three key parameters on the northern polar vortex, and Chapter 3 further expands this to consider how historical orbital and atmospheric configurations may have influenced their morphology. However, there are further important processes, parameters, and features that influence the polar vortices on Mars beyond those in the experiments of Chapters 2 and 3 that may influence polar vortex morphology or variability that are not considered herein. Whilst the idealised nature of Isca-Mars is useful in understanding key drivers of dynamics, there are some limitations to its use. For example, the prescribed dust distribution does not allow the natural generation

of large dust events, nor does it evolve with changing planetary parameters. Given that a significant caveat of the research within this thesis has been the prescribed dust profile of the newly-developed Isca-Mars, similar studies using an active dust scheme would be of interest to the Martian scientific community. In particular, the investigation in Chapter 3 into the isentropic mixing of a passive test tracer would be illuminating given its evident relevance for the transport of dust in the polar regions.

Furthermore, the use of one modelling framework (particularly in Chapters 2 and 3, where only one dynamical core is used but other MGCMs exist) somewhat limits the conclusions drawn from the research within this thesis. Additionally, Chapter 2 notes differences in OpenMARS and EMARS at polar altitudes that are likely driven by differences in the underlying GCMs (as these differences occur where observations are highly limited). It would be interesting to compare the results of the chapters herein with other model simulation outputs, and preferentially investigate results in the UK-LMD model (the underlying model used in MACDA/OpenMARS) and/or the GFDL MGCM (the underlying model used in EMARS). Identifying such model differences is not an issue limited to the Martian atmosphere: despite decades of advances in modelling capability and the processes represented, wide-ranging model intercomparisons of Earth's jet often reveal very different variability and responses to external forcings (albeit with the land-ocean differences on Earth providing an additional level of complexity).

One path that the Martian atmospheric community might take to resolve or understand these differences in models of the atmosphere of Mars would be the development of a model intercomparison project for Mars (much like the Coupled Model Intercomparison Project used for future climate change projections). Such a project would allow a detailed comparison of polar vortices (along with other dynamical and chemical processes of interest) across multiple models, their response to high dust loading, and their hemispheric differences. Future work may include more detailed studies into the causes of such differences, as well as their effects on circulation, dynamics, and geology. Such a study would allow us to fur-

ther our understanding of the stability of the annular polar vortex, which has implications for the mesospheric polar vortices on Earth, hurricanes, and potentially the polar vortices of other planetary bodies including Saturn's moon Titan.

5.3.3 Are Martian reanalyses believable?

Currently, there are three reanalysis products available for the Martian atmosphere, although only two span the entire period of interest within this thesis. One focus of Chapter 2 is the investigation into the Martian northern polar atmosphere as seen in reanalysis datasets, in particular the OpenMARS dataset (with brief comparisons made to the EMARS dataset). OpenMARS and EMARS assimilate variously observations of thermal profiles, water ice and dust opacities, ozone and water vapour column abundances into the UK-LMD (for OpenMARS) or GFDL (for EMARS) models [Greybush et al., 2012; Holmes et al., 2020]. These observations are obtained primarily from either TES (during MY 24 - 27) or MCS (MY 28 - 32; the OpenMARS reanalysis has subsequently been extended to MY 35 since the analysis undertaken in Chapter 2). The research in Chapter 2 demonstrates that these observations may cause significant intra-reanalysis differences depending on the retrieval instrument, in addition to those differences caused by the underlying model. Recent work using the OpenMARS precursor MACDA and EMARS has shown intra-reanalysis comparisons of temperature and zonal winds are in better agreement with each other than those same fields within the underlying free-running MGCMs [Mooring et al., 2022]. The gap between TES and MCS observations has led to calibration issues between the two eras of the reanalysis; given the relative sparsity of the observations available, their own systematic biases, and in particular the lack of overlap between the two instruments, it is difficult to know which period is necessarily more 'believable'.

One important avenue for future study is thus the comparison of reanalysis products available for the Martian atmosphere. Such work has already been discussed [e.g. Waugh

et al., 2016], but more in-depth analyses of recent products would be beneficial. Relevant to this thesis, there are significant hemispheric, inter-, and intra-reanalysis differences in polar vortex morphology that bear further investigation. Understanding key differences between reanalyses, and the belief we as a scientific community should put in spatial regions (e.g. due to latitudinal or altitudinal biases in retrievals) and temporal eras (e.g. due to differences in retrieval instruments), is key to their continued use and development.

5.3.4 How do we approach the great diversity of planetary atmospheres?

5.3.4.1 Planetary atmospheres within our solar system

Other planetary bodies within our solar system may reveal fascinating analogies to the annular polar vortices of Mars; Cassini observations have revealed annular polar vortices on Titan [Sharkey et al., 2021] that act as a significant barrier to mixing by analysis of chemical tracers [Teanby et al., 2008]. Recent work using the TitanWRF model has found a minimum in the winds and potential vorticity following the winter solstice in Titan's polar vortices, and attributed the annular morphology to descent and adiabatic heating at the poles [Shultis et al., 2022]. Future missions may be the key to understanding atmospheric dynamics on bodies within our solar system. NASA's Dragonfly mission, slated for launch in 2027 and set to explore Saturn's nitrogen- and methane-rich moon Titan from 2034, could provide sufficient observations to further the work of Sharkey et al. [2021].

Model simulations may complement upcoming missions, but simulating the atmospheric circulation on other planets will no doubt take many years to catch up to the capabilities that we have for simulating the atmosphere of Earth currently, even for relatively well-observed planets within our solar system (such as Mars, or Venus). This is due to a combination of factors, including the sparsity of the observations (in both their temporal and spatial coverage) available to us and the large variety of planetary parameters and atmospheric compositions. There are undoubtedly dynamical and chemical processes present in extraterrestrial atmospheres that are not seen on Earth, and therefore

new representations of these must be developed for more accurate simulations of these atmospheres. Such a variety in planetary atmospheres means that the modelling community's efforts must inherently be divided. Given the enormity of the task of modelling planetary atmospheres faithfully, taking an idealised and hierarchical modelling approach allows us to gain understanding of the potential processes that may be seen on a given planet, with the observations and knowledge that we have available to us. Employing a hierarchical approach in such studies broadly allows us to characterise important features of the dynamics and isolate key parameters or external forcings that define the circulation on specific planets [Maher et al., 2019b].

One approach to resolve this problem is the use of idealised parameter sweeps. Chapters 3 and 4 both perform parameter sweeps with Isca to study planetary atmospheres; such parameter sweeps may also be useful as a framework for comparative planetology within our solar system. For example, in a study across a parameter sweep of obliquity, rotation rate, and orbital period, polar vortices have been identified that share broad characteristics with the polar vortices of Earth, Mars, and Titan [Guendelman et al., 2022]. Such studies may not capture all the individual processes relevant for specific planets, but deepen understanding of fundamental dynamics driven by planetary or orbital parameters (rather than, say, atmospheric constituents).

Furthermore, more complex GCMs (or other models designed with a specific planet in mind) could also be employed to reveal key driving mechanisms and forcings in the atmospheres of solar system bodies. Previous research has identified similarities between the polar vortices of Mars and those in Earth's atmosphere, as well as on other planetary bodies in the solar system [e.g. Mitchell et al., 2014, 2021; Waugh, 2023]. Understanding how polar vortices behave across a variety of well-observed solar system bodies, and how they differ from Earth's stratospheric polar vortices, can develop our understanding of the circulation on the chosen planet, and also on Earth itself. Extending Earth-based GCMs to understand the atmospheric circulation on other planets is a test of their robustness; the

ready ability to simulate the atmospheres of other planets by changing appropriate parameters and values suggests that the processes simulated are sufficiently well-represented in models of Earth's atmosphere.

5.3.4.2 Exoplanetary atmospheres

Over 5000 exoplanets have been confirmed to date, and there are almost twice as many candidate exoplanet detections, across nearly 4000 planetary systems. Of these, biases in transit detection mean that confirmed exoplanets are often large and short-period [Kipping and Sandford, 2016]. As such, observed exoplanets are primarily Neptune-like or gas giants such as Jupiter, but a significant number of super-Earth type and terrestrial planets are also confirmed.[2] Confirmed exoplanets are also often tidally locked, with short orbital period, due to this bias. Through analysis of transmission spectra obtained by JWST and other telescopes, scientists are able to identify certain chemical components of an observed exoplanet's atmosphere. Model simulations may then be able to complement these observations and allow us to infer potential circulation patterns. Such analyses will be vital both for identifying potential candidates for habitability, and for furthering our understanding of the great variety of atmospheric dynamics present across the universe.

Comparative planetology appears to be at the dawn of a new and exciting era. Computational power and capability are now sufficient to perform large-scale simulations of the atmospheres of many planets, and recent studies have already begun to perform parameter sweeps over various planetary parameters to help characterise global atmospheric circulations across a variety of regimes [e.g. Guendelman and Kaspi, 2018; Guendelman et al., 2021; Toigo et al., 2020, and many more]. Isca itself has already been put to use exploring the dynamics of tidally and non-tidally locked exoplanets at varying levels of complexity [see for example Lewis et al., 2021; Penn and Vallis, 2017, 2018; Thomson and Vallis, 2019a]. A very exciting project, the Trappist-1 Habitable Atmosphere Intercompari-

[2] An up-to-date catalogue of detected exoplanets can be found at the NASA Exoplanet Catalog (https://exoplanets.nasa.gov/discovery/exoplanet-catalog/).

son (THAI), suggests the first model intercomparison protocol for planetary atmospheres within the Trappist-1 system and compares the simulations of four atmospheres across four models [Fauchez et al., 2021].

There is great diversity in exoplanetary atmospheres, and in the same manner that accurately simulating solar system planets will require some understanding of the most important features to capture, so too must choices be made when considering how best to answer relevant questions about exoplanets and their atmospheres. For example, the parameter sweep in Chapter 4 covers only two potential atmospheric parameters out of many. Previous work has shown the importance of a variety of planetary and atmospheric parameters for the atmospheres of exoplanets (and their dynamics and habitability), including radiative timescales, aerosols and atmospheric composition, orbital periods, planetary mass or radius, solar constant, or surface pressure or gravity [Boutle et al., 2020; Carone et al., 2017; Graham, 2021; Guendelman and Kaspi, 2018, 2019, 2020; Haqq-Misra et al., 2018; Kaspi and Showman, 2015]. Therefore, this experiment could be developed further by examining alternative parameters for their influence on the coupling between tropical edge metrics.

Atmospheric circulation is important for the distribution of heat and tracers throughout a planet's atmosphere; heat distribution across a planetary atmosphere is key for assessing its potential habitability. With the advent of JWST, we have the possibility of thermal retrievals and transmission spectra for a great number and variety of exoplanets, including Earth-sized rocky exoplanets. On January 11th, 2023, JWST confirmed its first exoplanet, LHS 475 b, which is 99% of the size of the Earth [NASA, 2023]. The availability of such observations promises an exciting future for understanding planetary atmospheres. Nonetheless, the information that we can glean from these retrievals is limited when compared to the observations made by satellites of Earth, Mars, and Venus. It is here that we then may employ global circulation models to provide valuable insight into the atmospheric dynamics and climate of such exoplanets, complementing their observations.

The use of GCMs to simulate the atmospheres of observed exoplanets, as well as potential unobserved planets, will complement such telescope observations and may help constrain further information about their characteristic atmospheric circulations. For example, recent work partitioning the global temperature field of a tidally locked exoplanet aims to identify features of atmospheric circulation that are identifiable in temperature retrievals through balancing arguments [Lewis and Hammond, 2022]. Improved computational efficiency and better constraints from observations will allow parameter sweeps (and other investigations) to further our understanding of atmospheric dynamics across a wide range of planetary atmospheres. Furthering our understanding of planetary atmospheric dynamics allows us to place our own atmosphere into a much larger and more exciting context than considering the dynamics seen here as an isolated case.

APPENDIX A

APPENDICES FROM CHAPTER 2

A.1 Supplementary Figures

We present here additional figures intended to supplement the main body of work. Figure A.1 shows yearly simulations run with a higher dust loading (surface mass mixing ratio double that of our other simulations; see Table 2.1 for details). This leads to higher temperatures and stronger winds than those seen in reanalysis. Significantly, however, we see that PV during the MY 28 dust storm is reduced in these model simulations (Figure A.1d). Winds are also weakened, in agreement with the nonlinear response to dust loading found in Guzewich et al. [2016].

Figure A.2 shows the seasonal evolution of polar cap PV, the location of the maximum PV, and eddy enstrophy, as calculated from the EMARS reanalysis. Both PV and eddy activity are more consistent between the TES and MCS eras in EMARS than in OpenMARS. The drop in PV and eddy activity during the MY 28 GDS is seen in this reanalysis as well as in OpenMARS, although the TES peak in PV and MCS pause in eddy enstrophy are not present. The vortex annularity appears much different however; it is significantly more

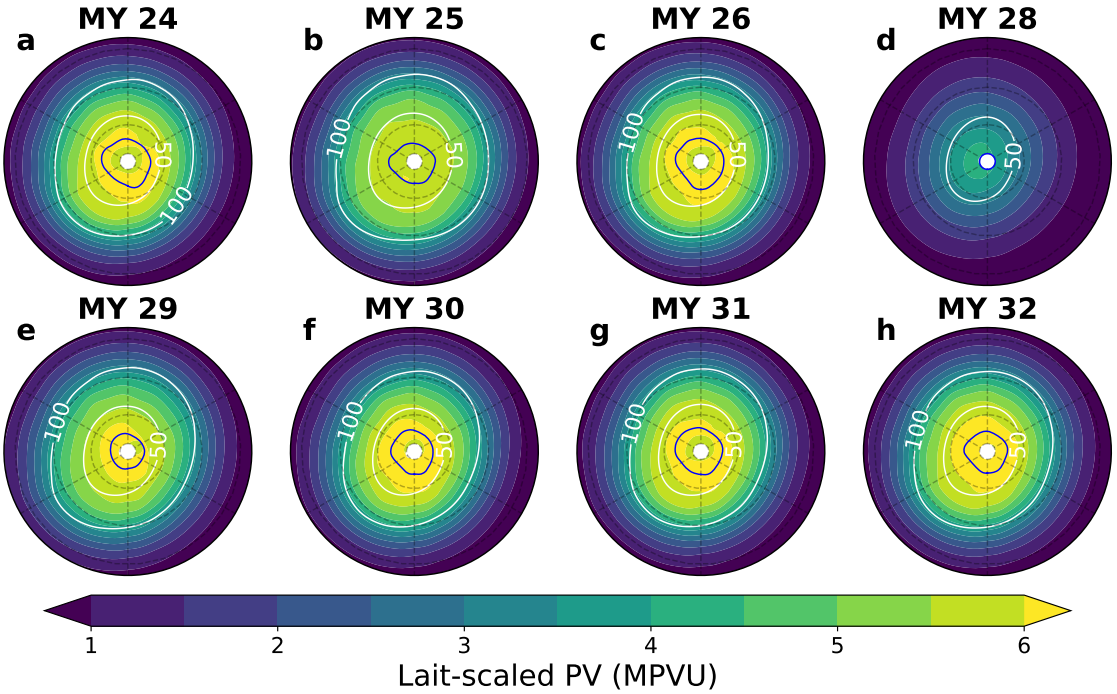

Figure A.1: **Horizontal cross-section of the northern polar vortex in 'high-dust' model simulations.** Winter-mean ($L_s = 270 - 300°$) north polar stereographic maps of Lait-scaled PV (shading) and zonal wind (contours) on the 300 K surface from additional 'high dust' simulations. The solid blue contour shows the latitude of maximum PV. Dashed latitude lines correspond to 60° N, 70° N, and 80° N, with each panel bounded at 55° N. Dashed longitude lines start from $0°E$ at the bottom of each panel. Note that the elevated topography of Tharsis province is located between $220 - 300°E$ (not shown).

annular in the TES era than the MCS.

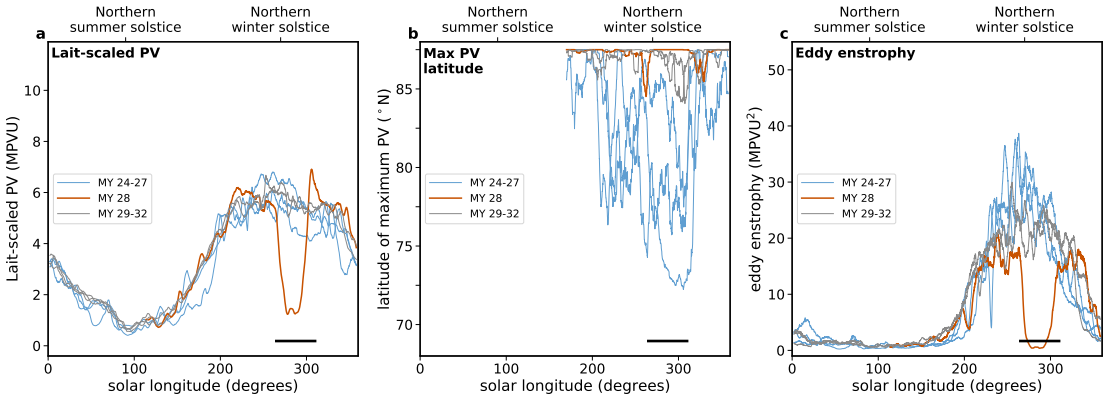

Figure A.2: **Evolution of the northern polar vortex in EMARS.** Smoothed evolution of (a) polar PV, (b) latitude of maximum PV, (c) and eddy enstrophy on the 350 K isentropic surface for data from the EMARS reanalysis. Polar PV and eddy enstrophy are calculated as in Figures 2.10 and 2.11, respectively. Lines are coloured according to the era of data (TES, MY 28, and MCS). The solid black line indicates the MY 28 global dust storm period.

APPENDIX B

APPENDICES FROM CHAPTER 3

B.1 Supplementary Figures

Supplementary figures B.1-B.6 show polar stereographic maps of PV and winds for all simulations, to illustrate the annular vortex more clearly, and how it responds to the varying parameters. Similarly, Figures B.7-B.12 show the mean meridional streamfunction ψ for all simulations, and are included to help visualise the circulation more clearly.

Figures B.1 through B.6 show potential vorticity on the 300K surface in all simulations. In all figures, $\varepsilon = 25°$ (for $\gamma = 0.093$ or $\gamma = 0$ simulation) or $\lambda = 1$ (for dust scale simulations) shows the absolute value of potential vorticity and zonal wind, and all other panels show the anomaly from this 'base' simulation.

Figures B.7 through B.12 illustrate the strength of the overturning circulation in all simulations. In all figures, $\varepsilon = 25°$ (for $\gamma = 0.093$ or $\gamma = 0$ simulations) or $\lambda = 1$ (for dust scale simulations) shows the absolute value of the mean meridional streamfunction, and all other panels show the anomaly from this 'base' simulation.

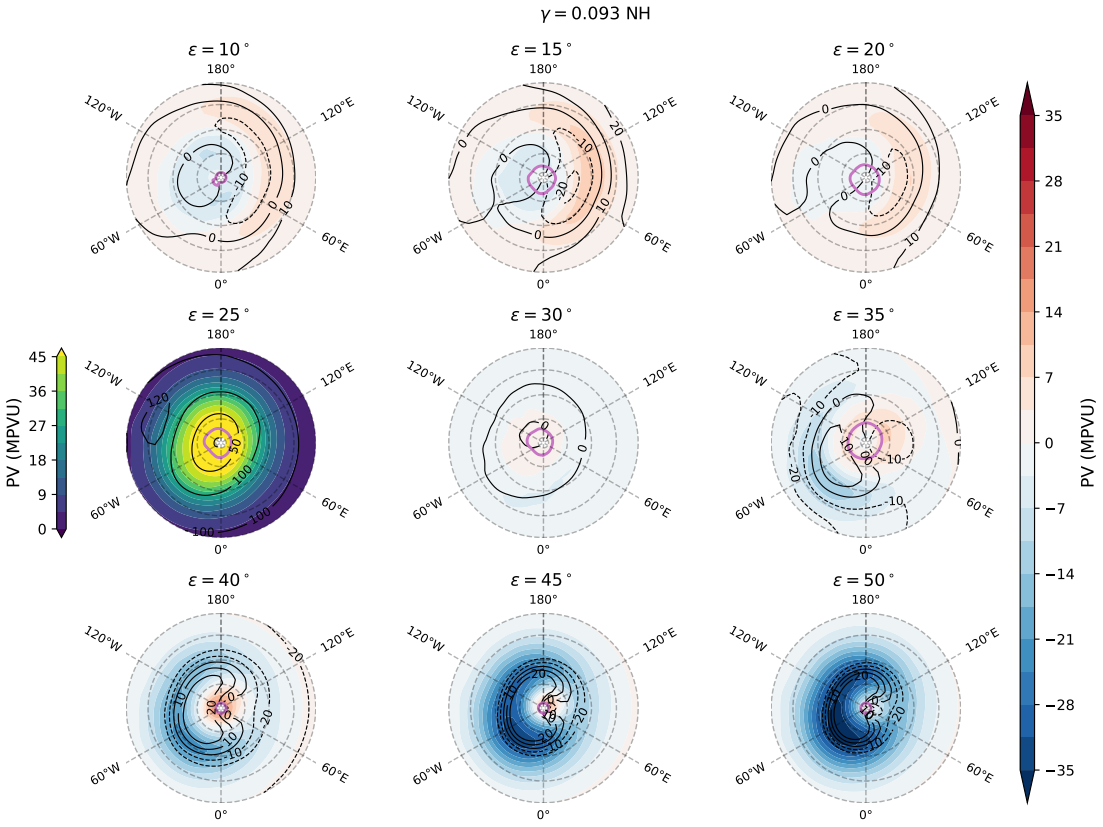

Figure B.1: **North polar stereographic map of PV (shading) and zonal winds (black contours) on the 300K surface in current-eccentricity simulations, averaged over 30 sols either side of the winter solstice.** $\varepsilon = 25$ shows absolute PV and zonal wind, and all other panels show the PV and wind anomaly from $\varepsilon = 25$ for the given value of ε. The purple contour indicates the latitude of maximum PV (ϕ_{PV}).

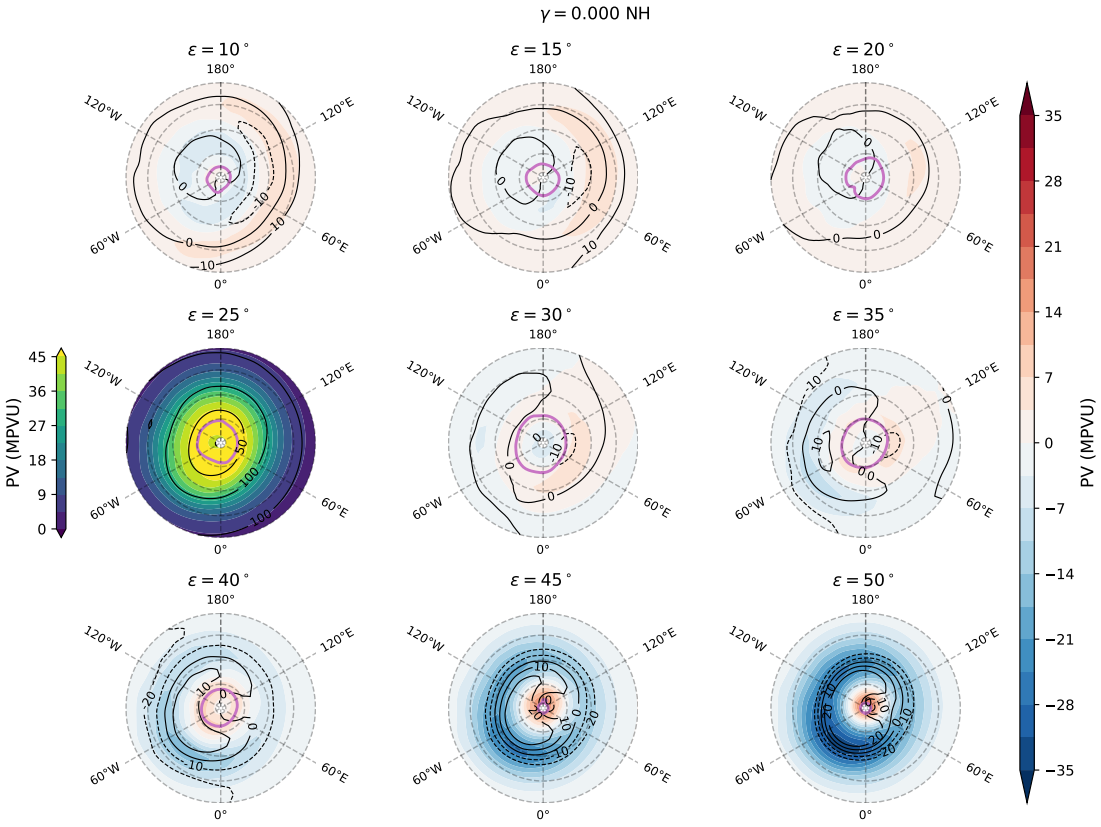

Figure B.2: **North polar stereographic map of PV (shading) and zonal winds (black contours) on the 300K surface in zero-eccentricity simulations, averaged over 30 sols either side of the winter solstice.** $\varepsilon = 25$ shows absolute PV and zonal wind, and all other panels show the PV and wind anomaly from $\varepsilon = 25$ for the given value of ε. The purple contour indicates the latitude of maximum PV (ϕ_{PV}).

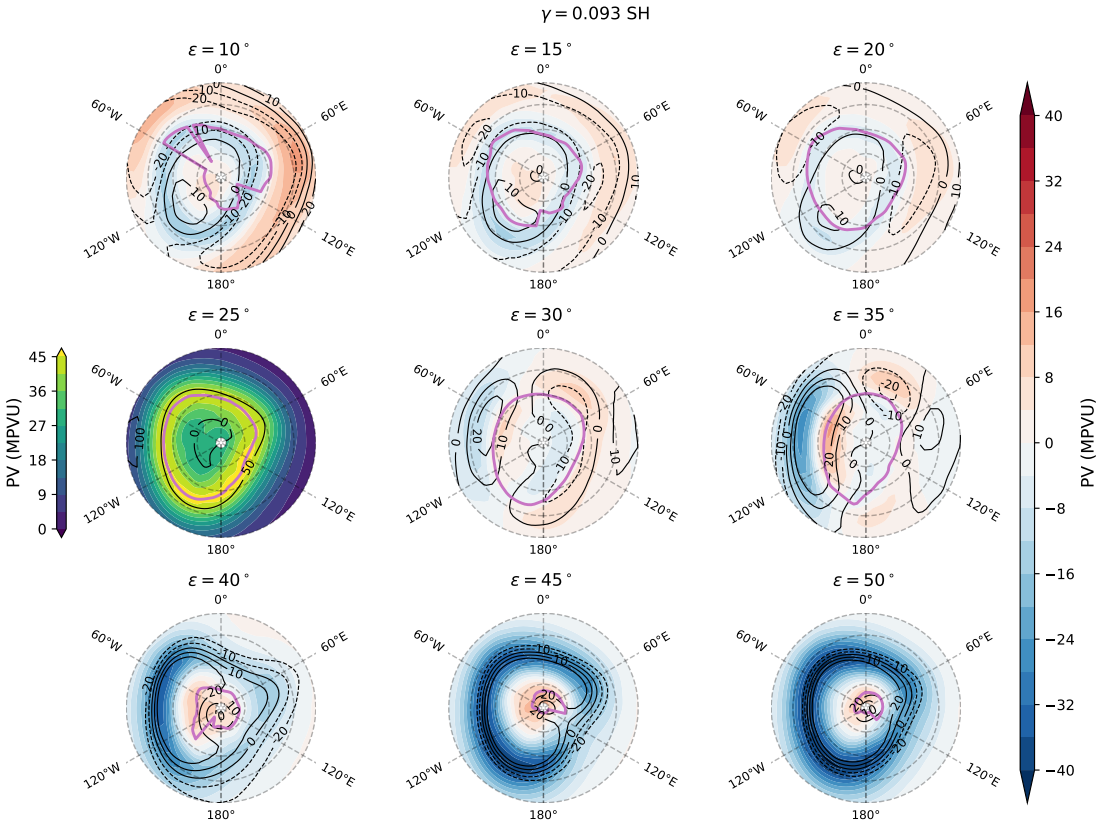

Figure B.3: **South polar stereographic map of PV (shading) and zonal winds (black contours) on the 300K surface in current-eccentricity simulations, averaged over 30 sols either side of the winter solstice.** $\varepsilon = 25$ shows absolute PV and zonal wind, and all other panels show the PV and wind anomaly from $\varepsilon = 25$ for the given value of ε. The purple contour indicates the latitude of maximum PV (ϕ_{PV}).

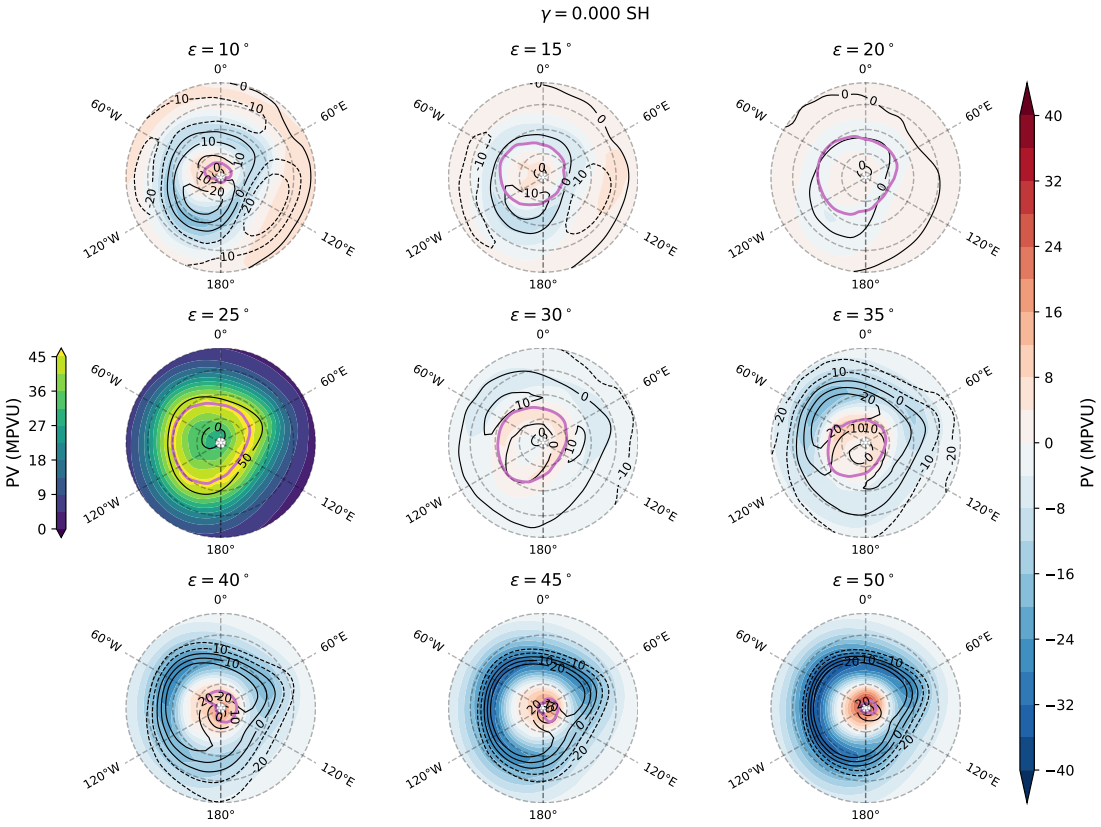

Figure B.4: **South polar stereographic map of PV (shading) and zonal winds (black contours) on the 300K surface in zero-eccentricity simulations, averaged over 30 sols either side of the winter solstice.** $\varepsilon = 25$ shows absolute PV and zonal wind, and all other panels show the PV and wind anomaly from $\varepsilon = 25$ for the given value of ε. The purple contour indicates the latitude of maximum PV (ϕ_{PV}).

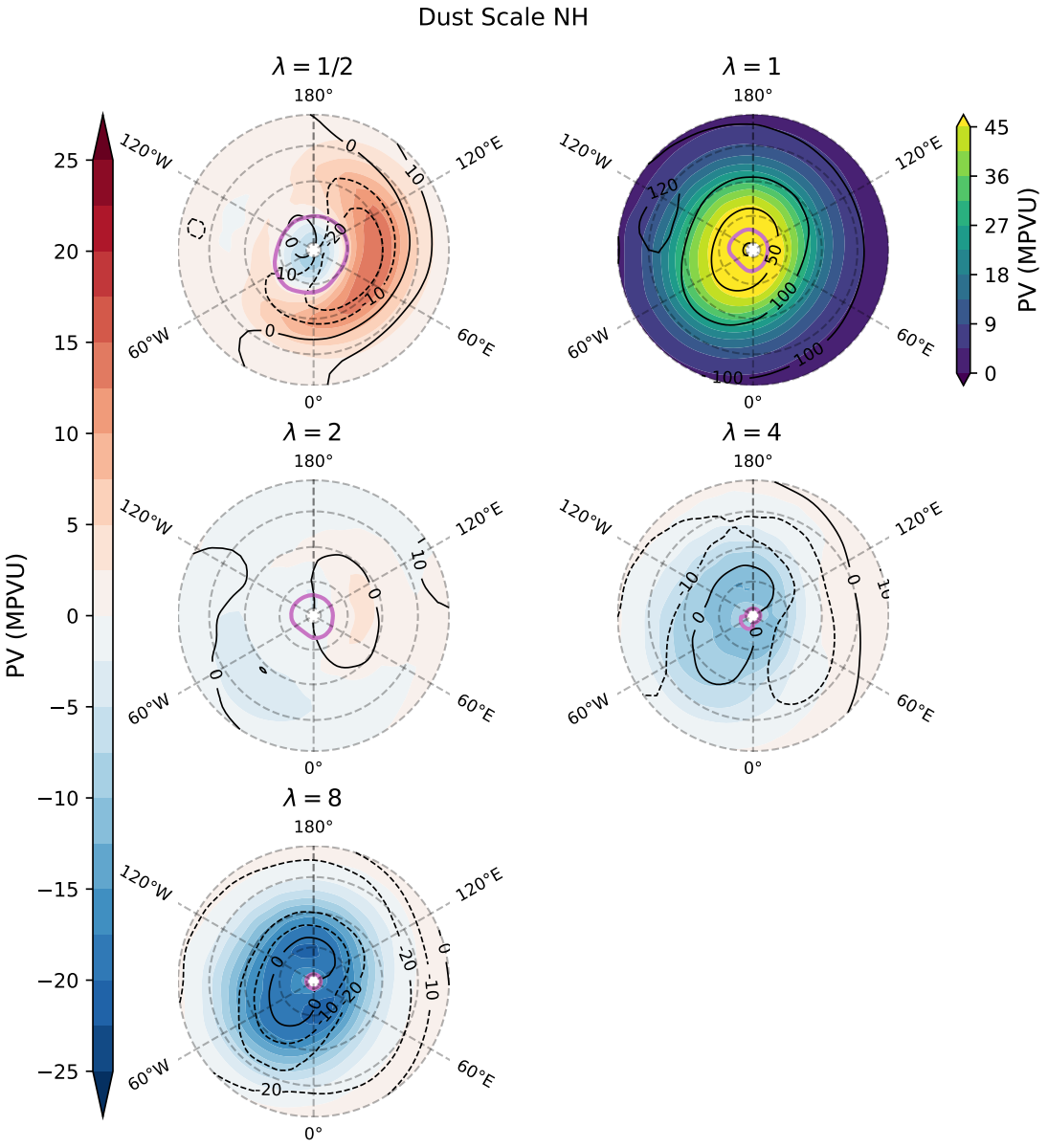

Figure B.5: **North polar stereographic map of PV (shading) and zonal winds (black contours) on the 300K surface in dust simulations, averaged over 30 sols either side of the winter solstice.** $\lambda = 1$ shows absolute PV and zonal wind, and all other panels show the PV and wind anomaly from $\lambda = 1$ for the given value of λ. The purple contour indicates the latitude of maximum PV (ϕ_{PV}).

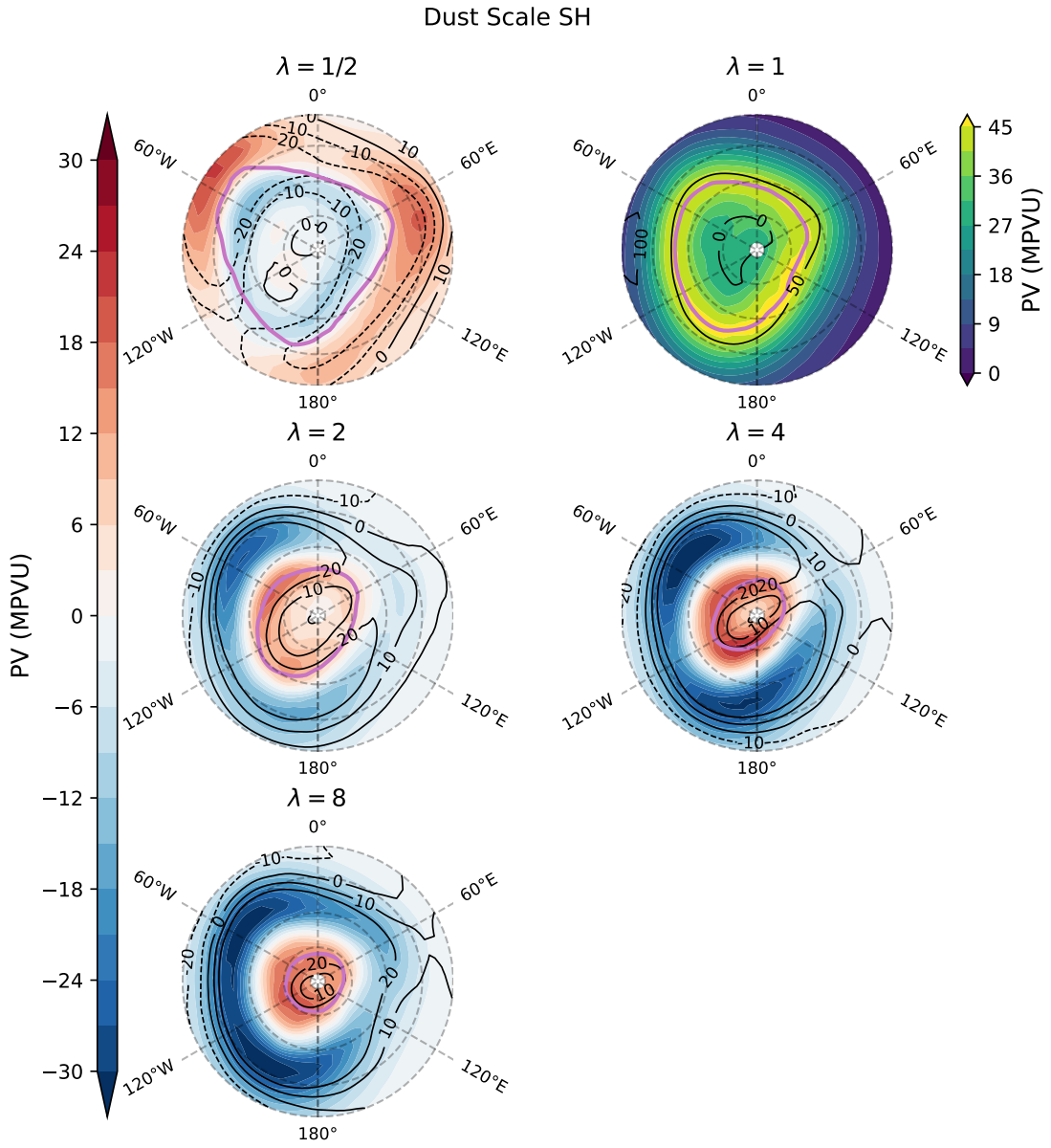

Figure B.6: **South polar stereographic map of PV (shading) and zonal winds (black contours) on the 300K surface in dust simulations, averaged over 30 sols either side of the winter solstice.** $\lambda = 1$ shows absolute PV and zonal wind, and all other panels show the PV and wind anomaly from $\lambda = 1$ for the given value of λ. The purple contour indicates the latitude of maximum PV (ϕ_{PV}).

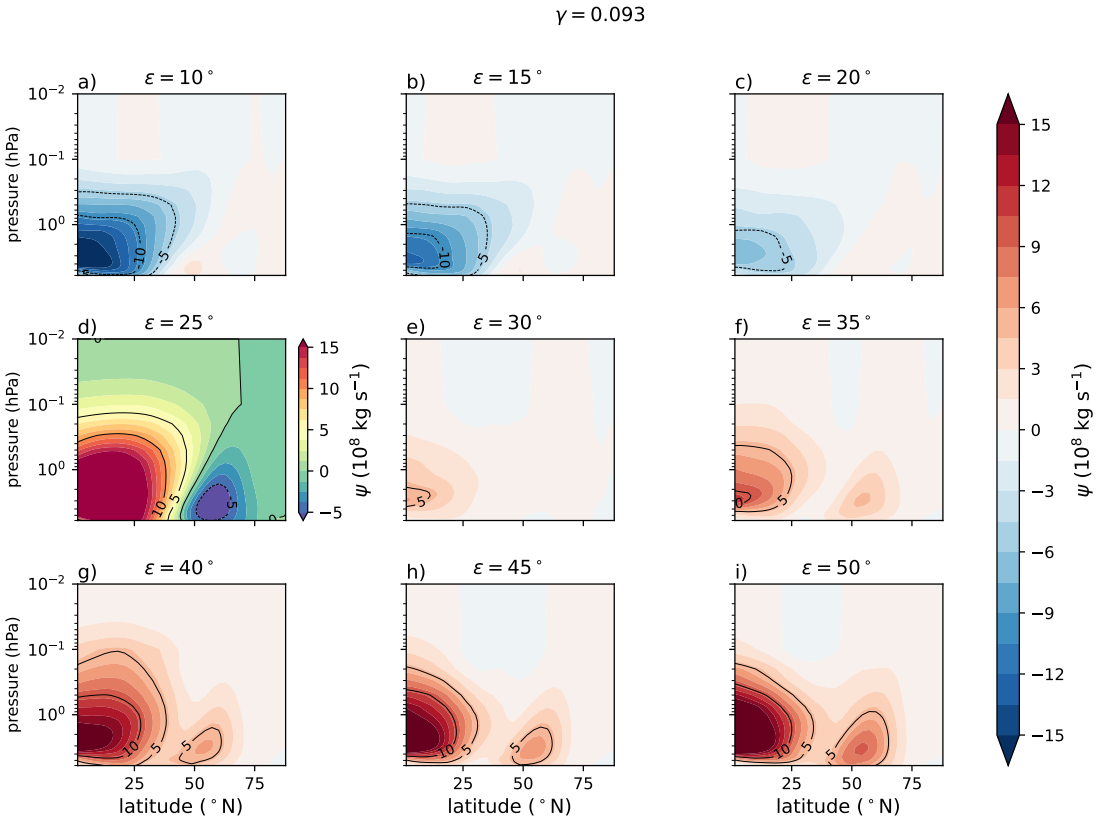

Figure B.7: **Northern winter mean meridional streamfunction averaged over 30 sols either side of the winter solstice for** $\gamma = 0.093$**.** $\varepsilon = 25$ shows absolute value of ψ, and all other panels show the anomaly from $\varepsilon = 25$ for the given value of ε.

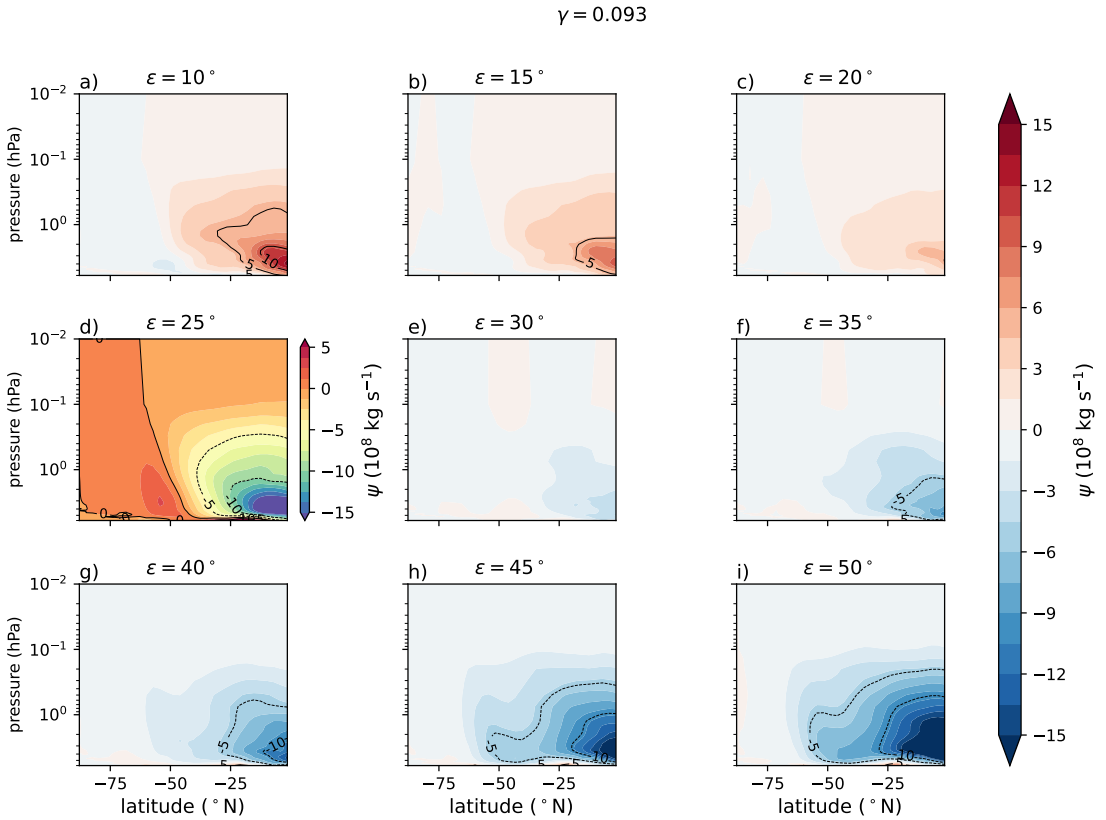

Figure B.8: **Southern winter mean meridional streamfunction averaged over 30 sols either side of the winter solstice for $\gamma = 0.093$.** $\varepsilon = 25$ shows absolute value of ψ, and all other panels show the anomaly from $\varepsilon = 25$ for the given value of ε.

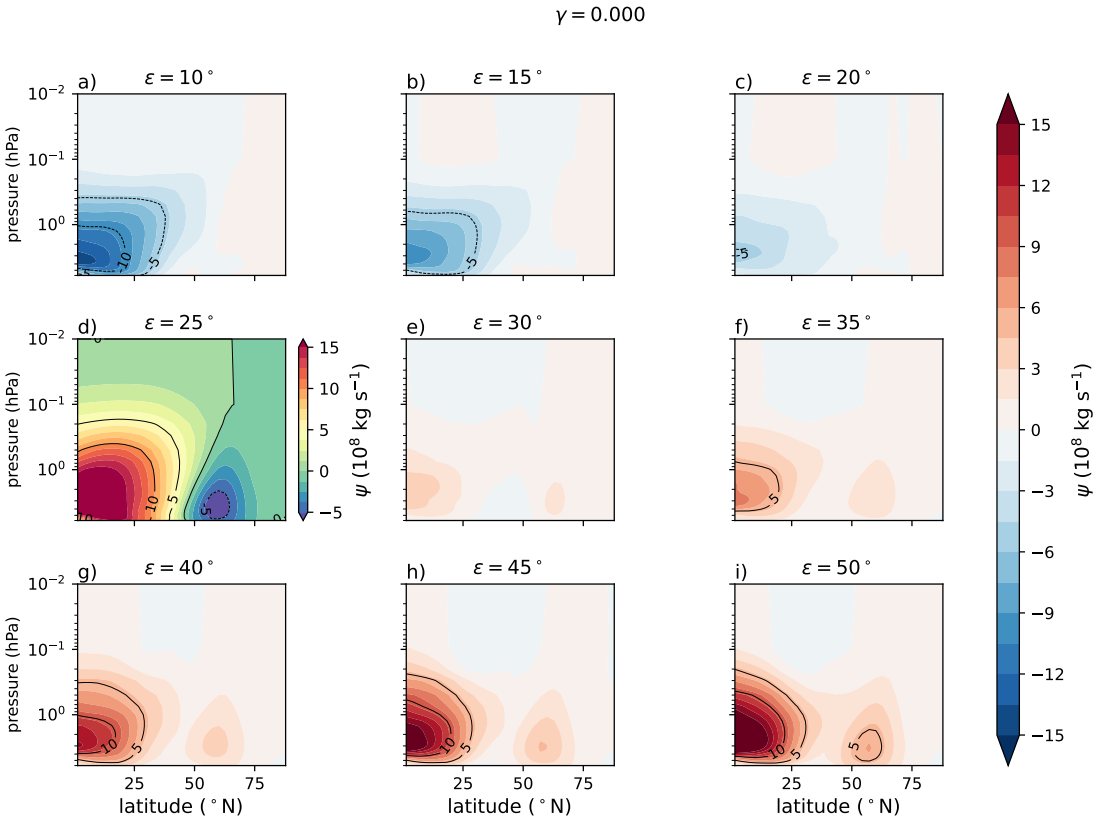

Figure B.9: **Northern winter mean meridional streamfunction averaged over 30 sols either side of the winter solstice for** $\gamma = 0.093$**.** $\varepsilon = 25$ shows absolute value of ψ, and all other panels show the anomaly from $\varepsilon = 25$ for the given value of ε.

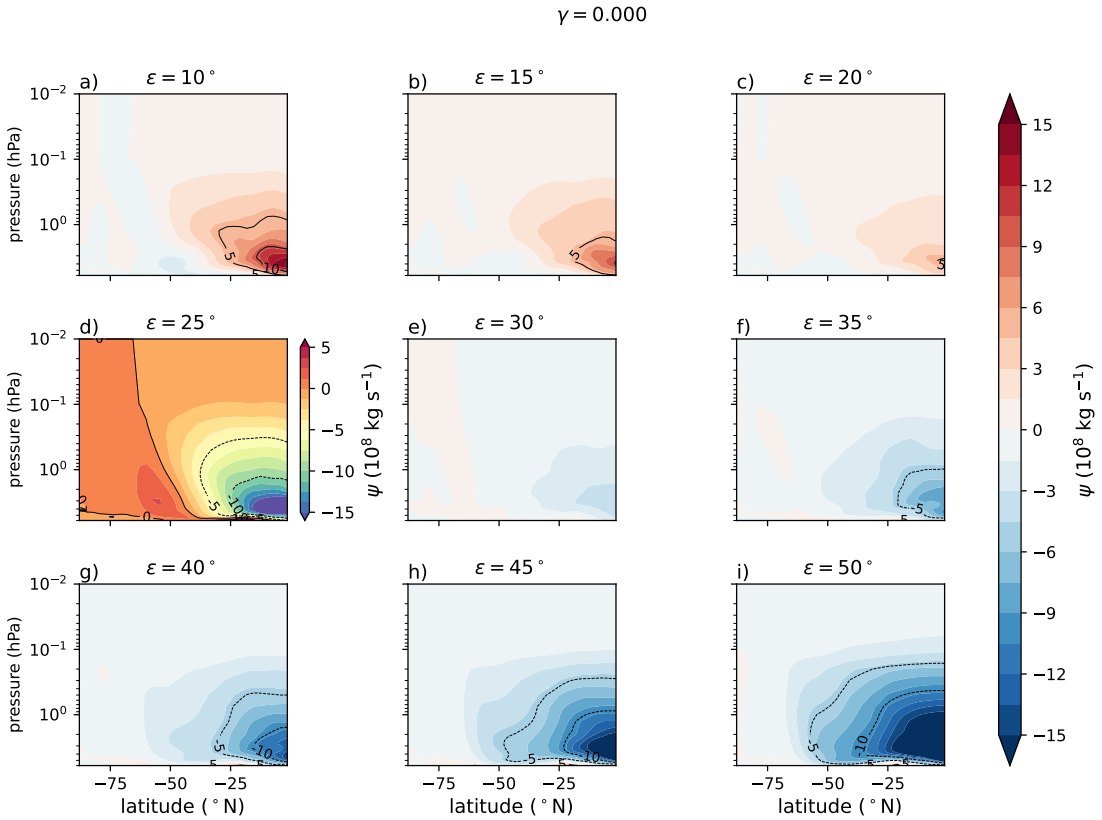

Figure B.10: **Northern winter mean meridional streamfunction averaged over 30 sols either side of the winter solstice for $\gamma = 0.000$.** $\varepsilon = 25$ shows absolute value of ψ, and all other panels show the anomaly from $\varepsilon = 25$ for the given value of ε.

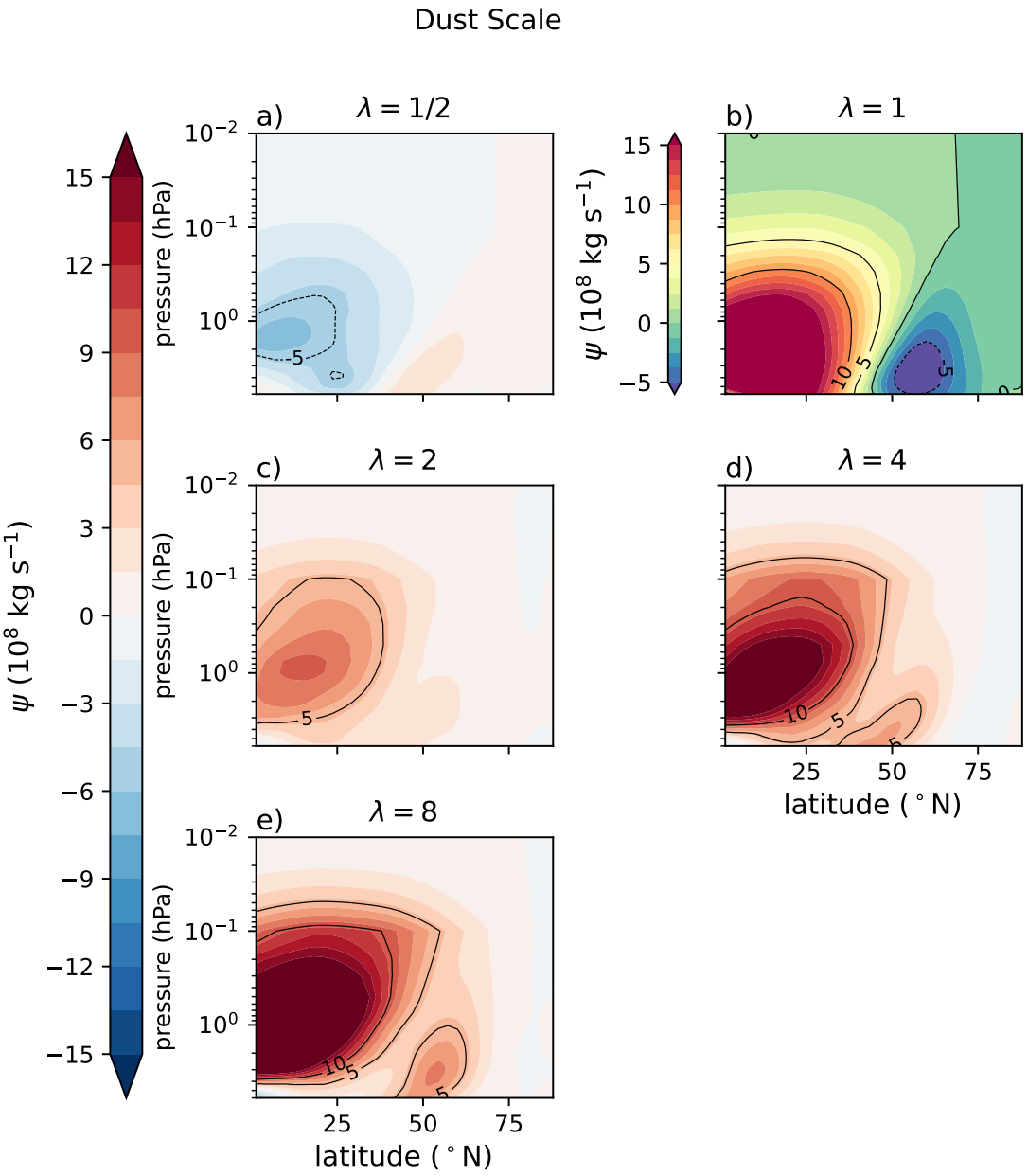

Figure B.11: **Northern winter mean meridional streamfunction averaged over 30 sols either side of the winter solstice for dust scale simulations.** $\varepsilon = 25$ shows absolute value of ψ, and all other panels show the anomaly from $\varepsilon = 25$ for the given value of ε.

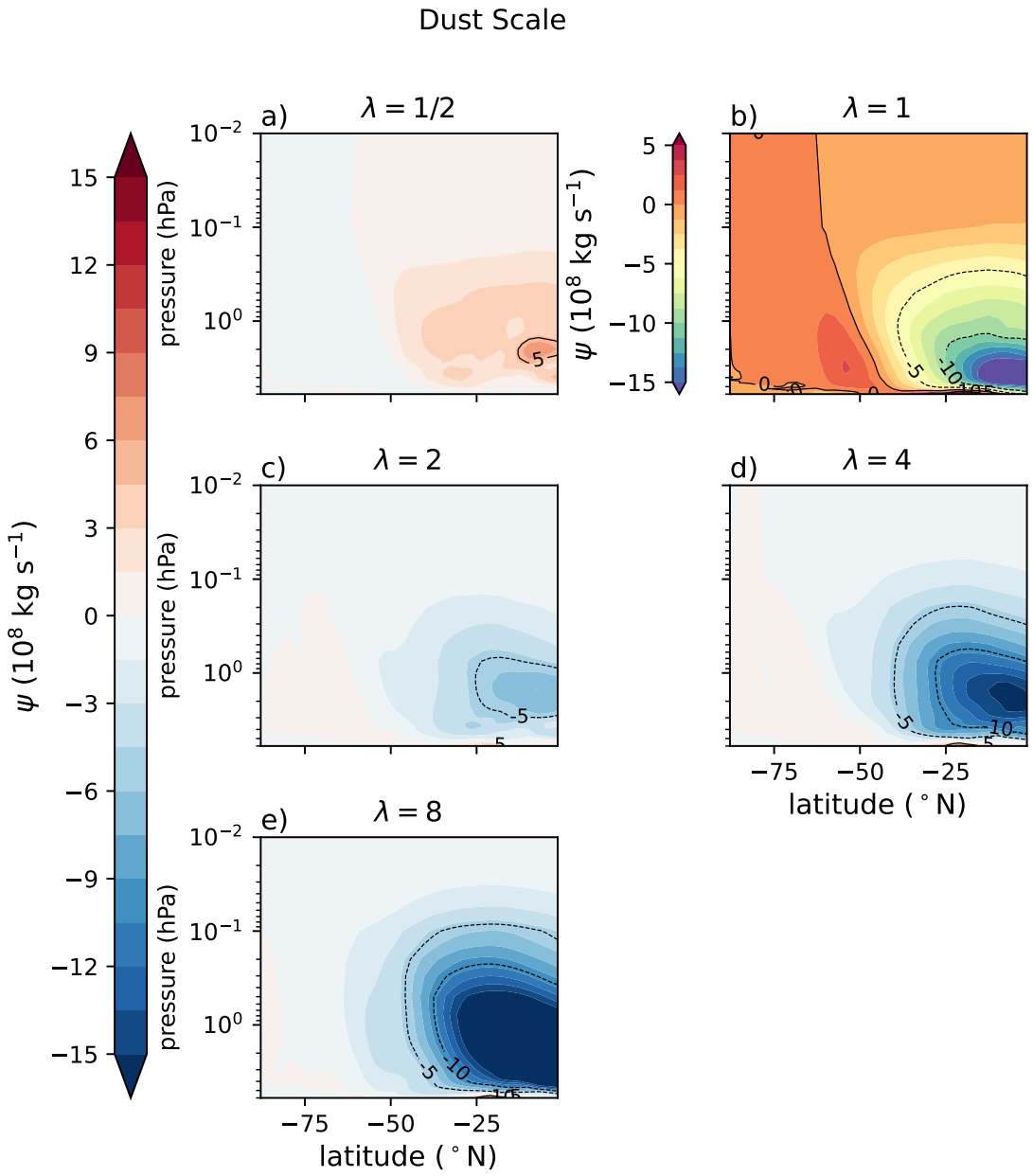

Figure B.12: **Northern winter mean meridional streamfunction averaged over 30 sols either side of the winter solstice for dust scale simulations.** $\varepsilon = 25$ shows absolute value of ψ, and all other panels show the anomaly from $\varepsilon = 25$ for the given value of ε.

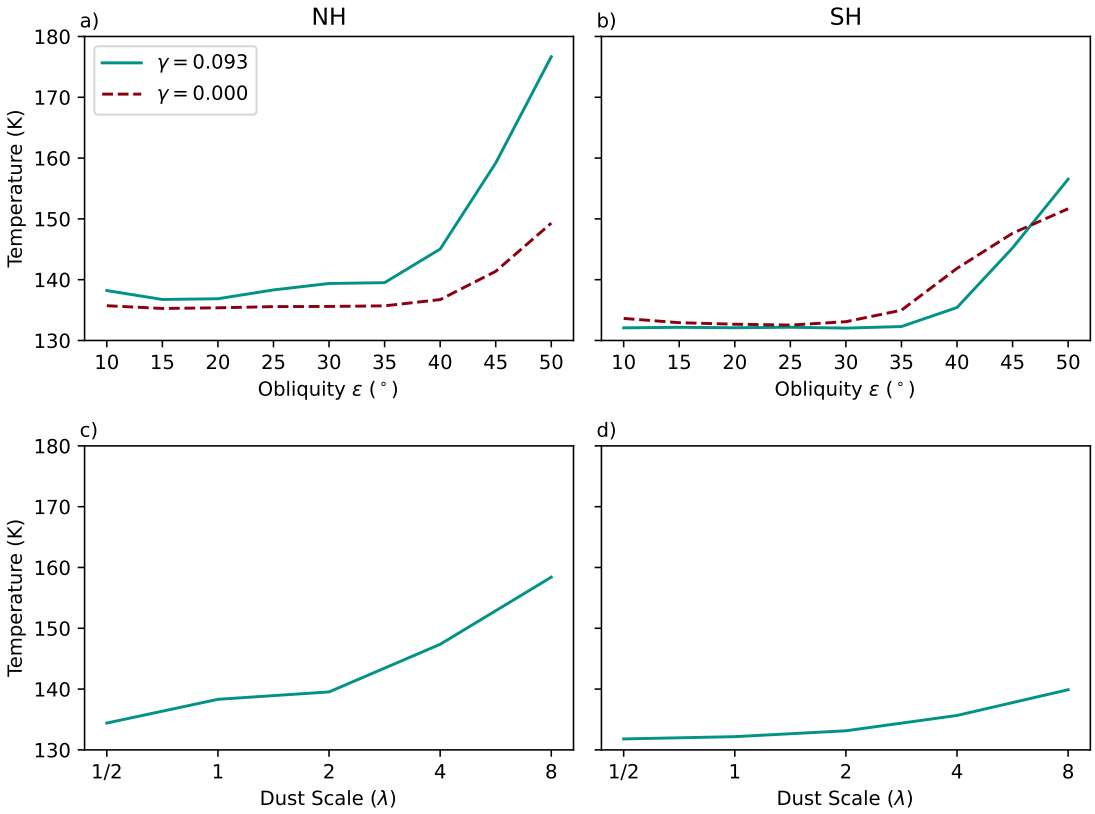

Figure B.13: **Polar winter temperature change with obliquity or dust scale.** Polar winter temperature (latitudinally-weighted average temperature over $75-90$°N/S on the 50Pa surface) in the northern (left) and southern (right) hemispheres. Winter mean is 60 sols averaged about $L_s = 270°$ ($L_s = 90°$) in the northern (southern) hemisphere. (top) obliquity simulations, and (bottom) dust scale simulations.

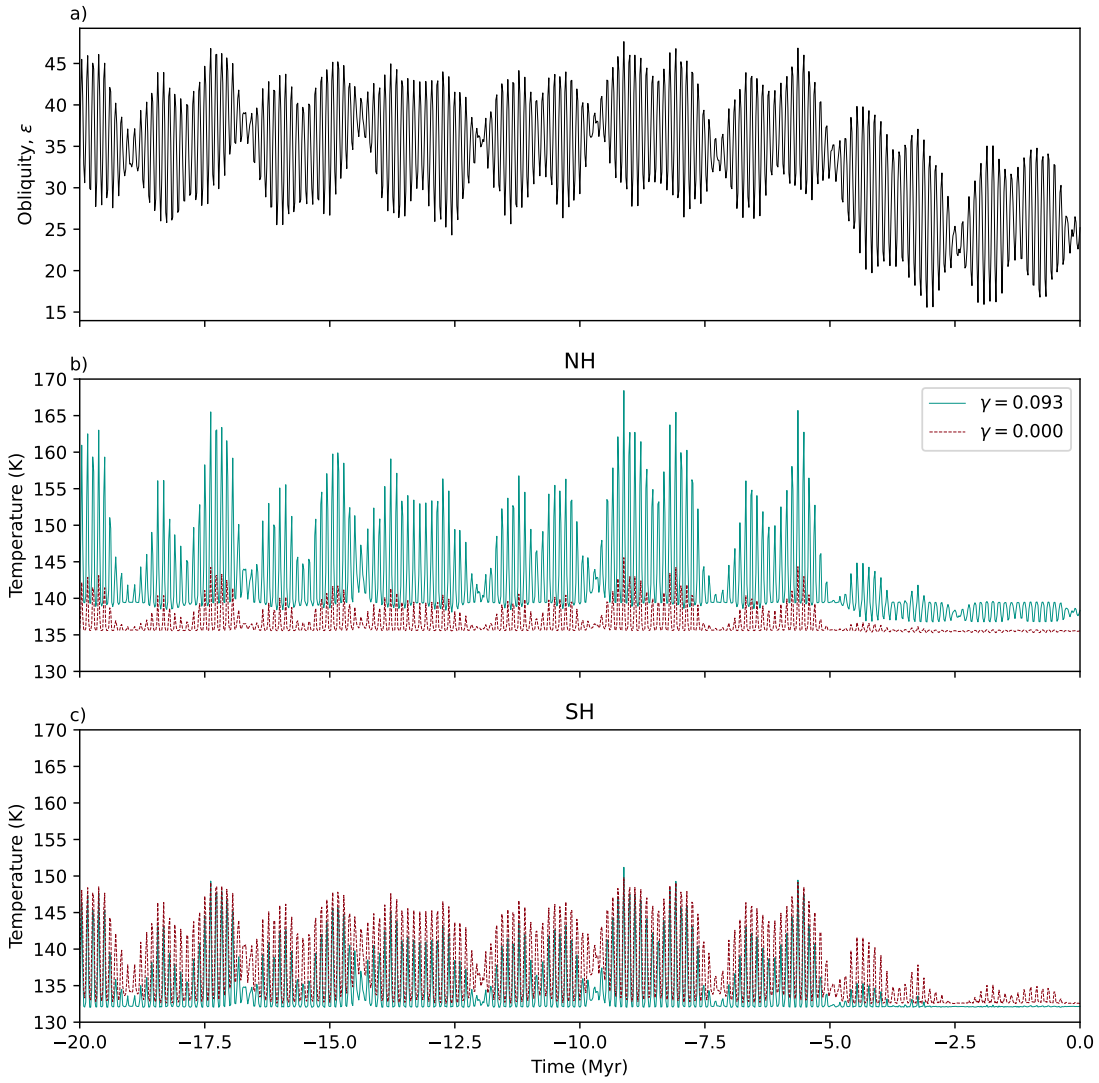

Figure B.14: **A time series of winter-time polar temperature (latitudinally-weighted average temperature over $75-90°$N/S on the 50Pa surface) according to historical integrations of obliquity.** Winter mean is 60 sols averaged about $L_s = 270°$ ($L_s = 90°$) in the northern (southern) hemisphere. (a) Obliquity from Laskar et al. [2004, data obtained here], and temperature changes with obliquity in (b) the northern hemisphere and (c) the southern hemisphere. We have chosen to include only variations based on obliquity due to the complication of the timing of perihelion with varying eccentricity also, although we show the time series for both $\gamma = 0.093$ (solid blue) and $\gamma = 0.000$ (dashed red).

APPENDIX C

APPENDICES FROM CHAPTER 4

C.1 Held-Suarez full temperature equation

The full temperature equation that the Held Suarez model follows is

$$\frac{\partial T}{\partial t} = -\nabla_p \cdot (T\mathbf{v}) - \frac{\partial (T\omega)}{\partial p} - k_T(\phi,\sigma)[T - T_{\text{eq}}(\lambda,\phi,p)], \tag{C.1}$$

where $\mathbf{v}$ is the horizontal velocity and $\omega = Dp/Dt$ is the vertical velocity in pressure coordinates.

C.2 Frierson grey radiation scheme

The details of the moist model used herein are given in Frierson et al. [2006], although we give a brief overview of the relevant details.

F06 simulations have an aquaplanet surface with no topography, with a shallow mixed layer chosen to conserve energy rather than with specified sea-surface temperatures. Mixed layer temperature evolves according to

$$C_O \frac{\partial T_s}{\partial t} = R_S - R_{Lu} + R_{Ld} - L_v E - S, \tag{C.2}$$

where C_O is a specified heat capacity, T_s is local surface temperature, L_v is the latent heat of vapourisation, E is the evaporative flux, S the sensible heat flux, and R_S, R_{Lu}, R_{Ld} are the net shortwave flux, upward and downward longwave fluxes, respectively.

In the infrared, atmospheric optical depths are defined by a surface value of form

$$\tau_0 = \tau_{0e} + (\tau_{0p} - \tau_{0e})\sin^2(\phi), \tag{C.3}$$

where τ_{0p} and τ_{0e} are surface values at the pole and equator, respectively. The optical depth varies with height according to

$$\tau = \tau_0 \left(f_l \left(\frac{p}{p_s} \right) + (1 - f_l) \left(\frac{p}{p_s} \right)^4 \right). \tag{C.4}$$

This choice of optical depth approximates the structure of water vapour within the atmosphere, without unreasonably long stratospheric relaxation timescales [Frierson et al., 2006].

The two-stream approximation is used to calculate radiative fluxes:

$$\frac{dU}{d\tau} = U - B \tag{C.5}$$

$$\frac{dD}{d\tau} = B - D, \tag{C.6}$$

where U and D are the upward and downward fluxes, and $B = \sigma T^4$ (σ here is the Stefan-Boltzmann constant).

Now, as in the temperature equation for the HS simulations, we have a diabatic source term. For F06/DF simulations, this is

$$Q_R = -\frac{1}{c_p \rho} \frac{\partial (U - D)}{\partial z}. \tag{C.7}$$

There are additionally surface fluxes, derived from standard drag laws, within the model. Full details are given in Frierson et al. [2006].

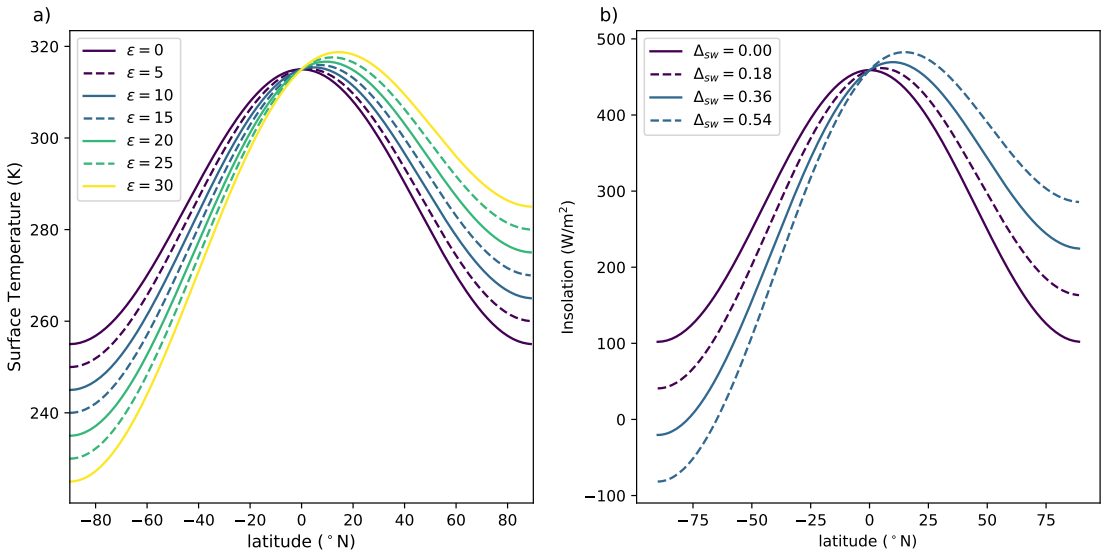

Figure C.1: **Prescribed forcings in simulations.** a) Equilibrium temperature profile for a range of values of ε in HS simulations. b) Incoming solar radiation for a range of values of Δ_{sw} in F06 simulations. Values of ε and Δ_{sw} correspond to the same latitude of maximal heating.

C.3 Supplementary Figures

We show the prescribed forcings that represent a change in obliquity (equilibrium surface temperature profile or incoming solar radiation) for our parameter sweep (Fig C.1).

C.3.1 The influence of a stratosphere

This section (Figs C.2-C.9) contains figures using simulations with the Polvani-Kushner (PK) stratosphere addition.

C.3.2 Taking the dry limit

This section (Figs C.10-C.17) contains figures created with simulations from the dry grey (DF) model.

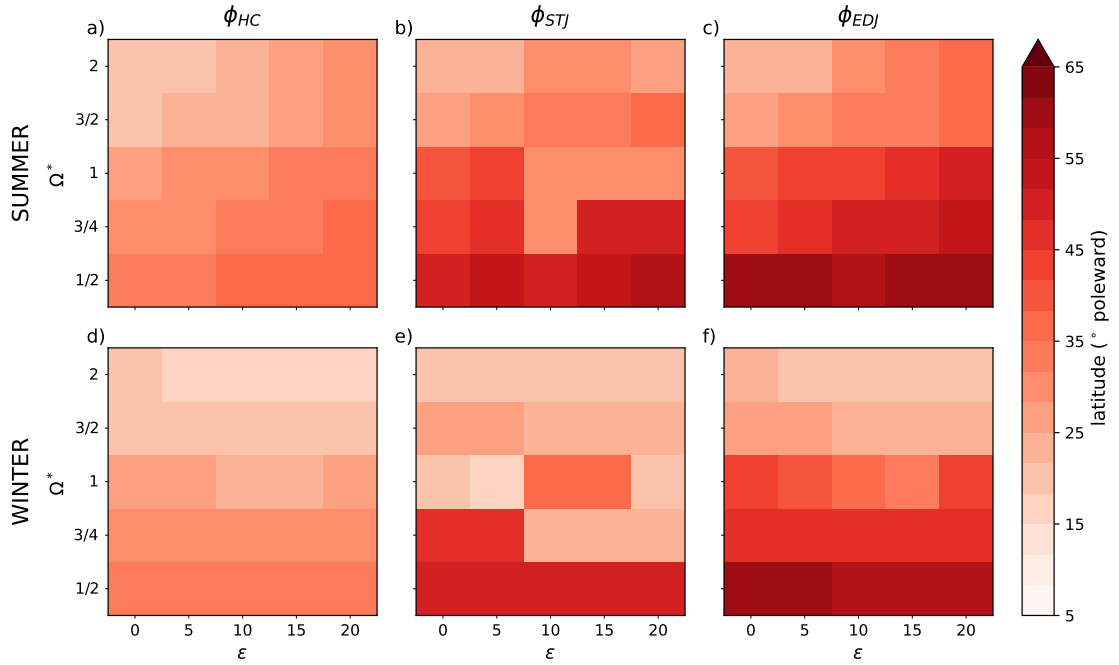

Figure C.2: **The influence of obliquity and rotation rate on the mean location of each metric.** The mean location of each metric (left: ϕ_{HC}; centre: ϕ_{STJ}; right: ϕ_{EDJ}), in the summer and winter hemisphere (top and bottom row, respectively). In each panel, one square represents one PK simulation, with obliquity and rotation rate on the x- and y-axis, respectively.

C.3.3 The number of maxima in upper- or lower-tropospheric winds

Finally, we show the location of each metric in all simulations, with the HS simulations characterised by the number of maxima in each jet. Figure shows that the separate latitudes of each metric in HS simulations may be characterised by the number of maxima - those simulations wherein there exist two maxima in u_{adj} sit separately from all other HS simulations.

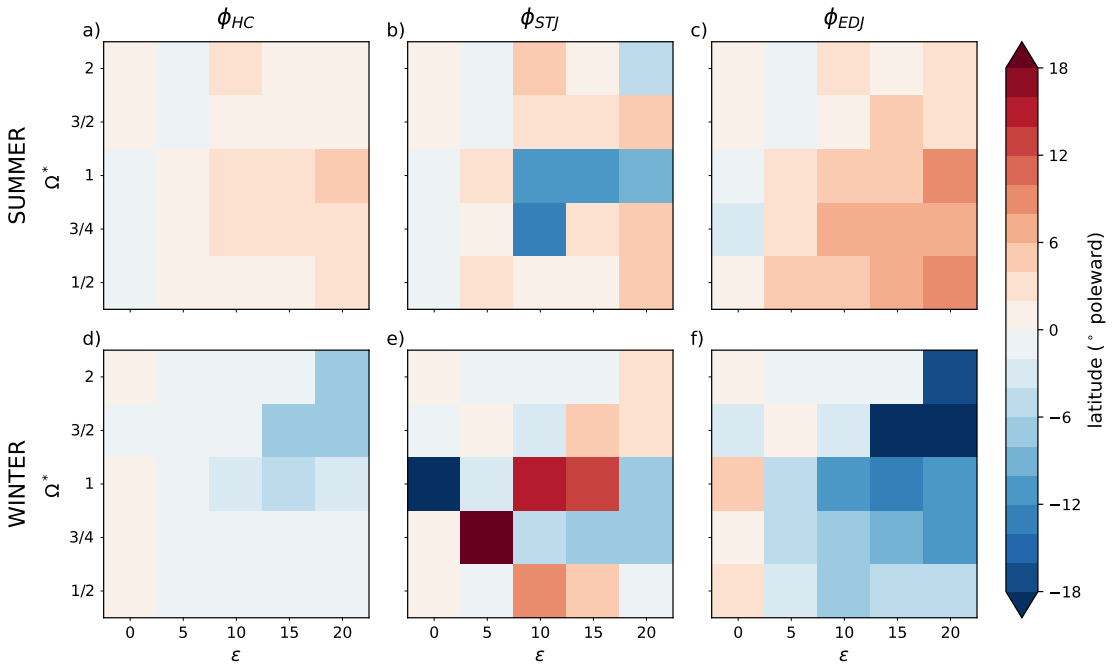

Figure C.3: **The difference in mean latitude in equivalent HS and PK simulations.** The difference (PK-HS) in mean location of each metric (left: ϕ_{HC}; centre: ϕ_{STJ}; right: ϕ_{EDJ}), in the summer and winter hemisphere (top and bottom row, respectively). In each panel, one square shows how much further poleward lies a metric in a PK simulation compared to the equivalent HS simulation, with obliquity and rotation rate on the x- and y-axis, respectively.

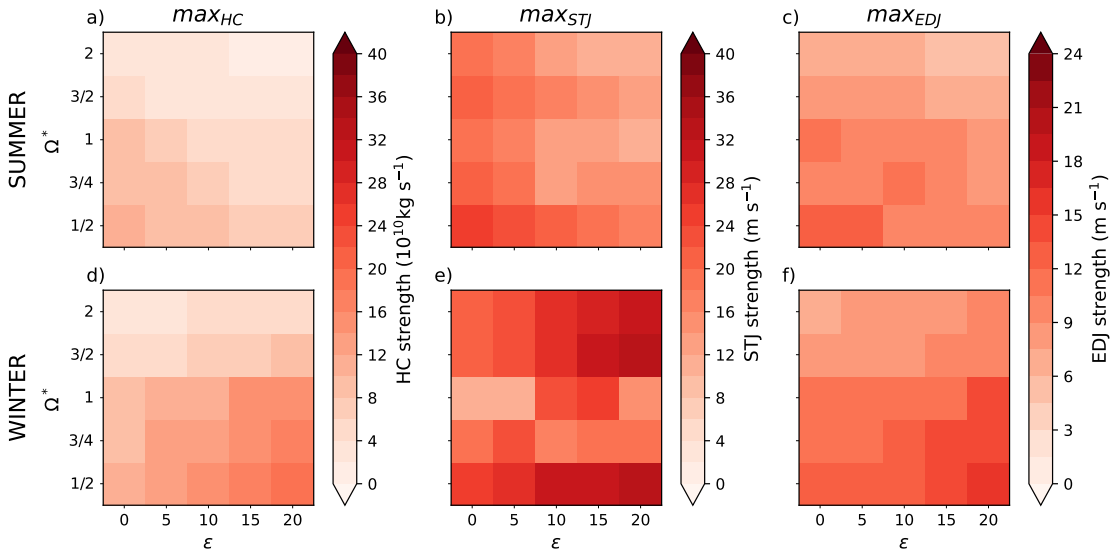

Figure C.4: **The influence of obliquity and rotation rate on the mean strength of the quantity defining each metric.** As in Figure C.2, except we show the mean strength of the quantities used to define each metric. The definitions of these strengths are given in the text.

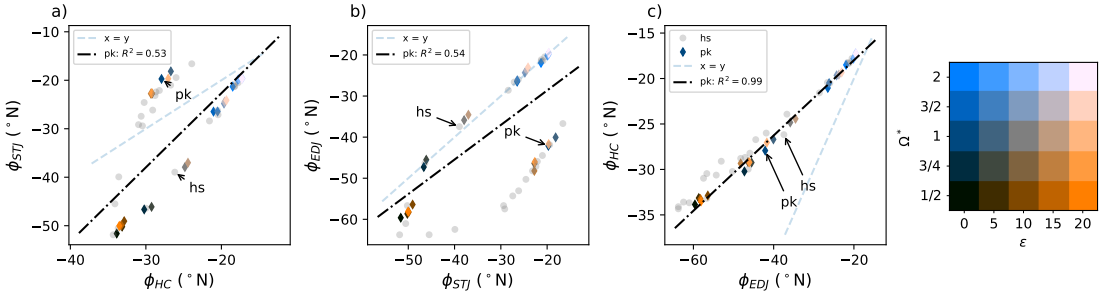

Figure C.5: **The relative latitudes of each metric.** The mean latitude of each metric in the SH plotted against the mean latitude of other metrics. Diamond markers represent PK simulations, and grey circular markers show HS simulations for comparison. Simulations with $\varepsilon = 0$ are indicated. PK markers are coloured according to the simulation's location in parameter space and, where appropriate, a linear regression is calculated (black dash-dotted) and its score is shown. A 1:1 line is also plotted in each panel (dashed grey).

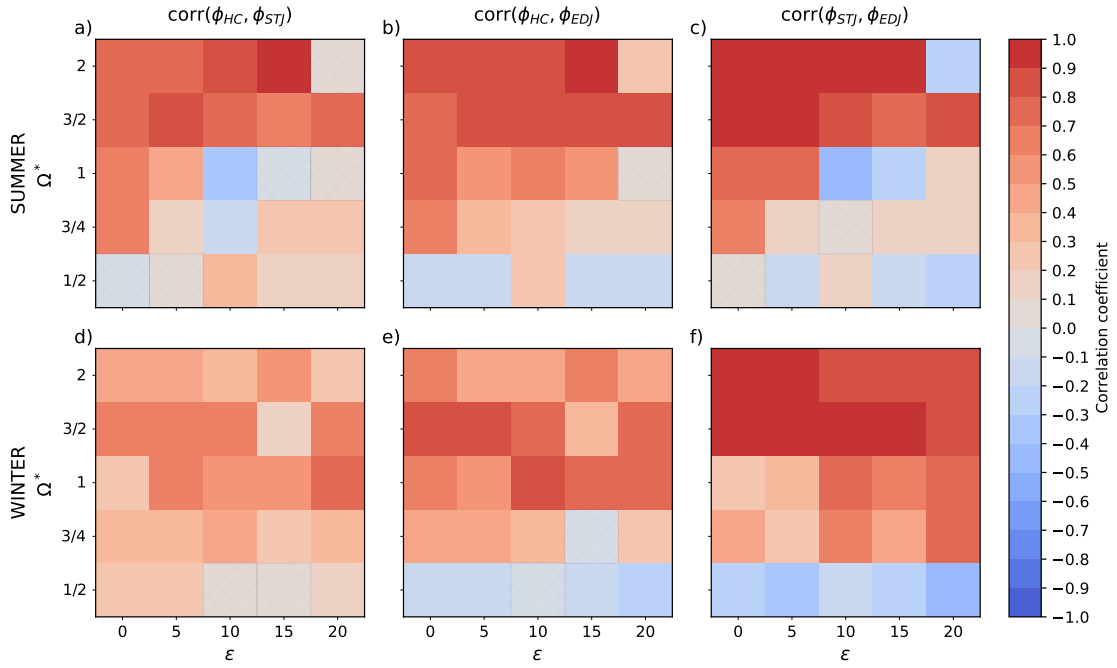

Figure C.6: **The influence of obliquity and rotation rate on the coupling between each metric.** The Pearson correlation coefficient (colour) between metrics (left: ϕ_{HC} and ϕ_{STJ}; centre: ϕ_{HC} and ϕ_{EDJ}; right: ϕ_{STJ} and ϕ_{EDJ}), in the summer and winter hemisphere (top and bottom row, respectively). In each panel, one square represents one PK simulation, with obliquity and rotation rate on the x- and y-axis, respectively. Squares are hatched where the relationship between the two metrics is not significant (p-value greater than 0.01).

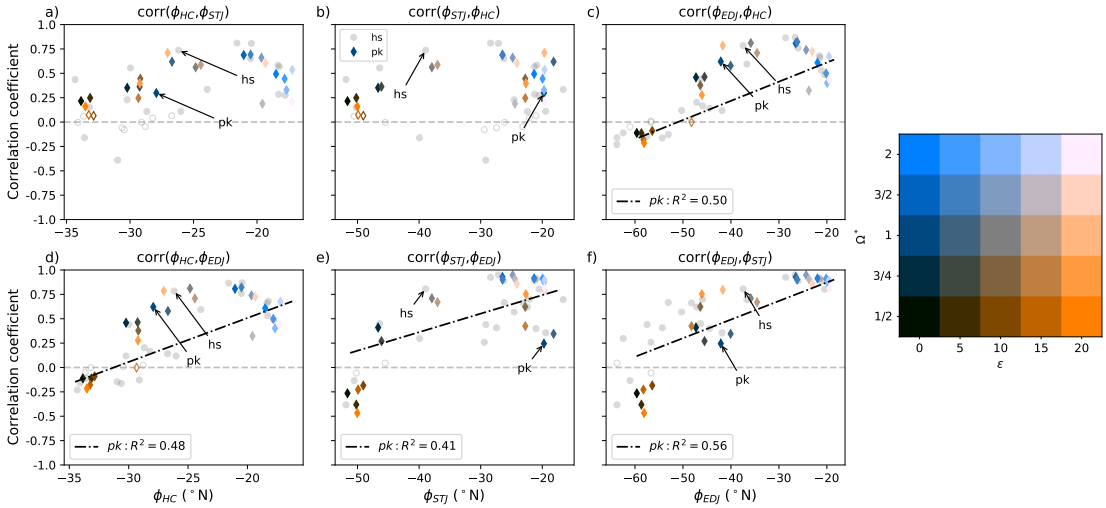

Figure C.7: **The influence of a metric's mean location on its coupling with other metrics.** The Pearson correlation coefficient between metrics as a function of each metric's mean latitude in the winter (southern) hemisphere (left: as a function of ϕ_{HC}; centre: as a function of ϕ_{STJ}; right: as a function of ϕ_{EDJ}). Diamond markers represent PK simulations, and grey circular markers show HS simulations for comparison. Simulations with $\varepsilon = 0$ are indicated. PK markers are coloured according to the simulation's location in parameter space, and are solid where the relationship between the two metrics has p-value less than 0.01. Where appropriate, linear regressions (black dash-dotted) have been fitted and their scores shown.

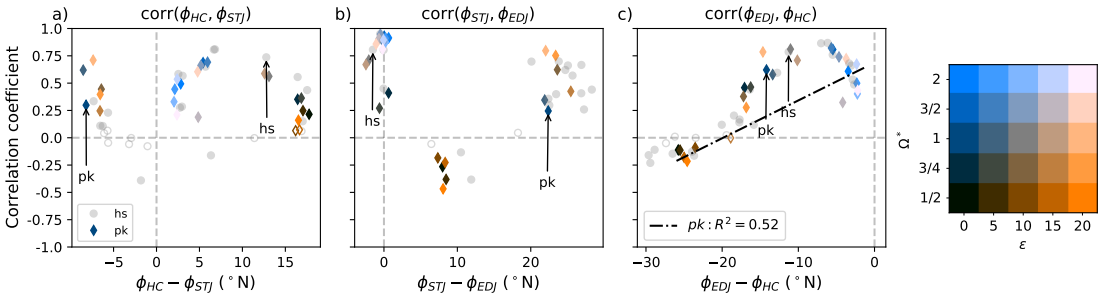

Figure C.8: **The influence of the separation in mean location of two metrics on their coupling.** The Pearson correlation coefficient between two metrics as a function of the separation between them in the winter (southern) hemisphere (left: as a function of ϕ_{HC}-ϕ_{STJ}; centre: as a function of ϕ_{STJ}-ϕ_{EDJ}; right: as a function of ϕ_{EDJ}-ϕ_{HC}). Diamond markers represent PK simulations, and grey circular markers show HS simulations for comparison. Simulations with $\varepsilon = 0$ are indicated. PK markers are coloured according to the simulation's location in parameter space, and are solid where the relationship between the two metrics has p-value less than 0.01. Where appropriate, linear regressions (black dash-dotted) have been fitted and their scores shown.

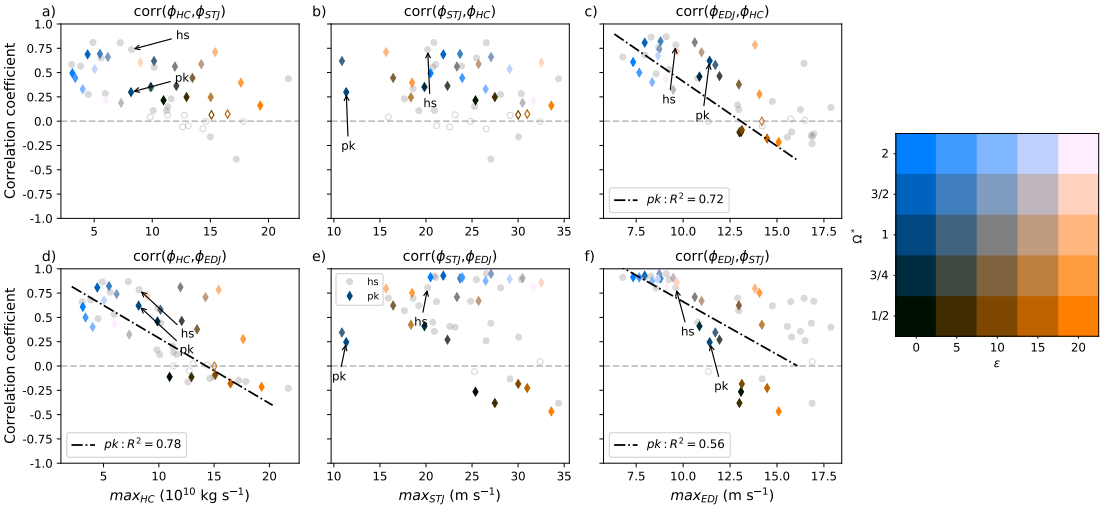

Figure C.9: **The influence of the mean strength of the quantity defining each metric on its coupling with other metrics.** As in Figure 4.8, except showing correlation coefficient between metrics as a function of the strength of the quantity defining each metric.

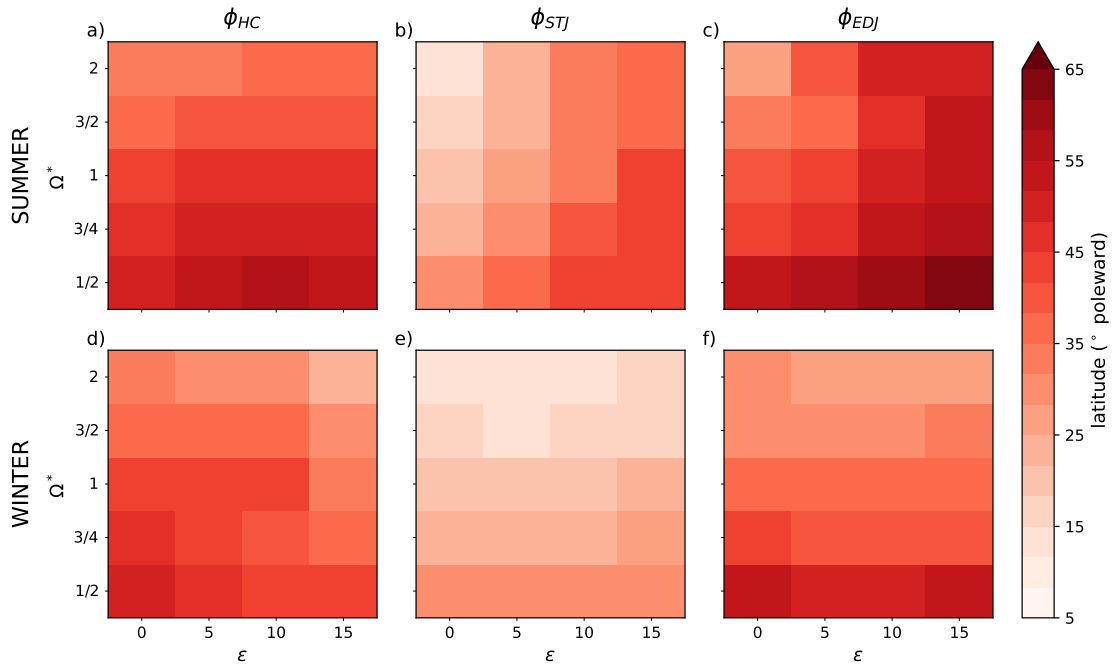

Figure C.10: **The influence of obliquity and rotation rate on the mean location of each metric in the dry grey model.** The mean location of each metric (left: ϕ_{HC}; centre: ϕ_{STJ}; right: ϕ_{EDJ}), in the summer and winter hemisphere (top and bottom row, respectively). In each panel, one square represents one DF simulation, with obliquity and rotation rate on the x- and y-axis, respectively.

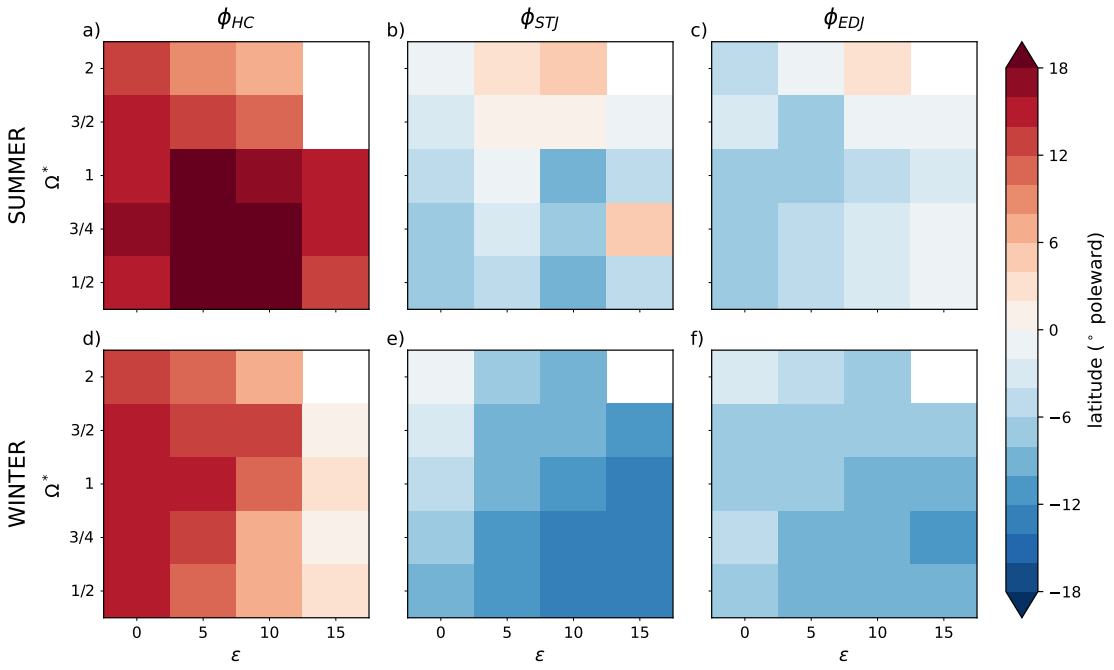

Figure C.11: **The difference in mean latitude in equivalent F06 and DF simulations.** The difference (DF-F06) in mean location of each metric (left: ϕ_{HC}; centre: ϕ_{STJ}; right: ϕ_{EDJ}), in the summer and winter hemisphere (top and bottom row, respectively). In each panel, one square shows how much further poleward lies a metric in a DF simulation compared to the equivalent F06 simulation, with obliquity and rotation rate on the x- and y-axis, respectively.

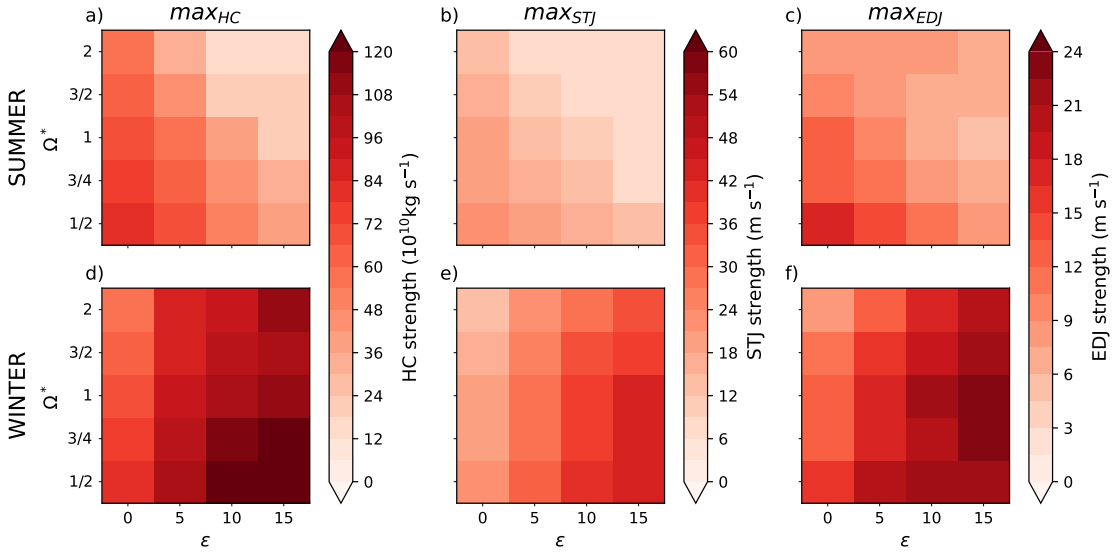

Figure C.12: **The influence of obliquity and rotation rate on the mean strength of the quantity defining each metric in the dry grey model.** As in Figure C.10, except we show the mean strength of the quantities used to define each metric. The definitions of these strengths are given in the text.

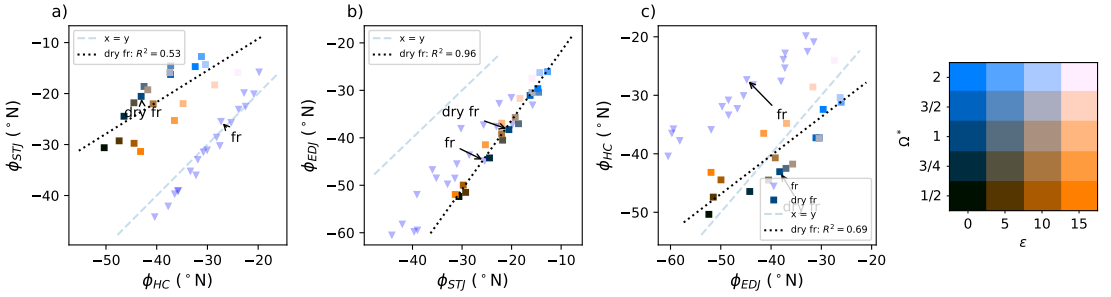

Figure C.13: **The relative latitudes of each metric in the dry grey model.** The mean latitude of each metric plotted against the mean latitude of other metrics. Square markers show dry DF simulations and are coloured according to the simulation's location in parameter space. Where appropriate, a linear regression is calculated (black dotted) and its score is shown. A 1:1 line is also plotted in each panel (dashed grey), and F06 simulations are shown in blue (triangular) for comparison. Simulations with $\varepsilon = 0$ are indicated.

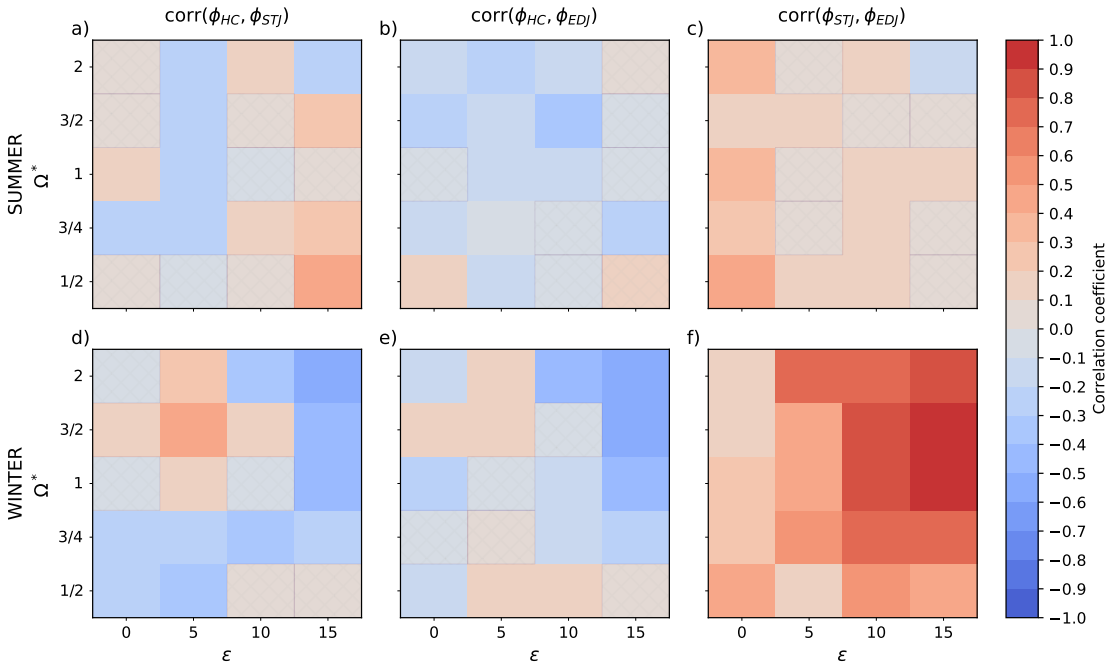

Figure C.14: **The influence of obliquity and rotation rate on the coupling between each metric in the dry grey model.** The Pearson correlation coefficient (colour) between metrics (left: ϕ_{HC} and ϕ_{STJ}; centre: ϕ_{HC} and ϕ_{EDJ}; right: ϕ_{STJ} and ϕ_{EDJ}), in the summer and winter hemisphere (top and bottom row, respectively). In each panel, one square represents one DF simulation, with obliquity and rotation rate on the x- and y-axis, respectively. Squares are hatched where the relationship between the two metrics is not significant (p-value greater than 0.01).

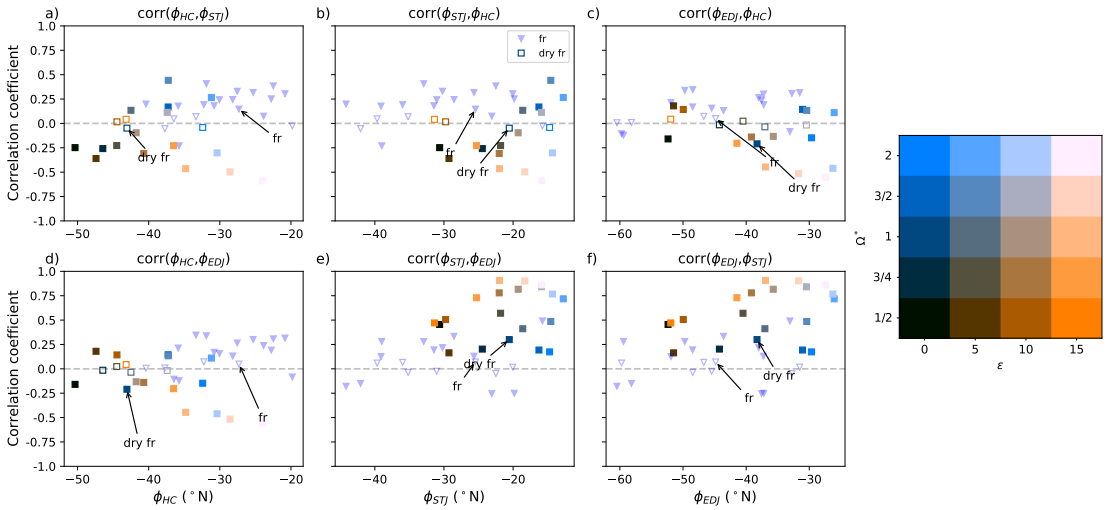

Figure C.15: **The influence of a metric's mean location on its coupling with other metrics in the moist model.** The Pearson correlation coefficient between metrics as a function of each metric's mean latitude in the winter (southern) hemisphere (left: as a function of ϕ_{HC}; centre: as a function of ϕ_{STJ}; right: as a function of ϕ_{EDJ}). Square markers show dry DF simulations, are coloured according to the simulation's location in parameter space, and are solid where the relationship between the two metrics has p-value less than 0.01. Where appropriate, a linear regression is calculated (black dotted) and its score is shown. A 1:1 line is also plotted in each panel (dashed grey), and F06 simulations are shown in blue (triangular) for comparison. Simulations with $\varepsilon = 0$ are indicated.

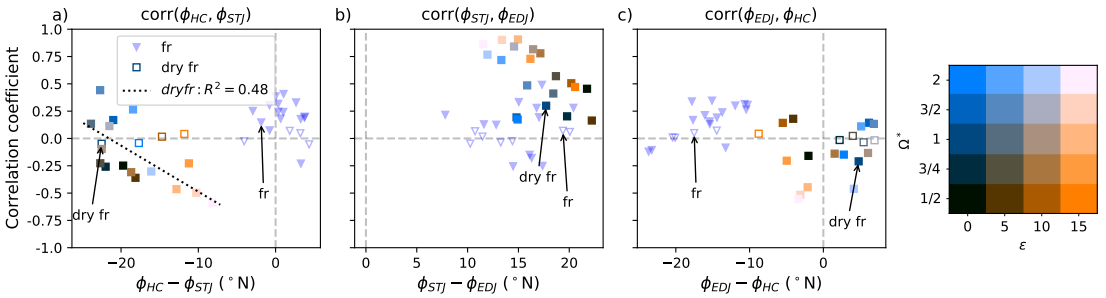

Figure C.16: **The influence of the separation in mean location of two metrics on their coupling in the moist model.** The Pearson correlation coefficient between two metrics as a function of the separation between them in the winter (southern) hemisphere (left: as a function of ϕ_{HC}-ϕ_{STJ}; centre: as a function of ϕ_{STJ}-ϕ_{EDJ}; right: as a function of ϕ_{EDJ}-ϕ_{HC}). Square markers show dry DF simulations, are coloured according to the simulation's location in parameter space, and are solid where the relationship between the two metrics has p-value less than 0.01. Where appropriate, a linear regression is calculated (black dotted) and its score is shown. A 1:1 line is also plotted in each panel (dashed grey), and F06 simulations are shown in blue (triangular) for comparison. Simulations with $\varepsilon = 0$ are indicated.

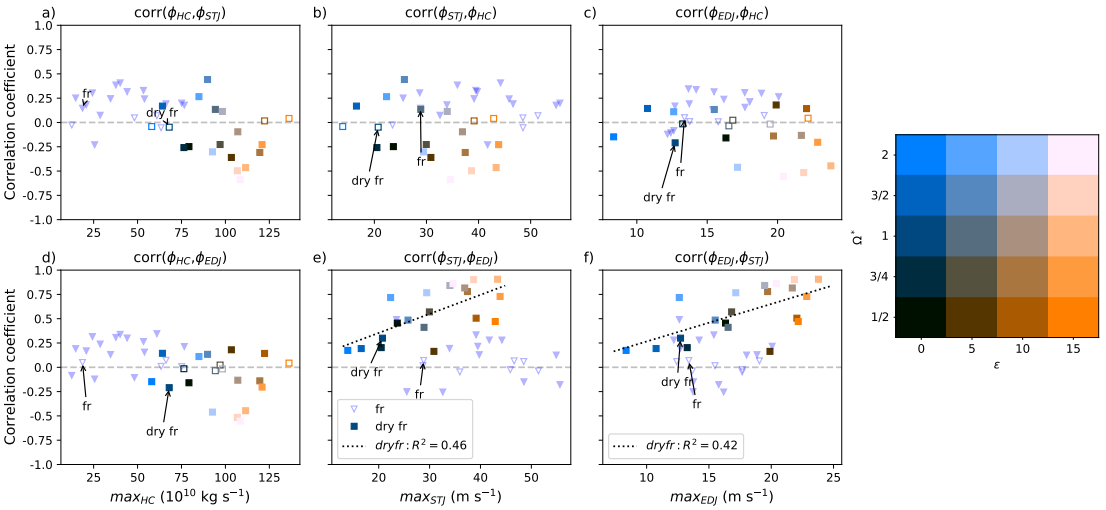

Figure C.17: **The influence of the mean strength of the quantity defining each metric on its coupling with other metrics.** As in Figure 4.15, except showing correlation coefficient between metrics as a function of the strength of the quantity defining each metric.

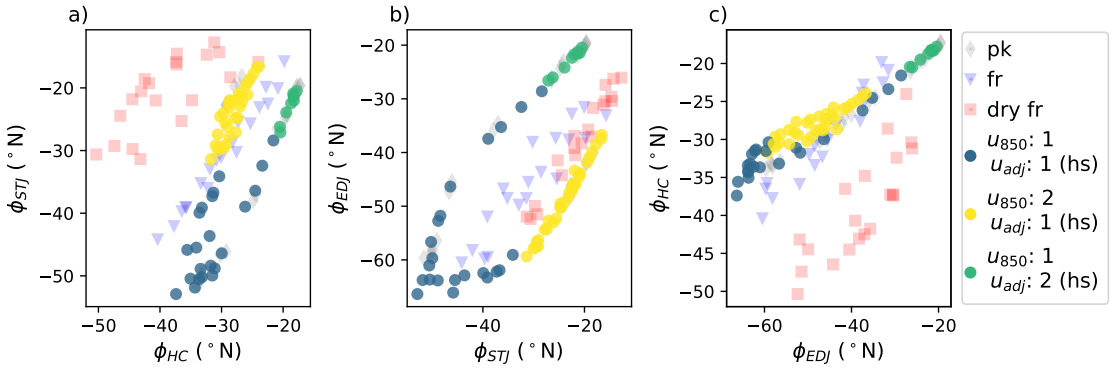

Figure C.18: **The relative latitude of each metric for all simulations, with HS simulations coloured according to the number of jet maxima.** The mean latitude of each metric plotted against the mean latitude of other metrics (winter). Circular markers show HS simulations, diamond markers represent PK simulations, triangular markers represent F06 simulations, and square markers represent DF simulations. HS markers are coloured according to the number of maxima in u_{850} and u_{adj}.

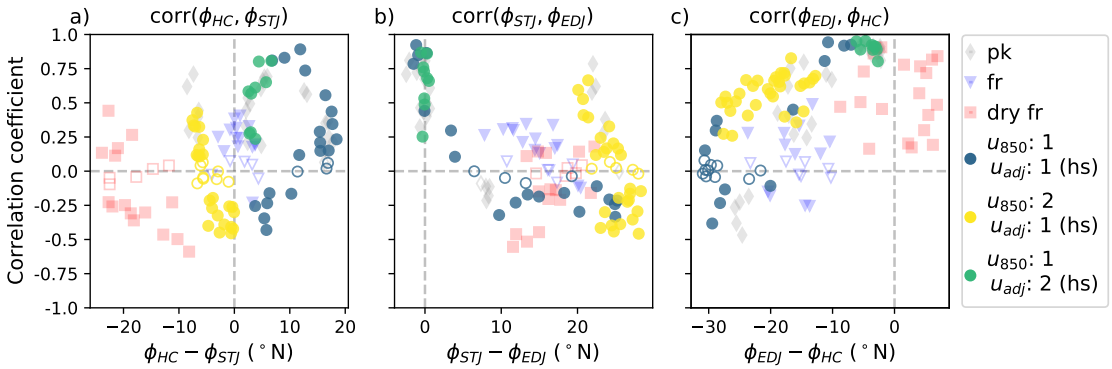

Figure C.19: **The influence of the number of jets and the separation in mean location of two metrics on their coupling, with HS simulations coloured according to the number of jet maxima.** The Pearson correlation coefficient between two metrics as a function of the separation between them in the winter (southern) hemisphere (left: as a function of ϕ_{HC}-ϕ_{STJ}; centre: as a function of ϕ_{STJ}-ϕ_{EDJ}; right: as a function of ϕ_{EDJ}-ϕ_{HC}). Circular markers show HS simulations, diamond markers represent PK simulations, triangular markers represent F06 simulations, and square markers represent DF simulations. HS markers are coloured according to the number of maxima in u_{850} and u_{adj}, and are solid where the relationship between the two metrics has p-value less than 0.01.

BIBLIOGRAPHY

Abalos, M., Legras, B., and Shuckburgh, E. (2016).
Interannual variability in effective diffusivity in the upper troposphere/lower stratosphere from reanalysis data.
Quarterly Journal of the Royal Meteorological Society, 142(697):1847–1861.

Achterberg, R. K., Conrath, B. J., Gierasch, P. J., Flasar, F. M., and Nixon, C. A. (2008).
Titan's middle-atmospheric temperatures and dynamics observed by the Cassini Composite Infrared Spectrometer.
Icarus, 194(1):263–277.

Adam, O., Grise, K. M., Staten, P., Simpson, I. R., Davis, S. M., Davis, N. A., Waugh, D. W., Birner, T., and Ming, A. (2018).
The TropD software package (v1): standardized methods for calculating tropical-width diagnostics.
Geoscientific Model Development, 11(10):4339–4357.

Adriani, A., Mura, A., Orton, G., Hansen, C., Altieri, F., Moriconi, M. L., Rogers, J., Eichstädt, G., Momary, T., Ingersoll, A. P., Filacchione, G., Sindoni, G., Tabataba-Vakili, F., Dinelli, B. M., Fabiano, F., Bolton, S. J., Connerney, J. E. P., Atreya, S. K., Lunine, J. I., Tosi, F., Migliorini, A., Grassi, D., Piccioni, G., Noschese, R., Cicchetti, A., Plainaki, C., Olivieri, A., O'Neill, M. E., Turrini, D., Stefani, S., Sordini, R., and Amoroso, M. (2018).
Clusters of cyclones encircling Jupiter's poles.
Nature, 555(7695):216–219.

Allison, M., Godfrey, D. A., and Beebe, R. F. (1990).
A Wave Dynamical Interpretation of Saturn's Polar Hexagon.
Science, 247(4946):1061–1063.

Andrews, D. G., Holton, J. R., and Leovy, C. B. (1987).
Tracer Transport in the Middle Atmosphere.
In *International Geophysics*, pages 343–391. Elsevier.

Archer, C. L. and Caldeira, K. (2008).
Historical trends in the jet streams.
Geophysical Research Letters, 35(8).

Ball, E. (2021).

BrisClimate/Roles_of_latent_heat_and_dust_on_the_Martian_polar_vortex: Analysis scripts second release.

Ball, E. R., Mitchell, D. M., Seviour, W. J. M., Thomson, S. I., and Vallis, G. K. (2021).
The Roles of Latent Heating and Dust in the Structure and Variability of the Northern Martian Polar Vortex.
The Planetary Science Journal, 2(5):203.

Banfield, D., Conrath, B., Gierasch, P., Wilson, R., and Smith, M. (2004).
Traveling waves in the martian atmosphere from MGS TES Nadir data.
Icarus, 170(2):365 – 403.

Barnes, J. R. and Haberle, R. M. (1996).
The Martian zonal-mean circulation: angular momentum and potential vorticity structure in GCM simulations.
Journal of Atmospheric Sciences, 53(21):3143–3156.

Barnes, J. R., Haberle, R. M., Wilson, R. J., Lewis, S. R., Murphy, J. R., and Read, P. L. (2017).
The Global Circulation.
Cambridge Planetary Science. Cambridge University Press.

Barnes, J. R., Walsh, T. D., and Murphy, J. R. (1996).
Transport timescales in the Martian atmosphere: General circulation model simulations.
Journal of Geophysical Research: Planets, 101(E7):16881–16889.

Bertrand, T., Wilson, R. J., Kahre, M. A., Urata, R., and Kling, A. (2020).
Simulation of the 2018 Global Dust Storm on Mars Using the NASA Ames Mars GCM: A Multitracer Approach.
J. Geophys. Res. (Planets), 125(7):e2019JE006122.
e2019JE006122 2019JE006122.

Birner, T., Davis, S. M., and Seidel, D. J. (2014).
The changing width of Earth's tropical belt.
Physics Today, 67(12):38–44.

Boutle, I. A., Joshi, M., Lambert, F. H., Mayne, N. J., Lyster, D., Manners, J., Ridgway, R., and Kohary, K. (2020).
Mineral dust increases the habitability of terrestrial planets but confounds biomarker detection.
Nature Communications, 11(1).

Bretagnon, P. (1974).
Long-period terms in the solar system.
Astron. Astrophys., 30(1):141–154.

Brueshaber, S. R., Sayanagi, K. M., and Dowling, T. E. (2019).
Dynamical regimes of giant planet polar vortices.
Icarus, 323:46–61.

Butler, A. H., Sjoberg, J. P., Seidel, D. J., and Rosenlof, K. H. (2017).
A sudden stratospheric warming compendium.
Earth System Science Data, 9(1):63–76.

Carone, L., Keppens, R., Decin, L., and Henning, T. (2017).
Stratosphere circulation on tidally locked ExoEarths.
Monthly Notices of the Royal Astronomical Society, 473(4):4672–4685.

Charney, J. G. and Drazin, P. G. (1961).
Propagation of planetary-scale disturbances from the lower into the upper atmosphere.
Journal of Geophysical Research, 66(1):83–109.

Chemke, R. and Kaspi, Y. (2015).
Poleward migration of eddy-driven jets.
Journal of Advances in Modeling Earth Systems, 7(3):1457–1471.

Chemke, R. and Kaspi, Y. (2017).
Dynamics of Massive Atmospheres.
The Astrophysical Journal, 845(1):1.

Clancy, R. T., Sandor, B. J., Wolff, M. J., Christensen, P. R., Smith, M. D., Pearl, J. C., Conrath, B. J., and Wilson, R. J. (2000).
An intercomparison of ground-based millimeter, MGS TES, and Viking atmospheric temperature measurements: Seasonal and interannual variability of temperatures and dust loading in the global Mars atmosphere.
J. Geophys. Res., 105(E4):9553–9572.

Clow, G. D. (1987).
Generation of liquid water on Mars through the melting of a dusty snowpack.
Icarus, 72(1):95–127.

Conrath, B. J. (1975).
Thermal structure of the Martian atmosphere during the dissipation of the dust storm of 1971.
Icarus, 24(1):36–46.

Conrath, B. J. (1981).
Planetary-scale wave structure in the Martian atmosphere.
Icarus, 48(2):246–255.

Courville, S. W., Perry, M. R., and Putzig, N. E. (2021).
Lower Bounds on the Thickness and Dust Content of Layers within the North Polar Layered Deposits of Mars from Radar Forward Modeling.
The Planetary Science Journal, 2(1):28.

Davis, N. and Birner, T. (2016).
Climate Model Biases in the Width of the Tropical Belt.
Journal of Climate, 29(5):1935 – 1954.

Davis, N. and Birner, T. (2017).
On the Discrepancies in Tropical Belt Expansion between Reanalyses and Climate Models and among Tropical Belt Width Metrics.
Journal of Climate, 30(4):1211 – 1231.

Davis, N. A. and Birner, T. (2019).
Eddy Influences on the Hadley Circulation.
Journal of Advances in Modeling Earth Systems, 11(6):1563–1581.

Davis, S. M. and Rosenlof, K. H. (2012).
A Multidiagnostic Intercomparison of Tropical-Width Time Series Using Reanalyses and Satellite Observations.
Journal of Climate, 25(4):1061 – 1078.

Domeisen, D. I. V., Grams, C. M., and Papritz, L. (2020).
The role of North Atlantic–European weather regimes in the surface impact of sudden stratospheric warming events.
Weather and Climate Dynamics, 1(2):373–388.

Dritschel, D. G. and Polvani, L. M. (1992).
The roll-up of vorticity strips on the surface of a sphere.
Journal of Fluid Mechanics, 234:47–69.

Eckermann, S. D., Ma, J., and Zhu, X. (2011).
Scale-dependent infrared radiative damping rates on Mars and their role in the deposition of gravity-wave momentum flux.
Icarus, 211(1):429–442.

Eyring, V., Bony, S., Meehl, G. A., Senior, C. A., Stevens, B., Stouffer, R. J., and Taylor, K. E. (2016).
Overview of the Coupled Model Intercomparison Project Phase 6 (CMIP6) experimental design and organization.
Geoscientific Model Development, 9(5):1937–1958.

Farman, J. C., Gardiner, B. G., and Shanklin, J. D. (1985).
Large losses of total ozone in antarctica reveal seasonal ClOx/NOx interaction.
Nature, 315(6016):207–210.

Fauchez, T. J., Turbet, M., Sergeev, D. E., Mayne, N. J., Spiga, A., Sohl, L., Saxena, P., Deitrick, R., Gilli, G., Domagal-Goldman, S. D., Forget, F., Consentino, R., Barnes, R., Haqq-Misra, J., Way, M. J., Wolf, E. T., Olson, S., Crouse, J. S., Janin, E., Bolmont, E., Leconte, J., Chaverot, G., Jaziri, Y., Tsigaridis, K., Yang, J., Pidhorodetska, D., Kopparapu,

R. K., Chen, H., Boutle, I. A., Lefevre, M., Charnay, B., Burnett, A., Cabra, J., and Bouldin, N. (2021).
TRAPPIST Habitable Atmosphere Intercomparison (THAI) Workshop Report.
The Planetary Science Journal, 2(3):106.

Faulk, S., Mitchell, J., and Bordoni, S. (2017).
Effects of Rotation Rate and Seasonal Forcing on the ITCZ Extent in Planetary Atmospheres.
Journal of the Atmospheric Sciences, 74(3):665 – 678.

Flasar, F. M., Achterberg, R. K., Conrath, B. J., Gierasch, P. J., Kunde, V. G., Nixon, C. A., Bjoraker, G. L., Jennings, D. E., Romani, P. N., Simon-Miller, A. A., Bézard, B., Coustenis, A., Irwin, P. G. J., Teanby, N. A., Brasunas, J., Pearl, J. C., Segura, M. E., Carlson, R. C., Mamoutkine, A., Schinder, P. J., Barucci, A., Courtin, R., Fouchet, T., Gautier, D., Lellouch, E., Marten, A., Prangé, R., Vinatier, S., Strobel, D. F., Calcutt, S. B., Read, P. L., Taylor, F. W., Bowles, N., Samuelson, R. E., Orton, G. S., Spilker, L. J., Owen, T. C., Spencer, J. R., Showalter, M. R., Ferrari, C., Abbas, M. M., Raulin, F., Edgington, S., Ade, P., and Wishnow, E. H. (2005).
Titan's Atmospheric Temperatures, Winds, and Composition.
Science, 308(5724):975–978.

Fletcher, L. N., Irwin, P. G. J., Orton, G. S., Teanby, N. A., Achterberg, R. K., Bjoraker, G. L., Read, P. L., Simon-Miller, A. A., Howett, C., de Kok, R., Bowles, N., Calcutt, S. B., Hesman, B., and Flasar, F. M. (2008).
Temperature and Composition of Saturn's Polar Hot Spots and Hexagon.
Science, 319(5859):79–81.

Fletcher, L. N., Orton, G. S., Sinclair, J. A., Guerlet, S., Read, P. L., Antuñano, A., Achterberg, R. K., Flasar, F. M., Irwin, P. G. J., Bjoraker, G. L., Hurley, J., Hesman, B. E., Segura, M., Gorius, N., Mamoutkine, A., and Calcutt, S. B. (2018).
A hexagon in Saturn's northern stratosphere surrounding the emerging summertime polar vortex.
Nature Communications, 9(1).

Forget, F., Byrne, S., Head, J. W., Mischna, M. A., and Schörghofer, N. (2017).
Recent Climate Variations, page 497–525.
Cambridge Planetary Science. Cambridge University Press.

Forget, F., Hourdin, F., Fournier, R., Hourdin, C., Talagrand, O., Collins, M., Lewis, S. R., Read, P. L., and Huot, J.-P. (1999).
Improved general circulation models of the Martian atmosphere from the surface to above 80 km.
J. Geophys. Res., 104(E10):24155–24176.

Forget, F., Hourdin, F., and Talagrand, O. (1998).
CO_2 Snowfall on Mars: Simulation with a General Circulation Model.

Icarus, 131(2):302 – 316.

French, R. G. and Gierasch, P. J. (1979).
The Martian polar vortex: Theory of seasonal variation and observations of eolian features.
Journal of Geophysical Research, 84(B9):4634.

Frierson, D. M. W., Held, I. M., and Zurita-Gotor, P. (2006).
A Gray-Radiation Aquaplanet Moist GCM. Part I: Static Stability and Eddy Scale.
Journal of the Atmospheric Sciences, 63(10):2548 – 2566.

Gavriel, N. and Kaspi, Y. (2021).
The number and location of Jupiter's circumpolar cyclones explained by vorticity dynamics.
Nature Geoscience, 14(8):559–563.

Gooding, J. L. (1986).
Martian dust particles as condensation nuclei: A preliminary assessment of mineralogical factors.
Icarus, 66(1):56 – 74.

Graham, R. J. (2021).
High pCO_2 Reduces Sensitivity to CO_2 Perturbations on Temperate, Earth-like Planets Throughout Most of Habitable Zone.
Astrobiology, 21(11):1406–1420.

Greybush, S. J., Kalnay, E., Wilson, R. J., Hoffman, R. N., Nehrkorn, T., Leidner, M., Eluszkiewicz, J., Gillespie, H. E., Wespetal, M., Zhao, Y., Hoffman, M., Dudas, P., McConnochie, T., Kleinböhl, A., Kass, D., McCleese, D., and Miyoshi, T. (2019).
The Ensemble Mars Atmosphere Reanalysis System (EMARS) Version 1.0.
Geoscience Data Journal, 6(2):137–150.

Greybush, S. J., Wilson, R. J., Hoffman, R. N., Hoffman, M. J., Miyoshi, T., Ide, K., McConnochie, T., and Kalnay, E. (2012).
Ensemble Kalman filter data assimilation of Thermal Emission Spectrometer temperature retrievals into a Mars GCM.
J. Geophys. Res. (Planets), 117(E11).

Grima, C., Kofman, W., Mouginot, J., Phillips, R. J., Hérique, A., Biccari, D., Seu, R., and Cutigni, M. (2009).
North polar deposits of Mars: Extreme purity of the water ice.
Geophysical Research Letters, 36(3).

Grise, K. M. and Davis, S. M. (2020).
Hadley cell expansion in CMIP6 models.
Atmospheric Chemistry and Physics, 20(9):5249–5268.

Guendelman, I. and Kaspi, Y. (2018).
An Axisymmetric Limit for the Width of the Hadley Cell on Planets With Large Obliquity and Long Seasonality.
Geophysical Research Letters, 45(24):13,213–13,221.

Guendelman, I. and Kaspi, Y. (2019).
Atmospheric Dynamics on Terrestrial Planets: The Seasonal Response to Changes in Orbital, Rotational, and Radiative Timescales.
The Astrophysical Journal, 881(1):67.

Guendelman, I. and Kaspi, Y. (2020).
Atmospheric Dynamics on Terrestrial Planets with Eccentric Orbits.
The Astrophysical Journal, 901(1):46.

Guendelman, I., Waugh, D. W., and Kaspi, Y. (2021).
The Emergence of a Summer Hemisphere Jet in Planetary Atmospheres.
Journal of the Atmospheric Sciences, 78(10):3337 – 3348.

Guendelman, I., Waugh, D. W., and Kaspi, Y. (2022).
Dynamical Regimes of Polar Vortices on Terrestrial Planets with a Seasonal Cycle.
The Planetary Science Journal, 3(4):94.

Guzewich, S. D., Toigo, A., and Waugh, D. (2016).
The effect of dust on the martian polar vortices.
Icarus, 278:100 – 118.

Haberle, R. M., Catling, D. C., Carr, M. H., and Zahnle, K. J. (2017a).
The Early Mars Climate System.
Cambridge Planetary Science. Cambridge University Press.

Haberle, R. M., Clancy, R. T., Forget, F., Smith, M. D., and Zurek, R. W. (2017b).
Introduction, page 1–2.
Cambridge Planetary Science. Cambridge University Press.

Haberle, R. M., Murphy, J. R., and Schaeffer, J. (2003).
Orbital change experiments with a Mars general circulation model.
Icarus, 161(1):66–89.

Hadley, G. (1735).
VI. Concerning the cause of the general trade-winds.
Philosophical Transactions of the Royal Society of London, 39(437):58–62.

Hansen, J. E. and Travis, L. D. (1974).
Light scattering in planetary atmospheres.
Space Science Reviews, 16(4):527–610.

Haqq-Misra, J., Wolf, E. T., Joshi, M., Zhang, X., and Kopparapu, R. K. (2018).
Demarcating Circulation Regimes of Synchronously Rotating Terrestrial Planets within the Habitable Zone.
The Astrophysical Journal, 852(2):67.

Harvey, V. L., Randall, C. E., and Hitchman, M. H. (2009).
Breakdown of potential vorticity-based equivalent latitude as a vortex-centered coordinate in the polar winter mesosphere.
J. Geophys. Res. (Atmospheres), 114(D22):D22105.

Haynes, P. and Shuckburgh, E. (2000a).
Effective diffusivity as a diagnostic of atmospheric transport: 1. Stratosphere.
Journal of Geophysical Research: Atmospheres, 105(D18):22777–22794.

Haynes, P. and Shuckburgh, E. (2000b).
Effective diffusivity as a diagnostic of atmospheric transport: 2. Troposphere and lower stratosphere.
Journal of Geophysical Research: Atmospheres, 105(D18):22795–22810.

Heavens, N. G., Johnson, M. S., Abdou, W. A., Kass, D. M., Kleinböhl, A., McCleese, D. J., Shirley, J. H., and Wilson, R. J. (2014).
Seasonal and diurnal variability of detached dust layers in the tropical Martian atmosphere.
J. Geophys. Res. (Planets), 119(8):1748–1774.

Held, I. M. and Hou, A. Y. (1980).
Nonlinear Axially Symmetric Circulations in a Nearly Inviscid Atmosphere.
Journal of Atmospheric Sciences, 37(3):515 – 533.

Held, I. M. and Suarez, M. J. (1994).
A Proposal for the Intercomparison of the Dynamical Cores of Atmospheric General Circulation Models.
Bulletin of the American Meteorological Society, 75(10):1825 – 1830.

Hendricks, E. A. and Schubert, W. H. (2009).
Transport and mixing in idealized barotropic hurricane-like vortices.
Quarterly Journal of the Royal Meteorological Society, 135(643):1456–1470.

Hill, S. A., Bordoni, S., and Mitchell, J. L. (2019).
Axisymmetric Constraints on Cross-Equatorial Hadley Cell Extent.
Journal of the Atmospheric Sciences, 76(6):1547–1564.

Hill, S. A., Bordoni, S., and Mitchell, J. L. (2022).
A Theory for the Hadley Cell Descending and Ascending Edges Throughout the Annual Cycle.
Journal of the Atmospheric Sciences.

Hollingsworth, J. L. and Barnes, J. R. (1996).
Forced Stationary Planetary Waves in Mars's Winter Atmosphere.
Journal of the Atmospheric Sciences, 53(3):428–448.

Holmes, J. A., Lewis, S. R., and Patel, M. R. (2020).
OpenMARS: A global record of martian weather from 1999-2015.
Planetary and Space Science, 188:104962.

Hoskins, B. J., McIntyre, M. E., and Robertson, A. W. (1985).
On the use and significance of isentropic potential vorticity maps.
Quarterly Journal of the Royal Meteorological Society, 111(470):877–946.

Hvidberg, C., Fishbaugh, K., Winstrup, M., Svensson, A., Byrne, S., and Herkenhoff, K. (2012).
Reading the climate record of the martian polar layered deposits.
Icarus, 221(1):405–419.

James, P. B., Christensen, P. R., Clancy, R. T., Lemmon, M. T., and Withers, P. (2017).
History of Mars Atmosphere Observations, page 20–41.
Cambridge Planetary Science. Cambridge University Press.

Juckes, M. N. and McIntyre, M. E. (1987).
A high-resolution one-layer model of breaking planetary waves in the stratosphere.
Nature, 328(6131):590–596.

Kahre, M. A., Murphy, J. R., Newman, C. E., Wilson, R. J., Cantor, B. A., Lemmon, M. T., and Wolff, M. J. (2017).
The Mars Dust Cycle, page 295–337.
Cambridge Planetary Science. Cambridge University Press.

Kang, S. M. and Polvani, L. M. (2011).
The Interannual Relationship between the Latitude of the Eddy-Driven Jet and the Edge of the Hadley Cell.
Journal of Climate, 24(2):563 – 568.

Kaspi, Y. and Showman, A. P. (2015).
Atmospheric Dynamics of Terrestrial Exoplanets Over a Wide Range of Orbital and Atmospheric Parameters.
The Astrophysical Journal, 804(1):60.

Kass, D. M., Kleinböhl, A., McCleese, D. J., Schofield, J. T., and Smith, M. D. (2016).
Interannual similarity in the Martian atmosphere during the dust storm season.
Geophysical Research Letters, 43(12):6111–6118.

Kass, D. M., Schofield, J. T., Kleinböhl, A., McCleese, D. J., Heavens, N. G., Shirley, J. H., and Steele, L. J. (2020).
Mars Climate Sounder Observation of Mars' 2018 Global Dust Storm.
Geophysical Research Letters, 47(23).

Kidston, J., Cairns, C. W., and Paga, P. (2013).
Variability in the width of the tropics and the annular modes.
Geophysical Research Letters, 40(10):2328–2332.

Kidston, J., Scaife, A. A., Hardiman, S. C., Mitchell, D. M., Butchart, N., Baldwin, M. P., and Gray, L. J. (2015).
Stratospheric influence on tropospheric jet streams, storm tracks and surface weather.
Nature Geoscience, 8(6):433–440.

Kim, H. and Lee, S. (2001a).
Hadley Cell Dynamics in a Primitive Equation Model. Part I: Axisymmetric Flow.
Journal of the Atmospheric Sciences, 58(19):2845 – 2858.

Kim, H. and Lee, S. (2001b).
Hadley Cell Dynamics in a Primitive Equation Model. Part II: Nonaxisymmetric Flow.
Journal of the Atmospheric Sciences, 58(19):2859 – 2871.

Kipping, D. M. and Sandford, E. (2016).
Observational biases for transiting planets.
Monthly Notices of the Royal Astronomical Society, 463(2):1323–1331.

Kopparapu, R., Wolf, E. T., Arney, G., Batalha, N. E., Haqq-Misra, J., Grimm, S. L., and Heng, K. (2017).
Habitable Moist Atmospheres on Terrestrial Planets near the Inner Edge of the Habitable Zone around M Dwarfs.
The Astrophysical Journal, 845(1):5.

Kopparapu, R., Wolf, E. T., Haqq-Misra, J., Yang, J., Kasting, J. F., Meadows, V., Terrien, R., and Mahadevan, S. (2016).
THE INNER EDGE OF THE HABITABLE ZONE FOR SYNCHRONOUSLY ROTATING PLANETS AROUND LOW-MASS STARS USING GENERAL CIRCULATION MODELS.
The Astrophysical Journal, 819(1):84.

Lait, L. R. (1994).
An Alternative Form for Potential Vorticity.
Journal of Atmospheric Sciences, 51(12):1754–1759.

Laskar, J., Correia, A., Gastineau, M., Joutel, F., Levrard, B., and Robutel, P. (2004).
Long term evolution and chaotic diffusion of the insolation quantities of Mars.
Icarus, 170(2):343–364.

Laskar, J., Levrard, B., and Mustard, J. F. (2002).
Orbital forcing of the martian polar layered deposits.
Nature, 419(6905):375–377.

Lee, S. and Kim, H. (2003).
The Dynamical Relationship between Subtropical and Eddy-Driven Jets.
Journal of the Atmospheric Sciences, 60(12):1490 – 1503.

Leovy, C. (2001).
Weather and climate on Mars.
Nature, 412(6843):245–249.

Leovy, C. and Mintz, Y. (1969).
Numerical Simulation of the Atmospheric Circulation and Climate of Mars.
Journal of the Atmospheric Sciences, 26(6):1167–1190.

Lewis, N. T., Colyer, G. J., and Read, P. L. (2021).
Characterizing Regimes of Atmospheric Circulation in Terms of Their Global Superrotation.
Journal of the Atmospheric Sciences, 78(4):1245–1258.

Lewis, N. T. and Hammond, M. (2022).
Temperature Structures Associated with Different Components of the Atmospheric Circulation on Tidally Locked Exoplanets.
The Astrophysical Journal, 941(2):171.

Lewis, S. R. (2003).
Modelling the martian atmosphere.
Astronomy and Geophysics, 44(4):4.06–4.14.

Lewis, S. R., Mulholland, D. P., Read, P. L., Montabone, L., Wilson, R. J., and Smith, M. D. (2016).
The solsticial pause on Mars: 1. A planetary wave reanalysis.
Icarus, 264:456–464.

Lindzen, R. S. and Hou, A. V. (1988).
Hadley Circulations for Zonally Averaged Heating Centered off the Equator.
Journal of Atmospheric Sciences, 45(17):2416 – 2427.

Linsenmeier, M., Pascale, S., and Lucarini, V. (2015).
Climate of Earth-like planets with high obliquity and eccentric orbits: Implications for habitability conditions.
Planetary and Space Science, 105:43–59.

Lu, J., Vecchi, G. A., and Reichler, T. (2007).
Expansion of the Hadley cell under global warming.
Geophysical Research Letters, 34(6).

Madeleine, J.-B., Forget, F., Millour, E., Montabone, L., and Wolff, M. (2011).
Revisiting the radiative impact of dust on Mars using the LMD Global Climate Model.
J. Geophys. Res., 116:E11010.

Madeleine, J.-B., Forget, F., Millour, E., Navarro, T., and Spiga, A. (2012).
The influence of radiatively active water ice clouds on the Martian climate.
Geo. Res. Lett., 39(23):L23202.

Maher, P., Gerber, E. P., Medeiros, B., Merlis, T. M., Sherwood, S., Sheshadri, A., Sobel, A. H., Vallis, G. K., Voigt, A., and Zurita-Gotor, P. (2019a).
Model Hierarchies for Understanding Atmospheric Circulation.
Reviews of Geophysics, 57(2):250–280.

Maher, P., Gerber, E. P., Medeiros, B., Merlis, T. M., Sherwood, S., Sheshadri, A., Sobel, A. H., Vallis, G. K., Voigt, A., and Zurita-Gotor, P. (2019b).
Model Hierarchies for Understanding Atmospheric Circulation.
Reviews of Geophysics, 57(2):250–280.

Manners, J., Edwards, J. M., Hill, P., and Thelen, J.-C. (2017).
SOCRATES Technical Guide: Suite Of Community RAdiative Transfer codes based on Edwards and Slingo.
Technical report, U. K. Met Office.

Manney, G. L., Butler, A. H., Lawrence, Z. D., Wargan, K., and Santee, M. L. (2022).
What's in a Name? On the Use and Significance of the Term “Polar Vortex”.
Geophysical Research Letters, 49(10).

Manney, G. L., Krüger, K., Pawson, S., Minschwaner, K., Schwartz, M. J., Daffer, W. H., Livesey, N. J., Mlynczak, M. G., Remsberg, E. E., Russell, J. M., and Waters, J. W. (2008).
The evolution of the stratopause during the 2006 major warming: Satellite data and assimilated meteorological analyses.
Journal of Geophysical Research, 113(D11).

Martin, T. Z. and Kieffer, H. H. (1979).
Thermal infrared properties of the Martian atmosphere: 2. The 15-μm band measurements.
Journal of Geophysical Research, 84(B6):2843.

McCleese, D. J., Schofield, J. T., Taylor, F. W., Abdou, W. A., Aharonson, O., Banfield, D., Calcutt, S. B., Heavens, N. G., Irwin, P. G. J., Kass, D. M., Kleinböhl, A., Lawson, W. G., Leovy, C. B., Lewis, S. R., Paige, D. A., Read, P. L., Richardson, M. I., Teanby, N., and Zurek, R. W. (2008).
Intense polar temperature inversion in the middle atmosphere on Mars.
Nature Geoscience, 1(11):745–749.

McCulloch, D., Sergeev, D. E., Mayne, N., Bate, M., Manners, J., Boutle, I., Drummond, B., and Kohary, K. (2023).
A modern-day Mars climate in the Met Office Unified Model: dry simulations.
Geoscientific Model Development, 16(2):621–657.

McDunn, T., Bougher, S., Murphy, J., Kleinböhl, A., Forget, F., and Smith, M. (2013).
Characterization of middle-atmosphere polar warming at Mars.
Journal of Geophysical Research: Planets, 118(2):161–178.

McIntyre, M. (1989).
On the Antarctic ozone hole.
Journal of Atmospheric and Terrestrial Physics, 51(1):29–43.

McIntyre, M. E. (1995).
The stratospheric polar vortex and sub-vortex : fluid dynamics and midlatitude ozone loss.
Philosophical Transactions of the Royal Society of London. Series A: Physical and Engineering Sciences, 352(1699):227–240.

McIntyre, M. E. and Palmer, T. N. (1983).
Breaking planetary waves in the stratosphere.
Nature, 305(5935):593–600.

Mellon, M. (2000).
High-Resolution Thermal Inertia Mapping from the Mars Global Surveyor Thermal Emission Spectrometer.
Icarus, 148(2):437–455.

Menzel, M. E., Waugh, D., and Grise, K. (2019).
Disconnect Between Hadley Cell and Subtropical Jet Variability and Response to Increased CO_2.
Geophysical Research Letters, 46(12):7045–7053.

Menzel, M. E., Waugh, D., Wu, Z., and Reichler, T. (2021).
A Refined View of the Subtropical Jet and Hadley Cell Coupling.
in prep.

MEPAG (ed. 2020).
Mars Scientific Goals, Objectives, Investigations, and Priorities: 2020.
page 89 p.

Millour, E., Forget, F., Spiga, A., Vals, M., Zakharov, V., Montabone, L., Lefèvre, F., Montmessin, F., Chaufray, J. Y., López-Valverde, M. A., González-Galindo, F., Lewis, S. R., Read, P. L., Desjean, M. C., Cipriani, F., and MCD Development Team (2018).
The Mars Climate Database (version 5.3).
In *From Mars Express to ExoMars*, page 68.

Mischna, M. A. (2003).
On the orbital forcing of Martian water and CO_2 cycles: A general circulation model study with simplified volatile schemes.
Journal of Geophysical Research, 108(E6).

Mitchell, D. M., Gray, L. J., Anstey, J., Baldwin, M. P., and Charlton-Perez, A. J. (2013).
The Influence of Stratospheric Vortex Displacements and Splits on Surface Climate.
Journal of Climate, 26(8):2668–2682.

Mitchell, D. M., Montabone, L., Thomson, S., and Read, P. L. (2014).
Polar vortices on Earth and Mars: A comparative study of the climatology and variability from reanalyses.
Quarterly Journal of the Royal Meteorological Society, 141(687):550–562.

Mitchell, D. M., Scott, R. K., Seviour, W. J. M., Thomson, S. I., Waugh, D. W., Teanby, N. A., and Ball, E. R. (2021).
Polar Vortices in Planetary Atmospheres.
Reviews of Geophysics, 59(4).

Montabone, L., Forget, F., Millour, E., Wilson, R., Lewis, S., Cantor, B., Kass, D., Kleinböhl, A., Lemmon, M., Smith, M., and Wolff, M. (2015).
Eight-year climatology of dust optical depth on Mars.
Icarus, 251:65 – 95.
Dynamic Mars.

Montabone, L., Marsh, K., Lewis, S. R., Read, P. L., Smith, M. D., Holmes, J., Spiga, A., Lowe, D., and Pamment, A. (2014).
The Mars Analysis Correction Data Assimilation (MACDA) Dataset V1.0.
Geoscience Data Journal, 1(2):129–139.

Montabone, L., Spiga, A., Kass, D. M., Kleinböhl, A., Forget, F., and Millour, E. (2020).
Martian Year 34 Column Dust Climatology from Mars Climate Sounder Observations: Reconstructed Maps and Model Simulations.
J. Geophys. Res. (Planets), 125(8):e2019JE006111.
e2019JE006111 10.1029/2019JE006111.

Montmessin, F., Forget, F., Rannou, P., Cabane, M., and Haberle, R. M. (2004).
Origin and role of water ice clouds in the Martian water cycle as inferred from a general circulation model.
J. Geophys. Res. (Planets), 109(E10):E10004.

Mooring, T. A., Davis, G. E., and Greybush, S. J. (2022).
Low-Level Jets and the Convergence of Mars Data Assimilation Algorithms.
Journal of Geophysical Research: Planets, 127(2).

Mulholland, D. P., Lewis, S. R., Read, P. L., Madeleine, J.-B., and Forget, F. (2016).
The solsticial pause on Mars: 2 modelling and investigation of causes.
Icarus, 264:465–477.

Murray, B. C., Soderblom, L. A., Cutts, J. A., Sharp, R. P., Milton, D. J., and Leighton, R. B. (1972).
Geological framework of the south polar region of Mars.
Icarus, 17(2):328–345.

Nakamura, N. (1996).

Two-Dimensional Mixing, Edge Formation, and Permeability Diagnosed in an Area Coordinate.
Journal of Atmospheric Sciences, 53(11):1524 – 1537.

Nakamura, N. (2008).
Quantifying Inhomogeneous, Instantaneous, Irreversible Transport Using Passive Tracer Field as a Coordinate.
In *Transport and Mixing in Geophysical Flows*, pages 137–164. Springer Berlin Heidelberg.

NASA (2023).
Webb confirms its first exoplanet.
https://exoplanets.nasa.gov/news/1722/webb-confirms-its-first-exoplanet/, page accessed 14/03/2023.

Nash, E. R., Newman, P. A., Rosenfield, J. E., and Schoeberl, M. R. (1996).
An objective determination of the polar vortex using Ertel's potential vorticity.
Journal of Geophysical Research: Atmospheres, 101(D5):9471–9478.

Nayvelt, L., Gierasch, P. J., and Cook, K. H. (1997).
Modeling and Observations of Martian Stationary Waves.
Journal of the Atmospheric Sciences, 54(8):986–1013.

Newman, C. E., Lewis, S. R., and Read, P. L. (2005).
The atmospheric circulation and dust activity in different orbital epochs on Mars.
Icarus, 174(1):135–160.

Newman, C. E. and Richardson, M. I. (2015).
The impact of surface dust source exhaustion on the martian dust cycle, dust storms and interannual variability, as simulated by the marswrf general circulation model.
Icarus, 257:47–87.

Nguyen, H., Evans, A., Lucas, C., Smith, I., and Timbal, B. (2013).
The Hadley Circulation in Reanalyses: Climatology, Variability, and Change.
Journal of Climate, 26(10):3357 – 3376.

O'Neill, M. E., Emanuel, K. A., and Flierl, G. R. (2015).
Polar vortex formation in giant-planet atmospheres due to moist convection.
Nature Geoscience, 8(7):523–526.

Penn, J. and Vallis, G. K. (2017).
The Thermal Phase Curve Offset on Tidally and Nontidally Locked Exoplanets: A Shallow Water Model.
The Astrophysical Journal, 842(2):101.

Penn, J. and Vallis, G. K. (2018).

Atmospheric Circulation and Thermal Phase-curve Offset of Tidally and Nontidally Locked Terrestrial Exoplanets.
The Astrophysical Journal, 868(2):147.

Perron, J. T. and Huybers, P. (2009).
Is there an orbital signal in the polar layered deposits on Mars?
Geology, 37(2):155–158.

Pierce, R. B. and Fairlie, T. D. A. (1993).
Chaotic advection in the stratosphere: Implications for the dispersal of chemically perturbed air from the polar vortex.
Journal of Geophysical Research: Atmospheres, 98(D10):18589–18595.

Pierrehumbert, R. T. (1991).
Large-scale horizontal mixing in planetary atmospheres.
Physics of Fluids A: Fluid Dynamics, 3(5):1250–1260.

Pierrehumbert, R. T. and Ding, F. (2016).
Dynamics of atmospheres with a non-dilute condensible component.
Proceedings of the Royal Society A: Mathematical, Physical and Engineering Sciences, 472(2190):20160107.

Pirraglia, J. A. (1975).
Polar Symmetric Flow of a Viscous Compressible Atmosphere: An Application to Mars.
Journal of the Atmospheric Sciences, 32(1):60–72.

Plaut, J. J., Picardi, G., Safaeinili, A., Ivanov, A. B., Milkovich, S. M., Cicchetti, A., Kofman, W., Mouginot, J., Farrell, W. M., Phillips, R. J., Clifford, S. M., Frigeri, A., Orosei, R., Federico, C., Williams, I. P., Gurnett, D. A., Nielsen, E., Hagfors, T., Heggy, E., Stofan, E. R., Plettemeier, D., Watters, T. R., Leuschen, C. J., and Edenhofer, P. (2007).
Subsurface Radar Sounding of the South Polar Layered Deposits of Mars.
Science, 316(5821):92–95.

Pollack, J. B., Colburn, D. S., Flasar, F. M., Kahn, R., Carlston, C. E., and Pidek, D. G. (1979).
Properties and effects of dust particles suspended in the Martian atmosphere.
J. Geophys. Res., 84:2929–2945.

Polvani, L. M. and Kushner, P. J. (2002).
Tropospheric response to stratospheric perturbations in a relatively simple general circulation model.
Geophysical Research Letters, 29(7):18–1–18–4.

Polvani, L. M. and Plumb, R. A. (1992).
Rossby Wave Breaking, Microbreaking, Filamentation, and Secondary Vortex Formation: The Dynamics of a Perturbed Vortex.
Journal of the Atmospheric Sciences, 49(6):462–476.

Qian, Y.-K., Peng, S., and Liang, C.-X. (2019).
Reconciling Lagrangian Diffusivity and Effective Diffusivity in Contour-Based Coordinates.
Journal of Physical Oceanography, 49(6):1521 – 1539.

Read, P. L., Gierasch, P. J., Conrath, B. J., Simon-Miller, A., Fouchet, T., and Yamazaki, Y. H. (2007).
Mapping potential-vorticity dynamics on Jupiter. I: Zonal-mean circulation from Cassini and Voyager 1 data.
Quarterly Journal of the Royal Meteorological Society, 132(618):1577–1603.

Read, P. L., Lewis, S. R., and Vallis, G. K. (2018).
Atmospheric Dynamics of Terrestrial Planets.
In *Handbook of Exoplanets*, pages 1–31. Springer International Publishing.

Richardson, M. I. and Wilson, R. J. (2002).
A topographically forced asymmetry in the martian circulation and climate.
Nature, 416(6878):298–301.

Rostami, M., Zeitlin, V., and Montabone, L. (2018).
On the role of spatially inhomogeneous diabatic effects upon the evolution of Mars' annular polar vortex.
Icarus, 314:376 – 388.

Sánchez-Lavega, A., Lebonnois, S., Imamura, T., Read, P., and Luz, D. (2017).
The Atmospheric Dynamics of Venus.
Space Science Reviews, 212(3-4):1541–1616.

Schneider, E. K. (1983).
Martian great dust storms: Interpretive axially symmetric models.
Icarus, 55(2):302–331.

Schoeberl, M. R. and Hartmann, D. L. (1991).
The Dynamics of the Stratospheric Polar Vortex and Its Relation to Springtime Ozone Depletions.
Science, 251(4989):46–52.

Scott, R. K., Seviour, W. J. M., and Waugh, D. W. (2020).
Forcing of the Martian polar annulus by Hadley cell transport and latent heating.
Quarterly Journal of the Royal Meteorological Society, 146(730):2174–2190.

Seager, R., Ting, M., Held, I., Kushnir, Y., Lu, J., Vecchi, G., Huang, H.-P., Harnik, N., Leetmaa, A., Lau, N.-C., Li, C., Velez, J., and Naik, N. (2007).
Model Projections of an Imminent Transition to a More Arid Climate in Southwestern North America.
Science, 316(5828):1181–1184.

Seviour, W. J. M., Waugh, D. W., and Scott, R. K. (2017).
The Stability of Mars's Annular Polar Vortex.
Journal of Atmospheric Sciences, 74(5):1533–1547.

Sharkey, J., Teanby, N. A., Sylvestre, M., Mitchell, D. M., Seviour, W. J., Nixon, C. A., and Irwin, P. G. (2021).
Potential vorticity structure of Titan's polar vortices from Cassini CIRS observations.
Icarus, 354:114030.

Shen, X., Wang, L., and Osprey, S. (2020).
The Southern Hemisphere sudden stratospheric warming of September 2019.
Science Bulletin, 65(21):1800–1802.

Shirley, J. H. (2015).
Solar System dynamics and global-scale dust storms on Mars.
Icarus, 251:128 – 144.
Dynamic Mars.

Shirley, J. H., McKim, R. J., Battalio, J. M., and Kass, D. M. (2020).
Orbit-Spin Coupling and the Triggering of the Martian Planet-Encircling Dust Storm of 2018.
J. Geophys. Res. (Planets), 125(6):e2019JE006077.
e2019JE006077 2019JE006077.

Shultis, J., Waugh, D. W., Toigo, A. D., Newman, C. E., Teanby, N. A., and Sharkey, J. (2022).
Winter Weakening of Titan's Stratospheric Polar Vortices.
The Planetary Science Journal, 3(4):73.

Singh, M. S. (2019).
Limits on the Extent of the Solsticial Hadley Cell: The Role of Planetary Rotation.
Journal of the Atmospheric Sciences, 76(7):1989 – 2004.

Smith, D. E., Zuber, M. T., Solomon, S. C., Phillips, R. J., Head, J. W., Garvin, J. B., Banerdt, W. B., Muhleman, D. O., Pettengill, G. H., Neumann, G. A., Lemoine, F. G., Abshire, J. B., Aharonson, O., David, C. B., Hauck, S. A., Ivanov, A. B., McGovern, P. J., Zwally, H. J., and Duxbury, T. C. (1999).
The Global Topography of Mars and Implications for Surface Evolution.
Science, 284(5419):1495–1503.

Smith, I. B., Hayne, P. O., Byrne, S., Becerra, P., Kahre, M., Calvin, W., Hvidberg, C., Milkovich, S., Buhler, P., Landis, M., Horgan, B., Kleinböhl, A., Perry, M. R., Obbard, R., Stern, J., Piqueux, S., Thomas, N., Zacny, K., Carter, L., Edgar, L., Emmett, J., Navarro, T., Hanley, J., Koutnik, M., Putzig, N., Henderson, B. L., Holt, J. W., Ehlmann, B., Parra, S., Lalich, D., Hansen, C., Hecht, M., Banfield, D., Herkenhoff, K., Paige, D. A., Skidmore, M., Staehle, R. L., and Siegler, M. (2020).

The Holy Grail: A road map for unlocking the climate record stored within Mars' polar layered deposits.
Planetary and Space Science, 184:104841.

Smith, M. D. (2004).
Interannual variability in TES atmospheric observations of Mars during 1999–2003.
Icarus, 167(1):148–165.

Solomon, A., Polvani, L. M., Waugh, D. W., and Davis, S. M. (2016).
Contrasting upper and lower atmospheric metrics of tropical expansion in the Southern Hemisphere.
Geophysical Research Letters, 43(19):10,496–10,503.

Solomon, S. (1990).
Progress towards a quantitative understanding of Antarctic ozone depletion.
Nature, 347(6291):347–354.

Spiga, A., Banfield, D., Teanby, N. A., Forget, F., Lucas, A., Kenda, B., Manfredi, J. A. R., Widmer-Schnidrig, R., Murdoch, N., Lemmon, M. T., Garcia, R. F., Martire, L., Özgür Karatekin, Maistre, S. L., Hove, B. V., Dehant, V., Lognonné, P., Mueller, N., Lorenz, R., Mimoun, D., Rodriguez, S., Beucler, É., Daubar, I., Golombek, M. P., Bertrand, T., Nishikawa, Y., Millour, E., Rolland, L., Brissaud, Q., Kawamura, T., Mocquet, A., Martin, R., Clinton, J., Stutzmann, É., Spohn, T., Smrekar, S., and Banerdt, W. B. (2018).
Atmospheric Science with InSight.
Space Science Reviews, 214(7).

Streeter, P. M., Lewis, S. R., Patel, M. R., Holmes, J. A., Fedorova, A. A., Kass, D. M., and Kleinböhl, A. (2021).
Asymmetric impacts on Mars' polar vortices from an equinoctial Global Dust Storm.
Journal of Geophysical Research: Planets, 126:e2020JE006774.
e2020JE006774 2020JE006774.

Teanby, N. A., Bézard, B., Vinatier, S., Sylvestre, M., Nixon, C. A., Irwin, P. G. J., de Kok, R. J., Calcutt, S. B., and Flasar, F. M. (2017).
The formation and evolution of Titan's winter polar vortex.
Nature Communications, 8(1).

Teanby, N. A., de Kok, R., Irwin, P. G. J., Osprey, S., Vinatier, S., Gierasch, P. J., Read, P. L., Flasar, F. M., Conrath, B. J., Achterberg, R. K., Bézard, B., Nixon, C. A., and Calcutt, S. B. (2008).
Titan's winter polar vortex structure revealed by chemical tracers.
Journal of Geophysical Research, 113(E12).

Thomson, S. I. and Vallis, G. K. (2019a).
The effects of gravity on the climate and circulation of a terrestrial planet.
Quarterly Journal of the Royal Meteorological Society, 145(723):2627–2640.

Thomson, S. I. and Vallis, G. K. (2019b).
Hierarchical Modeling of Solar System Planets with Isca.
Atmosphere, 10(12):803.

Tillman, J. E. (1988).
Mars global atmospheric oscillations: annually synchronized, transient normal-mode oscillations and the triggering of global dust storms.
J. Geophys. Res., 93:9433–9451.

Toigo, A. D., Lee, C., Newman, C. E., and Richardson, M. I. (2012).
The impact of resolution on the dynamics of the martian global atmosphere: Varying resolution studies with the MarsWRF GCM.
Icarus, 221(1):276–288.

Toigo, A. D. and Waugh, D. W. (2022).
Connections between the Transient Polar Warming and Solstitial Pause on Mars.
The Planetary Science Journal, 3(9):208.

Toigo, A. D., Waugh, D. W., and Guzewich, S. D. (2017).
What causes Mars' annular polar vortices?
Geo. Res. Lett., 44(1):71–78.

Toigo, A. D., Waugh, D. W., and Guzewich, S. D. (2020).
Atmospheric transport into polar regions on Mars in different orbital epochs.
Icarus, 347:113816.

Toon, O. B., Pollack, J. B., Ward, W., Burns, J. A., and Bilski, K. (1980).
The astronomical theory of climatic change on Mars.
Icarus, 44(3):552–607.

Vallis, G. K. (2017).
Atmospheric and Oceanic Fluid Dynamics.
Cambridge University Press.

Vallis, G. K., Colyer, G., Geen, R., Gerber, E., Jucker, M., Maher, P., Paterson, A., Pietschnig, M., Penn, J., and Thomson, S. I. (2018).
Isca, v1.0: a framework for the global modelling of the atmospheres of Earth and other planets at varying levels of complexity.
Geoscientific Model Development, 11(3):843–859.

Walker, C. C. and Schneider, T. (2006).
Eddy Influences on Hadley Circulations: Simulations with an Idealized GCM.
Journal of Atmospheric Sciences, 63(12):3333–3350.

Wang, H. and Richardson, M. I. (2015).
The origin, evolution, and trajectory of large dust storms on Mars during Mars years 24–30 (1999–2011).

Icarus, 251:112 – 127.
Dynamic Mars.

Ward, W. R. (1973).
Large-scale variations in the obliquity of mars.
Science, 181(4096):260–262.

Ward, W. R. and Rudy, D. J. (1991).
Resonant obliquity of Mars?
Icarus, 94(1):160–164.

Waugh, D., Toigo, A., and Guzewich, S. (2019).
Age of martian air: Time scales for martian atmospheric transport.
Icarus, 317:148 – 157.

Waugh, D. W. (2023).
Fluid Dynamics of Polar Vortices on Earth, Mars, and Titan.
Annual Review of Fluid Mechanics, 55(1):265–289.

Waugh, D. W., Grise, K. M., Seviour, W. J. M., Davis, S. M., Davis, N., Adam, O., Son, S.-W., Simpson, I. R., Staten, P. W., Maycock, A. C., Ummenhofer, C. C., Birner, T., and Ming, A. (2018).
Revisiting the Relationship among Metrics of Tropical Expansion.
Journal of Climate, 31(18):7565 – 7581.

Waugh, D. W., Sobel, A. H., and Polvani, L. M. (2017).
What Is the Polar Vortex and How Does It Influence Weather?
Bulletin of the American Meteorological Society, 98(1):37–44.

Waugh, D. W., Toigo, A. D., Guzewich, S. D., Greybush, S. J., Wilson, R. J., and Montabone, L. (2016).
Martian polar vortices: Comparison of reanalyses.
J. Geophys. Res. (Planets), 121(9):1770–1785.

Way, M. J., Aleinov, I., Amundsen, D. S., Chandler, M. A., Clune, T. L., Genio, A. D. D., Fujii, Y., Kelley, M., Kiang, N. Y., Sohl, L., and Tsigaridis, K. (2017).
Resolving Orbital and Climate Keys of Earth and Extraterrestrial Environments with Dynamics (ROCKE-3D) 1.0: A General Circulation Model for Simulating the Climates of Rocky Planets.
Astrophys. J., Supp., 231(1):12.

Wilson, R., Banfield, D., Conrath, B., and Smith, M. (2002).
Traveling waves in the Northern Hemisphere of Mars.
Geo. Res. Lett., 29:14.

Wilson, R. J. (1997).
A general circulation model simulation of the Martian polar warming.
Geophysical Research Letters, 24(2):123–126.

Wolff, M. J., Smith, M. D., Clancy, R. T., Arvidson, R., Kahre, M., Seelos, F., Murchie, S., and Savijärvi, H. (2009).
Wavelength dependence of dust aerosol single scattering albedo as observed by the Compact Reconnaissance Imaging Spectrometer.
J. Geophys. Res. (Planets), 114(E9):E00D04.

Wolff, M. J., Smith, M. D., Clancy, R. T., Spanovich, N., Whitney, B. A., Lemmon, M. T., Bandfield, J. L., Banfield, D., Ghosh, A., Landis, G., Christensen, P. R., Bell III, J. F., and Squyres, S. W. (2006).
Constraints on dust aerosols from the Mars Exploration Rovers using MGS overflights and Mini-TES.
J. Geophys. Res. (Planets), 111(E12):E12S17.

Wolkenberg, P., Giuranna, M., Smith, M., Grassi, D., and Amoroso, M. (2020).
Similarities and Differences of Global Dust Storms in MY 25, 28, and 34.
J. Geophys. Res. (Planets), 125(3):e2019JE006104.

Zurek, R. W. and Martin, L. J. (1993).
Interannual variability of planet-encircling dust storms on Mars.
Journal of Geophysical Research: Planets, 98(E2):3247–3259.